HABILITATION À DIRIGER DES RECHERCHES

Présentée par

Olivier Limousin
CEA-Saclay

The story of Caliste:
CdTe based pixel detectors for
Hard X- Ray astronomy in space

Soutenue le 08/09/2016 devant le jury composé de :

Pr. T. Patzak, Université Paris 7	Président et rapporteur interne
Dr. G. Calderini, CNRS/IN2P3	Rapporteur externe
Dr. A. Owens, ESA/ESTEC	Rapporteur externe
Pr. T. Takahashi, JAXA/ISAS	Examinateur
Pr. D. Barbier, INSA-Lyon	Examinateur
Pr. Y. Bonnassieux, École polytechnique	Examinateur
Pr. Säm Krucker, UCB et FHNW	Examinateur

Commissariat à l'énergie atomique et aux énergies alternatives – Centre de Saclay
Institut de recherche sur les lois fondamentales de l'Univers
Service d'astrophysique

« L'imagination est plus importante que la connaissance. »
A. Einstein

Acknowledgments

Forward (French)

Quelles sont les raisons qui peuvent conduire un chercheur à écrire une Habilitation à Diriger des Recherches ?

Voilà une question que je me suis posée pendant plus de 5 ans, estimant souvent que le fait de ne pas y trouver une réponse « scientifique » était une raison suffisante pour reporter l'échéance. J'ai aujourd'hui acquis la conviction que le moment est venu de me présenter à cet examen et j'expose ici brièvement les quelques raisons principales qui m'ont décidé à écrire ce document. Ces raisons sont sans doute discutables et reflètent une opinion personnelle mais, si elles peuvent servir à mes proches collègues à se lancer dans leur propre rédaction, alors cela mérite peut-être de s'y attarder un moment.

Mes collègues, ma hiérarchie, mon entourage ont souvent vanté auprès de moi le fait que l'HDR était un outil pour « faire le point », « dresser un bilan », « illustrer son expertise » ou ce type de vertus... Autant d'arguments qui n'ont pas fait mouche dans un premier temps, ces propositions étant un peu abstraites pour moi et surtout inutiles à mes yeux au regard de l'effort à fournir, jouissant par ailleurs d'un vif sentiment de reconnaissance au travail. Le plus ennuyeux de mon point de vue était sans doute de n'avoir jamais entendu (ou voulu entendre) parler des notions « d'habilitation » ni de de « direction de recherches » - mon métier actuel, et depuis une dizaine d'années, étant au sens du CEA de diriger des recherches en tant que chef de laboratoire et également en tant que responsable scientifique dans de nombreux projets, j'ai toujours eu l'impression d'être implicitement « habilité » par mon employeur à faire mon métier. Bref, je ne me suis jamais véritablement senti concerné.

Ce que j'ai finalement compris, c'est le sens que cela devait revêtir pour moi vis à vis de l'université et des étudiants en doctorat. C'est le principal maillon qui me manquait, en plus du temps : les étudiants. Après avoir personnellement dirigé trois thèses, entamé une quatrième, et avoir été membre de quelques jurys comme rapporteur ou examinateur, j'ai réalisé que l'absence d'HDR était un frein, une condition. Evidemment, dérogations et partenariats avec des collègues habilités ont toujours permis de sauver la face mais finalement, ne pas pouvoir figurer sur la page de garde d'une thèse d'un étudiant que l'on a encadré personnellement est tout de même gênant pour soi-même, pour l'étudiant et pour le laboratoire. C'est ma motivation principale dans cette démarche.

Ce germe de motivation, un peu administrative de fait, m'a conduit à réfléchir au statut de la recherche instrumentale au sein d'un grand institut de recherche fondamentale comme l'Irfu. La première observation que j'ai faite est que les « instrumentalistes habilités » ne sont pas légion, parmi les « jeunes » (je m'inclus dans cette population), les plus anciens ayant une thèse d'Etat. Pourtant le nombre de chercheurs instrumentalistes dans l'institut est très grand. Ceci traduit un sentiment courant, profondément ancré dans le vocabulaire quotidien, que les « scientifiques » sont les fondamentalistes et les « instrumentalistes » des ingénieurs. Il n'y a rien de péjoratif là-dedans et pourtant. Or le CEA offre à ses cadres un statut commun aux « chercheurs » et aux « ingénieurs », celui d'ingénieur-chercheur ; c'est un atout considérable pour constituer des équipes équilibrées. Finalement, les « instrumentalistes » sont des chercheurs à part entière dans un institut comme le mien et font de la science, leur science, au service d'autres sciences. Augmenter la population d'HDR parmi les « instrumentalistes » est une chance d'augmenter la visibilité de cette science instrumentale ou expérimentale, sans laquelle aucune découverte majeure n'est finalement confirmée. J'aime imaginer que le Boson de Higgs est une particule mathématique depuis 1964 et qu'elle devient réalité en 2013 dans les cathédrales de détecteurs du CERN. En bref, l'instrumentation étant une science parmi les autres, les chercheurs qui la pratiquent, doivent se plier aux mêmes processus d'habilitation que les autres chercheurs pour qui la démarche HDR semble plus naturelle.

Pour finir, ce document est l'occasion de relater l'approche de R & D que j'ai mise en œuvre et menée jusqu'à son terme, bien entendu avec une cohorte de spécialistes en physique des détecteurs, en électronique, en packaging et en astrophysique. C'est la première fois que nous disposerons d'un document de synthèse dans lequel la stratégie de développement et les principaux résultats de l'équipe figurent sans être « éparpillés » dans plusieurs publications et thèses. C'est la « petite histoire de Caliste ». J'ajoute l'adjectif « petite » car notre projet s'inscrit dans un paysage très

concurrentiel et très spécialisé. Notre contribution à la discipline qu'est le développement de détecteurs X durs à base de CdTe pour l'astronomie spatiale est forte mais modeste.

Et puis, j'ai promis à ma hiérarchie et à mes proches de le faire, alors c'est parti !

Résumé (French)

Immédiatement après le tir d'INTEGRAL le 17 Octobre 2002, j'ai entamé une réflexion sur les perspectives d'utilisation du CdTe comme spectro-imageur à rayons X-durs pour les futures missions d'astronomie spatiale à haute-énergie. Ce travail m'a conduit à réaliser que les limitations spectrométriques d'ISGRI pouvaient être surmontées en axant mes efforts vers la conception de nouveaux détecteurs à électrodes segmentées en petits pixels. En effet, ISGRI souffre d'une part de l'utilisation de détecteurs ohmiques de grande taille dont le courant d'obscurité élevé provoque un bruit électronique important dont la conséquence est une résolution spectrale modeste et un seuil bas relativement élevé.

D'autre part, le courant élevé limite la tension applicable au détecteur provoquant un signal lent et dépendant de la profondeur de pénétration des photons dans le volume en raison des piètres propriétés de transports des trous dans ce semiconducteur. Pour autant, du fait de ses propriétés intrinsèques de masse et de densité élevées, le CdTe reste le candidat idéal pour la détection des rayons X durs au regard de ses concurrents les plus sérieux : le germanium et le silicium.

En réduisant la taille des pixels, outre l'amélioration naturelle de la résolution spatiale, le courant dans chaque pixel s'en trouve proportionnellement réduit. Il en va de même pour la capacité parasite présentée à l'entrée des amplificateurs de charges connectés à chaque pixel. En abandonnant les contacts ohmiques au profit de contacts bloquants de type Schottky, le courant d'obscurité peut être réduit de trois ordres de grandeurs si les pixels sont suffisamment petits. Ceci a pour conséquence de pouvoir augmenter considérablement le champ électrique dans le volume du semiconducteur et d'obtenir des signaux suffisamment rapides pour limiter la perte de charge et la perte balistique et de fait, de rendre la réponse quasiment indépendante de la profondeur de pénétration des photons dans le volume. Voilà la motivation initiale à laquelle s'ajoute le fait que les signaux s'induisent différemment dans un détecteur coplanar que dans un détecteur à petits pixels segmentés où les trous sont écrantés par un champ de pondération désormais favorable. Bref, une fois n'est pas coutume, la réduction de la taille des pixels n'a que des avantages sur les performances d'un spectro-imageur. Naturellement, cette volonté de réduire la taille des pixels d'un facteur 100 environ soulève des défis technologiques importants. C'est ce défi que j'ai relevé ces dernières années et qui a donné naissance au concept de spectro-imageur miniature Caliste que je présente dans cette Habilitation à Diriger des Recherches.

François Lebrun, responsable scientifique d'ISGRI, également mon directeur de thèse, m'a formé dans l'idée que la résolution et le seuil sont des gages de sensibilité et doivent faire l'objet d'une attention particulière. C'est tout le sens de mon travail ces 15 dernières années. Mon objectif était donc très clair : passer la résolution spectrale de 6 keV à 60 keV à moins de 1 keV.

Pour relever ce défi, j'ai abordé de front la conception d'un système entièrement nouveau prenant en compte l'étude des détecteurs CdTe Schottky à anode segmentée, l'électronique intégrée optimisée pour la lecture de ces détecteurs particuliers, la conception de l'hybridation de l'un avec l'autre et la qualification spatiale de l'ensemble. J'ai constitué une équipe transverse SAp et SEDI, grâce au soutien d'Eric Delagnes, Philippe Lavocat et Philippe Rebourgeard qui nous ont permis de démarrer le développement d'IDeF-X, un ASIC conçu par Olivier Gevin et Francis Lugiez dans le but de réaliser des préamplificateurs de charges ultra-bas bruit pour la mesure de signaux faibles issus de pixels dotés d'un courant d'obscurité de moins de 10 pA et d'une capacité totale de l'ordre de 2 pF. Nous avons alors démontré qu'il était possible d'obtenir des niveaux de bruit très faibles conduisant à une résolution spectrale de 1 keV à 60 keV sur des diodes à un pixel. Rapidement, j'ai obtenu le soutien du CNES, tant pour le cofinancement de thèses en instrumentation spatiale que pour le financement d'activités de développements technologiques. Nous avons alors abordé la conception de nouveaux circuits microélectroniques plus avancés, multicanaux et dotés d'une chaîne complète de spectrométrie. Nous avons alors construit nos premières matrices de petits pixels au pas de 1 mm et élaboré la preuve de notre concept dans une configuration de laboratoire (Thèse de Bob Dirks). Ma rencontre avec la société 3D plus a permis de démarrer le projet Caliste en 2004. C'est un tournant majeur puisque j'ai identifié une solution technologique 3D sur laquelle nous pouvions travailler pour produire un spectro-imageur miniature permettant l'assemblage direct de détecteurs CdTe pixélisés avec une matrice de chaînes électroniques installées dans un composant hybride modulaire,

qui plus est, bâti sur quelques technologies éprouvées dans le domaine spatial. C'est en 2007 que nous avons sorti notre premier prototype Caliste-64. Les performances étaient au rendez-vous et nous sommes allégrement passés sous la barre d'1 keV à 60 keV sur matrice de 1 cm² avec des pixels de 1 mm de côté. La caractérisation complète du dispositif (Thèse d'Aline Meuris) a permis d'optimiser la conception du prototype suivant, Caliste-256, doté d'une nouvelle version de l'électronique frontale, programmable cette fois, et de pixels encore plus petits, 580 μm. Nous avons achevé ce prototype en 2009 et révélé des performances excellentes en matière de résolution spectrale (850 eV FWHM à 60 keV) et de seuil bas (1.5 keV). Cet objet fut mis en avant lors des phases initiales de développement du projet SIMBOL-X, abandonné depuis. Nous avons, avec le soutien de l'Irfu, poursuivi notre développement pour créer Caliste-HD. Ce dernier module pixélisé a vu le jour en 2011 avec une ultime version d'IDeF-X. Le but était cette fois non seulement de réduire encore le bruit électronique mais de revisiter la conception de la chaîne pour minimiser la puissance électrique totale et de simplifier l'interface électrique en vue de réaliser un démonstrateur de plan focal sur lequel huit modules sont juxtaposés (MACSI). A nouveau les performances ont été améliorées et la résolution spectrale a atteint 666 eV à 60 keV, un record. Ce détecteur, unique en son genre, a subi les essais de qualification permettant de lui attribuer un TRL6, le niveau de maturité le plus élevé que l'on puisse espérer d'un sous-système spatial encore au sol.

Finalement MACSI est une caméra de 2x4 cm² couverte de 2048 chaînes de spectrométrie à haute résolution spectrale. J'ajoute que ce détecteur de photons uniques est capable d'une précision de datation de l'ordre de la 100aine de nanoseconde. Il aurait finalement respecté le cahier des charges ambitieux de SIMBOL-X pour lequel nous l'avions imaginé. Puisque ceci n'arrivera pas dans ce contexte, je me suis employé à promouvoir notre technologie dans d'autres domaines d'applications et notamment en Physique Solaire. C'est ma rencontre avec Säm Krucker qui nous permettra d'obtenir notre place à bord de STIX, un spectro-imageur X dur dédiés à l'observation des éruptions solaire, qui sera placé en orbite en 2018 dans la charge utile de la mission ESA Solar Orbiter.

Entrés en phase B du projet, nous avons développé en un temps très court un module dédié à la géométrie particulière de STIX dont le principe d'imagerie repose sur la modulation du flux de photons par des masques à transformée de Fourier. Entre 2011 et 2015, nous avons conçu, produit et qualifié les 100 modules de qualité vol avec le soutien du CNES, de FHNW et les moyens industriels de 3D plus. Aujourd'hui les premiers équipements de vol sont en cours d'assemblage et il est temps d'aborder l'avenir par de nouveaux travaux de R & D.

C'est ce que j'ai entrepris de faire en proposant le projet MC2 pour Mini CdTe on Chip, qui repose simplement sur la volonté de poursuivre la réduction de la taille des pixels. Cette fois, je vise un pas inférieur à 300 μm, avec un bruit électronique si faible que la résolution spectrale à 60 keV atteindra 500 eV. Cette spécification technique très difficile pose un défi incroyable en microélectronique. Olivier Gevin et Alicja Michalowska ont réalisé des prouesses en concevant le circuit D^2R_1 dont les premiers pas sont très encourageants, aussi bien en matière de bruit que de tenue aux radiations. Lors des 5 prochaines années, je m'assigne la mission de réaliser un nouveau module intégrant ce composant ultra dense dans une unité de détection dont l'interface sera entièrement numérique.

Pour conclure, je veille aux retombées scientifiques comme sociétales de nos travaux en participant à de nombreux projets qui nous conduiront encore dans l'espace, à n'en pas douter.

Abstract

Immediately after the launch INTEGRAL on October 17, 2002, I started thinking about the prospect of using CdTe as the active detection medium of a hard X-ray imaging-spectrometer for future high-energy space astronomy missions. This work led me to realize that the ISGRI spectrometric limitations could be overcome by focusing my efforts in designing a new electrode sensor segmented into small pixels. Indeed, ISGRI suffers from the use of large detectors with ohmic contacts with high dark current causing significant electronic noise. The consequence is a modest spectral resolution and a relatively high low discrimination threshold.

On the other hand, the high current limits the applicable voltage to the detector and causes a slow signal depending on the depth of penetration of the photons in the volume, due to poor transport properties of holes in the semi-conductor. However, thanks to the intrinsic properties of mass and high density, CdTe remains the ideal candidate for the detection of hard X-rays compared to its most serious competitors: germanium and silicon.

By reducing the pixel size, in addition to natural improvement of the spatial resolution, the current in each pixel is proportionally reduced. It's the same for the parasitic capacitance presented at the input of the charge sensitive amplifiers connected to each pixel. By replacing the ohmic contacts for blocking Schottky contacts, the dark current can be reduced by three orders of magnitude if the pixels are small enough. Consequently, the electric field in the bulk of the semiconductor can be increased to get fast signals and limit the charge loss and ballistic deficit enabling a spectral response almost independent of the depth of penetration photons in the volume. This is the initial motivation, to which is added the fact that the signals induction is different in a coplanar detector and in a small pixels detector, where a favorable weight-field shields the holes. In short, reducing the pixel size has advantages on the performance of an imaging spectrometer. Naturally, the reduction of the pixel size by a factor of about 100 presents new significant technological challenges. This is the challenge I have faced in the recent years and which gave birth to the concept of miniature imaging spectrometer Caliste I presented in this "Habilitation".

François Lebrun, Chief Scientist ISGRI, also my former PhD supervisor, trained me in the idea that the energy resolution and the threshold are key parameters of instrument sensitivity and diserve special attention. This has been the focus of my work over the past 15 years. My goal was very clear: reduce the FWHM spectral resolution of 6 keV at 60 keV to less than 1 keV.

To meet this challenge, I tackled simultaneously the design of an entirely new system taking into account the studies of segmented anode CdTe Schottky detectors, the integrated electronics optimized for reading these particular sensors, the hybridization with one another and the space qualifiaction of the assembly. I set up a cross-functional team SAp and SEDI, with the support of Eric Delagnes, Philippe Lavocat and Philippe Rebourgeard that allowed us to start the development of IDeF-X, an ASIC designed by Olivier Gevin and Francis Lugiez in order to achieve ultra-low noise charge sensitive preamplifiers for the measurement of small signals from pixels with lower dark current than 10 pA and a total capacitance of about 2 pF. We showed that it was possible to obtain very low levels of noise leading to a FWHM spectral resolution of 1 keV to 60 keV with a single pixel diode. I quickly gained the support of CNES, both for co-financing of PhD theses in space instrumentation and the funding of technology development activities. We discussed the design of a more sophisticated version of our microelectronic circuits, with multi-channel and full spectroscopy channels. We built our first small pixel arrays with 1 mm pitch and developed a proof of concept in a laboratory configuation (Thesis: Bob Dirks). I started the Caliste project after I met 3D plus company in 2004. This was a major event for me because I identified a 3D technological solution on which we could work to produce a miniature imaging spectrometer that allows direct assembly of CdTe pixelated detectors with a matrix of electronic channels installed in a modular hybrid component, based on proven technologies for spaceborne applications. In 2007 we released our first Caliste-64 prototype. Performances were excellent and we succeeded to reach the symbolic resolution of 1 keV FWHM at 60 keV on a 1 cm^2 matrix with 1 mm pixels by side. The complete characterization of the device (Thesis: Aline Meuris) has helped to optimize the design of the next prototype, Caliste-256, equipped with a new version of the front-end electronics, this time programmable, with even smaller pixels down to 580 μm.

We completed the prototype in 2009, which showed excellent performance in terms of spectral resolution (850 eV FWHM at 60 keV) and low threshold (1.5 keV). Caliste-256 was put forward in the initial phases of development SIMBOL-X project, since abandoned. We have, with the support of DSM/IRFU, continued our development to create Caliste-HD. This last pixelated module was completed in 2011 with the final version of IDeF-X-HD. The goal this time was not only to further reduce electronic noise but also to revisit the chain design to minimize the total power and simplify the electrical interface to achieve a focal plane on which eight modules are juxtaposed (MACSI). Again, the performance has been improved and the spectral resolution reached 666 eV FWHM at 60 keV, a record. This detector, unique, underwent qualification testing to assign a TRL6, the highest level of maturity that one can expect from a space subsystem still on the ground.

Finally MACSI is a 2x4 cm^2 camera covered 2,048 spectrometry chains with high spectral resolution. I add that this single photon detector is capable of timing accuracies of the order of 100's of nanosecond. It would have complemented the ambitious specifications of SIMBOL-X for which we imagined this camera. Since this will not happen in this context, I worked to promote our technology in other fields of application and particularly in Solar Physics. This is my meeting with Säm Krucker that will allow us to get our seat on STIX, a hard X-ray imaging spectrometer dedicated to the observation of solar flares, which will be placed in orbit in 2018 in the payload of the ESA Solar Orbiter mission.

Showing up in Phase B of the project, we have developed in a very short time a module customized to the particular geometry of STIX whose imaging principle is based on the modulation of the photon flux by Fourier transform coded masks. Between 2011 and 2015, we designed, produced and tested 100 flight quality modules with support from CNES, FHNW and the industrial resources of 3D plus. Today the first flight equipment are being assembled and it is time to enter a new phase of R & D.

This is what I have undertaken starting the MC2 project standing for Mini CdTe on Chip, which is simply based on the desire to continue to reduce the pixel size. This time, I aim for less than 300 microns, with an extremely low electronic noise so that the spectral resolution at 60 keV will reach 500 eV FWHM. This is a very difficult technical specification and poses an incredible challenge in microelectronics. Olivier Gevin and Alicja Michalowska achieved these feats by performing the D2R1 ASIC whose first steps are very encouraging, both in terms of noise as well as radiation tolerance. During the next 5 years, I will complete this phase of works by developing and fabricating a new module in which the ultra-dense components are integrated into the sensor and the interface is fully digital. To conclude, I ensure the scientific and societal benefits of our work by participating in many projects that still lead us into space, no doubt.

Table of contents

II. List of publications

III. List of contributions

IV. The Story of Caliste

Introduction

I present this document to the University of Paris 7 – Denis Diderot to apply for the diploma of "Habilitation à Diriger des Recherches". The text is organized in four sections as follows:

I. **The first section is a** <u>summary of my research activities</u>. It contains my Curriculum Vitae, a notice of my credentials and works, followed by my detailed carreer description. The latter includes my administrative responsibilities, my scientific responsibilities, elements to justify my technical domain of expertise, a list of my instructing and teaching activities. Finally, it describes my involvement in the scientific community through the organization of international conferences.

II. **Section 2 is a complete** <u>list of my publications</u>. This list is introduced by a bibliometric analysis of my work and its impact in the scientific community. My publication list contains the papers published in conference proceedings, in peer-reviewed journals, monographs and book chapters and grand-public communications. The list is concluded by my contributions to scientific and technical proposals. Even if the scientific content of the latter is not properly devoted to the community, I decided to show up this wide list because it represents a significant part of my engineering activities.

III. **The third section of the document is a** <u>list of my contributions</u> **to conferences, international meetings and seminars**.

IV. **The last section is my** <u>dissertation</u>. I present the Story of Caliste, the heart of my research in instrumentation during the last 12 years, devoted to the development of X-ray photon detectors for Space Science. In my dissertation, I presented the field of development, my research approach and the most important results obtained with my research team and my students. A few papers I wrote illustrate this section. Following the dissertation I show the impact of my work in Science and in other application fields. I conclude with recent R&D works I have initiated to prepare the future of my research field.

I. Summary of activities

1. Curriculum vitae

Name: **Limousin**   First Name: **Olivier**
Birth date: January 1st, 1974   Place of birth: Versailles, France
Nationality: **French**   Family status: **married, 3 kids**

CEA Saclay — DSM/IRFU/Service d'Astrophysique (Astrophysics division)
AIM – Unité Mixte de Recherche CEA - CNRS - Université Paris VII – UMR n° 7158
Orme de Merisiers, Bat. 709, 91191 Gif-sur-Yvette, France
Tel. : +33 1 69 08 62 94 – Fax : +33 1 69 08 65 77 – E-mail : olimousin@cea.fr

Taking office (PhD CFR grant): October 1997
Permanent position (Research Engineer): November 2001
Current grade at CEA: E5 since July 2014

Current position
- **Research Engineer at Commissariat à l'énergie atomique de Saclay (CEA-Saclay)**
  Direction des Sciences de la Matière (DSM)
  Institut de Recherche sur les lois Fondamentales de l'Univers (IRFU)
  Service d'Astrophysique (SAp)
  Laboratoire Spectro-Imageurs-Spatiaux (LSIS)
- Head of Space Imaging Spectrometer Lab, LSIS
  12 permanent staff, 8 to 10 non-permanent staff
  R&D for space borne detectors
  Sub-millimeter bolometers; X-ray microcalorimeters; X and gamma ray semiconductor detectors; cryogenic infrared and visible sesnors.
  AERES evaluation of the lab, Vague D, 2013: A+ / A / A+ / A+ / A+ / A+

Controlled domain of expertise
- X and Gamma ray semiconductor detector physics
- Space instrumentation
- R&D team management and Head of Laboratory

Research field
- X and Gamma-ray Astronomy
- Space instrumentation and space born detectors
- X and Gamma ray semiconductor detector

Curriculum and diplomas
- 1996   Engineering degree, Material sciences, Institut National des Sciences Appliquées de Lyon, France
- 1996   Diplôme d'études approfondies (Master degree), Integrated electronics devices, INSA Lyon, Ecole Centrale Lyon, Université Lyon I, France
- 2001   Doctoral thesis (PhD), Space instrumentation, Toulouse III, France

Foreign languages
- English
- Spanish (ancestral notions)

2. Notice de titres et travaux (French)

1. Formation initiale

Immédiatement après l'obtention du Baccalauréat, série C, en 1991, j'ai intégré l'INSA Lyon. J'y ai suivi une formation d'ingénieur au sein du département *Génie Physique Matériaux* dans la spécialité *Matériaux et Dispositifs Semi-conducteurs*. Lors de ma dernière année de formation, j'ai parallèlement suivi un cursus pour l'obtention du *Diplôme d'Etudes Approfondies* (INSA Lyon, Ecole Centrale de Lyon, Université Claude Bernard) dans la spécialité *Matériaux et Dispositifs de l'Electronique Intégrée*. J'ai achevé cette phase de mes études en 1996 avec une formation cohérente en physique du solide et en physique des matériaux semi-conducteurs avec un accent sur les technologies associées et une orientation pour les technologies microélectroniques. Au cours de mon cursus, j'ai effectué principalement deux stages, l'un au Service d'astrophysique (SAp) du CEA Saclay en 1995, l'autre au Laboratoire de Physique des Matériaux (LPM) de l'INSA Lyon en 1996. Ces stages ont marqué ma vie professionnelle durablement. En effet, j'ai été initié aux travaux de recherches et au travail expérimental associé à un projet spatial (INTEGRAL/SPI) lors du premier stage alors que je me suis intéressé aux effets des radiations sur les défauts dans les oxydes des transistors MOS[1] lors du second ; autant de thèmes que je retrouverai ultérieurement. Ma trajectoire dans une carrière en recherche en instrumentation, qui plus est au CEA, m'est apparue comme une évidence.

2. Expériences professionnelles antérieures à l'embauche au DAPNIA

Au CEA LETI (1996-1997)
Désireux d'effectuer mon service militaire en tant que scientifique du contingent, j'ai naturellement postulé au CEA. C'est en tant que marin que j'ai intégré le Laboratoire de Couches Minces Optiques (CMO) du LETI au CEA Grenoble de 1996 à 1997. Mon travail consistait dans un premier temps à caractériser la Tenue au Flux Laser (TFL) de puissance de fonctions optiques multi-couches dans l'infrarouge réalisées dans le laboratoire, notamment dans le cadre du programme Laser Mégajoule. J'ai également effectué des études TFL de substrats purement cristallins destinés à des fonctions optiques dans des chaînes laser de puissance dans l'infrarouge. J'ai étudié l'influence sur la TFL de défauts particuliers piégés dans des empilements optiques complexes avant de me consacrer à la caractérisation fine et à l'étalonnage des spots lasers eux-mêmes. Ce contact avec la recherche technologique a été très enthousiasmant. J'ai intégré une équipe experte dans laquelle il était bénéfique de suivre la création d'un objet technique depuis sa conception jusqu'aux essais, en passant par la fabrication. J'ai réalisé l'importance d'un lien collaboratif étroit entre les différents acteurs, ingénieurs-chercheurs et techniciens. J'ai par ailleurs découvert la « force de frappe technologique » du LETI et le contexte de la recherche dans un milieu applicatif. Cette expérience a suscité en moi l'envie de me rapprocher d'un domaine plus fondamental.

Au CEA DAPNIA (1997-2000)
Déterminé à poursuivre mon parcours dans le domaine scientifique, j'ai accepté la proposition de thèse que m'a offerte François Lebrun au sein du SAp du DAPNIA[2] au CEA de Saclay (Contrat CFR[3]). Mon sujet portant sur la mise en œuvre et l'étude des propriétés spectrales de la caméra gamma ISGRI[4] constituant le plan détecteur pixélisé du

---

1. MOS, Metal Oxyde Semi-conducteur.

2. DAPNIA, Département d'Astrophysique, de physique des Particules, de physique Nucléaire et d'Instrumentation, ancien nom de l'Irfu.

3. CFR, Contrat de Formation par la Recherche.

4. Anglais (E.U.) ISGRI, Integral Soft Gamma Ray Imager.

télescope à masque codé IBIS[5]du satellite astronomique gamma INTEGRAL de l'ESA[6], j'allais pouvoir concilier des travaux de recherche dans un cadre instrumental avec mon attirance pour le secteur de la recherche fondamentale en astrophysique. Outre le projet de recherche lui-même, je me suis rapidement inséré dans l'équipe projet locale et dans une équipe internationale plus large où j'ai progressivement acquis des compétences généralistes sur la réalisation des projets spatiaux, scientifiques en particulier.

La caméra ISGRI est dédiée à l'étude de la physique des trous noirs, des objets compacts, des noyaux actifs de galaxies (AGN) et des restes de supernovae. Elle a été optimisée pour l'observation d'objets faibles, par exemple en vue de révéler l'origine de l'émission diffuse en gamma-mous de la Voie Lactée. ISGRI a également été conçue pour faciliter l'observation des régions centrales de notre galaxie, particulièrement le très ténu trou noir super-massif en son centre.

ISGRI est un imageur spectrométrique gamma de grande taille (~1/4 de m^2) réalisé à partir de cristaux de CdTe, un matériau semi-conducteur II-VI, à la fois lourd (Z~50) et dense (d = 5.85) et donc efficace à la détection des rayons X durs jusqu'à 1 MeV. Ce matériau offre de surcroît une résistivité élevée à température ambiante (~10^9 Ohm.cm) permettant son utilisation sans système de refroidissement actif à bord d'une charge utile embarquée. En revanche, les propriétés de transport de ses porteurs de charges sont modestes et compliquent l'acquisition du signal ce qui limite les performances spectrales de ce type de détecteur.

A l'époque, notre motivation pour ISGRI était d'améliorer à la fois les performances spectroscopiques et la sensibilité par rapport au NaI utilisé jusqu'alors, notamment dans la caméra gamma SIGMA[7] à bord du satellite Russe GRANAT (1989). S'agissant des performances spectroscopiques, la recherche des raies du ^{44}Ti dans les restes de supernovae était l'une des principales justifications scientifiques. Pour ce qui est de la sensibilité de la caméra, il s'est agi d'augmenter la surface de détection et de segmenter le plan détecteur, c'est-à-dire de le pixéliser ce qui a pour effet de limiter l'effet du rayonnement cosmique sur le bruit de fond instrumental ainsi que d'améliorer, c'est-à-dire réduire le seuil de détection à basse énergie jusqu'à 15 keV, précédemment limité à environ 35 keV avec du NaI. Cette problématique a été l'axe de mes recherches pendant ma thèse et bien au-delà finalement, puisque mes travaux actuels sont toujours colorés de cette problématique de fond – sensibilité et résolution spatiale, spectrale et temporelle. Ce travail sur les propriétés des détecteurs CdTe m'a permis de poser les bases de mon expertise sur les détecteurs semi-conducteurs X et gamma.

La réalisation d'ISGRI a été rendue possible par la juxtaposition d'une multitude de composants hybrides (dénommé *Polycells* dans ISGRI) associant 16 détecteurs CdTe à leur électronique de proximité analogique sous forme de quatre microcircuits ASIC-4C[8], par le truchement d'un substrat dédié en céramique. J'ai contribué à la mise au point de ces composants (CdTe, ASIC, Hybride) et au suivi de fabrication et à la qualification des *polycells* dans l'industrie (SAGEM, Lannion). Mes connaissances intimes des détecteurs, de l'électronique associée et des moyens d'essais se sont avérées nécessaires à « l'acceptance » des composants pour les différents modèles de la caméra, depuis le démonstrateur technologique (EM[9]) jusqu'aux modèles de vol (FM[10]). Cette expérience professionnelle s'est enrichie de ma rencontre et de ma collaboration étroite avec les concepteurs micro-électroniciens du LETI et du SEI[11]. J'ai appris avec Marc Arquès, Michel Rouger et Eric Delagnes l'importance d'un fonctionnement en équipe intégrée pour la réalisation d'objets aussi complexes que sensibles. Par ailleurs, ma première expérience de partenariat industriel aura eu une influence notoire sur ma façon de travailler avec les entreprises technologiques à l'avenir.

Au final, INTEGRAL a été tiré le 17 octobre 2002 avec à son bord ISGRI, le plus grand imageur CdTe jamais réalisé à l'époque – 16 384 pixels et 4096 ASICs. Il remplit toujours inlassablement sa mission en orbite au moment d'écrire ces lignes. Ce succès incontestable sera un tremplin pour mes activités de R&D pour des capteurs CdTe de nouvelle génération, mon cœur de métier.

---

5. Anglais (E.U.) IBIS, Imager on Board Integral Satellite.

6. ESA, European Space Agency.

7. SIGMA, Système d'Imagerie Gamma à Masque Aléatoire

8. Anglais (E.U.) ASIC = Application Specific Integrated circuit. ASIC 4C est le nom du circuit utilisé dans ISGRI avec 4 pour le nombre de chaînes par ASIC et C, l'indice du circuit dans sa troisième itération.

9. Anglais (E.U.) EM, Engineering Model ou modèle d'ingenierie.

10. FM, Flight Model ou modèle de vol.

11. SEI – Service d'Electronique et d'Informatique, ancien nom du SEDI, Service d'Electronique, Détecteurs et Informatique.

3. Travaux depuis l'embauche au DAPNIA/Irfu

Pour des raisons liées à des difficultés d'ordre technique sur ISGRI au moment de la finalisation du projet et pour la résolution desquelles ma participation était requise, j'ai accepté d'être recruté comme ingénieur au CEA avant d'achever ma thèse, donnant la priorité à ISGRI. J'ai soutenu ma thèse en novembre 2001 après la livraison et l'étalonnage du modèle de vol.

3.1. 2001-2003 – GLAST et Ma_Flux
• *GLAST – Fermi*
En 2001, le CEA/DAPNIA était engagé dans une participation matérielle au projet NASA GLAST, un télescope Gamma à très haute énergie pour l'observation des pulsars, AGN et Blazars ou encore des sources galactiques « non identifiées » et l'étude de l'origine des rayons cosmiques notamment.

Notre rôle au DAPNIA était d'assurer la fabrication du calorimètre électromagnétique LAT en collaboration avec le NRL[12] (USA), l'IN2P3 et le LLR/École polytechnique. L'instrument est constitué de l'empilement de barres de CsI entrelacées, lues par des photodiodes silicium. Ma principale contribution a été de développer des bancs de mesures et les méthodes associées pour caractériser le rendement de lumière de cristaux scintillants de CsI et les photo-détecteurs associés. Le projet s'est arrêté brutalement en 2003. Le CEA a poursuivi son implication par une contribution scientifique mais laissant sans suite les activités matérielles au laboratoire. GLAST-Fermi est aujourd'hui un immense succès scientifique.

• *R&D Ma_flux*
A la même période, mon travail de recherche sur les détecteurs CdTe s'est poursuivi dans le cadre du projet *Ma_Flux*. L'idée était de promouvoir les détecteurs CdTe dans leur configuration *Polycell*, jouissant d'une forte maturité technologique suite au programme ISGRI, pour des applications scientifiques nouvelles : l'exploration martienne *Mars Sample Return*. L'objectif était extrêmement ambitieux puisqu'il s'agissait de poser un laboratoire d'analyse de roches sur Mars, prélever des échantillons et les ramener sur Terre. J'ai participé à ce projet en collaboration avec l'IPGP[13], le CNES et DRT/LIST. J'ai étudié avec Bertrand Cordier un concept d'instrument et participé à la mise en œuvre d'un démonstrateur à base de CdTe destiné à l'analyse in-situ de roches martiennes par fluorescence X. Cette technique requiert des performances spectrales excellentes dans un système exceptionnellement compact et léger. En vue d'améliorer les performances spectrales, j'ai commencé à étudier les détecteurs CdTe de type diode Schottky. Une preuve de concept a été proposée et des essais ont été menés sur l'accélérateur AGLAE[14], en collaboration avec le Centre de Recherche et de Restauration des Musées de France au Louvre, avant que le projet ne s'arrête définitivement en 2003.

J'ai appris de ces situations de crise qu'un laboratoire est très sensible aux aléas programmatiques, politiques et financiers des projets spatiaux et que des efforts de R&D constants permettent non seulement de maintenir et stabiliser un niveau scientifique élevé en dépit des remous mais aussi d'assurer une capacité de rebond rapide.

3.2. 2002 – Chef de Groupe LDS (Laboratoire Détecteurs pour le Spatial)
A l'occasion d'une réorganisation complète du SAp, les activités de développement détecteur, d'interface scientifique aux instruments et d'intégration dans des charges utiles spatiales ont été regroupées dans un unique Laboratoire de Détection Spatiale dirigé par Bertrand Cordier. J'ai alors accepté de prendre en charge le groupe « Laboratoire Détecteurs pour le Spatial » constitué d'une douzaine de membres permanents. Ce fut formellement ma première expérience de management. Ce laboratoire couvrait essentiellement des sujets de R&D pour les détecteurs X, Gamma et Submillimétriques. Outre les aspects administratifs, j'ai concentré mon action en faveur de la carrière de mes collaborateurs et veillé au renfort technique du laboratoire par le recrutement de deux techniciens et d'un ingénieur. Ce rôle de chef de groupe m'a également permis de consolider ma connaissance des rouages de l'Irfu, feu DAPNIA et au-delà de l'ensemble du CEA.

---

12. Naval Research Laboratory.

13. IPGPG, Institut de Physique du Globe de Paris.

14. AGLAE, Accélérateur Grand Louvre d'Analyse Elémentaire.

3.3. 2003-2009 – la R&D CdTe et ses conséquences

• *R&D CdTe – premiers pas*

En analysant les facteurs limitant les performances spectrales de la caméra ISGRI, notamment en vol, j'ai identifié de nouvelles voies d'améliorations pour des systèmes de détection à base de CdTe. Le programme R&D CdTe est né ainsi : faire progresser simultanément les détecteurs CdTe, leurs électrodes, leur géométrie, l'électronique analogique intégrée, leur technique d'hybridation et l'architecture système. Partant du principe que nous accédérions à des avancées spectaculaires en regroupant nos forces, j'ai proposé au DAPNIA, avec Eric Delagnes, de créer une équipe mixte SEDI/SAp compétente sur tous les tableaux. Cette approche originale et visible nous a permis d'envisager une circulation rapide de l'information entre les laboratoires, de solliciter une large participation des compétences du département et incidemment de produire une définition technique optimale de nos spectro-imageurs spatiaux. En procédant ainsi, nous étions en mesure d'exploiter complètement les moindres possibilités technologiques dans la chaîne de détection, du photon jusqu'aux données, en se préparant à des utilisations scientifiques en orbite.

Sur le plan technique, le point de convergence était l'impérieuse nécessité de réaliser des pixels 10 à 100 fois plus petits qu'auparavant. La résolution spatiale s'en trouverait naturellement améliorée ainsi que la résolution spectrale, essentiellement du fait de la réduction du courant d'obscurité et de la capacité parasite dans chaque chaîne spectroscopique. J'ai encadré mon premier étudiant en thèse, Bob Petrus Franciscus Dirks, à partir de 2003, dans le but précis de modéliser et démontrer cette approche en vue d'orienter la conception de nouveaux détecteurs pixélisés à électrodes segmentées. Moyennant la conception d'une électronique intégrée entièrement nouvelle, tolérante aux radiations, fiable, et parfaitement ajustée aux propriétés de ce type de capteurs CdTe (famille de circuits IDeF-X – Olivier Gevin et Francis Lugiez), nous avons démontré la résolution spectrale de 1 keV FWHM à 60 keV, soit une amélioration d'un facteur 6 par rapport à ISGRI. Notons que le seuil de détection passait dans le même temps de 15 keV à ~3 keV, un progrès notoire pour les astrophysiciens des hautes énergies puisqu'ils entrevoyaient pour la première fois la possibilité d'observer dans les domaines X et gamma avec un instrument unique. Cette propriété de nos capteurs sera à l'origine des spécifications techniques du seuil de détection de SVOM/ECLAIRs à 4 keV, permettant à cet observatoire de sursauts gamma de voir des événements à des distances cosmologiques (Z~10 à 20). Ce résultat majeur offrira de nombreuses opportunités scientifiques par la suite impliquant le laboratoire dans d'autres expériences scientifiques.

• *R&D CdTe – Micro caméra CdTe Caliste*

L'emploi de petits pixels pose la difficulté de la réalisation d'un hybride compact, juxtaposable sur quatre côtés de surcroît, de sorte que la réalisation de caméras de grande taille reste possible. C'est pour cette raison que j'ai entamé dès 2004 des travaux de recherches technologiques dans le but d'identifier et pré-qualifier une technologie d'intégration compatible de nos exigences de performances scientifiques et des contraintes de l'environnement spatial (TRL[15] 3-4). Ma rencontre avec la société 3D PLUS a été sans doute l'un des moments clés de mes onze dernières années de recherches. En effet, en utilisant leur savoir-faire dans la réalisation de composants électroniques 3D (mémoires) et en « détournant » leur utilisation, j'ai proposé un concept nouveau de micro caméra gamma, le projet Caliste.

Entre 2004 et 2009, entouré d'une large équipe DAPNIA/Irfu (~15 pers. impliquées, noyau dur de 6 personnes), avec 3D PLUS et avec le soutien continu du CNES, j'ai conduit la réalisation de quatre versions de Caliste, du démonstrateur au prototype TRL 5 – une exigence pour une éventuelle participation à un programme spatial. Le point d'orgue de cette recherche fut sans doute la présentation donnée par ma seconde étudiante en thèse, Aline Meuris, à la conférence IEEE NSS/MIC[16] 2007 où nous révélions à notre communauté les performances spectaculaires de Caliste-64. J'ai ensuite achevé le programme de R&D CdTe dans sa première phase par le prototype Caliste-256, un spectro-imageur miniature au pas de 580 microns et offrant une résolution spectrale de 860 eV FHWM à 60 keV, avec un seuil bas de 1.3 keV ; des performances uniques au monde.

• *SVOM/ECLAIRs – SIMBOL-X*

Le premier aboutissement de cette R&D est l'instrument ECLAIRs, embarqué sur le satellite franco-chinois SVOM, pour lequel j'ai pris la responsabilité de fournir dès 2007 à l'IRAP[17], en charge de l'imageur CdTe, 300 modèles de

---

15. RL, *Technology Readiness Level* est une échelle de 1 à 9 qui caractérise le niveau de maturité technologique d'un système, spatial en particulier.

16. Anglais (E.U.) IEEE Nuclear Science Symposium and Medical Imaging Conference.

17. Institut de Recherche en Astrophysique et Planétologie, Toulouse.

vol de l'ASIC bas bruit – IDeF-X ECLAIRs. J'ai, dans ce projet, le rôle de Co-I et d'expert CdTe. Ce programme est encore en cours de développement actuellement.

Le second aboutissement fut le satellite SIMBOL-X (PI Ph. Ferrando, CEA), un observatoire utilisant la technique du vol en formation : un satellite emporte un miroir à rayon X-durs à incidence rasante, efficace jusqu'à 80 keV tandis que 20 mètres plus loin, un second satellite asservi au premier porte des plans focaux. Parmi eux, le détecteur HED (High Energy Detector) dont j'avais la responsabilité technique pendant l'étude, était équipé d'une mosaïque de détecteurs Caliste, couvrant le champ de vue avec une surface de 64 cm^2. Malheureusement l'ambitieux projet franco-italien s'est arrêté brutalement en 2009. Bien qu'elle fut un choc pour toute l'équipe et ses partenaires, cette nouvelle secousse n'a pas entamé ma détermination à réaliser une grande caméra à base de CdTe pixélisé à haute résolution spectrale.

3.4. 2.2.3.4 2009-2013 – L'implémentation dans des projets spatiaux, un nouveau cycle de R&D
• *MACSI, un démonstrateur de haute maturité technologique*
Le degré de maturité de Caliste d'une part et le niveau de définition de HED d'autre part m'ont conduit à proposer le développement de MACSI (Modular Assembly of Caliste Spectro-imager) à l'Irfu. L'institut m'a accordé, sur fonds propres, les moyens matériels et les ressources humaines pour achever le développement d'un 1/8ème équivalent de plan focal de SIMBOL-X. Pour l'occasion nous avons réalisé en 2011 une série de Caliste et de ses ASICs IDeF-X, tous deux dans leur version la plus avancée à ce jour, HD[18]. L'équipe R&D CdTe, avec le soutien des groupes d'intégration SEDI et SAp, qualité, système, mécanique et électronique ont produit leur effort pour réaliser un prototype complet d'une caméra de 2048 spectromètres indépendants au pas de 625 microns, à haute résolution spectrale et temporelle. Cet objet unique au monde présente un TRL-6. Il est prêt pour le vol et peut être répliqué.

J'ai pris l'initiative de proposer cet instrument dans des programmes spatiaux internationaux comme IXO[19] (ESA-NASA-JAXA) ou encore Spektrum Roentgen Gamma (Roscomos-IKI - DLR) et je continue de le faire jusqu'à trouver une application scientifique spatiale. Je considère aujourd'hui qu'une utilisation dans un nano-satellite pour l'observation solaire est envisageable. Je vante par ailleurs les capacités polarimétriques de l'instrument qui offre des perspectives scientifiques nouvelles en gamma, performances que j'ai démontrées, dans le cadre de notre collaboration *Lapolcaliste* avec l'université de Coimbra et l'INFN Bologne en 2011, en exposant Caliste à un faisceau mono-énergétique fortement polarisé sur la ligne ID-15A à l'ESRF[20].

• *Les retombées scientifiques spatiales, CINEMA, ASTRO-H, STIX, STEP...*
Suite à l'arrêt de notre projet SIMBOL-X, j'ai été invité par mes collègues japonais à rejoindre l'équipe ASTRO-H (télescope X et gamma spatial, « ex-concurrent » de SIMBOL-X) au titre de mon expertise sur les détecteurs CdTe et électroniques associées, massivement utilisés à bord de ce télescope en cours d'intégration. ASTRO-H a été lancé en 2016. J'ai entrepris avec Philippe Laurent de proposer une contribution européenne à ASTRO-H, nous garantissant un retour scientifique dès les premiers mois d'exploitation en vol. Nous avons organisé la fourniture par l'ESA de l'ensemble de cristaux de BGO[21] nécessaires à la fabrication des systèmes d'anti-coïncidences des instruments SGD (Soft Gamma-ray Detector) et HXI (Hard X-ray Imager). J'ai par ailleurs pris la responsabilité scientifique d'une activité financée par l'ESA pour l'étude des effets des radiations sur les microcircuits VATA et sur les détecteurs CdTe eux-mêmes. J'étudie également le comportement des détecteurs CdTe sur le long terme en simulant au sol les opérations prévues en orbite. Cette activité nous offre une connaissance très détaillée des capteurs (CdTe en configuration à bandes) d'ASTRO-H pour préparer au mieux les observations, nous implique dans des programmes scientifiques internationaux dans lesquels notre rôle est reconnu et enfin nous offre une visibilité accrue.

En 2009, j'ai été invité par le Pr. Robert Lin à donner un séminaire au Space Sciences Lab à l'Université de Californie Berkeley, laboratoire avec lequel nous avons depuis un accord cadre de collaboration pour l'utilisation de nos circuits IDeF-X dans l'espace sur des projets américains. Le premier des programmes concernés est une série de

---

18. HD pour High Dynamic.

19. IXO, Internation X-ray Observatory, un projet à l'initiative de l'ESA.

20. Anglais (E.U.) ESRF, European Synchrotron Radiation Facility, Grenoble, France.

21. Anglais (E.U.) BGO, Crystal scintillant, germanate bismuth.

trois nano-satellites dénommés CINEMA. Ils sont destinés à l'observation des *Energetic Neurtral Atoms* comme sonde pour l'étude des boucles de courant dans la magnétosphère terrestre. Un premier lancement a eu lieu en 2012 et deux satellites ont été tirés en 2013. Cette opportunité est double : d'une part, elle nous permet d'accéder à l'espace avec notre matériel pour atteindre le tant convoité TRL-9 et d'autre part elle m'a permis de m'insérer dans une communauté scientifique prestigieuse, source de nouvelles opportunités scientifiques et techniques pour le laboratoire. Cette rencontre signe également mes débuts dans le domaine de la physique solaire.

Suite à cette rencontre, j'ai travaillé avec le Pr. Säm Krucker, PI de l'instrument STIX[22]. Ce télescope X dur est dédié à l'observation des éruptions solaires et volera en 2018 à bord de la première mission moyenne du programme Cosmic Vision 2015-2025 de l'ESA, le satellite Solar Orbiter. La charge utile est actuellement en phase d'implé-mentation. C'est clairement le degré de maturité acquis en R&D qui m'a permis d'obtenir notre premier ticket pour l'espace pour Caliste, un succès pour l'ensemble de mon équipe. J'aime à dire que nous sommes entrés dans le projet STIX en phase B et avons pu démontrer notre faculté d'adaptation au projet en un temps record, produisant avec le soutien du CNES des prototypes dédiés au niveau de performance requis en moins d'un an. Pour STIX, je suis Lead Co-I et chef de projet de la contribution française à STIX. J'ai à ce titre obtenu les financements CNES et FHNW (Suisse). Ce succès en appelle d'autres puisque je participe également à l'instrument EPD/STEP[23] à bord de la même mission pour la fourniture d'ASICs IDeF-X BD couplés à des matrices de diodes Silicium du LBNL[24]. Aujourd'hui Solar Orbiter est sans doute le projet le plus important et le plus inattendu de ma carrière.

- *Valorisation*
  Depuis des années, j'envisage que les retombées de nos travaux dépassent le cadre purement scientifique, en témoignent les brevets dont je suis co-auteur. J'ai récemment obtenu un succès en co-proposant le projet ORI-GAMIX à l'ANR/Investissement d'avenir. Il s'agit d'un développement instrumental avec DRT/LIST, 3D PLUS et Canberra pour la réalisation de sondes de spectro-imagerie portables utilisant Caliste, dans le contexte post-Fukushima.

  Par ailleurs, le CEA/LETI/DTBS[25] utilise nos ASICs IDeF-X HD pour le projet d'inspection de bagages IMADIF. Une collaboration à plus long terme avec le LETI est à l'étude avec le SEDI/LDEF[26].

- *R&D MC2, un nouveau cycle de recherche en instrumentation*
  Bénéficiant du soutien du CNES, l'équipe de R&D CdTe est l'une des rares au monde, au sein d'un institut de re-cherche, capable de concevoir entièrement des systèmes de détection, y compris des ASICs spatialisables. L'avenir se prépare dès à présent en entamant un nouveau cycle de R&D depuis un niveau de maturité faible. C'est le projet R&D MC2 (Mini CdTe on Chip) dont le but est de produire un spectro-imageur CdTe à très haute densité de pixels dont la résolution sera limitée par la statistique de création de paires à 60 keV. Les premières briques frontales ont déjà été réalisées avec succès en technologie submicronique profonde pendant la thèse d'Alicja Michalowska encadrée par Olivier Gevin au LDEF pendant que les détecteurs CdTe correspondants sont étudiés et mis en œuvre dans le cadre de la thèse de Sébastien Dubos que j'encadrais au LSIS.

- *LSIS, Laboratoire de Spectro-imageurs Spatiaux du SAp/AIM*
  En 2012, Pierre-Olivier Lagage a ajusté l'organisation du SAp/UMR AIM et m'a proposé le poste de chef du Labo-ratoire Spectro-imageurs Spatiaux (LSIS). A cette occasion, mon groupe devenait un laboratoire plus visible et se trouvait enrichi de l'ensemble des activités de développement et caractérisations de détecteurs y compris dans les domaines des infrarouges moyens et domaines visibles, qui échappaient à mon périmètre jusqu'à présent. Le LSIS est un laboratoire en pointe dans de nombreux domaines qui portent dans le domaine des applications scientifiques spatiales mais également œuvrent pour l'astronomie au sol lorsque cela est pertinent. Nous assurons notre mission de recherche avec un large panel de compétences techniques en interaction avec l'ensemble des laboratoires de l'Irfu. Dans la plupart des domaines, nous sommes également proches des plates-formes tech-nologiques de l'INAC et du LETI. Nous disposons de moyens adaptés dans nos six laboratoires. Notre stratégie permet de pousser des développements parallèles à divers niveaux de maturité en essayant de coller au plus près

---

22. Anglais (E.U.) STIX, Spectrometer Telescope for Imaging X-rays.

23. Energetic Particles Detector/Supra-Thermal Electrons and Protons.

24. Lawrence Berkeley National Lab, États-Unis.

25. Département de micro Technologies pour la Biologie et la Santé.

26. Laboratoire de Détecteurs et Electronique Frontale, dirigé par E. Delagnes au SEDI.

des attentes des astrophysiciens, mais en étant également force de proposition. Cette nouvelle organisation m'a permis de donner une nouvelle impulsion au laboratoire en termes de dynamique collective. Les liens avec les autres laboratoires de SAp/AIM et de l'Irfu s'en trouvent aussi facilités.

C'est dans ce rôle de chef de laboratoire que j'ai présenté le LSIS à l'évaluation par l'AERES lors de la vague D. Mon laboratoire a obtenu début 2013 la note maximale A+ sur tous les plans, hormis A pour le critère relatif au rayonnement et à l'attractivité académique, point que je cherche à améliorer maintenant. Pour le reste de mes activités en tant que chef de laboratoire, j'assure le management de l'équipe au quotidien (entretiens annuels, suivi des carrières, recrutements, plan emploi, plan de charge et politique scientifique).

4. Perspectives

A l'avenir, je m'emploierai à porter nos développements dans l'espace en m'insérant en priorité dans des programmes de recherches scientifiques pour l'astronomie et la physique solaire notamment, en développant mes contacts récents qui s'étendent de la Russie (SORENTO/ROSKOSMOS) aux USA (SENIC/NASA) en passant par la Suisse (COXIP – BEEP/FHNW) et le Japon.

S'agissant de la R&D CdTe, je persiste dans l'idée que notre équipe intégrée SAp/SEDI est efficace et sait être force d'innovation, et le sera d'autant plus si nous nous rapprochons de la PME 3D PLUS dans un mode de partenariat ou de laboratoire commun. J'ai entamé cette démarche par notre première proposition scientifique commune auprès du CNES en 2013. Nous démarrerons ensemble une thèse cofinancée en 2014 pour accélérer le processus.

Enfin, sur le plan managérial, je continuerai de développer le LSIS pour réussir nos engagements actuels mais aussi en vue de nous préparer aux grands défis scientifiques comme ATHENA+, un observatoire X spatial révolutionnaire, une mission « large » de l'ESA à l'horizon 2030.

3. Note on my credentials and works

1. Education

After I obtained my Baccalaureate in Science series (Bac C) in 1991, I entered the National Institute of Applied Science in Lyon (INSA – Institut National Des Sciences Appliquées de Lyon, France). I obtained my Engineering Degree in Material Sciences in the specialty of semiconductor materials and devices. During my last year of study, I followed in parallel with my engineering courses, the lectures to obtain my Diplôme d'Etudes Approfondies (Master degree) at INSA with Ecole Centrale de Lyon and University Claude Bernard, in the domain of Integrated Electronics Semiconductor Devices. I finally obtained two diplomas in 1996 with a coherent scientific education in solid-state physics and semiconductor materials physics, with a focus on associated technologies and an orientation on microelectronic technologies. Along my education path, I performed two internships: one at the Astrophysics division of CEA in 1995 and the other in the Material Physics Lab (LPM) at INSA Lyon in 1996. Those two internships had a lasting impact on my carreer. As a matter of fact, during my first internship, I was educated to space science projects (INTEGRAL/SPI) while in my second period I focused on the effect of radiation on MOS[1] transistor oxides – two research fields that I would return to later. My path in the field of instrumention made my application to CEA as obvious.

2. Professional experience before hiring at CEA/DSM/DAPNIA

2.1. CEA LETI (1996–1997)
Eager to perform my military obligations as a scientist, I naturally applied to CEA. As a marine in the French Navy, I joined the Laboratory of Thin Otpical Layers (CMO) of the CEA LETI in Grenoble from 1996 to 1997. My job was initially to characterize the Laser Flux Resistance (LFR) of power multi-layer optical functions in the infrared carried out in the LFR on purely crystalline substrates for optical functions in power laser systems in the infrared range. I studied the influence on LFR on particulate defects trapped into complex optical stacks before devoting myself to the fine characterization and calibration of laser spots themselves. This contact with technological research has been very exciting. I joined concept, design to testing, through production. I realized the importance of a close collaborative relationship between different actors, researchers, engineers and technicians. I also discovered the "technological strike force" of LETI and the context of research in an application oriented environment. This experience instilled in me the desire to get closer to a more fundamental field.

2.2. CEA DAPNIA (1997–2000)
Determined to continue my career in science, I accepted the PhD proposal that François Lebrun offered to me within the SAp DAPNIA[2] at CEA Saclay (Contract CFR[3]). My topic being related to the implementation and study of the spectral properties of the gamma camera ISGRI[4] constituting the pixelated detector plane of the coded mask telescope INTEGRAL IBIS[5] gamma astronomy satellite of ESA[6], I was able to reconcile research in the instrumental implementation with my attraction to quickly integrated into the local project team and in a wider international team where I gradually acquired generalist skils on the implementation of space projects, scientific projects in particular.

The ISGRI camera is dedicated to the study of the physics of black holes, compact objects, active galactic nuclei (AGN) and supernova remnants. It has been optimized for observing faint objects, for example to determine the origin

---

1. MOS, Metal Oxyde Semiconductor

2. DAPNIA, "Département d'Astrophysique, de physique des Particules, de physique Nucléaire et d'Instrumentation", former name of Irfu.

3. CFR, "Contrat de Formation par la Recherche".

4. ISGRI, Integral Soft Gamma Ray Imager.

5. IBIS, Imager on Board Integral Satellite.

6. ESA, European Space Agency.

of the diffuse emission of gamma-soft Milky Way. ISGRI was also designed to facilitate observations of the central regions of our galaxy, particularly of the faint emission of the super-massive black hole at its center.

ISGRI is a gamma ray large imaging spectrometer (~ 1/4 m^2) centred on CdTe crystals, a II-VI semiconductor material, both heavy (Z ~ 50) and dense (d = 5.85) and therefore efficient for the detection of hard X-rays up to 1 MeV. This material offers additional high resistivity at room temperature (~ 10^9 Ohm.cm) allowing its use without requiring an active cooling system aboard a payload. However, the transport properties of its charge carriers are modest and complicate the signal acquisition, which limits the overall spectral performance of this type of detector.

At the time, our motivation for ISGRI was to improve both the spectroscopic performance and sensitivity compared to NaI(Tl) used up to now, particularly in the SIGMA[7] gamma camera onboard the Russian satellite GRANAT (1989). Regarding the spectroscopic performance, the search for ^{44}Ti gamma rays from supernova remnants was a major scientific justification. In terms of the sensitivity of the camera, it was to increase the detection surface and the detector segmentation level. In other words, we had to realize a pixel detector array, which has the effect of limiting the effect of Cosmic rays on the instrumental background. It also reduces the low energy detection threshold down to 15 keV, previously limited to about 35 keV obtained with NaI(Tl). This issue was the focus of my research during my PhD and beyond finally, since my current work is still colored with this issue - sensitivity and spatial, spectral and temporal resolution. This work on the properties of CdTe detectors allowed me to lay the foundations of my expertise on the X- and gamma ray semiconductor detectors.

Achieving ISGRI was made possible by the juxtaposition of a multitude of hybrids (referred to as Polycells in ISGRI) involving 16 CdTe single detectors close to their analog electronic microcircuits made of four ASIC-4C[8] and hybridized on a dedicated ceramic substrate. I contributed to the development of these components (CdTe, ASIC, hybrid) and to the monitoring of the production and qualification of polycells in industry (SAGEM, Lanion). My intimate knowledge of the detectors, of their associated electronic and test benches was essential for the acceptance of components for the different models of the camera, from the technological demonstrator (EM[9]) to the flight models (FM[10]). My meetings and close collaboration with the microelectronics designers of LETI and SEI[11] have enriched this professional experience. I learned with Marc Arquès, Michel Rouger and Eric Delagnes the importance of an integrated team for the realization of such objects, as complex as sensitive. Moreover, my first industrial partnership experience has had a profound influence on the way I work with technological companies today.

In the end, INTEGRAL was launched on October 17, 2002 with ISGRI aboard, the largest CdTe imager ever made at the time – 16,384 pixels and 4096 ASICs. When writing these lines, it still fulfills its mission, orbiting endlessly after 13 years of continuous operation in space. This undeniable success was a springboard for my R&D work towards next generation CdTe sensors, a subject that is close to my heart.

3. Works since hiring at DAPNIA/Irfu

For reasons related to technical difficulties on ISGRI at the time of the finalization of the project and where my participation was expected to be decisive, I agreed to be recruited as an engineer at CEA before completing my thesis, to give the highest priority in my work to ISGRI. I defended my thesis in November 2001 after the delivery and the calibration of the instrument flight model.

3.1. 2001-2003 – GLAST and Ma_Flux
- *GLAST – Fermi*
  In 2001, CEA/DAPNIA was engaged in a hardware participation in the NASA project GLAST, a very high energy gamma ray telescope for observing pulsars, AGN and Blazars or "unidentified" galactic sources and the study of the origin of cosmic rays in particular.

---

7. SIGMA, « Système d'Imagerie Gamma à Masque Aléatoire ».

8. ASIC = Application Specific Integrated circuit. ASIC 4C is the name the circuit in ISGRI with "4" standing for the number of channel per chip and "C" the index of the circuit iteration.

9. EM, Engineering Model.

10. FM, Flight Model.

11. SEI – « Service d'Electronique et d'Informatique », former name of SEDI, « Service d'Electronique, Détecteurs et Informatique ».

Our role at DAPNIA was to ensure the production of the electromagnetic calorimeter LAT in collaboration with NRL[12] (USA), IN2P3 and LLR/École polytechnique. The instrument consisted of the stack of interlaced CsI bars, readout by silicon photodiodes. My main contribution was to develop the performance test benches and associated methods for characterizing the CsI crystal light yield and associated photodetectors performance. The project stopped abruptly in 2003. The CEA continued its involvement with a scientific contribution but leaving no further hardware activities in the laboratory. Fermi-GLAST went on to become a huge scientific success.

- *R&D Ma_flux*
  At the same time, my research on CdTe detectors continued under the Ma_Flux project. The idea was to promote CdTe detectors in their Polycell configuration, enjoying a strong technological maturity acquired with ISGRI and following the program towards new scientific applications: Mars exploration and Mars Sample Return. The objective was extremely ambitious; to implement a rock analysis laboratory on Mars, to collect samples and to bring them back to Earth. I participated in this project in collaboration with the IPGP[13], CNES and DRT/LIST. I studied with Bertrand Cordier an instrument concept and participated in the implementation of a CdTe based demonstrator for in-situ analysis of Martian rocks by means of X-ray fluorescence analysis. This technique requires excellent spectral performance of an exceptionally compact and lightweight system. To improve the spectral performance, I began to study CdTe Schottky diode type detectors. A proof of concept was proposed and tests conducted on the AGLAE[14] accelerator in collaboration with the Centre de Recherche et de Restauration des Musées de France au Louvre, before the project was terminated in 2003.

  I learned from these crisis situations that a laboratory is very sensitive to the programmatic political and financial hazards of space projects and constant R&D efforts not only help maintaining and stabilizing a high scientific level despite these disturbences but also ensure capacity for rapid rebound.

3.2. 2002 –LDS group leader (Space Detector Lab - Laboratoire Détecteurs pour le Spatial)

On the occasion of a complete reorganization of the SAp, the detector development activities, instrument interface to science activities and integration in space payloads activities were combined into a single Space Detection Laboratory led by Bertrand Cordier. I then agreed to take over the group «Space Detectors Laboratory «, which consists of a dozen permanent members. This was my first formal management experience. This laboratory mainly covered topics of R&D for X, Gamma and submillimeter detectors. Apart from the administrative aspects, I have focused my action for the career of my staff and reinforced the technical capabilities of the laboratory by recruiting two technicians and an engineer. This role of group leader also allowed me to consolidate my knowledge of the IRFU, former DAPNIA and beyond all, of the CEA.

3.3. 2003-2009 – R&D CdTe and consequences

- *R&D CdTe – first steps*
  By analyzing the factors limiting the spectral performance of the ISGRI camera, including flight performances, I identified new ways to improve CdTe-based detection systems. The R&D-CdTe program was born: the aim was to simultaneously develop and improve CdTe detectors, their electrodes, their geometry, integrated analog electronics, their hybridization technique and their system architecture. Assuming that we would reach significant advances by combining our strengths, I suggested to the DAPNIA, with Eric Delagnes, to create a mixed team SEDI/Sap, qualified in all areas. This original and visible approach allowed us to envisage a rapid flow of information between laboratories, to solicit broad participation of the department skills and incidentally to produce optimal technical definition of our space imaging spectrometers. By doing so, we were able to fully exploit every technological possibility in the detection chain, from the photon to the data, and preparing for scientific exploitation in orbit.

  Technically, the focal point was the pressing need to achieve pixels 10 to 100 times smaller than before. The spatial resolution is improved naturally as is spectral resolution, mainly due to the reduction of dark current and parasitic capacitance in each spectroscopic chain. I supervised my first PhD student, Bob Franciscus Petrus Dirks, from 2003, with the specific aim to model and demonstrate this approach to guide the design of new pixelated detectors equipped with segmented electrodes. Through the design of a completely new integrated electronics,

---

12. Naval Research Laboratory.

13. IPGPG, « Institut de Physique du Globe de Paris ».

14. AGLAE, « Accélérateur Grand Louvre d'Analyse Elémentaire ».

radiation tolerant, reliable, and perfectly adjusted to the properties of this type of CdTe sensors (IDeF-X circuit family - Olivier Gevin and Francis Lugiez), we demonstrated a spectral resolution 1 keV FWHM at 60 keV, an improvement by a factor of 6 compared to the ISGRI best result. Note that the low-energy detection threshold was simultaneously brought down from 15 keV to 3 keV, a notable progress for high-energy astrophysicists who see for the first time the opportunity to observe both in the low X and gamma range with a unique instrument. This property of our sensors means that the technical specifications for the detection threshold of SVOM/ECLAIRs can be reduced to 4 keV, allowing the observation of GRBs to see events at cosmological distances (Z~10-20). This major result will provide many scientific opportunities later in other scientific experiments.

- *R&D CdTe – Caliste CdTe Micro camera*
The use of small pixels raises the difficulty of making a compact hybrid component, stackable on four sides in addition, so that the realization of large cameras is possible. This is the reason why in 2004 I started technological research work in order to identify and pre-qualify hybridization technology compliant with our scientific performance requirements and the constraints of the space environment (TRL[15] 3-4). My meeting with the 3D PLUS Company was probably one of the key moments of my past twelve years of research. Indeed, using their expertise in making 3D electronic components (memory stacks) and "turn away" their use, I proposed a new concept of micro gamma camera, the Caliste[16] Project.

Between 2004 and 2009, surrounded by a large team DAPNIA/IRFU (~ 15 persons involved, with a hard core of 6 people), with 3D PLUS and with the constant support of CNES, I drove the realization of four versions of Caliste, from the demonstrator to the prototype at TRL 5 – a requirement for a possible participation in a space program. The highlight of this research was undoubtedly the presentation by my second PhD student Aline Meuris, IEEE conference NSS/MIC/RTSD[17] Honolulu 2007, when we revealed to our community the spectacular performance of Caliste-64. I then completed the first phase of the R&D CdTe program designing and manufacturing the Caliste-256 prototype, a miniature imaging spectrometer with 580 microns pitch and showing up a spectral resolution of 860 eV FHWM at 60 keV, with a low-energy threshold of 1.3 keV; a unique performance in the world.

- *SVOM/ECLAIRs – SIMBOL-X*
The first outcome of this R&D is the ECLAIRs instrument, onboard the French-Chinese satellite SVOM, for which I have taken the responsibility since 2007 to deliver to IRAP[18] (in charge of the CdTe imager) 300 flight models of our low-noise ASIC – IDeF-X ECLAIRs. I have, in this project, the role of Co-I and CdTe expert. This program is still under development and is planned for flight in 2023.

The second outcome was SIMBOL-X satellite (PI: Ph. Ferrando, CEA.). SIMBOL-X is an observatory using the technique of formation flying: a satellite carries a hard X-ray grazing incidence mirror, efficient to deflect the photons up to 80 keV while 20 meters away, a second satellite slaved to the first carries the focal planes. Among them, the HED detector (High Energy Detector), which I had technical responsibility during the phase A study, is equipped with a mosaic of Caliste to form the detector array, covering the field of view with an area of 64 cm^2. Unfortunately the ambitious Franco-Italian project stopped abruptly in 2009. Although it was a shock to the whole team and its partners, this news has not dented my determination to achieve a great camera based on pixelated CdTe with high spectral response.

3.4. 2009-2013 – Start of Space projects – new R&D cycle
- *MACSI, a prototype with high technological maturity*
The degree of maturity of Caliste on the one hand and the HED definition level on the other hand led me to propose the development of MACSI (Modular Assembly of Caliste Spectro-Imager) to IRFU. The institute gave me, on its own financial funds, the necessary material and human resources to complete the development of a 1/8th equivalent focal plane of SIMBOL-X. For the occasion we realized in 2011 a series of Caliste and its associated IDeF-X ASICs, both in their most advanced version to date HD[19]. The R&D-CdTe team, with the support of SEDI and SAp integration groups, quality, system, mechanics and electronics produced their effort to build a complete prototype of a camera

---

15. RL, *Technology Readiness Level* is a scale from 1 to 9, which characterizes the technological maturity of a system.

16. Caliste name has been proposed by Marie-Cécile Vassal, project manager at 3D PLUS.

17. IEEE Nuclear Science Symposium and Medical Imaging Conference.

18. « Institut de Recherche en Astrophysique et Planétologie, Toulouse ».

19. HD stands for "High Dynamic".

composed of 2048 independent spectrometers with 625 microns pitch, high spectral and temporal resolution. This unique assembly in the world is now of TRL-6, meaning it is ready for flight and can be replicated.

I took the initiative of proposing this instrument for inclusion on international space programs as IXO[20] (ESA-NA-SA-JAXA) or Spektrum Roengen Gamma (Roscosmos-IKI – DLR) and I will continue to do this until we find a scientific oppportunity for MACSI in Space. I consider today that the use a nano-satellite for solar observation is possible. I also advertise the polarimetric capabilities of the instrument that offers new scientific perspectives at gamma ray energies. I have demonstrated the polarimetric performance within our Lapolcaliste collaboration with the University of Coimbra and INFN Bologna in 2011 by exposing to Caliste a mono-energetic beam highly polarized on the ID-15A line at the ESRF[21].

- *Space science benefits, CINEMA, ASTRO-H, STIX, STEP...*
Following the end of our SIMBOL-X project, I was invited by my Japanese colleagues to join the Astro-H team (X and gamma ray Space Telescope, «former competitor» of SIMBOL-X) in view of my expertise on CdTe detectors and associated electronics, extensively used onboard the HXI and SGD telescopes. Astro-H is scheduled for launch very soon and is currently in its final integration phase. I started with Philippe Laurent to propose a European contribution to Astro-H, guaranteeing us a scientific return from the first months of operation in flight. We organized the procurement by ESA of all BGO[22] crystals needed to manufacture the anti-coincidence shileds of the SGD instrument systems (Soft Gamma-ray Detector) and HXI (Hard X-ray Imager). I also took the scientific responsibility of an activity funded by ESA to study radiation effects on microcircuits VATA and CdTe detectors themselves. I also studied the behavior of CdTe detectors in the long term by simulating on the ground the operations planned in orbit. This activity offers us a very detailed knowledge of sensors (CdTe strip configuration) of Astro-H for mission planning, i.e. to better prepare the observations. These activities draw us into international scientific programs in which our role is recognized and finally it gives us increased visibility.

In 2009, I was invited by Pr. Robert Lin to give a seminar at the Space Sciences Lab at the University of California Berkeley with which we have had a cooperation framework agreement for the use of our chips IDeF- X in space on American projects. The first project of the program is a series of three nano-satellites called CINEMA. They are devoted to the observation of Energetic Neurtral Atoms as a probe for studying the current loops in the Earth's magnetosphere. The first launch took place in 2012 and two satellites were launched in 2013. This opportunity is twofold: first, it allows us to access the space with our equipment to reach the coveted TRL-9 and furthermore it allowed me to insert myself in a prestigious scientific community, providing new scientific and technological opportunities for my laboratory. This meeting with Robert Lin also triggered my first steps in the field of Solar physics.

Following this meeting, I worked with Pr. Säm Krucker, P.I. of the STIX[23] instrument. This hard X-ray telescope is dedicated to the observation of solar flares and will fly in 2018 aboard the first medium size mission (M1) of the Cosmic Vision 2015-2025 Program of ESA, the Solar Orbiter satellite. The payload is currently in its implementation phase. The manufacturing of our contribution has just ended recently. This is clearly the maturity acquired during our R&D program, which allowed me to get our first access to space for Caliste, a success for my entire team. I like to say that we have entered the STIX project in phase B and we were able to demonstrate our ability to adapt the project in record time, producing with the support of CNES, prototypes dedicated to the level of performance required in less than one year. For STIX, I am Lead Co-I and Project Manager of the French contribution to STIX. As such I secured the CNES and FHNW (Switzerland) fundings to proceed. This success has led to other particpations since I am also participating in the instrument EPD/STEP[24] aboard the same mission to supply ASICs IDeF X BD, coupled to Silicon diode arrays by LBNL[25]. Today Solar Orbiter is probably my largest project but also the most unexpected of my career.

- *Valorisation*
For years, I envision benefits of our work beyond the purely scientific context, evidenced by the patents, which I

---

20. IXO, International X-ray Observatory, an ESA large mission.

21. ESRF, European Synchrotron Radiation Facility, Grenoble, France.

22. BGO, Scintillating cristal.

23. STIX, Spectrometer Telescope for Imaging X-rays.

24. Energetic Particles Detector/Supra-Thermal Electrons and Protons.

25. Lawrence Berkeley National Lab, USA.

am co-author. I recently obtained a successful co- proposing the ORIGAMIX project to the ANR/Investissement d'Avenir. This is an instrumental development with DRT/LIST, 3D PLUS and Canberra for the realization of a portable imaging-spectrometer using Caliste-HD, in the post-Fukushima context. This program is very successful and triggered an industry-oriented program of ANR with ANDRA named IGAN, to promote this system in the nuclear industry world.

Furthermore, the CEA/LETI/DTBS[26] is now using our ASICs IDeF-X HD for IMADIF luggage inspection project. A longer-term collaboration with the LETI is under consideration with the SEDI/LDEF[27].

- *R&D-MC2, a new R&D cycle for advanced fine-pitch CdTe imaging spectrometers*
  With the support of CNES, the R&D-CdTe team is one of the few in the world, in a research institute, able to fully develop detection systems, including space qualified ASICs. We now prepare for the future by starting a new R&D cycle from a low level of maturity. The R&D-MC2[28] project, whose purpose is to produce a CdTe imaging spectrometer with very high density of pixels, will show an energy resolution limited by the pair creation statistics at 60 keV (Fano limit). The first building blocks have already been implemented successfully in deep-submicron technology during the thesis of Alicja Michalowska directed by Olivier Gevin at LDEF, while the corresponding CdTe detectors are studied and implemented as part of the thesis of Sébastien Dubos that I directed at LSIS. The detector prototypes have been built and promising results obtained. We pursue the assembly with the support of JAXA/ISAS to prepare a first high-resolution prototype.

- *LSIS, Space Imaging Spectrometer Lab at SAp/AIM*
  In 2012, Pierre-Olivier Lagage, head of Sap/AIM at that time, has adjusted the organization of his Astrophysics division and offered me the position of Head of the Space Imaging Spectrometer Lab (LSIS). On this occasion, my group was becoming a more visible laboratory and was enriched by all development activities and detectors characterizations including the fields of infrared and visible areas that were beyond my scope thus far. The LSIS is a laboratory at the forefront in many areas that are in the field of space science applications, but also works in groundbased astronomy when relevant. We assure our research mission with a wide range of technical skills in interaction with all the laboratories of the IRFU. In most areas, we are also close to the technological platforms of INAC and LETI. We have adapted means for our missions in our six laboratories. Our strategy is to push in parallel instrument developments at various levels of maturity by trying to stick as close to the expectations of astrophysicists but also being force proposal. This new organization has enabled me to give new impetus to the laboratory in terms of group dynamics. Links with other laboratories SAp/AIM and IRFU are thereby also facilitated.

  I submitted the LSIS to scientific evaluation by AERES in wave D. My laboratory has obtained early 2013 the maximum score "A+" on all counts, but a "A" with respect to criteria relative to the international visibility and the academic attractiveness. This is a point I seek to improve now. For the rest of my activities as a laboratory manager, I assure the daily management of the team (annual interviews, monitoring of careers, recruitment, employment plan, workload and scientific policy).

4. Prospect

In the future, I will work to bring our developments in space with a high priority in scientific research programs in astronomy and solar physics in particular, by developing my recent contacts that extend from Russia (SORENTO/Roskosmos), USA (NASA), through Switzerland (COXIP – BEEP/FHNW) and Japan (JAXA).

Regarding R&D-CdTe, I persist in the belief that our integrated team SAp/SEDI is known to be effective and innovative, and will be more and more if we reinforce our links with SMEs such as 3D PLUS creating partnership or joint laboratory. I started this process through our first joint scientific proposal from CNES in 2013.
Finally, at the management level, I will continue to develop the LSIS to succeed in our current commitments but also to prepare for the next major scientific challenges such as ATHENA+, a revolutionary space X Observatory, a Large ESA mission to 2030.

---

26. « Département de micro Technologies pour la Biologie et la Santé».

27. « Laboratoire de Détecteurs et Electronique Frontale », directed by E. Delagnes at SEDI.

28. MC2 is standing for Mini Cadmium telluride on Chip.

4. Detailed career

Dates	Assignment	Job title and events
Current position	Irfu/SAp/LSIS	• Head of LSIS (Space Imaging-Spectrometers Lab) • Instrument Physicist in the field of CdTe detectors for Space astrophysics • CEA Expert in « Space Instrumentation / X and Gamma ray semiconductor detectors » • Project manager and Lead Co-Investigator for Solar Orbiter/STIX Caliste-SO, CNES-ESA-FHNW (Switzerland) • Team leader for SolO/EPD/STEP (Allemagne/Univ. Kiel), CINEMA (USA/SSL), Scientific valorisation program of IDeF-X • Leader of ASTRO-H French team (ESA-JAXA), ASIC et CdTe expertise for SGD and HXI instruments • Team member of ASTRO-H (JAXA-NASA-ESA) • Principal Investigator of the ESRF « Lapolcaliste » (INFN, Coimbra, CEA), a experimental program for gamma ray polarization measurements with Caliste • Co-leader of R&D on Silicon based Compton cameras in the frame of "projet d'interface Labex UnivearthS, IP5" • Principal investigator of CdTe detectors "MC2" R&D program (CEA-Cnes) and MACSI (CEA) • Team leader of WP3 ORIGAMIX, a national program for nuclear safety, Investissement d'avenir/ANR (DRT/LIST, CEA, 3D PLUS CANBERRA) • Team member of phase 0 studies for LOFT/WFM (ESA M3) and IXO (ESA-JAXA-NASA)
2002 to 2009	rfu/SAp/LDS	• Group Leader « Space Detector Lab» under the responsibility of B. Cordier. • Instrument Physicist in the field of CdTe detectors for Space astrophysics • Principal investigator of R&D-CdTe program (CEA-CNES) • Leader of the HED hard X-ray detector plane aboard SIMBOL-X satellite • Co-Investigator of ECLAIRs, responsible for the supply of readout ASIC IDeF-X V2 and CdTe expert • NRBC program – Coded mask aperture and Compton based CdTe camera for nuclear safety
2001 to 2002	DAPNIA/ SAp/Labo gamma	• Instrument physicist • Responsible of the test benches in the frame of the French contribution to the calorimeter of GLAST (NASA/Fermi) • Ma_Flux R&D (Cnes), A XRF CdTe based probe for the martian soil analysis
1997 to 2001	DAPNIA/ SAp/Labo gamma	• PhD student and first position of research engineer (permanent staff) at CEA, team member of INTEGRAL/ISGRI (ESA-CNES-CEA) in the field of CdTe detectors, associated electronics and hybridization process. Fab, calibration, system level test bench
1996 to 1997	LETI/CMO	• Scientist of military contingent, French Navy, in the field of laser induced damage on thin optical coating for military applications. Calibration of high power laser beams.

5. Scientific responsibilities

Dates	Collaborations	Scientific responsibilities
Since 2009	LIST – 3D PLUS CANBERRA & GIE INTRA	• Scientific leader of ANR/Investissement d'avenir ORIGAMIX project, WP3
	ESA – CNES - FHNW	• Lead Co-Investigator of Solar Orbiter/STIX/Caliste-SO
	Interne Irfu	• Scientific leader of MACSI, a CdTe camera with high spatial, spectral and temporal resolution
	CNES	• Scientific leader of R&D CdTe – MC^2, development of high pixel density CdTe detectors
	CNES-IRAP	• Co-Investigator of ECLAIRs
	UCB/SSL-LBNL	• Co-Investigator of Cinema Trio, NSF, scientific cubesat program
	ESA – Univ. Kiel	• Co-Investigator Solar Orbiter/EPD/STEP
	INFN-Univ. de Coimbra	• Principal investigator of the Compton polarimeter experiment "Lapolcaliste"
	JAXA - ESA	• Team member of ASTRO-H, HXI and SGD
	APC	• Co-Investigator of Compton based Camera, WP5 Labex UnivearthS
2002-2009	CEA-CNES-ASI	• Principal investigator if the R&D-CdTe program, Creation of Caliste 64 and Caliste 256

6. Scientific and technical expertise

1. Scientific and technical expertise tasks

Dates	Intitution	Role	Mission
2009	JAXA	Review committee member	ASTRO-H Engineering Peer Review, Stanford, Etats-Unis
2002, 2004 and 2009	Irfu/SEDI	Reviewer	Scientific and technical Committee of SEDI, the electronics, detectors and computer division – three cases.
2004-2014	IEEE Transaction on Nuclear Sciences	Reviewer	Reading committee, >10 articles
2005-2015	Nuclear Instruments And Methods in Physics Research	Reviewer	Reading committee, > 25 revues
2006-2015	Experimental Astronomy	Reviewer	Reading committee, few articles
2011-2014	Radiation Measurements	Reviewer	Reading committee, few articles
2008	CEA	Reviewer	Report on safety in critical infrastructures – « Projet SIC/Camera Gamma à masque codé/ Compton à base de CdTe de type INTEGRAL/ IBIS/ISGRI »

2. Boards and committees

Dates	Intitution	Position	Committee/Board name
2015	CNES	Member Board member	"Centre de Compétence Technique Optoélectronique"
2004-2015	Irfu/SAp	Member	Space Radiations Group
2007-2013	Irfu/SAp	Elected member	Scientific and technical Committee of the Astrohysics division
2004-2011	CNES	Member	"Centre de Compétence Technique Optoélectronique"

Dates	Intitution	Position	Committee/Board name
2011	CEA/ONERACNES/INSU	Board member	"Consolidation des Technologies Spatiales en France"
2011	Irfu/IN2P3	Team member and Co-author	Prospective study group
2004	DAPNIA/IN2P3	Member of semi-conductor group	Prospective study group

3. Jurys

Dates	Intitution	Position	PhD Thesis Title
2007	Dr. Y. Li CEA/SEDI	Referee	"Recherche et Développement de Capteurs Actifs Monolithiques CMOS pour la Détection de Particules Elémentaires" Université Paris 11
2010	Dr. N. Remoué IRAP	Examiner	"Caractérisation de détecteurs CdTe Schottky pour la Caméra X/Gamma d'ECLAIRs" Université Toulouse 3
2013	Dr. C. Buis CEA/LETI	Referee	"Etude des corrélations entre les défauts structuraux et les inhomogénéités spatiales des détecteurs de rayons X à base de CdTe pour l'imagerie médicale" Université Saint-Etienne.
2013	I. MATEU IRAP	Referee	"Systèmes de détection digitaux par traitement numérique des impulsions X-dur des applications spatiales" Université Toulouse 3
2013	A. Habib CEA/LETI	Examiner	"Détecteurs radiologiques grande surface, multi-énergie" Université de Grenoble
2015	S. Wang École polytechnique	Examiner	"Etude d'une TPC, cible active pour la polarimétrie et l'astronomie gamma par creation de paires dans HARPO" Université Paris XI, École polytechnique

7. Experience in instructing students and post-docs

1. PhD (supervisor)

Dates	Student	Title
2014	Paul Serrano	"Développement de détecteurs à ionisation directe de type CdTe et Micromegas miniatures pour la spectro-imagerie polarimétrique" Université Paris 7, ED127 Financement ED127/Paris XI
2011-2013	Dr. Sébastien Dubos	"Nouveau spectro-imageur CdTe à ultra-haute résolution spatiale, spectrale et temporelle pour l'astronomie X dur et gamma" Université Paris 7, ED127 Financement CEA-CNES
2006-2009	Dr. Aline Meuris	"Etude et optimisation u plan de détection de haute énergie en Cd(Zn)Te de la mission spatiale d'astronomie X et gamma Simbol-X" Université Paris 7, ED127 Financement CEA-CNES
2003-2006	Dr. Bob P.F. Dirks	"Study and modelling of the new generation Cd(Zn)Te X- and Gamma-ray detectors for space applications" Cotutelle de thèse, Université Paris 7, ED127 et Université de Twente, Pays Bas Financement CEA – CNES

2. Postdocs

Dates	Student	Research
2015	Dr. Daniel Maier	"Étude de la stabilité en orbite des détecteurs CdTe des instruments SGD et HXI à bord d'ASTRO-H." Financement CNES
2012-2013	Dr. Youri Dolgorouky	"Étude de caméra Compton à base de Détecteur Si strippés double face (DSSD) utilisant des ASICs IDeF-X BD pour la lecture." Financement Labex UnivearthS
2006-2007	Dr. Philippe Paul	"Etude d'une caméra Compton CdTe à masque codé pour des applications de type NRBC." Financement NRBC/A3

3. Student supervision

Dates	Student	Diploma
2007-2010	Maxime Taupin	Engineering degree/Ingénieur Optoélectronique IFIPS Paris sud, Alternance. • "Etude des propriétés physiques de détecteurs CdTe Pixélisés" • "Etude la hauteur de barrière de diodes Schottky CdTe pour la détection de photons X" • "Mise en œuvre de prototype de détecteurs CdTe stripes"
1997-2015	35 students	• "Collèges", "lycées" and "CPGE": 9 training periods • DUT and BTS: 9 training periods • Engineering schools: 9 training periods • Licence and Master 1 : 4 training periods • Master 2 : 1 training period, 3 mini-projects

8. Teaching activities

Dates	Degree	Domain/Title
2005-2007	Master Pro, Université Paris 7	"Détecteurs Semi-conducteurs X et Gamma"
2006	Université de Limoges	"Détecteurs pour l'astronomie, l'accent sur les détecteurs HE"
2002	Summer school	Mission concept and payload design in X and Gamma ray astronomy
2001	Professionnal training professeurs du secondaire	"ISGRI: Imageur Gamma du télescope IBIS du Satellite Integral"

9. Conference organization

Dates	Role	Conference
2015-	• Chairman	NDIP17, New Developments in Photodetection 2017, France
2015-2016	• Scientific Program Committee member	SPIE conference on Space Telescope and Instrumention 2016: Ultra violet to Gamma ray, Edinburgh, UK
2012-2013	• Local Organization Committee member	12th ASTRO-H Science Meeting & 4th ASTRO-H Summer School, 2014, Paris, France
2012-2013	• Chairman • Vice Editorial manager • Invited Editor of Nuclear Instruments & Methods In Physics Research Section A • Referee	NDIP14, New Developments in Photodetection 2014, Tours, France
2010-2011	• Co-Chair • Invited editor of Nuclear Instruments & Methods In Physics Research Section A • Vice Editorial manager • Referee • Scientific sessions Chaiman	NDIP11, New Developments in Photodetection 2011, Lyon, France
2007-2008	• Chairman of the industrial exhibition • Invited editor of Nuclear Instruments & Methods In Physics Research Section A • Referee • Scientific sessions Chaiman	NDIP08, New Developments in Photodetection 2008, Aix-Les-Bains, France
2004-2005	• Chairman of the industrial exhibition • Invited editor of Nuclear Instruments & Methods In Physics Research Section A • Referee	NDIP05, New Developments in Photodetection 2005, Beaune, France

II. List of publications

1. Bibliometry

Total number of scientific publications = 120
- 46 articles published in peer-reviewed journals
- 58 articles published in conference proceedings
- 3 patents
- 13 other publications and books

and 62 research proposals with 27 as scientific leader.

Currently a dozen of papers are in preparation.

	ISI Web of Knowledge	Scholar.google.fr	ADS/NASA	Research Gate
Number of publications	103	121	92	121
Hirsch Factor	12	16	12	/
Citations	871	1738	1011	1671
Citations w/o self citations	744	/	/	/
Score	/	/	/	RG = 29.20 (15% of the highest scores)

January 20, 2016 ISI WEB OF KNWOLEDGE mentions 103 publications. According to this bibliometry tool, I account a total of 744 citations without self-citations. My average rate of citation is 8,46 per article while my annual citation rate is 52/year, in the last 15 years at CEA. In the last 5 years, the rate is closer to 80 citations/year.
From one tool to another, the citation rate is variable which affects the impact factor.

According to ISI WEB OF KNOWLEDGE, my five most cited articles are cited respectively 303, 85, 67, 22 and 22 times:
- I am co-author of the first [3.4-33] with my former Thesis director, François Lebrun. This paper is a reference for the ISGRI camera users on the INTEGRAL satellite.
- I am the sole author of the second article [3.4-37]. This paper is a review of the CdTe detector technologies and trends at that time.
- The third and fourth most cited paper [3.3-39 and 3.3-22] are related to ASTRO-H. I am a co-author of this article under my role of official ASTRO-H team member.
- My fifth most cited paper [3.4-24] is one of the most important in my eyes because it revealed to the CdTe community the existence of Caliste-64, the first accomplishment of our R&D program towards a high performance CdTe pixel detector for space science. The rest of the text is essentially devoted to this enabling technology.

The Hirsch impact factor illustrates the popularity of an article in the scientific community. A value between 5 and 15 is common in the instrumentation domain where articles are devoted to very specific technologies, thus not cited. My results are good with respect to most popular actors in the CdTe field.

Searching the impact of research into the CdTe community, into the ISI WEB OF KNOWLEDGE database with the following criteria: "CdTe OR CZT OR CdZnTe" in title, "CdTe detectors OR detectors OR spectrometers" OR "Spec-

trometers" in the topics or "Limousin" in the authors, I find 5547 publications H=53. I am then co-author of the most cited paper and the sole author of the 19th most cited paper.

Enventually, I observe that my citation rate (Figure 1) continually improves since the year 2000. The conclusion is that the effect of our work and the visibility of my research group is increasing.
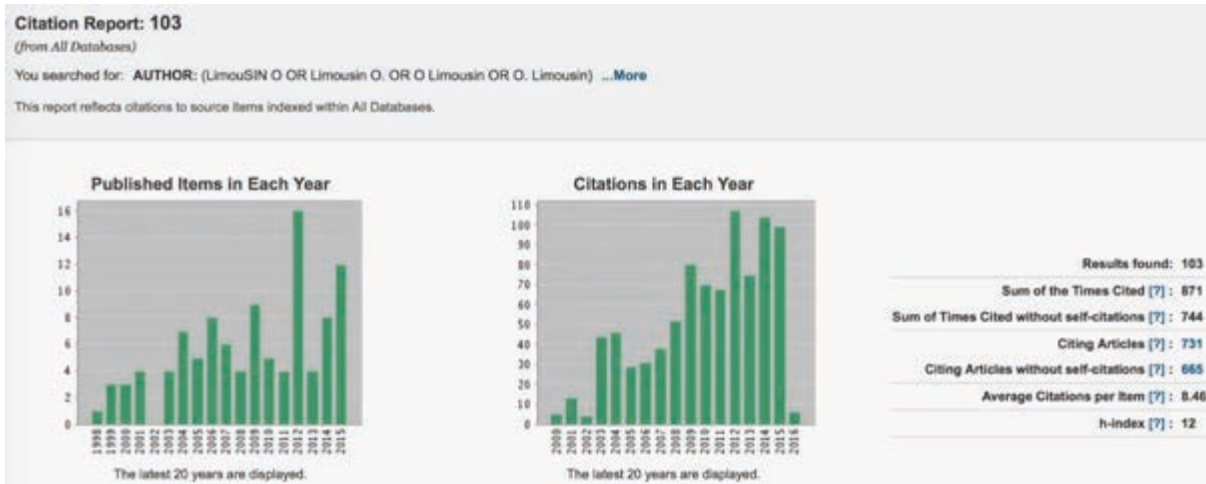
Figure 1. Citation report for O. Limousin, ISI WEB OF KWONELDGE as January 20, 2016.

2. Patents

1. Process for flip-chip connection of an electronic component
O. Limousin (CEA), F. Soufflet (3D Plus)
WO/2012/120448, 2011

2. Dispositif Electronique Tridimensionnel
O. Limousin (CEA), F. Lugiez (CEA)
FR2902927 (B1), 2007

3. Device for locating and imaging gamma or X-radiation sources
P. Laurent (CEA), O. Limousin (CEA)
US 20100177869, 2006

3. Conference proceedings papers

1. Performance and qualification of CdTe pixel detectors for the Spectrometer/Telescope for Imaging X-rays
O. Grimm, M. Bednarzik, G. Birrer, N. Arnold, V. Commichau, G. Hurford, S. Krucker, O. Limousin, A. Meuris.
Proceedings of Pixel 2014 conférence, 2014.

2. Development of a stacked detector system for the X-ray range and its possible applications
D. Maier, O. Limousin, A. Meuris, S. Pürckhauer, A. Santangelo, T. Schanz, C. Tenzer.
Proc. SPIE. 9154, High Energy, Optical and Infrared Detectors for Astronomy VI, id. 915422, 2014.

3. Caliste-SO: the X-ray spectrometer unit of the STIX instrument onboard the Solar Orbiter space mission
A. Meuris, O. Limousin, O. Gevin, M-C. Vassal, F. Souffelt, N. Fiant, M. Bednarzik, C. Wild, S. Stutz, G. Birrer, C. Blondel, I. Le Mer, D-D. Huynh, M. Donati, O. Grimm, V. Commichau, G. Hurdford, S. Krucker, F. Gonzalez, M. Billot.
Proc. SPIE. 9154, High Energy, Optical and Infrared Detectors for Astronomy VI, id. 91540Y, 2014.

4. Soft gamma-ray detector (SGD) onboard the ASTRO-H mission
Y. Fukazawa, H. Tajima, S. Watanabe, R. Blandford, K. Hayashi, A. Harayama, M. Kawaharada, M. Kokubun, P. Laurent, F. Lebrun, O. Limousin, G. Madejski, K. Makishima, T. Mizuno, K. Mori, T. Nakamori, K. Nakazawa, H. Noda, H. Odaka, M. Ohno, M. Ohta, S. Saito, G. Sato, R. Sato, S. Takeda, H. Takahashi, T. Takahashi, Y., Tanaka, Y. Terada, H. Uchiyama, Y. Uchiyama, K. Yamaoka, Y. Yatsu, D. Yonetoku, T. Yuasa.
Proc. SPIE. 9154, High Energy, Optical and Infrared Detectors for Astronomy VI, id. 91442C, 2014.

5. The Hard X-ray Imager (HXI) for the ASTRO-H Mission
G. Sato, M. Kokubun, K. Nakazawa, E. Teruaki, Y. Fukazawa, A. Harayama, K. Hayashi, J. Kataoka, J. Katsuta, H. M. Kawaharada, P. Laurent, F. Lebrun, O. Limousin, K. Makishima, T. Mizuno, K. Mori, T. Nakamori, H. Noda, H. Odaka, M. Ohno, M. Ohta, S. Saito, R. Sato, H. Tajima, H. Takahashi, T. Takahashi, S. Takeda, Y. Terada, H. Uchiyama, Y. Uchiyama, S. Watanabe,K., Yamaoka, Y. Yatsu, T. Yuasa.
Proc. SPIE. 9154, High Energy, Optical and Infrared Detectors for Astronomy VI, id. 914427, 2014.

6. The ASTRO-H X-ray astronomy satellite
T. Takahashi, K. Mitsuda, R. Kelley, F. Aharonian, H. Akamatsu, F. Akimoto, S. Allen, N. Anabuki, L. Angelini, K. Arnaud, M. Asai, M. Audard, H. Awaki, P. Azzarello, C. Baluta, A. Bamba, N. Bando, M. Bautz, T. Bialas, R. D. Blandford, K. Boyce, L. Brenneman, G. Brown, E. Cackett, E. Canavan, M. Chernyakova, M. Chiao, P. Coppi, E. Costantini, J. de Plaa, J.-W. den Herder, M. DiPirro, C. Done, T. Dotani, J. Doty, K. Ebisawa, T. Enoto, Y. Ezoe, A. Fabian, C. Ferrigno, A. Foster, R. Fujimoto, Y. Fukazawa, S. Funk, A. Furuzawa, M. Galeazzi, L. Gallo, P. Gandhi, K. Gilmore, M. Guainazzi, D. Haas, Y. Haba, K. Hamaguchi, A. Harayama, I. Hatsukade, K. Hayashi, T. Hayashi, K. Hayashida, J. Hiraga, K. Hirose, A. Hornschemeier, A. Hoshino, J. Hughes, U. Hwang, R. Iizuka, Y. Inoue, K. Ishibashi, M. Ishida, K. Ishikawa, K. Ishimura, Y. Ishisaki, M. Itoh, N. Iwata, N. Iyomoto, C. Jewell, J. Kaastra, T. Kallman, T. Kamae, J. Kataoka, S. Katsuda, J. Katsuta, M. Kawaharada, N. Kawai, T. Kawano, S. Kawasaki, D. Khangaluyan, C. Kilbourne, M. Kimball, M. Kimura, S. Kitamoto, T. Kitayama, T. Kohmura, M. Kokubun, S. Konami, T. Kosaka, A. Koujelev, K. Koyama, H. Krimm, A. Kubota, H. Kunieda, S. LaMassa, P. Laurent,

F. Lebrun, M. Leutenegger, O. Limousin, M. Loewenstein, K. Long, D. Lumb, G. Madejski, Y. Maeda, K. Makishima, M. Markevitch, C. Masters, H. Matsumoto, K. Matsushita, D. McCammon, D. McGuinness, B. McNamara, J. Miko, J. Miller, E. Miller, S. Mineshige, K. Minesugi, I. Mitsuishi, T. Miyazawa, T. Mizuno, K. Mori, H. Mori, F. Moroso, T. Muench, K. Mukai, H. Murakami, T. Murakami, R. Mushotzky, H. Nagano, R. Nagino, T. Nakagawa, H. Nakajima, T. Nakamori, S. Nakashima, K. Nakazawa, Y. Namba, C. Natsukari, Y. Nishioka, M. Nobukawa, H. Noda, M. Nomachi, S. O'Dell, H. Odaka, H. Ogawa, M. Ogawa, K. Ogi, T. Ohashi, M. Ohno, M. Ohta, T. Okajima, T. Okazaki, N. Ota, M. Ozaki, F. Paerels, S. Paltani, A. Parmar, R. Petre, C. Pinto, M. Pohl, J. Pontius, F. S. Porter, K. Pottschmidt, B. Ramsey, R. Reis, C. Reynolds, C. Ricci, H. Russell, S. Safi-Harb, S. Saito, S.-I. Sakai, H. Sameshima, K. Sato, R. Sato, G. Sato, M. Sawada, P. Serlemitsos, H. Seta, Y. Shibano, M. Shida, T. Shimada, P. Shirron, A. Simionescu, Simmons, R. Smith, G. Sneiderman, Y. Soong, L. Stawarz, Y. Sugawara, S. Sugita, A. Szymkowiak, H. Tajima, H. Takahashi, H. Takahashi, S.-I. Takeda, Y. Takei, T. Tamagawa, K. Tamura, T. Tamura, T. Tanaka, Y. Tanaka, Y. Tanaka, M. Tashiro, Y. Tawara, Y. Terada, Y. Terashima, F. Tombesi, H. Tomida, Y. Tsuboi, M. Tsujimoto, H. Tsunemi, T. Tsuru, H. Uchida, H. Uchiyama, Y. Uchiyama, Y. Ueda, S. Ueda, S. Ueno, S. Uno, M. Urry, E. Ursino, C. de Vries, A. Wada, S. Watanabe, T. Watanabe, N. Werner, N. White, D. Wilkins, S. Yamada, T. Yamada, H. Yamaguchi, K. Yamaoka, N. Yamasaki, M. Yamauchi, S. Yamauchi, T. Yaqoob, Y. Yatsu, D. Yonetoku, A. Yoshida, T. Yuasa, I. Zhuravleva, A. Zoghbi, J. ZuHone.
Proc. SPIE. 9154, High Energy, Optical and Infrared Detectors for Astronomy VI, id. 914425, 2014.

7. WPOL: a DSSD-based hard X-ray wide field imager and polarimeter
P. Laurent, W. Bertoli, E. Breelle, Y. Dolgorouky, C. Gouiffès, M. Khalil, O. Limousin, F. Lebrun, J. Rodriguez.
Proc. SPIE. 9154, High Energy, Optical and Infrared Detectors for Astronomy VI, id. 91441J, 2014.

8. PACT: a sensitive 100 keV-10 MeV all sky pairs and Compton telescope
P. Laurent, V. Tatischeff, N. de Seréville, O. Limousin, W. Bertoli, E. Bréelle, Y. Dolgorouky, A. Gostojic, C. Hamadache, M. Khalil, J. Kiener.
Proc. SPIE. 9154, High Energy, Optical and Infrared Detectors for Astronomy VI, id. 91440I, 2014.

9. The spectrometer telescope for imaging X-rays (STIX) on board Solar Orbiter
N. Vilmer, S. Krucker, D. Karol Seweryn, P. Orleanski, O. Limousin, A. Meuris, A. S. Brun, O. Grimm, H.P. Groebelbauer, J. Rendtel.
40th COSPAR Scientific Assembly. Proceedings, 2014.

10. Thermal simulations of the STIX instrument for ESA Solar Orbiter mission
A. Przepiórka, K. Seweryn, N. Arnold, A. Bernet, L. Blecha, K. Grassmann, O. Grimm, G. J. Hurford, H. P. Gröbelbauer, Säm Krucker, O. Limousin, J. Martignac, A. Meuris, P. Orleański, H. Önel, K. R. Skup.
Proc. Of the 43rd International Conference on Environmental Systems, AIAA 2013-3391, 2013.

11. Hardware simulator of Caliste-SO detectors for STIX instrument
P. Podgórski, D. Ścisłowski, M. Kowaliński, T. Mrozek, M. Stęślicki, J. Barylak, A. Barylak, J. Sylwester, S. Krucker, G. J. Hurford, N. G. Arnold, P. Orleański, A. Meuris, O. Limousin, O. Gevin, O. Grimm, L. Etesi, N. Hochmuth, M. Battaglia, A. Csillaghy, I. W. Kienreich, A. Veronig, S. Bloomfield, M. Byrne, A. M. Massone, M. Piana, S. Giordano, K. R. Skup, R. Graczyk, M. Michalska, W. Nowosielski, A. Cichocki, M. Mosdorf.
Proc. SPIE. 8903, Photonics Applications in Astronomy, Communications, Industry, and High-Energy Physics Experiments 2013 89031V, 2013

12. Low energy characterization of Caliste HD, a CdTe based imaging spectrometer
S. Dubos, O. Limousin, C. Blondel, R. Chipaux, Y. Menesguen, A. Meuris, T. Orduna, T. Tourette, A. Sauvageon.
IEEE NUCLEAR SCIENCE SYMPOSIUM – CONFERENCE RECORD, 2012.

13. Multi-Correlated Double Sampling vs. Analog shaper: Low power ASIC for pixelated CdTe.
A. Michalowska, O. Gevin, O. Limousin, C.S. Tindall.
IEEE NUCLEAR SCIENCE SYMPOSIUM – CONFERENCE RECORD, 2012.

14. Low power, low noise, Charge Sensitive Amplifier in CMOS 0.18 µm technology for the readout of fine pitch pixelated CdTe detector
O. Gevin, A. Michalowska, O. Limousin, C.S. Tindall, S. Dubos, D. Renaud, X Coppolani.
IEEE NUCLEAR SCIENCE SYMPOSIUM – CONFERENCE RECORD, 2012.

15. Instrument data processing unit for spectrometer/telescope for imaging X-rays (STIX)
Konrad R. Skup, A. Cichocki, R. Graczyk, M. Michalska, M. Mosdorf, W. Nowosielski, P. Orleański, A. Przepiórka, K. Seweryn, M. Stolarski, M. Winkler, J. Sylwester, M. Kowalinski, T. Mrozek, P. Podgorski, A. O. Benz, S. Krucker, G. J. Hurford, N. G. Arnold, H. Önel, A. Meuris, O. Limousin, O. Grimm.
Proc. SPIE. 8454, Photonics Applications in Astronomy, Communications, Industry, and High-Energy Physics Experiments 2012 84540K, 2012.

16. The Spectrometer Telescope for Imaging X-rays (STIX) on board the Solar Orbiter mission
A. O. Benz, S. Krucker, G. J. Hurford, N. G. Arnold, P. Orleański, H.-P. Gröbelbauer, S., Kobler, L. Iseli, H. J. Wieh, A. Csillaghya, L. Etesi, N. Hochmuth, M. Battaglia, M. Bednarzik, R. Resanovič, O. Grimm, G. Viertel, V. Commichau, A. Meuris, O. Limousin, S. Brun, N.Vilmer, K. R. Skup, R. Graczyk, M. Stolarski, M. Michalska, W. Nowosielski, A. Cichocki, M. Mosdorf, K. Seweryn, A. Przepiórka, J. Sylwester, M. Kowalinski, T. Mrozek, P. Podgorski, G. Mann, H. Aurass, E. Popow, H. Önel, F. Dionies, S. Bauer, J. Rendtel, A. Warmuth, M.Woche, D. Plüschke, W. Bittner, J. Paschke, D. Wolter, H. F. Van Beek; F. Farnik, J. Kasparova, A. M. Veronig, I. W. Kienreich, P. T. Gallagher, D. S. Bloomfield, M. Piana, A. M. Massone, B. R. Dennis, R. A. Schwartz, R. P. Lin.
Proceedings of the SPIE - The International Society for Optical Engineering, 8443, 2012.

17. A 3D CZT hard X-ray polarimeter for a balloon-borne payload
E. Caroli, J. M. Alvarez, N. Auricchio, C. Budtz-Jørgensen, R. M. Curado da Silva, S. Del Sordo, P. Ferrando, P. Laurent, O. Limousin, J. L. Galvèz, C. P. Gloster, M. Hernanz, J. Isern, I. Kuvvetli, J. M. Maia, A. Meuris, J. B. Stephen, A. Zappettini.
Proc. SPIE. 8443, Space Telescopes and Instrumentation 2012: Ultraviolet to Gamma Ray 84434O, 2012

18. Recent Trends in Development of CdTe and CdZnTe, Proceedings of The Extreme sky
S. Del Sordo, L. Abbene, E. Caroli, N. Auricchio, J. B. Stephen, E. Quadrini, A. Zappettini, R. M. Curado da Silva, O. Limousin, A. Meuris, P. Ubertini.
Sampling the Universe above 10 keV. October 13-17 2009, Otranto (Lecce) Italy.

19. The ASTRO-H X-ray Observatory
T. Takahashi, K. Mitsuda, R. Kelley, H. Aarts, F. Aharonian, H. Akamatsu, F. Akimoto, S. Allen, N. Anabuki, L. Angelini, K. Arnaud, M. Asai, M. Audard, H. Awaki, P. Azzarello, C. Baluta, A. Bamba, N. Bando, M. Bautz, R. Blandford, K. Boyce, G. Brown, E. Cackett, M. Chernyakova, P. Coppi, E. Costantini, J. de Plaa, J.-W. den Herder, M. DiPirro, C. Done, T. Dotani, J. Doty, K. Ebisawa, M. Eckart, T. Enoto, Y. Ezoe, A. Fabian, C. Ferrigno, A. Foster, R. Fujimoto, Y. Fukazawa, S. Funk, A. Furuzawa, M. Galeazzi, L. Gallo, P. Gandhi, K. Gendreau, K. Gilmore, D. Haas, Y. Haba, K. Hamaguchi, I. Hatsukade, T. Hayashi, K. Hayashida, J. Hiraga, K. Hirose, A. Hornschemeier, A. Hoshino, J. Hughes, U. Hwang, R. Iizuka, Y. Inoue, K. Ishibashi, M. Ishida, K. Ishimura, Y. Ishisaki, M. Ito, N. Iwata, N. Iyomoto, J. Kaastra, T. Kallman, T. Kamae, J. Kataoka, S. Katsuda, H. Kawahara, M. Kawaharada, N. Kawai, S. Kawasaki, D. Khangaluyan, C. Kilbourne, M. Kimura, K. Kinugasa, S. Kitamoto, T. Kitayama, T. Kohmura, M. Kokubun, T. Kosaka, A. Koujelev, K. Koyama, H. Krimm, A. Kubota, H. Kunieda, S. LaMassa,

P. Laurent, F. Lebrun, M. Leutenegger, O. Limousin, M. Loewenstein, K. Long, D. Lumb, G. Madejski, Y. Maeda, K. Makishima, G. Marchand, M. Markevitch, H. Matsumoto, K. Matsushita, D. McCammon, B. McNamara, J. Miller, E. Miller, S. Mineshige, K. Minesugi, I. Mitsuishi, T. Miyazawa, T. Mizuno, H. Mori, K. Mori, K. Mukai, T. Murakami, H. Murakami, R. Mushotzky, H. Nagano, R. Nagino, T. Nakagawa, H. Nakajima, T. Nakamori, K. Nakazawa, Y. Namba, C. Natsukari, Y. Nishioka, M. Nobukawa, M. Nomachi, S. O'Dell, H. Odaka, H. Ogawa, M. Ogawa, K. Ogi, T. Ohashi, M. Ohno, M. Ohta, T. Okajima, A. Okamoto, T. Okazaki, N. Ota, M. Ozaki, F. Paerels, S. Paltani, A. Parmar, R. Petre, M. Pohl, F. S. Porter, B. Ramsey, R. Reis, C. Reynolds, H. Russell, S. Safi-Harb, S.-I. Sakai, H. Sameshima, J. Sanders, G. Sato, R. Sato, Y. Sato, K. Sato, M. Sawada, P. Serlemitsos, H. Seta, Y. Shibano, M. Shida, T. Shimada, K. Shinozaki, P. Shirron, A. Simionescu, C. Simmons, R. Smith, G. Sneiderman, Y. Soong, L. Stawarz, Y. Sugawara, H. Sugita, S. Sugita, A. Szymkowiak, H. Tajima, H. Takahashi, S.-I. Takeda, Y. Takei, T. Tamagawa, T. Tamura, K. Tamura, T. Tanaka, Y. Tanaka, M. Tashiro, Y. Tawara, Y. Terada, Y. Terashima, F. Tombesi, H. Tomida, Y. Tsuboi, M. Tsujimoto, H. Tsunemi, T. Tsuru, H. Uchida, Y. Uchiyama, H. Uchiyama, Y. Ueda, S. Ueno, S. Uno, M. Urry, E. Ursino, C. de Vries, A. Wada, S. Watanabe, N. Werner, N. White, T. Yamada, S. Yamada, H. Yamaguchi, N. Yamasaki, S. Yamauchi, M. Yamauchi, Y. Yatsu, D. Yonetoku, A. Yoshida, T. Yuasa.
Proc. SPIE. 8443, Space Telescopes and Instrumentation 2012: Ultraviolet to Gamma Ray 84431Z, 2012.

20. **Soft gamma-ray detector for the ASTRO-H Mission**
    H. Tajima, R. Blandford, T. Enoto, Y. Fukazawa, K. Gilmore, T. Kamae, J. Kataoka, M. Kawaharada, M. Kokubun, P. Laurent, F. Lebrun, O. Limousin, G. Madejski, K. Makishima, T. Mizuno, K. Nakazawa, M. Ohno, M. Ohta, G. Sato, R. Sato, H. Takahashi, T. Takahashi, T. Tanaka, M. Tashiro, Y. Terada, Y. Uchiyama, S. Watanabe, K. Yamaoka, D. Yonetoku.
    Proc. SPIE. 8443, Space Telescopes and Instrumentation 2012: Ultraviolet to Gamma Ray 844326, 2012.

21. **The Hard X-ray Imager (HXI) for the ASTRO-H mission**
    M. Kokubun, K. Nakazawa, T. Enoto, Y. Fukazawa, J. Kataoka, M. Kawaharada, P. Laurent, F. Lebrun, O. Limousin, K. Makishima, T. Mizuno, K. Mori, T. Nakamori, H. Odaka, M. Ohno, M. Ohta, G. Sato, R. Sato, H. Tajima, H. Takahashi, T. Takahashi, T. Tanaka, Y. Terada, H. Uchiyama, Y. Uchiyama, S. Watanabe, Y. Yatsu, T. Yuasa.
    Proc. SPIE. 8443, Space Telescopes and Instrumentation 2012: Ultraviolet to Gamma Ray 844325, 2012.

22. **The silicon micro-strip detector plane for the LOFT/wide-field monitor**
    A. Goldwurm, P. Ferrando, D. Götz, P. Laurent, F. Lebrun, O. Limousin, S. Basa, W. Bertoli, E. Delagnes, Y. Dolgorouky, O. Gevin, A. Gros, C. Gouiffes, F. Jeanneau, C. Lachaud, M. Llored, C. Olivetto, G. Prevot, D. Renaud, J. Rodriguez, C. Rossin, S. Schanne, S. Soldi, P. Varniere.
    Proc. SPIE. 8443, Space Telescopes and Instrumentation 2012: Ultraviolet to Gamma Ray 84432H, 2012.

23. **Caliste HD: A new fine pitch Cd(Zn)Te imaging spectrometer from 2 keV up to 1 MeV**
    A. Meuris, O. Limousin, O. Gevin, F. Lugiez, I. Le Mer, F. Pinsard, M. Donati, C. Blondel, A. Michalowska, E. Delagnes, M.-C. Vassal, F. Soufflet.
    IEEE NUCLEAR SCIENCE SYMPOSIUM – CONFERENCE RECORD, 2011.

24. **Multi-dimensional optimization of charge preamplifier in 0.18 um CMOS technology for low Power CdTe spectro-imaging system**
    A. Michalowska, O. Gevin, O. Limousin, X. Coppolani.
    IEEE NUCLEAR SCIENCE SYMPOSIUM – CONFERENCE RECORD, 2011.

25. The COSPIX mission: focusing on the energetic and obscured Universe

P. Ferrando, A. Goldwurm, P. Laurent, O. Limousin, V. Beckmann, M. Arnaud, X. Barcons, D. Bomans, I. Caballero, F. Carrera, S. Chaty, J. Chenevez, R. Chipaux, F. Christensen, A. Claret, S. Corbel, J. Croston, E. Daddi, M. De Becker, A. Decourchelle, D. Elbaz, M. Falanga, C. Ferrari, C. Feruglio, D. Götz, C. Gouiffès, C. Hailey, M. Hernanz, I. Kreykenbohm, J. Malzac, J. Martignac, F. Mattana, A. Meuris, G. Miniutti, K. Nalewajko, I. Negueruela, S. O'Dell, S. Paltani, R. Petre, P.-O. Petrucci, M. Pierre, F. Pinsard, G. Ponti, G. Rauw, N. Rea, M. Renaud, J.-L. Robert, J. Rodriguez, A. Rozanska, A. Santangelo, J.-L. Sauvageot, S. Soldi, M. Tagger, C. Tenzer, R. Terrier, G. Trap, P. Varnière, J. Wilms, W. Zhang, J. Zurita Heras.
Proceedings of the 25th Texas Symposium on Relativistic Astrophysics. December 6-10, 2010. Heidelberg, Germany, 2010.

26. Hard X-ray Imager (HXI) for the ASTRO-H mission

M. Kokubun, K. Nakazawa, T. Enoto, Y. Fukazawa, K. Gilmore, J. Kataoka, M. Kawaharada, P. Laurent, F. Lebrun, O. Limousin, K. Makishima, T. Mizuno, K. Mori, T. Nakamori, M. Ohno, M. Ohta, G. Sato, H. Tajima, H. Takahashi, T. Takahashi, T. Tanaka, Y. Terada, H. Uchiyama, Y. Uchiyama, S. Watanabe, Y. Yatsu, K. Yamaoka.
Proc. SPIE. 7732, Space Telescopes and Instrumentation 2010: Ultraviolet to Gamma Ray 773215, 2010.

27. The Hard X-ray Imager onboard IXO

K. Nakazawa, T. Takahashi, O. Limousin, M. Kokubun, S. Watanabe, P. Laurent, M. Arnaud, H. Tajima.
Proc. SPIE. 7732, Space Telescopes and Instrumentation 2010: Ultraviolet to Gamma Ray 77321L, 2010

28. Soft Gamma-ray Detector for the ASTRO-H Mission

H. Tajima, R. Blandford, T. Enoto, Y. Fukazawa, K. Gilmore, T. Kamae, J. Kataoka, M. Kawaharada, M. Kokubun, P. Laurent, F. Lebrun, O. Limousin, G. Madejski, K. Makishima, T. Mizuno, K. Nakazawa, M. Ohno, M. Ohta, G. Sato, R. Sato, H. Takahashi, T. Takahashi, T. Tanaka, M. Tashiro, Y. Terada, Y. Uchiyama, S. Watanabe, K. Yamaoka, D. Yonetoku.
Proc. SPIE. 7732, Space Telescopes and Instrumentation 2010: Ultraviolet to Gamma Ray 773216, 2010.

29. The ASTRO-H Mission

T. Takahashi, K. Mitsuda, R. Kelley, F. Aharonian, F. Akimoto, S. Allen, N. Anabuki, L. Angelini, K. Arnaud, H. Awaki, A. Bamba, N. Bando, M. Bautz, R. Blandford, K. Boyce, G. Brown, M. Chernyakova, P. Coppi, E. Costantini, J. Cottam, J. Crow, J. de Plaa, C. de Vries, J.-W. den Herder, M. DiPirro, C. Done, T. Dotani, K. Ebisawa, T. Enoto, Y. Ezoe, A. Fabian, R. Fujimoto, Y. Fukazawa, S. Funk, A. Furuzawa, M. Galeazzi, P. Gandhi, K. Gendreau, K. Gilmore, Y. Haba, K. Hamaguchi, I. Hatsukade, K. Hayashida, J. Hiraga, K. Hirose, A. Hornschemeier, J. Hughes, U. Hwang, R. Iizuka, K. Ishibashi, M. Ishida, K. Ishimura, Y. Ishisaki, N. Isobe, M. Ito, N. Iwata, J. Kaastra, T. Kallman, T. Kamae, H. Katagiri, J. Kataoka, S. Katsuda, M. Kawaharada, N. Kawai, S. Kawasaki, D. Khangaluyan, C. Kilbourne, K. Kinugasa, S. Kitamoto, T. Kitayama, T. Kohmura, M. Kokubun, T. Kosaka, T. Kotani, K. Koyama, A. Kubota, H. Kunieda, P. Laurent, F. Lebrun, O. Limousin, M. Loewenstein, K. Long, G. Madejski, Y. Maeda, K. Makishima, M. Markevitch, H. Matsumoto, K. Matsushita, D. McCammon, J. Miller, S. Mineshige, K. Minesugi, T. Miyazawa, T. Mizuno, K. Mori, H. Mori, K. Mukai, H. Murakami, T. Murakami, R. Mushotzky, Y. Nakagawa, T. Nakagawa, H. Nakajima, T. Nakamori, K. Nakazawa, Y. Namba, M. Nomachi, S. O'Dell, H. Ogawa, M. Ogawa, K. Ogi, T. Ohashi, M. Ohno, M. Ohta, T. Okajima, N. Ota, M. Ozaki, F. Paerels, S. Paltani, A. Parmer, R. Petre, M. Pohl, S. Porter, B. Ramsey, C. Reynolds, S.-I. Sakai, R. Sambruna, G. Sato, Y. Sato, P. Serlemitsos, M. Shida, T. Shimada, K. Shinozaki, P. Shirron, R. Smith, G. Sneiderman, Y. Soong, L. Stawarz, H. Sugita, A. Szymkowiak, H. Tajima, H. Takahashi, Y. Takei, T. Tamagawa, T. Tamura, K. Tamura, T. Tanaka, Y. Tanaka, Y. Tanaka, M. Tashiro, Y. Tawara, Y. Terada, Y. Terashima, F. Tombesi, H. Tomida, M. Tozuka, Y. Tsuboi, M. Tsujimoto, H. Tsunemi, T. Tsuru, H. Uchida, Y. Uchiyama, H. Uchiyama, Y. Ueda, S. Uno, M. Urry, S. Watanabe, N. White, T. Yamada, H. Yamaguchi, K. Yamaoka, N. Yamasaki, M. Yamauchi, Yamauchi, Y. Yatsu, D. Yonetoku, A. Yoshida.
Proc. SPIE. 7732, Space Telescopes and Instrumentation 2010: Ultraviolet to Gamma Ray 77320Z, 2010.

30. **IDeF-X HD: A low power multi-gain CMOS ASIC for the readout of Cd(Zn)Te detectors**
A. Michalowska, O. Gevin, O. Lemaire, F. Lugiez, P. Baron, H. Grabas, F. Pinsard, O. Limousin, E. Delagnes.
IEEE NUCLEAR SCIENCE SYMPOSIUM – CONFERENCE RECORD, 2010.

31. **Study of Background Rejection Systems for the IXO Mission**
P. Laurent, O. Limousin, V. Tatischeff.
Bulletin of the American Astronomical Society – 213th American Astronomical Society Meeting, Vol. 41, p. 361, 2009.

32. **CdTe Based Hard X-ray Imager Technology For Space Borne Missions**
O. Limousin, E. Delagnes, P. Laurent, F. Lugiez, O. Gevin, A. Meuris.
Bulletin of the American Astronomical Society – 213th American Astronomical Society Meeting, Vol. 41, p. 347, 2009.

33. **ECLAIRs, the Trigger Telescope for the SVOM Mission**
N. Remoue, D. Barret, O. Godet, P. Mandrou, R. Pons, M. Fesquet, D. Gotz, O. Limousin, S. Schanne, P. Sizun, C. Lachaud, F. Gonzales, M. Jouret.
AIP CONFERENCE PROCEEDINGS, 1133, 2009, p. 76-78.

34. **The High Energy Detector of Simbol-X**
A. Meuris, O. Limousin, F. Lugiez, O. Gevin, C. Blondel, I. Le Mer, F. Pinsard, C. Cara, A. Goetschy, J. Martignac, G. Tauzin, S. Herve, P. Laurent, R. Chipaux, Y. Rio, J. Fontignie, B. Horeau, M. Authier, P. Ferrando.
AIP CONFERENCE PROCEEDINGS, 1126, 2009, p. 25.

35. **Development of the ECLAIRs camera, a 6400 CdTe array for X/Gamma detection**
K. Lacombe, N. Remoue, C. Amoros, D. Barret, O. Gevin, O. Godet, J. Lande, E. Lecomte, O. Limousin, F. Lugiez, J. Narbonne, R. Pons, D. Rambaud, P. Ramon, G. Rouaix.
IEEE NUCLEAR SCIENCE SYMPOSIUM – CONFERENCE RECORD, 2009.

36. **IDeF-X SX0: A Low Power CMOS ASIC for the readout of Cd(Zn)Te Detectors**
O. Gevin, F. Lugiez, E. Delagnes, O. Limousin, A. Meuris.
IEEE NUCLEAR SCIENCE SYMPOSIUM – CONFERENCE RECORD, 2009.

37. **Micro hard-X ray camera: from Caliste 64 to Caliste 256**
A. Meuris, O. Limousin, F. Lugiez, O. Gevin, E. Delagnes, I. Le Mer, M. Chavassieux, F. Pinsard, C. Blondel, F. Daly, M. C. Vassal, R. Bocage, F. Soufflet.
IEEE NUCLEAR SCIENCE SYMPOSIUM – CONFERENCE RECORD, 2009.

38. **Caliste 64: detection unit of a spectro imager array for a hard X-ray space telescope**
A. Meuris, O. Limousin, F. Lugiez, O. Gevin, F. Pinsard, C. Blondel, I. Le Mer, E. Delagnes, M. C. Vassal, F. Soufflet, R. Bocage.
Proc. SPIE. 7021, High Energy, Optical, and Infrared Detectors for Astronomy III 702113, 2008.

39. **DPIX, an assembly of 6400 CdTe detectors for gamma-ray bursts detection with ECLAIRs**
N. Remoue, D. Barret, P. Mandrou, K. Lacombe, R. Pons, C. Amoros, J. Lande, D. Rambaud, J. P. Dezalay, J. Narbonne, Y. Soulie, W. Marty, P. Ramon, G. Rouaix, B. Houret, O. Limousin, O. Gevin, F. Lugiez, A. Penquer.
Proc. SPIE. 7021, High Energy, Optical, and Infrared Detectors for Astronomy III 702126, 2008.

40. The Wide-Field X and Gamma-Ray Telescope ECLAIRs aboard the Gamma-Ray Burst Multi-Wavelength Space Mission SVOM
P. Mandrou, S. Schanne, B. Cordier, R. Pons, D. Barret, C. Amoros, K. Lacombe, M. Fesquet, O. Limousin, P. Sizun, F. Lebrun, F. Gonzalez, M. Jouret.
AIP Conf. Series, Vol. 1065, p. 338-341, 2008.

41. Effects of cosmic protons and trapped electrons on the INTEGRAL/ISGRI instrument
A. Claret, O. Limousin, F. Lugiez, P. Laurent, F. Lebrun, M. Renaud, A. Sauvageon.
IEEE RADECS CONF RECORD, 2007, pLN3-1.

42. IDeF-X V1.1: performances of a new CMOS 16 channels analogue readout ASIC for Cd(Zn)Te detectors
F. Lugiez, O. Gevin, P. Baron, E. Delagnes, O. Limousin.
IEEE NUCLEAR SCIENCE SYMPOSIUM – CONFERENCE RECORD, 2007.

43. CALISTE 64, an innovative CdTe hard X-ray micro-camera
A. Meuris, O. Limousin, F. Lugiez, O. Gevin, F. Pinsard, I. Le Mer, E. Delagnes, M. C. Vassal, F. Soufflet, R. Bocage.
IEEE NUCLEAR SCIENCE SYMPOSIUM - CONFERENCE RECORD, 2007.

44. IDeF-X ECLAIRs: An ultra low noise CMOS ASIC for the readout of Cd(Zn)Te Detectors
O. Gevin, P. Baron, X. Coppolani, E. Delagnes, F. Daly, O. Limousin, F. Lugiez, A. Meuris, F. Pinsard.
IEEE NUCLEAR SCIENCE SYMPOSIUM - CONFERENCE RECORD, 2007.

45. Development of a CdTe detector plane for gamma-ray burst detection in the X-ray band (< 100 keV)
D. Barret, M. Ehanno, R. Pons, O. Gevin, O. Limousin, F. Lugiez, A. Penquer, A. Bardoux.
36th COSPAR Scientific Assembly. Proceedings, #3610, 2006.

46. The focal plane of the Simbol-X space mission
B. P. F. Dirks, P. Ferrando, U. Briel, O. Gevin, E. Kendziorra, P. Laurent, O. Limousin, F. Lugiez, J. Martignac, M. Authier, C. Chapron, P. Lechner, G. Pareschi, Y. Rio, J. P. Roques, P. Salin, L. Strueder.
Proc. SPIE. 6276, High Energy, Optical, and Infrared Detectors for Astronomy II 627617, 2006.

47. Simbol-X: mission overview
P. Ferrando, M. Arnaud, U. Briel, O. Citterio, R. Cledassou, P. Duchon, F. Fiore, P. Giommi, A. Goldwurm, G. Hasinger, E. Kendziorra, P. Laurent, F. Lebrun, O. Limousin, G. Malaguti, S. Mereghetti, G. Micela, G. Pareschi, Y. Rio, J. P. Roques, L. Struder, G. Tagliaferri.
Proc. SPIE. 6266, Space Telescopes and Instrumentation II: Ultraviolet to Gamma Ray 62660F, 2006.

48. IDeF-X V1.1: Performances of a New CMOS 16 Channels Analogue Readout ASIC for Cd(Zn)Te Detectors
F. Lugiez, O. Gevin, P. Baron, E. Delagnes, O. Limousin.
IEEE NUCLEAR SCIENCE SYMPOSIUM – CONFERENCE RECORD, 2006.

49. SIMBOL-X a formation flying mission for hard X-rays astrophysics
P. Ferrando, A. Goldwurm, P. Laurent, O. Limousin, J. Martignac, F. Pinsard, Y. Rio, J. P. Roques, O. Citterio, G. Pareschi, G. Tagliaferri, F. Fiore, G. Malaguti, U. Briel, G. Hasinger, L. Strueder.
Proc. SPIE. 5900, Optics for EUV, X-ray, and Gamma-Ray Astronomy II 59000P, 2005.

50. IDeF-X V1.0: Performances of a new CMOS multi channel analogue readout ASIC for Cd(Zn)Te detectors
O. Gevin, F. Lugiez, O. Limousin, B. P. F. Dirks, C. Blondel, X. Coppolani, P. Baron, E. Delagnes.
IEEE NUCLEAR SCIENCE SYMPOSIUM – CONFERENCE RECORD, 2005.

51. 3D modeling of Cd(Zn)Te detectors for the SIMBOL-X Space mission
B. P. F. Dirks, O. Limousin, P. Ferrando, R. Chipaux.
Proc. SPIE. 5501, High-Energy Detectors in Astronomy 412, 2004.

52. SIMBOL-X: a new generation hard X-ray telescope
P. Ferrando, M. Arnaud, B. Cordier, A. Goldwurm, O. Limousin, J. Paul, J.L. Sauvageot, P.O. Petrucci, M. Mouchet, G. Bignami, O. Citterio, S. Campana, G. Pareschi, G. Tagliaferri, U. Briel, G. Hasinger, L. Strueder, P. Lechner, E. Kendziorra, M. Turner.
Proc. SPIE. 5168, Optics for EUV, X-ray, and Gamma-Ray Astronomy 65, 2004.

53. ISGRI CdTe camera in-flight behavior
O. Limousin, A. Claret, E. Delagnes, P. Laurent, F. Lebrun, F. Lugiez, A. Sauvageon, R. Terrier.
IEEE NUCLEAR SCIENCE SYMPOSIUM – CONFERENCE RECORD, 2004.

54. IDeF-X ASIC for Cd(Zn)Te spectro-imaging systems
O. Limousin, O. Gevin, F. Lugiez, R. Chipaux, E. Delagnes, B. Dirks, B. Horeau.
IEEE NUCLEAR SCIENCE SYMPOSIUM – CONFERENCE RECORD, 2004.

55. The ECLAIRs micro-satellite for multi-wavelength studies of gamma-ray burst prompt emission
S. Schanne, J.L. Atteia, D. Barret, S. Basa, M. Boer, B. Cordier, F. Daigne, A. Ealet, P. Goldoni, A. Klotz, O. Limousin, P. Mandrou, R. Mochkovitch, S. Paltani, J. Paul, P. Petitjean, R. Pons, G. Skinner.
IEEE NUCLEAR SCIENCE SYMPOSIUM – CONFERENCE RECORD, 2004.

56. The MAX mission: focusing on high sensitivity gamma-ray spectroscopy
P. von Ballmoos, H. Halloin, J. Paul, N. Abrosimov, K. Andersen, P. Astier, S. Basa, D. Barret, P Bastie, A. Bazzano, A. Bignami, A. Blanchard, B. Cordier, T. Courvoisier, P. Courtois, A. Ealet, B. Hamelin, M. Harris, M. Hernanz, J. Isern, P. Jean, J. Knodlseder, P. Laurent, F. Lebrun, X. Leyre, O. Limousin, A. Marcowith, V. Martinot, A. Mazure, L. Natalucci, J.F. Olive, R. Pain, S. Paltani, N. Prantzos, H. Riemann, R. Sadat, H. Sainct, G. Skinner, R.K. Smither, P. Ubertini, F. Vedrenne, G. Weidenspointner.
Proceedings of the 5th INTEGRAL Workshop on the INTEGRAL Universe, ESA SP-552), 2004, p. 747.

57. The IBIS gamma-ray telescope on INTEGRAL

P. Ubertini, F. Lebrun, G. Di Cocco, L. Bassani, A. Bazzano, A.J. Bird, K. Broenstad, E. Caroli, M. Cocchi, G. De Cesare, M. Denis, S. Di Cosimo, A. Di Lellis, F. Giannotti, P. Goldoni, A. Goldwurm, G. La Rosa, C. Labanti, P. Laurent, O. Limousin, G. Malaguti, I.F. Mirabel, L. Natalucci, P. Orleansky, M.J. Poulsen, M. Quadrini, B. Ramsey, V. Reglero, L. Sabau, B. Sacco, A. Santangelo, A. Segreto, R. Staubert, J. Stephen, M. Trifoglio, L. Vigroux, R. Volkmer, M.C. Weisskopf, A. Zdziarski, A. Zehnder.
AIP PROCEEDINGS, 510, 2000, p. 684.

58. A basic component for ISGRI, the CdTe gamma camera on board the INTEGRAL satellite

M. Arques, N. Baffert, D. Lattard, J.L. Martin, G. Masson, F. Mathy, A. Noca, J.P. Rostaing, P. Trystram, P. Villard, J.C. Cretolle, F. Lebrun, J.-P. Leray, O. Limousin.
IEEE NUCLEAR SCIENCE SYMPOSIUM – CONFERENCE RECORD, 1998.

4. Peer reviewed journals papers

1. Energy calibration via correlation
D. Maier, O. Limousin.
NUCLEAR INSTRUMENTS & METHODS IN PHYSICS RESEARCH SECTION A, 812, 2016, p. 43.

2. The Spectrometer/Telescope for Imagin X-rays on Solar Orbiter: Flight design, challenges and trade-offs
S. Krucker, M. Bednarzik, O. G rimm, G.J. Hurford, O. Limousin, A. Meuris, P. Orleański, K. Seweryn, K.R. Skup.
NUCLEAR INSTRUMENTS & METHODS IN PHYSICS RESEARCH SECTION A, in press, 2015.

3. Fast-neutron induced background in LaBr3:Ce detectors
J. Kiener, V. Tatischeff, I. Deloncle, N. de Séréville, P. Laurent, C. Blondel, M. Chabot, R. Chipaux, A. Coc, S. Dubos, A. Gostojic`, N. Goutev, C. Hamadache, F. Hammache, B. Horeau, O. Limousin, S. Ouichaoui, G. Prévot, R. Rodríguez-Gasén, M.S. Yavahchova.
NUCLEAR INSTRUMENTS & METHODS IN PHYSICS RESEARCH SECTION A, 798, 2015, p. 152.

4. Hard X-ray polarimetry with Caliste, a high performance CdTe based imaging spectrometer
S. Antier, P. Ferrando, O. Limousin, E. Caroli, R-M Curado da Silva, C. Blondel, R. Chipaux, V. Honkimaki, B. Horeau, P. Laurent, J-M Maia, A. Meuris, S. Del Sordo, J.-B. Stephen.
EXPERIMENTAL ASTRONOMY, Vol. 39, Issue 2, 2015, p. 233-258.

5. R&D on a novel spectro-imaging polarimeter with Micromegas detectors and a Caliste readout system
D. Attié, C. Blondel, L. Boilevin-Kayl, D. Desforges, E. Ferrer-Ribas, I. Giomataris, O. Gevin, F. Jeanneau, O. Limousin, A. Meuris, T. Papaevangelou, A. Peyaud.
NUCLEAR INSTRUMENTS & METHODS IN PHYSICS RESEARCH SECTION A, 787, 2015, p. 312.

6. ASTRO-H CdTe detectors proton irradiation at PIF
O. Limousin, D. Renaud, B. Horeau, S. Dubos, P. Laurent, F. Lebrun, R. Chipaux, C. Boatella Polo, R. Marcinkowski, M. Kawaharada, S. Watanabe, M. Ohta, G. Sato, T. Takahashi.
NUCLEAR INSTRUMENTS & METHODS IN PHYSICS RESEARCH SECTION A, in press, 2015.

7. WPOL, a future space Compton wide field polarimeter: Optimization for polarimetry
M. Khalil, P. Laurent, F. Lebrun, Y. Dolgorouky, O. Limousin, W. Bertoli, E. Breelle.
NUCLEAR INSTRUMENTS & METHODS IN PHYSICS RESEARCH SECTION A, 787, 2015, p. 288.

8. ORIGAMIX, a CdTe-based spectro-imager development for nuclear appli cation
S. Dubos, H. Lemaire, S. Schanne, O. Limousin, F. Carrel, V. Schoepff, C. Blondel
NUCLEAR INSTRUMENTS & METHODS IN PHYSICS RESEARCH SECTION A, 787, 2015, p. 302.

9. **Fine pitch CdTe-based hard-X-ray polarimeter performance for space science in the 70–300 keV energy range**
S. Antier, O. Limousin, P. Ferrando.
NUCLEAR INSTRUMENTS & METHODS IN PHYSICS RESEARCH SECTION A, 787, 2015, p. 297.

10. **Caliste-SO, a CdTe based spectrometer for bright solar event observations in hard X-rays**
A. Meuris, O. Limousin, O. Gevin, C. Blondel, J. Martignac, M.-C. Vassal, F. Soufflet, N. Fiant, M. Bednarzik, S. Stutz, O. Grimm, V. Commichau.
NUCLEAR INSTRUMENTS & METHODS IN PHYSICS RESEARCH SECTION A, 787, 2015, p. 72.

11. **Conceptual design of the International Axion Observatory (IAXO)**
E. Armengaud, F. T. Avignone, M. Betz, P. Brax, P. Brun, G. Cantatore, J. M. Carmona, G. P. Carosi, F. Caspers, S. Caspi, S. A. Cetin, D. Chelouche, F. E. Christensen, A. Dael, T. Dafni, M. Davenport, A. V. Derbin, K. Desch, A. Diago, B. Döbrich, I. Dratchnev, A. Dudarev, C. Eleftheriadis, G. Fanourakis, E. Ferrer-Ribas, J. Galán, J. A. García, J. G. Garza, T. Geralis, B. Gimeno, I. Giomataris, S. Gninenko, H. Gómez, D. González-Díaz, E. Guendelman, C. J. Hailey, T. Hiramatsu, D. H. H. Hoffmann, D. Horns, F. J. Iguaz, I. G. Irastorza, J. Isern, K. Imai, A. C. Jakobsen, J. Jaeckel, K. Jakovčić, J. Kaminski, M. Kawasaki, M. Karuza, M. Krčmar, K. Kousouris, C. Krieger, B. Lakić, O. Limousin, A. Lindner, A. Liolios, G. Luzón, S. Matsuki, V. N. Muratova, C. Nones, I. Ortega, T. Papaevangelou, M. J. Pivovaroff, G. Raffelt, J. Redondo, A. Ringwald, S. Russenschuck, J. Ruz, K. Saikawa, I. Savvidis, T. Sekiguchi, Y. K. Semertzidis, I. Shilon, P. Sikivie, H. Silva, H. ten Kate, A. Tomas, S. Troitsky, T. Vafeiadis, K. van Bibber, P. Vedrine, J. A. Villar, J. K. Vogel, L. Walckiers, A. Weltman, W. Wester, S. C. Yildiz, K. Zioutas.
JOURNAL OF INSTRUMENTATION, Vol. 9, Issue 05, 2014, T05002.

12. **The spectrometer/telescope for imaging X-rays on board the ESA Solar Orbiter spacecraft**
S. Krucker, A.O. Benz, G.J. Hurford, N.G. Arnold, P. Orleanski, H-P. Gröbelbauer, D. Casadei, S.Kobler, L. Iseli, H.J. Wiehl, A. Csillaghy, L. Etesi, N.Hochmuth, M. Battaglia, M. Bednarzik, R. Resanovic, O. Grimm, G. Viertel, V. Commichau, A. Howard, A. Meuris, O. Limousin, S. Brun, N. Vilmer, K.R. Skup, R. Graczyk, M. Stolarski, M. Michalska, W. Nowosielski, A. Cichocki, M. Mosdorf, K. Seweryn, A. Białek, J. Sylwester, M. Kowalinski, T. Mrozek, P. Podgorski, G. Mann, H. Önel, H. Aurass, S.-M. Bauer, W. Bittner, F. Dionies, J.Paschke, D. Plüschke, E. Popow, J. Rendtel, A. Warmuth, M. Woche, D. Wolter, H.F. VanBeek, F. Farnik, R.P. Lin.
NUCLEAR INSTRUMENTS & METHODS IN PHYSICS RESEARCH SECTION A, 732, 2013, p. 295.

13. **Low Energy characterization of Caliste HD, a fine pitch CdTe-based Imaging Spectrometer**
S. Dubos, O. Limousin, C. Blondel, R. Chipaux, Y. Dolgorouky, O. Gevin, Y. Ménesguen, A. Meuris, T. Orduna, T. Tourette, A. Sauvageon.
IEEE TRANSACTION ON NUCLEAR SCIENCE, 60, 5, 2013, p. 3824.

14. **The front-end electronics of the Spectrometer Telescope for Imaging X-rays (STIX) on the ESA Solar Orbiter satellite**
O. Grimm, M. Bednarzik, V. Commichau, R. Graczyk, H.-P. Grobelbauer, G. Hurford, S. Krucker, O. Limousin, A. Meuris, P. Orleanski, A. Przepiorka, K. Seweryn, K. Skup, G. Viertel.
JOURNAL OF INSTRUMENTATION, Vol. 7, 2012, C12015.

15. Solar Particle Acceleration Radiation and Kinetics (SPARK) A mission to understand the nature of particle acceleration
S. A. Matthews, D. R. Williams, K.-L. Klein, E. P. Kontar, D. M. Smith, A. Lagg, S. Krucker, G. J. Hurford, N. Vilmer, A. L. MacKinnon, V. V. Zharkova, L. Fletcher, I. G. Hannah, P. K. Browning, D. E. Innes, G. Trottet, C. Foullon, V. M. Nakariakov, L. M. Green, H. Lamoureux, C. Forsyth, D. M. Walton, M. Mathioudakis, A. Gandorfer, V. Martinez-Pillet, O. Limousin, E. Verwichte, S. Dalla, G. Mann, H. Aurass, T. Neukirch.
EXPERIMENTAL ASTRONOMY, 33, 2-3, 2012, p. 237.

16. Caliste-SO X-ray micro-camera for the STIX instrument on-board Solar Orbiter space mission
A. Meuris, Hurford, Bednarzik, O. Limousin, O. Gevin, I. Le Mer, J. Martignac, B. Horeau, O. Grimm, R. Resano-vic, S. Krucker, P. Orleanski.
NUCLEAR INSTRUMENTS & METHODS IN PHYSICS RESEARCH SECTION A, 695, 2012, p. 288.

17. Imaging X-ray detector front-end with High Dynamic Range: IDeF-X HD
A. Michalowska, O. Gevin, I. Lemaire, F. Lugiez, P. Baron, O. Limousin, E. Delagnes.
NUCLEAR INSTRUMENTS & METHODS IN PHYSICS RESEARCH SECTION A, 695, 2012, 415.

18. Characterization of polarization phenomenon in Al-Schottky CdTe detectors using a spectroscopic analysis method
A. Meuris, O. Limousin, C. Blondel.
NUCLEAR INSTRUMENTS & METHODS IN PHYSICS RESEARCH SECTION A, 654, 1, 2011, p. 293.

19. Caliste 256: A CdTe imaging spectrometer for space science with a 580 μm pixel pitch
O. Limousin, F. Lugiez, O. Gevin, A. Meuris, C. Blondel, E. Delagnes, M. Donati, I. Le Mer, J. Martignac, F. Pinsard, M. C. Vassal, R. Bocage, F. Soufflet.
NUCLEAR INSTRUMENTS & METHODS IN PHYSICS RESEARCH SECTION A, 647, 1, 2011, p. 46.

20. Caliste 64, a new CdTe micro-camera for hard X-ray spectro-imaging
A. Meuris, O. Limousin, F. Lugiez, O. Gevin, C. Blondel, F. Pinsard, M. C. Vassal, F. Soufflet, I. Le Mer.
NUCLEAR INSTRUMENTS & METHODS IN PHYSICS RESEARCH SECTION A, 610, 1, 2009, p. 154.

21. Charge sharing in CdTe pixilated detectors
A. Meuris, O. Limousin, C. Blondel.
NUCLEAR INSTRUMENTS & METHODS IN PHYSICS RESEARCH SECTION A, 610, 1, 2009, p. 294.

22. Micro Hard-X Ray Camera: From Caliste 64 to Caliste 256
A. Meuris, O. Limousin, F. Lugiez, O. Gevin, E. Delagnes, I. Le Mer, M. Chavassieux, F. Pinsard, C. Blondel, F. Daly, M.-C. Vassal, R. Bocage, F. Soufflet.
IEEE TRANSACTION ON NUCLEAR SCIENCE, 56, 4, 2009, p. 1835.

23. IDeF-X ECLAIRs: A CMOS ASIC for the Readout of CdTe and CdZnTe Detectors for High Resolution Spectroscopy
O. Gevin, P. Baron, X. Coppolani, F. Daly, E. Delagnes, O. Limousin, F. Lugiez, A. Meuris, F. Pinsard, D. Renaud.
IEEE TRANSACTION ON NUCLEAR SCIENCE, 56, 4, 2009, p. 2351.

24. Caliste 64, an innovative CdTe hard X-ray micro-camera
A. Meuris, O. Limousin, F. Lugiez, O. Gevin, F. Pinsard, I. Le Mer, E. Delagnes, M. C. Vassal, F. Soufflet, R. Bocage.
IEEE TRANSACTION ON NUCLEAR SCIENCE, 55, 2, 2008, p. 778.

25. Compton telescope with a coded aperture mask: Imaging with the INTEGRAL/IBIS compton mode
M. Forot, P. Laurent, F. Lebrun, O. Limousin.
ASTROPHYSICAL JOURNAL, 668, 2, 2007, p. 1259.

26. Development of a modular CdTe detector plane for gamma-ray burst detection below 100 keV
M. Ehanno, C. Amoros, D. Barret, K. Lacombe, R. Pons, G. Rouaix, O. Gevin, O. Limousin, F. Lugiez, A. Bardoux, A. Penquer.
ADVANCES IN SPACE RESEARCH, 40, 8, 2007, p. 1259.

27. IDeF-X V1.0: A new 16-channel low-noise analog front-end for Cd(Zn)Te detectors
O. Gevin, F. Lugiez, O. Limousin, P. Baron, C. Blondel, X. Coppolani, B. P. F. Dirks, E. Delagnes.
NUCLEAR INSTRUMENTS & METHODS IN PHYSICS RESEARCH SECTION A, 567, 1, 2006, p. 140.

28. Leakage current measurements on pixelated CdZnTe detectors
B. P. F. Dirks, C. Blondel, F. Daly, O. Gevin, O. Limousin, F. Lugiez.
NUCLEAR INSTRUMENTS & METHODS IN PHYSICS RESEARCH SECTION A, 567, 1, 2006, p. 145.

29. Compton telescope with coded aperture mask: Application to the INTEGRAL/IBIS Compton mode
M. Forot, P. Laurent, F. Lebrun, O. Limousin.
NUCLEAR INSTRUMENTS & METHODS IN PHYSICS RESEARCH SECTION A, 567, 1, 2006, p. 158.

30. The ECLAIRs micro-satellite mission for gamma-ray burst multi-wavelength observations
S. Schanne, J. -L. Atteia, D. Barret, S. Basa, M. Boer, F. Casse, B. Cordier, F. Daigne, A. Klotz, O. Limousin, R. Manchanda, P. Mandrou, S. Mereghetti, R. Mochkovitch, S. Paltani, J. Paul, P. Petitjean, R. Pons, G. Ricker, G. Skinner.
NUCLEAR INSTRUMENTS & METHODS IN PHYSICS RESEARCH SECTION A, 567, 1, 2006, p. 327.

31. The ECLAIR's micro-satellite for multi-wavelength studies of gamma-ray burst prompt emission
S. Schanne, J.L. Atteia, D. Barret, S. Basa, M. Boer, B. Cordier, F. Daigne, A. Ealet, P. Goldoni, A. Klotz, O. Limousin, P. Mandrou, R. Mochkovitch, S. Paltani, J. Paul, P. Petitjean, R. Pons, G. Skinner.
IEEE TRANSACTION ON NUCLEAR SCIENCE, 52, 6, 2005, p. 2778.

32. IDeF-X ASIC for Cd(Zn)Te spectro-imaging systems
O. Limousin, O. Gevin, F. Lugiez, R. Chipaux, E. Delagnes, B. Dirks, B. Horeau.
IEEE TRANSACTION ON NUCLEAR SCIENCE, 52, 5, 2005, p. 1595.

33. INTEGRAL: In flight behavior of ISGRI and SPI
F. Lebrun, J.P. Roques, A. Sauvageon, R. Terrier, P. Laurent, O. Limousin, F. Lugiez, A. Claret.
NUCLEAR INSTRUMENTS & METHODS IN PHYSICS RESEARCH SECTION A, 541, 1-2, 2005, p. 323.

34 Particle effects on the ISGRI instrument on-board the INTEGRAL satellite
A. Claret, O. Limousin, F. Lugiez, R. Laurent, M. Renaud.
IEEE TRANSACTION ON NUCLEAR SCIENCE, 51, 6, 2004, p. 3413.

35. ISGRI: The INTEGRAL Soft Gamma-Ray Imager
F. Lebrun, J.P. Leray, P. Lavocat, J. Cretolle, M. Arques, C. Blondel, C. Bonnin, A. Bouere, C. Cara, T. Chaleil, F. Daly, F. Desages, H. Dzitko, B. Horeau, P. Laurent, O. Limousin, F. Mathy, V. Mauguen, F. Meignier, F. Molinie, E. Poindron, M. Rouger, A. Sauvageon, T. Tourrette.
ASTRONOMY AND ASTROPHYSICS, 411, 1, 2003, PL141.

36. Status of the Integral/IBIS telescope modeling and of the response matrices generation
P. Laurent, O. Limousin, M. Cadolle-Bel, P. Goldoni, G. Malaguti, E. Caroli, G. De Cesare, M. Del Santo, A.J. Bird, J. Grygorczuk, J.M. Torrejon.
ASTRONOMY AND ASTROPHYSICS, 411, 1, 2003, pL185.

37. New trends in CdTe and CdZnTe detectors for X- and gamma-ray applications
O. Limousin.
NUCLEAR INSTRUMENTS & METHODS IN PHYSICS RESEARCH SECTION A, 504, 1-3, 2003, p. 24.

38. Qualification model of the space ISGRI CdTe gamma-ray camera
O. Limousin, C. Blondel, C. Bonnin, J. Cretolle, A. Goldwurm, B. Horeau, P. Laurent, F. Lebrun, J.P. Leray.
NUCLEAR INSTRUMENTS & METHODS IN PHYSICS RESEARCH SECTION A, 471 ; 1-2, 2001, p. 174.

39. Polycell: the elementary detection unit of the ISGRI CdTe gamma-ray camera
O. Limousin, M. Arques, J. Cretolle, F. Lebrun, J.P. Leray, N. Baffert, D. Lattard, J.L. Martin, G. Mason, A. Noca, F. Mathy, J.P. Rostaing, P. Trystram, P. Villard, P. Baron, E. Delagnes, M. Rouger.
NUCLEAR INSTRUMENTS & METHODS IN PHYSICS RESEARCH SECTION A, 458, 1-2, 2001, p. 551.

40. The integral/IBIS Telescope modeling
P. Laurent, O. Limousin, G. Malaguti, E. Caroli, G. de Cesare, A.J. Bird, J. Grygorczuk, J.M. Torrejon.
ESA SPECIAL PUBLICATIONS, ISBN 92-9092-677-5, 2001, p. 587.

41. ISGRI: The CdTe gamma-ray camera onboard INTEGRAL
F. Lebrun, J.P. Leray, O. Limousin, C. Blondel, P. Laurent, P. Goldoni, A. Goldwurm, A. Sauvageon.
ESA SPECIAL PUBLICATIONS, ISBN 92-9092-677-5, 2001, p. 591.

42. The ISGRI CdTe gamma-ray camera: first steps
O. Limousin, C. Blondel, J. Cretolle, H. Dzitko, P. Laurent, F. Lebrun, J.P. Leray, M. Arques, N. Baffert, F. Mathy, A. Noca, P. Trystram, P. Villard, P. Baron, E. Delagnes, M. Rouger.
NUCLEAR INSTRUMENTS & METHODS IN PHYSICS RESEARCH SECTION A, 442, 2000, p. 244.

43. The ISGRI CdTe gamma-ray camera: first steps (ERRATUM)
O. Limousin, C. Blondel, J. Cretolle, H. Dzitko, P. Laurent, F. Lebrun, J.P. Leray, M. Arques, N. Baffert, F. Mathy, A. Noca, P. Trystram, P. Villard, P. Baron, E. Delagnes, M. Rouger.
NUCLEAR INSTRUMENTS & METHODS IN PHYSICS RESEARCH SECTION A, 442, 3, 2000, p. 650.

44. Basic component for ISGRI, the CdTe gamma camera on board the INTEGRAL satellite
M. Arques, N. Baffert, D. Lattard, J.L. Martin, G. Masson, F. Mathy, A. Noca, J.P. Rostaing, P. Trystram, P. Villard, J. Cretolle, F. Lebrun, J.P. Leray, O. Limousin.
IEEE TRANSACTION ON NUCLEAR SCIENCE, 46, 3, 1999, p. 181.

45. The basic component of the ISGRI CdTe gamma-ray camera for space telescope IBIS on board the INTEGRAL satellite
O. Limousin, J.M. Duda, F. Lebrun, J.P. Leray.
NUCLEAR INSTRUMENTS & METHODS IN PHYSICS RESEARCH SECTION A, 428, 1, 1999, p. 216.

46. Nature of the galactic soft gamma-ray emission
F. Lebrun, P. Goldoni, A. Goldwurm, P. Laurent, O. Limousin, J. Paul.
ASTROPHYSICS LETTERS AND COMMUNICATIONS, 38, 1-6, 1999, p. 457.

5. Monographs and book chapters

1. Chapter 5 / Advanced pixel detectors for hard X-ray astronomy
O. Limousin, A. Meuris, O. Gevin, S. Dubos.
Solid-State Radiation Detectors: Technology and Applications, Salah Awadalla, CRC Press, 2015.

2. Proceedings of the Seventh International Conference on New Development in Photo-detection
P. Bourgeois, F. Carrel, R. Chipaux, B. Cordier, A. Dominjon, A. Meuris, O. Limousin, P. Nédélec, S. Normand, V. Puill, A. Penquer, J.-C. Vanel.
NUCLEAR INSTRUMENTS & METHODS IN PHYSICS RESEARCH SECTION A, Special Issue, Tours, 2014.

3. Proceedings of the Sixth International Conference on New Development in Photodetection
P. Bourgeois, B. Cordier, A. Dominjon, H. El Mamouni, O. Limousin, P. Nédélec, S. Normand, V. Puill, A. Penquer, J.-C. Vanel.
NUCLEAR INSTRUMENTS & METHODS IN PHYSICS RESEARCH SECTION A, Lyon, 2011.

4. Chapitre 9/Caliste Micro-camera for Hard X-ray Astronomy
O. Limousin, A. Meuris, O. Gevin, F. Lugiez.
Seminconductor Radiation Detection Systems, K. Iniewsky, CRC Press, 2010.

5. Proceedings of the Fifth International Conference on New Development in Photode-tection
P. Bourgeois, B.Cordier, H. El Mamouni, S. Kerhoas-Cavata, O. Limousin, P. Nédélec, V. Puill, J.-C. Vanel.
NUCLEAR INSTRUMENTS & METHODS IN PHYSICS RESEARCH SECTION A, Aix-les-Bains, 2008.

6. Proceedings of the Fourth International Conference on New Development in Photo-detection
P. Bourgeois, H. El Mamouni, P. Goret, P. Le Dû, O. Limousin, P. Nédélec, V. Puill, J.-C. Vanel.
NUCLEAR INSTRUMENTS & METHODS IN PHYSICS RESEARCH SECTION A, Beaune, 2005.

7. Mise en œuvre et étude des propriétés spectrales de la gamma-caméra ISGRI
O. Limousin.
Thèse Toulouse III, 2001.

8. Étude de la génération et de la relaxation en température des défauts d'interface in-duits par irradiation dans les transistors NMOS
O. Limousin.
DEA Lyon I, INSA Lyon, Ecole Centrale Lyon, 1996.

6. Publications for the grand public

1. 1, 2, 3… Soleil
O. Limousin, A. S. Brun *et al.*
Les Savanturiers N°11, 2015.

2. Des Spectro-imageurs de nouvelle génération – Dans l'Univers extrême et violent
O. Limousin, E. Delagnes.
Clefs CEA N° 58, 2009.

3. Nouveaux détecteurs pour la détection de rayons X et gamma à température ambiante
O. Limousin.
Dossier de Presse: « 40 ans d'astrophysique spatiale au CEA » – section CEA, 2006.

4. La mesure du très lointain
J. Paul, D. Elbaz, O. Limousin, G. Destefanis.
Clefs CEA N°54, 2006.

5. La caméra ISGRI à bord d'Integral, notre experience
O. Limousin, pour l'équipe ISGRI.
CNES Journal CCT (Centre de competences Techniques), 2005.

7. Scientific proposals

NB: Underlined proposals led to funding and effective research programs.

1. DLIGHT – Digital Light InteGrated Hybrid Technology
V. Schoepff (DRT), O. Limousin (DSM), N. Menaa (CANBERRA) *et al.*
Project call H2020-FETOPEN-2014-2015-RIA/2015.

2. IGAN – Imagerie Gamma Neutrons
V. Schoepff (DRT), O. Limousin (DSM), N. Menaa (CANBERRA) *et al.*
Project call ANR – ANDRA/2014.

3. LOFT: The Large Observatory for X-ray Timing
M. Tavani (INAF), V. Tatscheff (CSNSM), on behalf of the ASTROGAM Consortium.
M4 ESA call, January 2015.

4. ASTROGAM
M. Feroci (INAF), on behalf of the LOFT Consortium.
M4 ESA call, January 2015.

5. NGRG, studying Gamma-Ray Bursts In the Optical-IR, Starting Just Seconds After The Burst
B. Grossan (University of California, Berkeley).
Project call NASA, 2014.

6. HiGEM, Hybrisation Germanium sur détecteurs pixéllisés (DRT/LIST, DSM/Irfu, 3D PLUS, AREVA/CANBERRA)
K. Boudergui (DRT), F. Carrel (DRT), O. Limousin (DSM), N. Menaa (CANBERRA), P. Maurice (3D PLUS) *et al.*
Project call ANR/2014.

7. Étude initiale de l'utilisation de la technologie WDoD pour le spatial – application à une caméra CdTe à haute densité de pixels
O. Limousin (PI), P. Maurice (3D Plus).
R&T CNES, 2014.

8. SORENTO
S. Bogatchev (PI), LPI, O. Limousin (French proposal leader) CEA.
Call for Ideas, CNES, 2014.

9. WP1-1-B: Mini gamma cameras in the framework of the BEEP nanosatellite, in collaboration with the FHNW institute and EPFL in Switzeland, and closely with the 3D PLUS company (Buc);
O. Limousin, A. Meuris.
Research Project Call: Nanosat, IDEX-Paris Saclay 2014.

10 New Frontiers in plasma physics: novel observing windows and techniques
S. A. Matthews (PI) *et al.* (Univ. College London, MSSL).
ESA call for L -Class missions L2/L3, 2013.

11. WP2-4: BEEP, Bright Eruptive Event Polarimeter
O. Limousin, A. Meuris.
Research Project Call: Nanosat, IDEX-Paris Saclay 2013.

12. MCAP, A balloon borne X-ray polarimeter
Ph. Laurent (PI) *et al.*
Scientific prospect, call for ideas 2014, CNES 2013.

13. HYBISA (DRT/LIST, DSM/Irfu, 3D PLUS, CANBERRA FRANCE, IRSN, GIE INTRA)
F. Carrel (DRT), O. Limousin (DSM), N. Menaa (CANBERRA), P. Maurice (3D PLUS) *et al.*
Project call ANR/CSOSG 2013.

14. MC2: développement d'une mini camera spectrométrique CdTe à très haute densité de pixels pour l'astronomie haute énergie spatiale – Tranche 3
O. Limousin (PI), P. Maurice (3D Plus).
R&T CNES, 2013.

15. IDeF-X BD, French contribution to Solar Orbiter/EPD (Energetic Particle Detector) / STEIN
Wimmmer-Schweingruber (PI, Univ Kiel), O. Limousin (Lead Co-I),
Opportunité DLR/Univ-Kiel 2013.

16. Solar Energetic Neutral-atom Imaging Coronagraph (SENIC) instrument development
A.Y. Shih (NASA/GSFC), G. Hurford (FHNW), C. Tindall (LBNL), J. Sample (UCB/SSL), O. Limousin (CEA), O. Gevin (CEA), L. Wang (UCB/SSL), G. Li (Univ. of Alabama).
Instrument Development Call NASA, 2013.

17. Solar Energetic Neutral-atom Imaging Coronagraph (SENIC) instrument development
A.Y. Shih (NASA/GSFC), R. Lin (UCB/SSL), G. Hurford (UCB/SSL), C. Tindall (LBNL), J. Sample (UCB/SSL), O. Limousin (CEA), O. Gevin (CEA), L. Wang (UCB/SSL), G. Li (Univ. of Alabama).
Instrument Development Call NASA, 2012.

18. BEEP, Bright Eruptive Event Polarimeter
O. Limousin (PI), A. Meuris.
Call for Ideas CNES, 2012.

19. Étude de détecteurs Silicium pour un future télescope gamma spatial (0.1-100 MeV)
Ph. Laurent (PI), O. Limousin *et al.*
R&T CNES, 2012.

20. SORENTO
S. Kuzin (PI) LPI, O. Limousin (French proposal leader) CEA.
APPEL A IDEES CNES, 2012.

21. SRG/ART-XC II – Focusing Hard X-ray Space telescope
Ph. Ferrando *et al.*, French participation.
Proposition de recherche scientifique Spatiale CNES 2012.

22. ESRF, ASTROPOL, polarisation measurement performances of a detector system fully representative of an X-ray telescope focal plane instrument
Ph. Ferrando (CEA), O. Limousin (CEA), E. Caroli (INFN), R.C da Silva (Coimbra) *et al.*
ESRF Research Proposal, Beam line ID15A, mars 2012.

23. LOFT WFM, a DSSD based Wide Field Monitor for LOFT
A. Goldwurm (PI) *et al.*
M-Class Mission Assessment Study M3, 2012.

24. X-POSIT: X-ray Polarimetric Spectroscopic Imaging Telescope Lebrun (PI) et al.
E. Caroli (PI) *et al.*, INAF.
ESA call for S-Class missions, 2012.

25. CuSP: 3D CZT BALOON
E. Caroli (PI) *et al.*
INAF 2012.

26. COXIP (Compact space X-ray imager and Polarimeter
D. Casadei (PI, Fhnw).
Swiss Space Office opportunity for Nanosat program, 2012.

27. ORIGAMIX (DRT/LIST, DSM/Irfu, 3D PLUS, CANBERRA FRANCE, IRSN, GIE INTRA)
F. Carrel (DRT), O. Limousin (DSM), N. Menaa (CANBERRA), P. Maurice (3D PLUS) *et al.*
Project call ANR/RSNR, Investissement d'avenir, 2012.

28. MC2: développement d'une mini camera spectrométrique CdTe à très haute densité de pixels pour l'astronomie haute énergie spatiale – Tranche 2
O. Limousin, O. Gevin.
R&T CNES, 2011.

29. CALISTE-SO, French Contribution to STIX
O. Limousin (Lead Co-I).
Space Research Mission of opportunity, CNES 2011.

30. SOLAR PROBE+ PAC/XIS (X-ray Imager of the Sun)
R. Lin (UC Berkeley Former PI), *et al.*
Nasa Instrument development call/Proposition de recherche scientifique Cnes, 2011.

31. MEGAMIX (DRT/LIST, DSM/Irfu, 3D PLUS, CANBERRA FRANCE, IRSN, GIE INTRA)
F. Carrel (DRT), O. Limousin (DSM), N. Menaa (CANBERRA), P. Maurice (3D PLUS) *et al.*
Project calls FUI13, 2011.

32. CINEMA Trio
R. Lin (SSL Former PI) *et al.*
Collaboration opportunity NSF/NASA/SSL nanosat program, 2011.

33. ASTRO-H activities in Europe
O. Limousin (PI), Ph. Laurent.
ESA/Jaxa Opportunity, 2011.

34. Solar Orbiter/STIX (Spectrometer/Telescope for Imaging X-rays)
N. Vilmer (PI), O. Limousin.
Space Research, Mission of opportunity, CNES 2010.

35. CALISTE-SO, French Contribution to STIX, PHASE B
O. Limousin (Lead Co-I).
Space Research, Mission of opportunity CNES 2010.

36. SRG/ART-XC I – Focusing Hard X-ray Space telescope
Ph. Ferrando *et al.*, French participation.
Proposition de recherche scientifique Spatiale CNES 2010

37. MC2: développement d'une mini camera spectrométrique CdTe à très haute densité de pixels pour l'astronomie haute énergie spatiale – Tranche 1
O. Limousin, O. Gevin.
R&T CNES, 2010.

38. SPARK (Solar Particle Acceleration Radiation and Kinetics)
S. A. Matthews (PI) *et al.* (Univ. College London, MSSL).
ESA call for M-Class missions M3, 2010

39. COSPIX
Ph. Ferrando (PI) *et al.*
ESA call for M-Class missions M3, 2010

40. IXO-HXI, a Hard X-ray imager for IXO space observatory
Takahashi (PI) *et al.* (Jaxa/Isas).
ESA call for L-Class missions L1, 2010.

41. Gamma-ray instrumentation development
F. Lebrun (APC), O. Limousin (CEA/AIM).
Project proposal "Interface" for labex UnivearthS, 2010.

42. CAPSITT (Compton and Pair Silicon Timing Tracker)
F. Lebrun (PI) *et al.*
ESA call for M-Class missions M3, 2010.

43. ESRF, POLCALISTE, Polarisation performance of the Schottky CdTe Caliste detector modules
O. Limousin (CEA), E. Caroli (INFN), R.C da Silva (Coimbra) *et al.*
ESRF Research Proposal, Beam Line ID15A, septembre 2010.

44. <u>ESRF, POLCALISTE, Polarisation performance of the Schottky CdTe Caliste detector modules</u>
O. Limousin (CEA), E. Caroli (INFN), R.C da Silva (Coimbra) *et al.*
ESRF Research Proposal, Beam Line ID15A, mars 2010.

45. <u>MACSI : Mosaic Assembly of Caliste Spectro-imager</u>
O. Limousin (PI) *et al.*
CEA/Irfu, 2009.

46. MC2, Mini CdTe on –Chip (hybridation CdTe pixélisé sur ASIC 2D)
O. Limousin, O. Gevin.
R&T CNES, 2009.

47. IDeF-X XXL, Circuit frontal sub-micronique pour la detection des photons jusqu'à 1 MeV
O. Limousin, O. Gevin.
R&T CNES, 2009.

48. COSTETA, Compton Semiconductor Telescope
O. Limousin (PI) *et al.*
R&T CNES, 2009.

49. XEUS HXI French Contribution
O. Limousin, Ph. Laurent.
R&T CNES, 2009

50. Étude et développement d'ASICs de lecture de détecteurs matriciels en CdTe pour applications spatiales en technologie sub-micronique profonde
O. Limousin, O. Gevin, *et al.*
R&T CNES, 2008

51. Développement de l'instrument NITON, destine à la mesure de la radioactivité naturelle dans l'atmosphère et à la surface de Mars
J.-C. Sabroux (PI) *et al.*
R&T CNES, 2008.

52. ALTO, Response measurement under Protons beam of the Caliste prototype, a CdTe micro camera for the Simbol-X Space mission, associated with a scintillation detector
O. Limousin, B. Horeau, Ph. Laurent *et al.*
Research Proposal Tandem-ALTO, 2008.

53. Étude de détecteurs spectrométriques gamma à haute résolution spectrale et spatiale à base de Cd(Zn)Te de gros volume à électrodes segmentées
O. Limousin (PI) *et al.*
R&T CNES, 2007.

54. SVOM : Mission sino-française pour l'observation multi longueurs d'onde des sursauts gamma
J. Paul (PI) *et al.*
Space Research Proposal, CNES 2006-2007.

55. ECLAIRs : une mission pour l'observation multi longueurs d'onde des sursauts gamma
J. Paul (PI) et al.
Space Research Proposal, CNES 2005-2006.

56. Étude et développement de nouveaux détecteurs Cd(Zn)Te à anode segmentée pour la spectro-imagerie X et gamma à temperature ambiante
O. Limousin (PI) *et al.*
R&T CNES, 2006.

57. Étude et développement de nouveaux détecteurs Cd(Zn)Te à anode segmentée pour la spectro-imagerie X et gamma à température ambiante
O. Limousin (PI) *et al.*
R&T CNES, 2005.

58. SIMBOL-X, Flying in formation X-ray telescope
Ph. Ferrando (PI) *et al.*
Space Research Proposal, CNES 2005.

59. NRBC fiche A3, Gamma Caméra embarquable à masque code
O. Limousin, M. Talvard.
Research proposal, 2005.

60. Étude et développement de nouveaux détecteurs Cd(Zn)Te à anode segmentée pour la spectro-imagerie X et gamma à température ambiante
O. Limousin (PI) *et al.*
R&T CNES, 2004.

61. SIMBOL-X, Flying in formation X-ray telescope
Ph. Ferrando (PI) *et al.*
Space Research Proposal, CNES 2004.

62. ECLAIRs : un microsatellite pour l'observation multi longueurs d'onde des sursauts gamma
J. Paul (PI) *et al.*
Space Research Proposal, CNES 2004.

63. Étude et développement de nouveaux détecteurs Cd(Zn)Te à anode segmentée pour la spectro-imagerie X et gamma à température ambiante
O. Limousin (PI) *et al.*
R&T CNES, 2003.

64. ECLAIRs : Un microsatellite pour l'étude multi-longueurs d'onde des sursauts gamma
J. Paul (PI) *et al.*
Space Research Proposal, CNES 2002.

III. List of contributions

1. Posters in international conferences

1. Caliste – MM, a New Soft X-ray Spectro-Polarimeter Based on Gaseous Detector with Outer and Contactless Electronics
P. Serrano, E. Ferrer-Ribas, O. Limousin, D. Attié, F. Janneau, T. Papaevangelou.
IEEE NUCLEAR SCIENCE SYMPOSIUM – NSS-RTSD-MIC, 2015.

2. IDeF-X BD: a Low Noise Dual Polarity ASIC for the Readout of Silicon Detectors
O. Gevin, E. Delagnes, D.-D. Huynh, O. Limousin, F. Lugiez.
IEEE NUCLEAR SCIENCE SYMPOSIUM – NSS-RTSD-MIC, 2015.

3. Monte Carlo Evaluation of a Czt 3d Spectrometer Suitable for a Hard X- and Soft-Gamma Rays Polarimetry Balloon Borne Experiment
E. Caroli, G. De Cesare, R. M. Curado da Silva, N. Auricchio, C. Budtz-Jørgensen, S. Del Sordo, P. Ferrando, J. L. Galvèz, M. Hernanz, J. Isern, I. Kuvvetli, P. Laurent, O. Limousin, J. M. Maia, M. Moita, N. Produit, J. B. Stephen, A. Zappettini.
IEEE NUCLEAR SCIENCE SYMPOSIUM – NSS-RTSD-MIC, 2015.

4. Caliste-SO, a CdTe based spectrometer for bright solar events observation in hard X-rays
A. Meuris, O. Limousin, O. Gevin, C. Blondel, J. Martignac, M.-C. Vassal, F. Soufflet, N. Fiant, M. Bednarzik, S. Stutz, O. Grimm, V. Commichau.
NDIP 14, Tours, France, 2014.

5. ASTRO-H CdTe detecotrs proton irradiation at PIF
D. Renaud, O. Limousin, B. Horeau, P. Laurent.
NDIP 14, Tours, France, 2014.

6. WPOL, a future space Compton wide filed polarimeter: first light
M. Khalil, P. Laurent, F. Lebrun, Y. Dolgorouky, O. Limousin, W. Bertoli, E. Breelle.
NDIP 14, Tours, France, 2014.

7. The spectrometer telescope for imaging X-rays (STIX) on board Solar Orbiter
N. Vilmer, A. Meuris, O. Limousin, Brun, S. Allan S. Krucker, P. Orleanski, O. Grimm, H.P. Groebelbauer, K. Seweryn, J. Rendtel.
40th COSPAR Scientific assembly, Poster TFS-L-172 D2.3-0036-14, Moscou, 2014.

8. A Balloon-Borne 3D CZT Spectrometer for Hard X-ray Polarimetry
E. Caroli, J. M. Alvarez, N. Auricchio, C. Budtz-Jrgensen, R. M. Curado da Silva, S. Del Sordo, P. Ferrando, J. L. Galvz, M. Hernanz, J. Isern, I. Kuvvetli, P. Laurent, O. Limousin, J. M. Maia, A. Meuris, N. Produit, J. B. Stephen, A. Zappettini.
IEEE NUCLEAR SCIENCE SYMPOSIUM – NSS-MIC, 2013.

9. **Characterization of CdTe Pixel Detectors for the Spectrometer Telescope Imaging X-rays (STIX)**
   M. Bednarzik, R. Resanovic, O. Grimm, V. Commichau, O. Limousin, A. Meuris, G. Hurford, N. Arnold, S. Krucker.
   IEEE NUCLEAR SCIENCE SYMPOSIUM – NSS-MIC, 2013.

10. **Low energy characterization of Caliste HD, a CdTe based imaging spectrometer**
    S. Dubos, O. Limousin, C. Blondel, B. Cordier, P. Ferrando, W. Marty, Y. Menesguen, A. Meuris, T. Orduna, T. Tourrette, A. Sauvageon, S. Schanne.
    IEEE NUCLEAR SCIENCE SYMPOSIUM – NSS-MIC, 2012.

11. **Multi-Correlated Double Sampling vs. Analog shaper: Low power ASIC for pixelated CdTe.**
    A. Michalowska, O. Gevin, O. Limousin, C.S. Tindall.
    IEEE NUCLEAR SCIENCE SYMPOSIUM – NSS-MIC, 2012.

12. **Low power, low noise, Charge Sensitive Amplifier in CMOS 0.18 μm technology for the readout of fine pitch pixelated CdTe detector**
    O. Gevin, A. Michalowska, O. Limousin, C.S. Tindall, S. Dubos, D. Renaud, X. Coppolani.
    IEEE NUCLEAR SCIENCE SYMPOSIUM – NSS-MIC, 2012.

13. **Fabrication and Characterization of segmented CdTe Detectors intended for imaging X-rays on-board Solar Orbiter**
    M. Bednarzik, R. Resanovic, Paul Scherrer Institut, Switzerland; O. Grimm, V. Commichau, ETH Zurich, Switzerland; O. Limousin, A. Meuris, CEA Saclay, France; G. Hurford, A. Benz, S. Krucker, University of Applied Sciences for Northwestern Switzerland, Switzerland.
    IEEE NUCLEAR SCIENCE SYMPOSIUM – NSS-MIC, 2012.

14. **A Small 3D CZT Payload for Hard X Ray Polarimetry and Spectroscopic Imaging**
    E. Caroli, J. M. Alvarez Pastor, N. Auricchio, C. Budtz-Jrgensen, R. M. Curado da Silva, S. Del Sordo, P. Ferrando, P. Laurent, O. Limousin, J. L. Galvez, C. P. Gloster, M. Hernanz, J. Isern, I. Kuvvetli, J. M. Maia, A. Meuris, N. Produit, J. B. Stephen, A. Zappettini.
    IEEE NUCLEAR SCIENCE SYMPOSIUM – NSS-MIC, 2012.

15. **Cadmium Telluride micro-Spectrometers Hard X ray Polarimeter for a balloon borne payload**
    E. Caroli, M. Hernanz, P. Ferrando, S. Del Sordo, J. Stephen, P. Laurent, J. M. Alvarez, N. Auricchio, C. Budtz-Jorgensen, R. M. Curado da Silva4, O. Limousin, J. L. Galvez, P. C. Gloster, J. Isern, M. A. Maia, Jorge.
    39th COSPAR Scientific Assembly, Mysore, India, 2012.

16. **The Spectrometer Telescope for Imaging X-rays (STIX) on-board Solar Orbiter**
    A.O. Benz, N. Arnold, M. Bednarzik, F. Farnik, P. Gallagher, O. Grimm, G. Hurford, S. Krucker (PI), O. Limousin, G. Mann, A. Meuris, P. Orleański, J. Sylwester, A. Veronig, N. Vilmer.
    XXVIIIth IAU General Assembly, Beijing, Chine, 2012.

17. The spectrometer telescope for imaging X-rays (STIX) on board Solar Orbiter mission
A. O. Benz, S. Krucker, G. J. Hurford, N. G. Arnold, P. Orleański, H.-P. Gröbelbauer, S., Kobler, L. Iseli, H. J. Wieh, A. Csillaghya, L. Etesi, N. Hochmuth, M. Battaglia, M. Bednarzik, R. Resanovič, O. Grimm, G. Viertel, V. Commichau, A. Meuris, O. Limousin, S. Brun, N.Vilmer, K. R. Skup, R. Graczyk, M. Stolarski, M. Michalska, W. Nowosielski, A. Cichocki, M. Mosdorf, K. Seweryn, A. Przepiórka, J. Sylwester, M. Kowalinski, T. Mrozek, P. Podgorski, G. Mann, H. Aurass, E. Popow, H. Önel, F. Dionies, S. Bauer, J. Rendtel, A. Warmuth, M.Woche, D. Plüschke, W. Bittner, J. Paschke, D. Wolter, H. F. Van Beek; F. Farnik, J. Kasparova, A. M. Veronig, I. W. Kienreich, P. T. Gallagher, D. S. Bloomfield, M. Piana, A. M. Massone, B. R. Dennis, R. A. Schwartz, R. P. Lin.
SPIE, Amsterdam, The Netherlands, 2012.

18. Multi-Dimensional Optimization of Charge Preamplifier in 0.18µm CMOS Technology for Low Power CdTe Spectro-Imaging System
A. Michalowska, O. Gevin, O. Limousin.
IEEE NSS MIC RTSD, Valencia, Spain, 2011.

19. Polarisation Performance of the CdTe/CZT Caliste Detector Modules
O. Limousin, P. Ferrando, C. Blondel, B. Horeau, A. Meuris, P. Laurent, R. Chipaux, E. Caroli, S. Del Sordo, J. Stephen, R. M. C. Da Silva, J. M. Maia Pereira, V. Honkimaki.
IEEE NSS MIC RTSD, Valencia, Spain, 2011.

20. Caliste-SO X-ray micro-camera for the STIX instrument on-board Solar Orbiter space mission
A. Meuris, G. J. Hurford, M. Bednarzik, O. Limousin, O. Gevin, I. Le Mer, J. Martignac, B. Horeau, O. Grimm, R. Resanovic, S. Krucker, P. Orleanski.
NDIP 11, Lyon, France, 2011.

21. Imaging X-ray detector front-end with high dynamic range: IDeF-X HD
A. Michalowska, O. Gevin, O. Lemaire, F. Lugiez, P. Baron, O. Limousin, E. Delagnes.
NDIP 11, Lyon, France, 2011.

22. Development of the XRDPIX 32 CdTe matrix for the ECLAIRs X/Gamma camera
K. Lacombe, C. amoros, D. Barret, O. Gevin, O. Godet, J. Lande, E. Lecomte, O. Limousin, R. Pons, D. Rambaud, P. Ramon, N Remoue, G. Rouaix.
SPIE Astronomical Telescopes + Instrumentation, 2010.

23. Observing Solar Hard X-rays from Heliospheric Orbits
G. J. Hurford, A. Benz, B.R. Dennis, S. Krucker, O. Limousin R.P. Lin, N. Vilmer.
Solar Physics Division Meeting, Miami, USA, 2010.

24. IDeF-X SX0: A low power CMOS ASIC for the readout of Cd(Zn)Te detectors
O. Gevin, F. Lugiez, E. Delagnes, O. Limousin, A. Meuris.
IEEE NSS MIC RTSD, Orlando, USA, 2009.

25. Development of the ECLAIRs camera, a 6400 CdTe array for X/Gamma detection
K. Lacombe, N. Remoue, C. Amoros, D. Barret, O. Gevin, O. Godet, J. Lande, E. Lecomte, O. Limousin, F. Lugiez, J. Narbonne, R. Pons, D. Rambaud, P. Ramon, G. Rouaix.
IEEE NSS MIC RTSD, Orlando, USA, 2009.

26. Micro hard-X ray camera: From Caliste 64 to Caliste 256
A. Meuris, O. Limousin, F. Lugiez, O. Gevin, E. Delagnes, I. Le Mer, M. Chavassieux, F. Pinsard, C. Blondel, F. Daly, M.C. Vassal, R. Bocage, F. Soufflet.
IEEE NSS MIC RTSD Dresden, Germany, 2008.

27. Charge sharing in CdTe pixilated detectors, NDIP 08
A. Meuris, O. Limousin, C. Blondel.
NDIP08, Aix les Bains, France, 2008.

28. DPIX: an assembly of 6400 CdTe pixels for gamma-ray bursts detection with ECLARIs
N. Remoue, D. Barret, P. Mandrou, K. Lacombe, R. Pons, C. Amoros, G. Rouaix, B. Houret, J.-P. Dezalay, O. Limousin, O. Gevin, F. Lugiez, A. Penquer.
SPIE Astronomical Telescopes + Instrumentation, Marseille, France, 2008.

29. IDeF-X ECLAIRs: An ultra low noise CMOS ASIC for the readout of Cd(Zn)Te detectors
O. Gevin, P. Baron, X. Coppolani, E. Delagnes, F. Daly, O. Limousin, F. Lugiez, A. Meuris, F. Pinsard.
IEEE NSS MIC RTSD, Hawaii, USA, 2007.

30. 3D modeling of Cd(Zn)Te detectors for the SIMBOL-X Space mission
B.P.F. Dirks, O. Limousin, P. Ferrando, R. Chipaux.
SPIE, High-Energy Detectors in Astronomy, 2004.

2. Main talks in worshops, international meetings and invitations

1. FOXSI
O. Limousin, D. Renaud.
FOXSI meeting, GSFC USA, 2016.

2. SORENTO Lab Model
O. Limousin, Judas, Mamode.
SORENTO meeting, Saclay France, 2015.

3. LOFT: possible French controbtion to LOFT FE ASICS for SDD's
O. Limousin, Judas, Mamode.
LOFT consortium meeting, Frascatti Italie, 2014.

4. CdTe Bonding Technologies
O. Limousin.
Astro-H Design Meeting, Tokyo Japon, 2013.

5. ESA CdTe activities at Saclay
O. Limousin, B. Horeau, D. Renaud, P. Laurent
Astro-H Design Meeting, Tsukuba, Japon, 2013.

6. CdTe Detector Developments for High Energy Astrophysics in Space at CEA Saclay
O. Limousin, A. Meuris, Ferrando.
Spectrum Röntgen Gamma – ART XC, Moscou, Russie, 2011.

7. CdTe activities at Saclay
O. Limousin, B. Horeau, D. Renaud, P. Laurent
Astro-H Design Meeting, Tokyo, Japon, 2010.

8. CdTe Detector Developments for High Energy Astrophysics in Space at CEA Saclay
O. Limousin.
Solar Orbiter – STIX IDSR, Zurich, Suisse, 2010.

9. Cospix Detector Payload
O. Limousin.
COSPIX Workshop, contribution invitée, Paris, France, 2010.

10. IXO Technological Development Activities WFI/HXI – HXI developments in France
O. Limousin, K. Nakazawa, Stefanescu, P. Laurent.
IXO Workshop, ESA-ESTEC Pays-Bas, 2009.

11. Developments of new CdTe Hard X-ray spectro-imagers
O. Limousin, A. Meuris.
XTP Chinese mission meeting, Paris, France, 2009.

3. Main talks into international conferences

1. First Flight Models of Caliste-SO Hard X-ray Spectrometers for the STIX Instrument on-Board Solar Orbiter
O. Limousin.
IEEE NSS-MIC/RTSD, "CdTe Applications", San Diego, USA, 2015.

2. CdTe Pixel detectors for space Sciences in HXR – Recent developments at CEA
O. Limousin.
Rhessi-13, « Intrumentation», Windish, Switzerland, 2014.

3. MACSI: a 8 cm² CdTe focal plane for hard X-ray astronomy
O. Limousin.
IEEE NSS-MIC/RTSD, "CdTe", Anaheim, USA, 2012.

4. Revue des technologies des détecteurs astro X et X dur en France
O. Limousin, *Invited Talk.*
Colloque R&D Insu 2011, Grenoble, France, 2011.

5. Pixel Semiconductor Detectors Developments for Hard X-ray and Gamma Ray Astrophysics in Space at CEA Saclay
O. Limousin, *Invited Talk*
Gamma workshop, Toulouse, France, 2010.

6. Detector Developments for Hard X-ray Astrophysics in Space at CEA Saclay
O. Limousin.
Colloque « Rencontre Technologies Spatiales RTS 2010 » CNES, Paris, France, 2010.

7. Avec les télescopes spatiaux, sur la piste des étoiles
O. Limousin, Minier, Bouchet, Imbault.
Conférence CEA « Cyclope Juniors », Saclay, France, 2009.

8. New HXI technologies in the IXO era
O. Limousin.
IXO meeting, Boston, USA, 2009.

9. Caliste 64, first prototype of elementary camera for the high energy detector of SIM-BOL-X mission
O. Limousin, A. Penquer.
7ᵗʰ International conference on Space Optics, ICSO 08, Toulouse, France, 2008.

10. Mise en œuvre de la détection des rayons X durs et gamma pour l'astrophysique Spatiale
   O. Limousin.
   Journées Techniques CETAMA, Saclay, France, 2003.

11. ISGRI CdTe Camera in-flight behavior
   O. Limousin.
   IEEE NSS-MIC/RTSD 2003, "Space Application", Portland, USA, 2003.

12. New trends in CdTe detectors in X and gamma-ray applications
   O. Limousin, Invited talk.
   New Development in Photodetection 2002, Beaune, France, 2002.

13. Qualification model of the space ISGRI CdTe gamma-ray camera
   O. Limousin, Invited talk.
   Imaging 2000, Stockholm, Suède, 2000.

14. IBIS, Imager on board the Integral Satellite
   O. Limousin, F. Lebrun.
   GDR Haute énergie, Strasbourg, France, 1997.

4. Seminars

1. Caliste ou comment répondre à des questions que l'on ne vous a pas forcément posées ?
50 ans d'Astrophysique au CEA, Cité des Sciences et de l'Industrie, Paris, France, 2015.

2. Les succès de Caliste, un détecteur hyper performant pour l'astronomie spatiale en X–Durs
Séminaire hiérarchie DSM, Saint-Lambert des Bois, France, 2011.

3. Detector Developments for High Energy Astrophysics in Space at CEA Saclay
Séminaire Université de Californie, Space Sciences Lab, Berkeley, USA, 2009.

4. Le Tellurure de Cadimium imagerie et spectrométrie gamma spatiale
Petit déjeuner de Presse CEA, Paris, France, 2006

5. Le Tellurure du Cadmium : imagerie gamma pour l'astrophysique spatiale
Séminaire CdTe LETI/LIST/DAPNIA, Saclay, France, 2004.

6. Mise en œuvre de la détection des rayons X durs et gamma pour l'astrophysique Spatiale
Séminaire Instrumentation DRFC, CEA, Cadarache, France, 2004.

7. Mise en œuvre de la détection des rayons X durs et gamma pour l'astrophysique Spatiale
Séminaire des « Centres de Compétences Technique du Cnes, Toulouse, France, 2004.

8. Développement de nouveaux détecteurs CdTe et CdZnTe pour l'astronomie gamma Spatiale
Séminaire Journées APC, Paris, France, 2003.

9. XMM, INTEGRAL, SIMBOL-X, ECLAIRs
Forum du Service d'Astrophysique, CEA, Saclay, France, 2003.

10. Groupe détecteurs pour le Spatial
Forum du Service d'Astrophysique, CEA, Saclay, France, 2002.

11. Détecteur CdTe pour l'astrophysique Spatiale
Séminaire DIMRI, CEA, « », Saclay, France, 2002.

12. ISGRI : Imageur du télescope IBIS à bord du Satellite Integral
Séminaire Technique LETI, CEA, Grenoble, France, 2000.

IV. The Story of Caliste

1. Introduction

The discovery of the X–ray sky in the 1960s paved the way to a new fundamental field of research in astrophysics, recognized by the 2002 Nobel Prize in Physics to R. Giacconi, a pioneer.

In the high-energy domain, the atmosphere is opaque to the radiations which implies that astronomical observatories need to be placed in orbit, annoyingly complicating their design, their construction but also their use and maintenance. I would add that access to space also certainly limits the nature of collaboration and the number of projects for strategic reasons and financial reasons.

Increasing power of space observatories has revealed high-energy emission from objects of all scales in the Universe, from compact sources such as black holes and neutron stars to diffuse hot plasma pervading galaxies and clusters of galaxies. The study of compact objects on the one hand and the acceleration process studies are in two words the favorite research topics of high-energy astronomers in the field of X-ray and beyond.

Space telescopes must be equipped with «optical» systems and imaging-spectrometers which have the role to measure the energy of the photons and determine their arrival direction in order to provide "coloured" images of the sky. In addition to that, it is of scientific interest to record the arrival time of photons for variable objets. Eventually, the determination of the polarization degree of the incident radiation, which is a common measure in visible or IR, is an emerging capability in the high-energy domain.

Naturally, the gamma ray sky being still relatively unknown and most of the sources being faint, the means of observation can require wide fields of view and long observing times.

The celestial sources which I will briefly present hereafter, are usually weak, distant and sometimes furtive. Added to this is the fact that sources radiate X-ray photons in an area where the cosmic background, as well as the intrumental background is intense, limiting the sensitivity of the telescopes. The observation in the field of X-ray continues to be an instrumental field particularly difficult but in constant progress, noticibly thanks to the appearance of grazing incidence mirrors beyond 10 keV.

In the following, I will show my contribution and that of my close colleagues to this instrumental progress and our pursuit of performance for the sensors in particular.

After a brief overview on astronomical sources of interest in the range of hard X-ray photons, I will summarize the main results obtained with INTEGRAL/ISGRI, my first instrumental project. I will derive the new challenges towards direct imaging and fine spectrometry. This will allow me to introduce my research development approach and pursue with the core of my research: the development of Caliste, a CdTe based imaging spectrometer in hard X-ray astronomy.

I will demonstrate my mid-term future plans introducing my most recent R&D work on fine pitch spectrometers and I eventually conclude my dissertation showing the impact of my research in terms of mission opportunities, valorization and forthcoming projects.

2. Hard X-ray Astronomy

Understanding the accretion process of matter onto Black Holes is fundamental since it has profound implications for astrophysics and physics. For example general relativity effects can be tested in the Black Hole environment and the interaction of matter with super-massive Black Holes is predicted to play a role in formation and evolution of host galaxies.

Furthermore, the origins of the highest energy photons and cosmic rays are still unknown and firm evidences of hadrons acceleration in suspected astronomical sites are missing. Observing these processes at work in various acceleration sites are mandatory steps for resolving these issues.

Accretion process and acceleration mechanisms are best revealed by their emissions in the X–ray and hard X–ray ranges, the latter probing the most energetic and violent environments and their non thermal population of energetic particles.

1. Celestial objects of interest in the Hard X-ray domain

X and Gamma-ray celestial sources are associated with the most violent physical phenomena of the Universe. Most of these sources involve the presence or formation of a compact object such as either a supermassive black hole, or, at smaller scales, "stellar" black holes (BH) or neutron stars (NS) that are nothing else but the residue of dead massive stars.

The electromagnetic spectrum emitted by the sources extends continuously from radio waves to ultra high-energy gamma rays, up to a few Tera electron Volts in the case of blazar type AGNs. Each energy band is preferentially, and sometimes exclusively, associated with a given type of emission process and physical conditions causing the emission of photons. Observing these photons, therefore, holds crucial information on the celestial bodies, their nature, geometry, and/or their interactions with their environment. Observations of the sky in all energy ranges allow scientists to better know the contents of the Universe and better probe its history.

During the last thirty years, the performances of X-ray telescopes have greatly improved in terms of sensitivity angular and spectral resolutions thanks to advances in optical techniques and sensors (detectors + readout electronics). This has led to a considerable increase in the understanding of the most violent phenomena in the Universe, as for example the physics of compact objects (BH, NS) and related accretion phenomena, and of particle acceleration processes by shock waves. The X-ray and hard X-ray radiation is also a key diagnostic of the hot plasmas in galaxy clusters with implications on galaxy evolution and cosmology. All has not been fully understood nor observed, and the X-ray astronomy history continues to be written today, thanks to new challenging technical developments, with, among others, the NuSTAR mission launched in 2012, and Astro-H, just launched.

X and gamma sources can be broadly classified in two categories: point sources (at the scale of the current angular resolution) typically related to the physics very close to astrophysical objects, and large scale sources as e.g. the supernovae shocks (sites of particle acceleration) or the diffuse intra-cluster hot plasma. In both cases, the emission can be a mix of thermal (from the plasma) and non-thermal (from a population of accelerated particles) emissions. Hereafter I give a brief description of the main celestial objects of interest in the high-energy domain.

1.1. Death of the stars - Supernovae
One the most important source of X and gamma rays is related to the processes involved at the end of the life of stars. During its working life, a star gradually consumes its hydrogen through nuclear fusion: this is the main sequence, ie

the longest phase of a star's life. When the amount of hydrogen fuel decreases beyond a critical threshold, the star leaves the main sequence.

In the case of low-mass stars (less than 4 times the mass of the Sun), they will move towards the red giant branch, which will give rise to planetary nebulae and white dwarfs.

Conversely, the most massive stars will join the category of giant and supergiant stars before ending their lives in supernovae, giving birth to BHs or NSs. These two mechanisms are at the origin of emissions in X and gamma radiations.

In the case of low-mass stars, the end of the nuclear reactions in the heart will be accompanied by the rise of the pressure and temperature resulting in the combustion of heavier elements. Helium will start burning, generating carbon then oxygen. These reactions generate such a large amount of energy that the radiation pressure pushes away the external layers of the stars. The stars are getting larger and larger while the temperature at the surface gets lower, giving to the object its typical red color: red giant. When the nuclear fuel reserve is getting lower and lower, the core of the star is contracting under the effect of gravity while external layers are fully ejected in the interstellar medium. The C and O remaining core radiates and ionizes the ejected layers, forming beautiful planetary nebulae. The core of the star remains alone as a white dwarf and slowly cools down.

In the particular case of the evolution of a white dwarf into a binary system, conditions may be reached for the compact object to capture external layers of a companion star. Falling on the white dwarf surface, the accreted matter is getting warm and the pressure rises up to a point where thermonuclear reactions are triggered, provoking the system to shine again. If the mass of the white dwarf is close to 1.4 $M_\odot$ (the Chandrasekhar limit) the accretion process will lead to the general thermonuclear conflagration. This explosion will disperse the entire material at very high speed into the interstellar medium. This process is called thermonuclear supernova, or supernova type Ia. The process is accompanied with the spread of a large mass of radiaocative Ni-56, decaying into Co-56 and finally into Fe-56. A neighbor decay chain starting from Ni-57 to Fe-57 is also at play. These isotopes are observable nuclear lines (Co-56 at 847 and 1238 keV, Co-57 at 122 keV, Fe fluorescence at 6.4 keV) with gamma ray detectors. These lines have been observed SN2014J [5.8.1]. Supernova of type Ia are precisely shining the same flux due to the process driven by the white dwarf mass and are used as "standard candles" at cosmological distances to probe the universe. Thermonuclear supernovae do not give any residue after explosion.

When the mass of the star is higher (> 8 to 10 $M_\odot$), the star burns nuclei with higher and higher mass. The thermonuclear fusion ends when the core of the star is made of stable Iron. When the Iron core reaches the mass limit of Chandrasekhar, it collapses in a fraction of second to reach its highest compression level, far above the density of atoms. The super dense core forms a proto-neutron star, which triggers shock waves. The latter ignites nuclear reactions in the inner layers of the star envelope where many heavy nuclei are formed, including radioactive isotopes. The schock wave together with the gigantic quantity of neutrinos momentum, spread out the external layers of the stars bringing them to extreme temperatures. The process is very luminous and is the sign of a supernova. After a few days, the luminosity is fed by the radioactivity of the inner isotopes, Co-56 being the principal engine. Following the event, the luminosity is decreasing and the shock wave blasts the interstellar medium for hundreds of years. This type of supernova is called gravitational supernova, type II or core-collapse. Core collapse supernovae leave as compact residues either a black hole or a neutron star.

Among others, Ti-44 is one of the radioisotopes of interest due to its pretty long decay time (~85.4 years). It is produced in both thermonuclear and core-collapse supernovae with different yields depending on the geometry of the system. It produces observable gamma ray lines at 67.8, 78.4 and 1156 keV. Because the lifetime of large mass stars is short, the supernovae take place close to the star formation regions. The analysis of Ti-44 is therefore a tracer of supernovae remnants in our galaxy (cf. Figure 1). It has been observed unambiguously only in Cas A [5.8.2 and 5.8.3]. Another candidate for Ti-44 evidence has been found in SN 1987 A by INTEGRAL [8.4]. No other candidates were found so far.
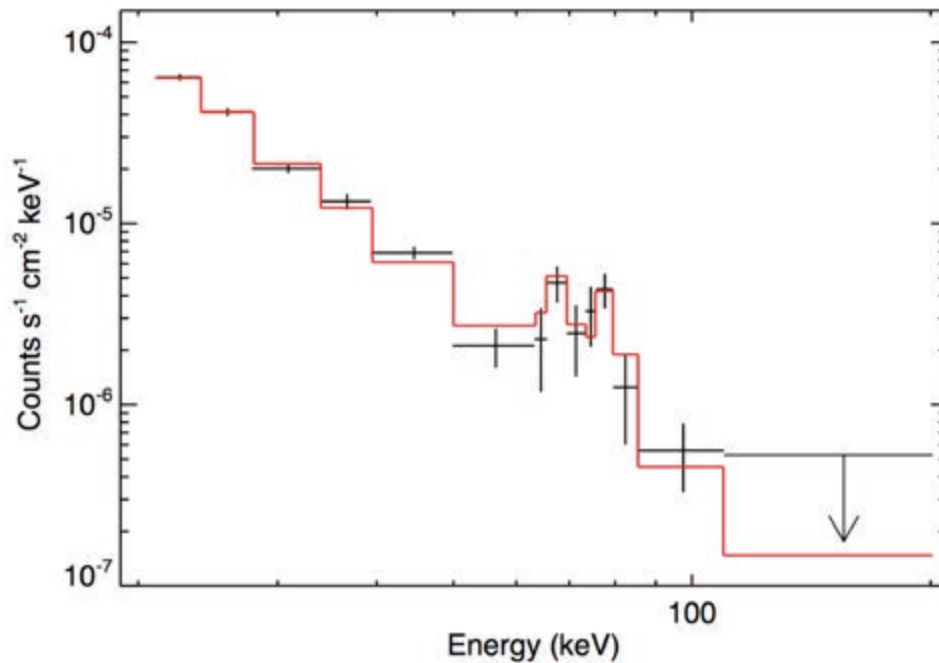
Figure 1. ^{44}Ti lines at 67.9 and 78.4 keV in Cas A observed with INTEGRAL/ISGRI (Renaud et al. 5.8.2).

1.2. Pulsars and synchrotron radiations

Following the explosion of a core collapse supernova, the residue of the original star may contract as an extremely dense, highly magnetized (up to ~10^{11} T or 10^{15} G) and rapidly rotating neutron star (~10-100 rev./s). A consequence of the rotation and the strong magnetic field is the production of jets radiating towards the observer periodically. This periodic radiation is detected from radio waves to high-energy gamma rays. Pulsars are very complex objects interacting with their environment and are still subject to observations and analysis in the X and gamma ray ranges in particular.

Certainly the most famous pulsar radiating in X-rays is found in a Supernova remnant in the constellation of Taurus. It is known as the Crab Nebula and consists of a rapidly rotating neutron star, (white dot near the center on Figure 2) that powers the activity seen in X-rays. The inner X-ray ring is thought to be a shock wave that marks the boundary between the surrounding nebula and the flow of matter from the pulsar. Energetic particles move outward to brighten the outer ring and produce an extended X-ray glow. The jets perpendicular to the ring are due to matter and antimatter particles spewing out from the poles of the pulsar.

When the neutron star is associated with a stellar companion in a binary system, stellar matter falls on the neutron star surface. The strong magnetic field may influence the accretion process bringing matter to the neutron star magnetic poles. Hot spots are created and emit predominantly in the X-ray domain. We talk about X-ray pulsars.

Another source of X- and gamma emissions is due to the effect of the magnetosphere of the star on the material surrounding it. Electrons are accelerated by the rapidly rotating intense magnetic field surrounding the pulsar, and emit synchrotron radiation through interaction with this same field. These radiations depend strongly on the electrons bulk velocity, and therefore can cover a large part of the spectrum, from infrared to hard X-rays or even beyond (synchrotron radiation emissions up to 25 GeV have been observed in the Crab Nebula). It is also polarized and pulsed, and its observation in the X-rays and gamma rays - typically between 0.1 and 1 MeV - helps to understand the magnetosphere of pulsars (Figure 3).
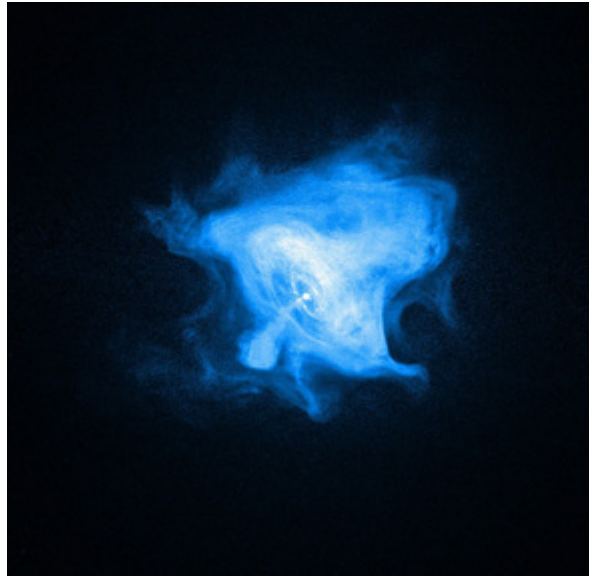
Figure 2. The Crab pulsar in SN1054, in X-rays. The picture, the taken the Chandra Observatory, reveals the complex structure of the system with its synchrotron engine. Creator/Photographer: Chandra X-ray Observatory The Chandra X-ray Observatory, which was launched and deployed by Space Shuttle Columbia on July 23, 1999

1.3. Accretion mechanisms: X-ray binaries and black holes

In addition to the mechanisms described above and explaining the X and gamma emission consecutive to the death of stars, another high-energy phenomenon leads to the production of continuous spectra at these wavelengths. This is the effect of the material accretion around compact stars as neutron stars or black holes.

Gravitational fields created by these objects are such that they can catch the material in their periphery, accelerating the gas and imparting energy. This capture will be significant if a close star acts as a "supplier" of material, typically in a binary system configuration (neutron star or pulsar – star, or black hole – star). The material captured by the compact object in the outer layers of the star companion "will wrap" around it, forming an accretion disk (Figure 3). Temperatures up to about 10^7 K can be reached when the inner regions of the disc are at their closest locations to the compact object (the last stable orbit around a BH or the surface of a NS). This light can be observed in X-rays up to a few keV. This is attributed to thermal emission in such systems.

More than thirty years of hard X-ray astronomy has shown that this picture is clearly too simplistic. Very early on a hard spectral component have been discovered on top of the soft thermal emission, and is seen up to energies of 1-10 MeV. This component is usually attributed to an inverse Compton process of the soft thermal photons on very energetic electrons (either thermalised or not) present in a corona-like environment probably surrounding both the disc and the compact object.
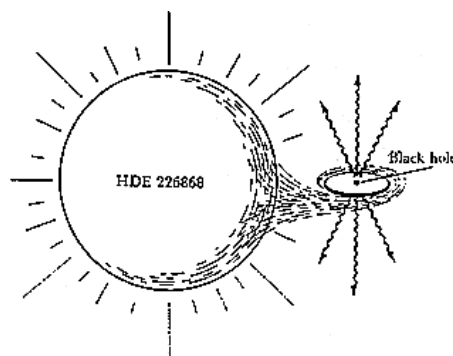

Figure 3. Sketch view of binary system (Cyg X-1) made of a supergiant star and an accreting black hole. The accreted matter falling in spiral on the compact object radiates in X rays.

1.4. Galactic center high energy emission

In addition to X and gamma sources related to final stages of the life of stars, some of the radiation originates in the interstellar medium of our galaxy. These emissions could result from the interaction of supernova remnants with the interstellar medium, but it can also originate from diffuse sources.

The study of the emission line at 511 keV gamma produced by the annihilation of a pair electron / positron is possibly an indicator of the distribution of antimatter in the galaxy. The sources and the distribution of this antimatter in the galactic bulge is a topic of current research: the maps produced by the INTEGRAL space mission recently ruled out a contribution of dark matter annihilation of positrons, a hypothesis previously favored. The main candidates would rather be again supernovae and X-ray binary systems/microquasars.

1.5. AGN

At a larger scale, a fraction of galaxies produce intense light at high energy when they are powered by the accretion on a super-massive black holes lying at their center. The centers of these galaxies are named Active Galactic Nuclei and are the source of electromagnetic radiation amongst the most luminous in the universe. This type of object can radiate throughout the entire electromagnetic spectrum. The emission processes are similar to those described for binary systems and black holes: heating of accretion disks and emission of powerful jets of matter. As a matter of fact, AGNs are candidate sources for ultra-high energy cosmic rays. AGNs are categorized into different classes according to observational characteristics, which are interpreted in a unified model as resulting from the orientation of their disk with respect to the observer.

1.6. Solar flares

Finally, closer to home, our Sun also radiates in the high-energy domain. In particular, solar flares can be accompanied by intense X-ray and gamma ray emissions. The vicinity of the active regions of the Sun and its atmosphere are subjected to intense magnetic fields distributed in an extremely complex manner. These fields communicate magnetic energy to the plasma. This energy is released quickly in the interplanetary medium during the eruptions and dissipated as radiation and particle flow.
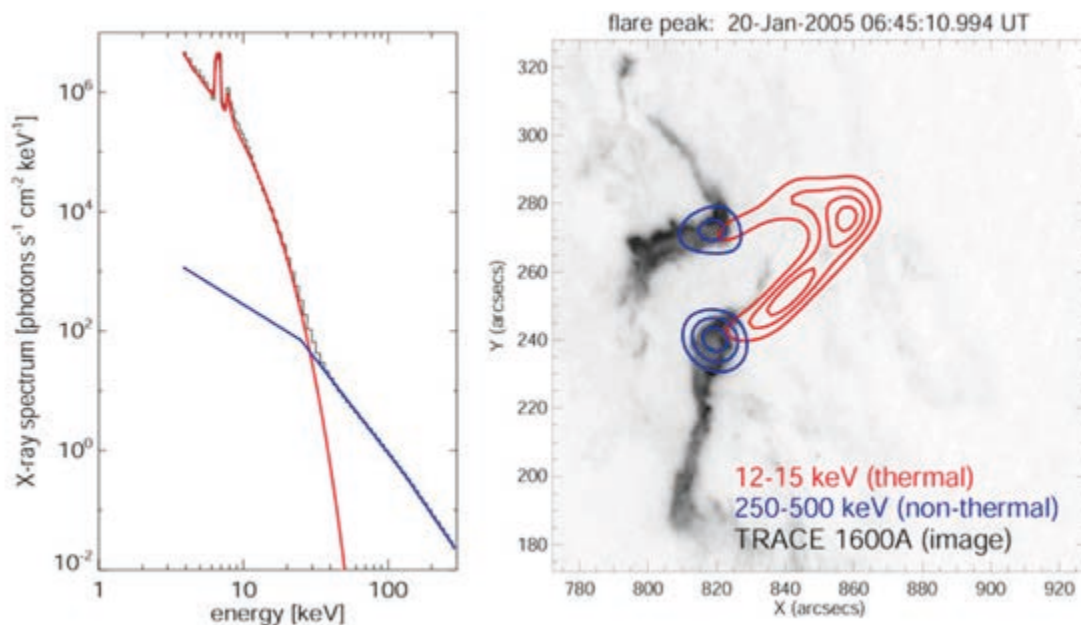

Figure 4. Left – Solar flare spectrum. Right – Corresponding image of a solar flare in X-rays.
The thermal emission corrresponds to the hot plasma while the non-thermal radiation at higher energy
indicates particle acceleration [4.12].

The most prominent emission mechanism producing solar hard X-rays is bremsstrahlung of electrons as they encounter ambient ions. For thermal electrons (i.e. those that have a Maxwellian distribution of their velocity), hard X-ray emission is typically seen from coronal magnetic loops with temperatures above ~10 MK. A typical thermal hard X-ray spectrum is given in Figure 4 – left, showing the thermal bremsstrahlung emission in red. The second component seen at higher energies is bremsstrahlung emission from electrons with a distribution function different from a Maxwellian one, indicating acceleration phenomena induced by the release of magnetic energy during solar flares. While the acceleration site is thought to be in the solar corona, the most intense non-thermal emission is produced when flare-accelerated electrons hit the much denser chromosphere and produce intense hard X-ray sources at the footpoints of flaring loops in Figure 4 – right.

The observations of «thermal» radiation provide information on the evolution of the solar plasma temperatures during the eruption while the «non-thermal» radiation at higher energy is indicative of acceleration phenomena at the Sun surface. The study of the polarization of these emissions would be a step forward in the sense that it would increase the understanding of the underlying micro-physics of solar flares. The missions deployed so far have not given enough accurate results in terms of polarization measurements.

2. Implication on the Hard X-ray telescope design

Below ~ 10 keV, astrophysics missions such as XMM–Newton and Chandra use X–ray mirrors based on grazing incidence reflection properties. This allows extremely good angular resolution, down to 0.5 arcsec for Chandra, and a good signal to noise ratio thanks to the focusing of the X–rays onto a small detector surface. This technique has been so far limited to energies below ~ 10 keV because of the maximum focal length that can fit in a single rocket fairing. Hard X–ray and gamma–ray imaging instruments thus use a different imaging technique, for example that of coded masks, as those onboard the INTEGRAL or SWIFT missions. This non-focusing technique has intrinsically a much lower sensitivity than focusing telescopes and does not allow reaching angular resolutions better than a few arc minutes. In addition to the difference in angular resolution, there is also roughly two orders of magnitude of difference in point source sensitivity between X–ray and gamma–ray telescopes.

This transition of techniques unfortunately happens roughly at the energy above which the identification of a non-thermal component is unambiguous with respect to thermal emission. Considered from the low energy side, that obviously strongly limits the interpretation of the high quality X–ray measurements in this range, and particularly those related to the acceleration of particles. Considered from the high-energy side, that prevents the mapping of the gamma–ray emission of extended sources to the required scales to understand the emission mechanisms by comparison with lower energy data. The hard X–ray range is the energy domain where fundamental problems of astrophysics have their essential signatures, either via non thermal emissions characterizing populations of particles accelerated to extreme energies, or via thermal emissions revealing the presence of very hot comptonizing plasmas as those believed to exist close to compact objects. In addition, whereas low energy X–rays are stopped by a relatively small amount of matter, hard X–rays are extremely penetrating and can reveal sources that are otherwise left hidden. This has been shown in particular by the measurements made by the IBIS/ISGRI instrument, a CdTe based soft gamma-ray imager, onboard INTEGRAL, which has led to the discovery of a number of highly absorbed sources, mainly pulsars in supergiant binary systems but also of obscured AGNs, which are fundamental to understand the Cosmic X-ray Background.

A clear requirement for future high-energy astrophysics missions is thus to bridge this gap of sensitivity, by offering instrumentation in the hard X–ray range with a sensitivity and angular resolution similar to those of the current X–ray telescopes. In order to take up this challenge, a hard X–ray-focusing optics is mandatory. Such optics can readily be implemented by a simple extension of the current X–ray mirror technology to long focal lengths.

The straight consequence of using focusing optics to drastically improve the hard X-ray telescopes sensitivity is to create the corresponding detector planes. The sensors in question must be able to cover a large filed of view thus being in the range of 100 cm^2, to sample the point spread function of the mirror system with highest achievable spatial resolution (500 µm pitch typical) and to get outstanding energy resolution (~1% at 60 keV) without bringing too many constraints at system level, such as power and mass. Top-level requirements will be rediscussed in 3.3.

3. INTEGRAL/ISGRI heritage

1. INTEGRAL's heritage

The INTEGRAL (INTErnational Gamma-Ray Astrophysics Laboratory) ESA satellite is successfully operating since 2002. The mission is devoted to the gamma-ray sky observation between 15 keV up to 10 MeV. The payload comprises essentially two instruments: IBIS (Imager on Board the INTEGRAL Satellite), an imager with spectroscopic capabilities and SPI (SPectrometer on INTEGRAL), a cooled Ge spectrometer system with imaging capabilities.

IBIS is based on a coded mask aperture system combined with a gamma camera about 3 meters away. IBIS uses two pixelated gamma cameras: a CdTe array recording photons up to 1 MeV and a CsI array above 250 keV. The pixel detector technology enables a crucial improvement of the sensitivity and a significant extension of the energy range down to 15 keV. The extension towards the low energy is a major feature as the spectral shape of astronomical sources offers higher statistics as the energy gets lower and therefore a better signal to noise ratio.

The angular resolution of a coded mask telescope is given by its mask element size and by the mask to detector distance. The latter is limited only by the mission resources (dimension, mass). The imaging performance of a coded mask telescope is governed by the spatial resolution of the detector. Each pixel of the camera is an individual spectrometer. High-Z and high-density semi-conductor detectors operating at room temperature such as CdTe are the most promising candidates. The limitation on the pixel size comes mainly from the number of electronic channels one can operate simultaneously since one complete spectroscopic channel per pixel is necessary. To limit the volume, the electronics power consumption and the related heat dissipation, dedicated integrated circuits (ASICs) are used. These considerations have driven the IBIS design. The detector of IBIS is made up of two square detection planes of the same dimensions. The upper layer, ISGRI (Integral Soft Gamma-Ray Imager) visible in Figure 6, specifically covers the low energy domain from 15 keV up to about 200 keV but is sensitive up to 600 keV while the lower one called PICsIT (Pixelated Imaging CsI Telescope) takes care of the higher energies. Both ISGRI and PICsIT response can be combined to operate in a Compton mode.
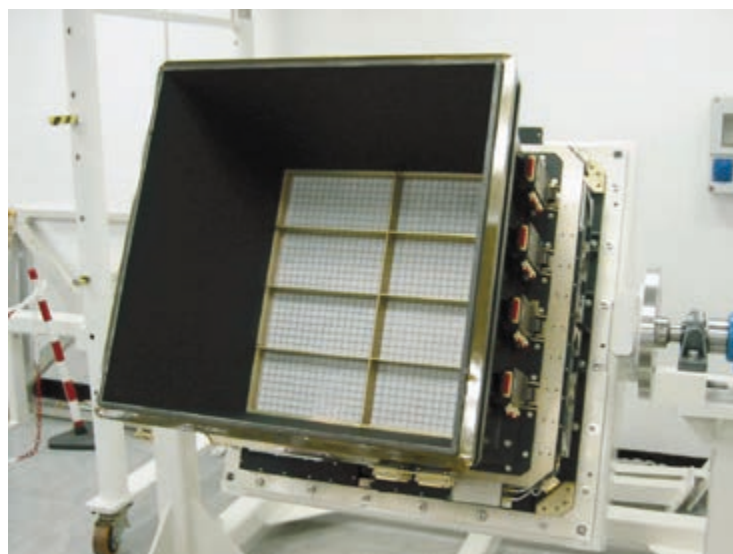

Figure 5. IBIS detector stack surrounded by passive and active shielding. The white colored detector is ISGRI, a 16,384 channels CdTe imaging spectrometer.

ISGRI pixels are square CdTe detectors 4 × 4 mm² and 2 mm thick. There are 16,384 pixels providing a useful area of 2621 cm². ISGRI is the first very large CdTe gamma camera to be flown. Thanks to a mask-to-detector distance of 3.15 m, 12 arcmin angular resolution can be achieved. ISGRI provides sky images with a 5' sampling resulting in source location accuracy better than one arcmin for the brightest sources.

2. Some of the major results obtained with INTEGRAL

INTEGRAL is a very successful mission and has completed its entire original scientific program. It has now been operated inflight for 13 years, and continues to be operated harvesting high-energy data.

Summarizing the top most results, one could select the following discoveries:
- The source catalog from IBIS, essentially fed by ISGRI, now accounts for 956 sources. Most of the sources are black holes and neutron star candiates or extra-galactic sources like AGN or Seyfert (Figure 6). [8.5]
- The Compact sources as the origin of the soft gamma-ray emission of the Milky Way published in Nature [8.6]
- The observation of Ti-44 lines in Cas A [8.1]
- Discovery of gamma-ray polarized emission from the Crab, a GRB and Cyg X-1
- Discovery of pair plasma annihilation at 511 keV from a microquasar.

Another success of INTEGRAL is the excellent behavior of the ISGRI detectors in flight, perfectly in line with the prediction performed during the implementation phase of the hardware [4.33].
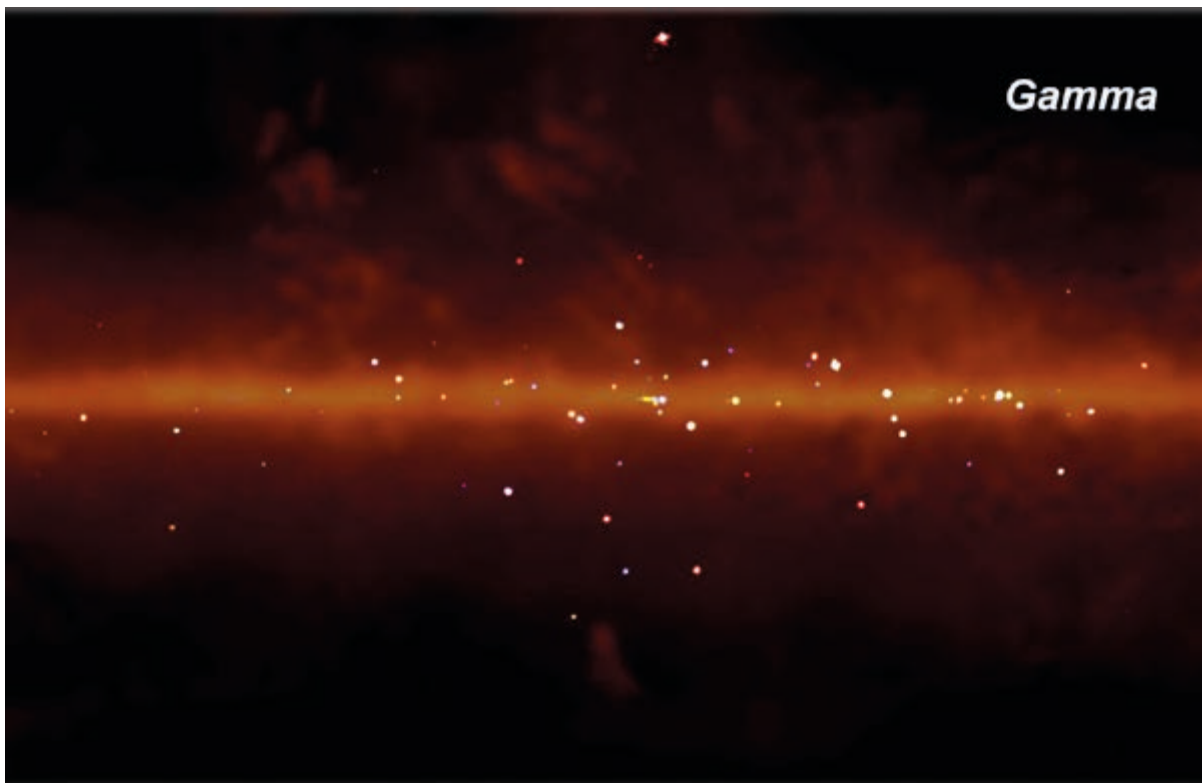INTEGRAL will be back on Earth in 2029 and will continue observations until then.

Figure 6. Gamma ray sky observed with INTEGRAL/IBIS (Courtesy of F. Lebrun, CEA/APC).

3. New era of direct imaging in Hard X-rays

Thanks to emerging space technologies, the design of orbital missions using multiple spacecraft flying in formation was envisionned since 2000. Alternatively, long extendable optical benchs are also deployable in space.

At the beginning of 2004, the French national space agency (CNES) has issued a call for a scientific payload to be flown on a formation flight demonstrator mission to be launched about a dozen years later. The Simbol–X mission has been proposed in this context by Dr. Ph. Ferrando astrophysicist at CEA/SAp/APC and Dr. G. Pareschi astrophysicist at the Observatorio Astronomico di Brera. Simbol–X was a hard X–ray pointed « deformable » telescope with a 20 m long focal length optics that would extend the focusing techniques used in the X-ray domain up to ~ 80 keV. The choice was made to set up a configuration of two satellites:
  • The first satellite payload being a hard X-ray grazing incidence mirror assembly
  • The second satellite hosting the focal plane.

The telescope would offer both an increase in sensitivity and angular resolution by two orders of magnitude compared to the current instruments in flight operating above 10 keV, *i.e.* ISGRI on board INTEGRAL satellite or the BAT detector onboard Swift. The sensitivity improvement is illustrated in Figure 7 where the continuum sensitivity curves of Simbol-X vs. INTEGRAL /IBIS/ISGRI in the same energy range are plotted. The sensitivity is defined as the minimum observable flux of a source in a given exposure time, at a given confidence level.
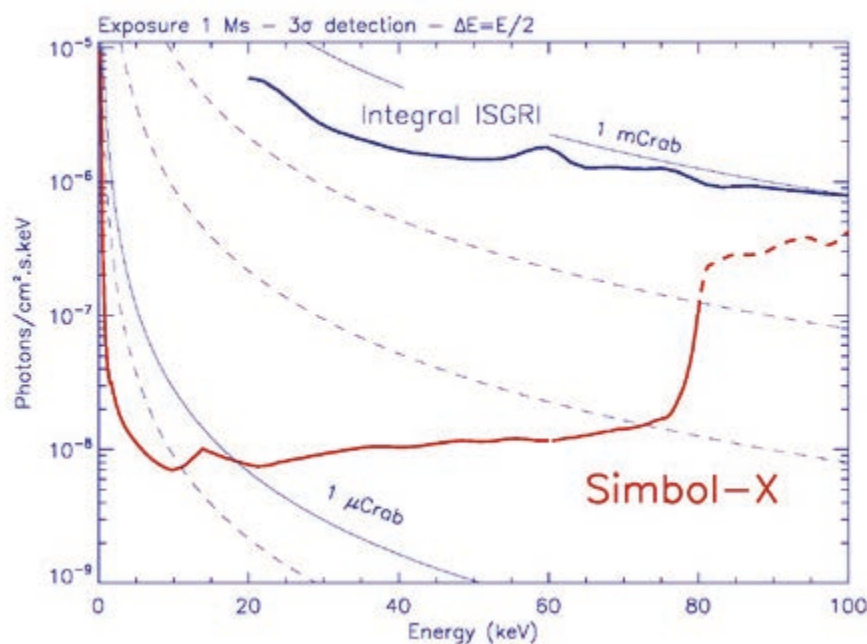

Figure 7. SIMBOL-X sensitivity against INTEGRAL/ISGRI sensitivity. The improvement in the hard X-ray domain is mostly due to the use of grazing incidence optics instead of a coded mask aperture system [3.3.52].

The parameters that drive the design of the focal plane assembly are:
  • The energy range
  • The spectral resolution at the 6.4 keV Fe lines
  • The spectral resolution at the 67.9 keV and 78.4 keV ^{44}Ti lines,
  • The field of view of the optics to be 12 arcmin
  • The request for oversampling the optics point-spread function of 20 arcsec Half Energy Width
  • The need for a very low background

This set of top-level requirements has led to us to combine a stack of two different detector technologies, taking advantage of the excellent response of silicon based sensors below 10 keV and the unique response of CdTe above 10 keV. We also considered the optimization of the system with respect to background and demonstrated the efficiency of a plastic scintillator based anticoincidence system to veto the ever-present cosmic ray particle induced background.

Below 10 keV, silicon sensors are perfectly suited to perform high angular and high spectral resolution. On "*low energy*" X-ray missions, like Chandra or XMM-Newton CCDs have been used. They are however pretty slow to read, of the order of a few seconds for Full Frame read-out. This is not compliant with the requirements set for Simbol-X on the background level, which could be achieved only through the use of an active anti-coincidence shield. New Active Pixel Sensors were thus instead chosen for the program. Based on monolithic DEPFET Macro Pixel, they are much faster to read out (hundreds of microseconds), have a very good spectral response (energy resolution < 130 eV FWHM at 6 keV), and can be operated in principle at "room" temperature, even if in space some cooling is required to keep radiation damage low (operating T of - 40°C for Simbol-X).

Above 10 keV, the unprecedented focusing technique of SIMBOL-X required the development of entirely new detector concepts. Due to its well known advantages, that have a high efficiency up to ~100 keV, room temperature or moderately cooled operations, good spectrometric performances, and adequate maturity for space applications, we chose to go ahead with Cd(Zn)Te semiconductor detectors. Moreover, this kind of detectors has been extensively and successfully used in space, both on INTEGRAL and SWIFT. Nowadays, CdTe based detectors are also taking advantage of mature electrode deposition techniques with photolithography process which enables high quality pixelated contacts on monolithic single crystals. The pixel size was only limited by the flip chip mounting technology on hybrid modular components and by the power budget that constrains the number of independent active channels into the camera.

Assuming a 20-meter focal length with a 12-arcmin field of view and a 20-arcsec angular resolution (the best angular resolution proposed up to now at 30 keV), we derived the camera sensitive area to be 64 square centimeters. This is much larger than any available Cd(Zn)Te single crystal. Such a camera has to be an assembly of sub-arrays, possibly a mosaic of elementary sub-arrays installed next to each other.

On the other hand, in order to guarantee a comfortable oversampling of the focal point, ~3 mm in diameter at Half Energy Width in this configuration, 750 μm maximum pixel pitch is required to get a good enough image reconstruction and accurate source localization. A 625-μm pixel pitch has been chosen for Simbol-X in 2004 as a good compromise between the surface of detection (64 cm^2) and the number of active channels (16,384), and thus the power budget (< 1 mW/channel).

Combining small pixel detectors (small detector capacitance and low dark current) operated at moderately cool temperature (~ - 40°C to - 20°C), new development in low noise and low power micro-electronics front-ends and suitable hybridization process, it is possible to achieve a uniform spectral response much better than 1.3 keV FWHM at 68 keV, specified by scientists to study envelop ejection speed in supernovae remnants for instance.

One should note that the CdTe imaging spectrometers that we intended to develop at that time and that I will present in more details further in the text, are single-photon detectors. In other words, they are not read out by frame like CCDs but each individual photon is able to trigger the data acquisition system when its energy is high enough compared to the electronic noise. This technique has several impacts at the expense of the power consumption. First, despite the fact that CdTe is a pretty slow sensor, it allows a very accurate time tagging of each event (typical accuracy of ~1 μs). This performance is far above the scientific need but allows an efficient use of a fast veto system for cosmic-ray background rejection. Second, the dead time is pretty short (about 20 μs). This allows being « open » on the sky a large fraction of the time.

Top-level requirements and associated detector parameters are summarized in Table 1. **Note this table has driven the last 10 years of R&D in my team.**

Table 1. Top level requirements of SIMBOL-X and corresponding detector parameters.

Parameter	Simbol-X Requirement	Associated detector parameters
Energy band	~ 0.5 to > 80 keV	– Silicon pixel sensor < 10 keV – Cd(Zn)Te sensor up to 80 keV, 1 to 2 mm thick crystals
Spectral resolution	$E/\Delta E = 40$ @ 6 keV $E/\Delta E = 50$ @ 68 keV	<10 electrons rms at Si level <100 electrons rms at Cd(Zn)Te level.
Field of view (50 % vignetting)	> 9' – goal 13' (diameter)	64 cm² sensitive area
Angular resolution	< 20'' – goal 15''	625 µm Pixel pitch 16384 channels
Absolute reconstruction pointing	~ 2'' (radius, 90 %)	No constraint at detector level
On axis effective area	> 600 cm² @ 8 keV > 450 cm² @ 20 – 40 keV > 100 cm² @ 70 keV	
On axis continuum sensitivity	< 1 µCrab (3 σ, 1 Ms) in 20 – 40 keV band	Need of anti-coincidence system, requires high timing accuracy at Cd(Zn)Te level < 300 ns.
On axis line sensitivity @ 68 keV	< 10^{-7} ph/cm²/s (3 σ, 1 Ms)	Need of anti-coincidence system, requires high timing accuracy at Cd(Zn)Te level < 300 ns rms.
Absolute timing accuracy	< 100 µs – goal 50 µs	No constraint from science at detector level
Mission duration	> 2 years of scientific programs (~ 3 yrs of mission)	Modular detection units, high reliability and radiation hardness

4. Developments for hard X-ray astronomy at CEA

1. New trends in CdTe based detectors

1.1. Paper #1 [3.4.37]: New trends in CdTe and CdZnTe detectors for X and gamma ray applications…

In June 2002, I was asked to give an invited talk to the « International Conference on New developments in Photodetection » to assess the new trends in CdTe and CdZnte destectors for X and gamma ray applications. I demonstrated that:

- Hard X-ray Astronomy is pulling the R&D works towards high spatial and high-resolution detectors bringing the CdTe community to the highest level of performance.
- The massive use of CdTe and CdZnTe in some applications raised the maturity of these materials for use in space but also in nuclear applications and medical applications as well.
- The trend was to further develop fine pitch detectors simply because, reducing the size of the pixels, taking advantage of photolithography electrode patterning of CdTe sensors, the stray capacitance and dark current of the detectors decrease proportionaly with the pixel surface. Combined with appropriate microelectronics must lead to excellent energy resolution.
- The trend to drastically reduce the pixel dark current and the stray capacitance helps using long shaper time, more appropriate to complete charge collection.
- The Schottky type detector, developed by JAXA/ISAS, started to be mature enough to envision super low dark current in individual pixels, bringing the noise level to its minimum, even in moderately cooled detectors.
- A consequence of the Schottky contact structure is to allow using high depletion voltage, facilitating the complete charge collection of carriers, particularly the holes. Combined with long shapers, this key advantage helps getting rid of the charge loss correction implemented in ISGRI, technique that I extensively studied during my PhD.
- Infocus and HEFT, some precursors of NuStar, were already showing spectacular results on fine pitch design using CZT crystals.

At that time, we did not have yet any spectroscopic results to show up but we were able to define from that work the requirements of our own development. I came up with the idea of building a Schottky CdTe fine pitch modular unit, inspired from all the development illustrated in the paper, inheriting from the modular design if the ISGRI basic detector named Polycell.

The resulting paper published in Nuclear Instruments and Methods in Physics Research Section A is copied in the next pages.

Since that time, I have been proposed to joint the Local Organizing Committee of the conference and I am now the president of this event that occurs every three years.

New trends in CdTe and CdZnTe detectors for X- and gamma-ray applications

O. Limousin*

CEA/DSM/DAPNIA Service d'Astrophysique, CEA/Saclay, Gif-sur-Yvette Cedex 91191, France

Abstract

The CdTe gamma-ray camera IBIS/ISGRI, on board the *INTEGRAL* satellite launched in October 2002, is currently the largest spectro-imager of this type in the world. The development of this detector, for research in the field of astrophysics, has provided the opportunity to demonstrate the feasibility of massive integration of CdTe nuclear detectors, taking advantage of the CdTe good spectral performances and high modularity. Many other groups in the world work also to further develop detectors using this material in view of improving its spectral performances (crystal quality, electrode geometry and type, electronics and filtering, etc.), the spatial resolution (pixelization of monolithic crystals) and the detection efficiency at high energy (thickness). In this review, I will detail the main directions in which to strive in order to explore these fields in the upcoming years through examples of techniques or applications.
© 2003 Elsevier Science B.V. All rights reserved.

Keywords: CdTe; CdZnTe; Bulk detectors; Pixel arrays

1. Introduction

In the field of X- and gamma-ray detection applications, many materials have been studied to invent detectors combining high stopping power, good spectral performances and imaging capabilities. Inorganic scintillators coupled to photodiodes or photomultiplier tubes often offer high stopping power, thanks to large size, high Z and high-density available crystals. However, they give rather poor energy resolution. On the other hand, semiconductor devices like silicon (Si) or germanium (Ge) lead to excellent energy resolution. However, Si offers a low stopping power for high-energy photons, limiting its use to low energy. On

the other hand, the small band-gap of germanium requires operations of the detectors at cryogenic temperatures. For these reasons, semiconductors with high atomic numbers, high density and wide band-gap have been developed since the early 1970s. Cadmium telluride (CdTe) and cadmium zinc telluride (CdZnTe) are two of these materials that offer the opportunity to achieve excellent spectral and spatial resolution for compact hard X- and gamma-ray detection systems operating without cryogenics. Since the 1990s, the progresses in the technology of manufacturing high-quality single crystals of CdTe and CdZnTe (size, stability and reproducibility) have changed the situation in many fields of application, mainly in medical imaging and high-energy astronomy, by using room temperature detectors with a good energy resolution bounded by scintillators and cooled

*Tel.: +33-1-69-08-62-94; fax: +33-1-69-08-65-77.
E-mail address: limousin@cea.fr (O. Limousin).

germanium spectral performances. I will present in this paper some examples of detectors that appear to me especially promising.

1.1. General properties of CdTe/CdZnTe

Thanks to relatively high atomic numbers ($Z_{Cd} = 48, Z_{Te} = 52$), which give a dominant photoelectric absorption probability up to 300 keV against Compton scattering interaction process (Fig. 1), and thanks to a high density ($\sim 6\,g\,cm^{-3}$), which gives a good stopping power, CdTe shows high quantum efficiency suitable for detection of photons in the typical range of 10 to 500 keV. Furthermore, its wide band-gap leads to a very high resistivity (10^9–$10^{11}\,\Omega\,cm$) and allows operations at room temperature. By comparison with silicon or germanium data (see Table 1), it is clear that CdTe has a privileged position. Finally, the intrinsic spectral resolution, simply taking into account statistical fluctuations of electron–hole pair creation, compares well with that of germanium. This makes CdTe a very promising material since manufacturing difficulties and signal processing problems are overcome. Current manufacturing technologies of CdTe and CdZnTe allow working with crystal volumes up to 1 or 2 cm^3 (CdTe crystals are available in sizes larger than those of CdZnTe). These crystals are thick enough to operate efficiently in the MeV region (cf. Fig. 2). I will present a few detectors involving such large crystals in the following sections.

1.2. CdTe versus CdZnTe

There are two main families of cadmium telluride detectors: CdZnTe grown by *High Pressure Bridgman* technique [2] and CdTe grown by the *Traveling Heater Method* [3]. Basically, the choice depends on the design of the application. We have to consider concurrently the size of the application (number of crystals, individual detector element volume, cost, reproducibility, homogeneity, etc.), and the expected spectral performances. As a general rule, due to the manufacturing process [4], CdTe is easier to produce in large quantities than CdZnTe. Large size CdTe crystals up to 50 mm wafers diameter,
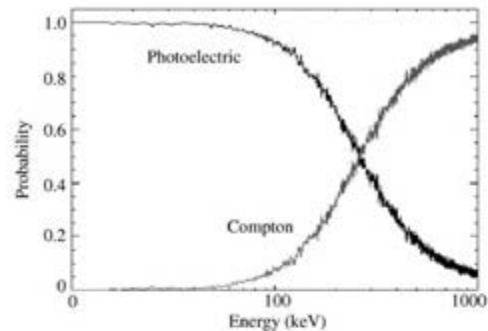

Fig. 1. Probability of interaction type in CdTe as a function of the incident photon energy (Monte Carlo simulation).

Table 1

Comparison of intrinsic physical properties of some semiconductor nuclear detectors. E_{gap} band-gap energy, ε ionization potential, $\Delta E_{intrinsic}$ intrinsic resolution due to statistical fluctuations of electron–hole pair creation at 100 keV

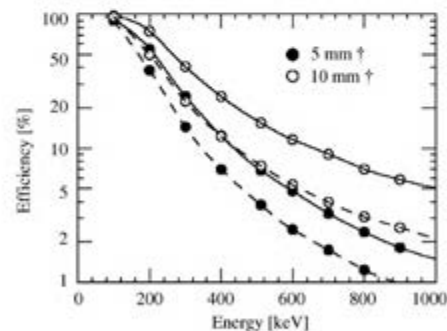| Semiconductor	Density (g cm^{-3})	Atomic number	E_{gap} (eV)	ε (eV/pair)	$\Delta E_{intrinsic}$ (eV) at 100 keV
Si	2.33	14	1.12	3.6	450
Ge	5.33	32	0.67	2.9	400
CdTe	5.85	48, 52	1.44	4.43	700
CdZnTe	5.81	48, 52	1.6	4.6	620

Fig. 2. Detection efficiency of CdTe at different energies for a thickness of 5 mm (closed circles) and 10 mm (open circles). Dashed line: Photoelectric only. Solid line: Photoelectric and multiple Compton scattering included. Simulation of a collimated gamma-ray beam at the center of a 1 cm × 1 cm surface detector from Takahashi et al. [1].

without grain boundaries, are available with good reproducibility and homogeneity. This contributes to make CdTe cheaper. On the other hand, CdZnTe offers a higher resistivity than CdTe due to the widening of the band-gap in the presence of Zn in the lattice. This makes the dark current value very low at room temperature. As shown in Table 2, electron transport properties are often better in CdZnTe than in CdTe, which is favorable in a single carrier detector design as shown below. Hole properties are better in CdTe than in CdZnTe but in both cases, electrons are much faster than holes. This causes an incomplete charge collection (physical trapping and electronic ballistic deficit) depending on the interaction depth of the photons. The consequence on the spectral response is a tailing of the gamma-ray line peaks towards low energies. Spectral performances are mainly limited by the effect of the low transport of holes.

1.3. Signal induction in CdTe/CdZnTe

The signal induced after a photon interaction into a biased semiconductor is due to the generated charge motion through the sensitive volume, along the applied electric field lines. Charge carrier motion is sensed by capacitive coupling, so that the system geometry defines the charge influence repartition between electrodes. The famous Ramo's theorem formalizes a difference between the applied electric field (stationary regime) and the weighting field (transient regime due to charge injection) [5]. The applied field E is responsible for carrier velocity and trajectory while the weighting field E_W is used to calculate the induced charge Q_L on electrodes due to carrier motion. The instantaneous current due to the photo-generated carrier charge $q_0 = q(n + p)$ can be written as

$$I(t) = q(\mu_e n + \mu_h p)\vec{E} \cdot \vec{E_W}$$

where μ_e and μ_h are the charge carrier mobility of electrons and holes, respectively, q the electron electrical charge and n and p are electrons and holes concentrations, respectively. As long as charge carriers move of dx during dt towards electrodes in the crystal, they induce a charge dQ_L on the detector anode. The feedback capacitor of a charge sensitive preamplifier connected to the anode collects this charge (eventually through a coupling capacitor), which is the integral of the instantaneous current over the transit time of each carrier. It is a combination of each charge carrier stretch of path covered. The pulse rise-time depends on the slowest drift carrier, which depends on the penetration depth of the photon. When the transit time is long in comparison with the peaking time of the shaper amplifier, this leads to a ballistic deficit, i.e. an incomplete charge collection. For instance, in a 2 mm thick CdTe crystal biased under 100 V, the longest transit time for holes is $\sim 6\,\mu s$ (photon interaction close to the anode) while the fastest transit time for electrons is $\sim 500\,ns$ (photon interaction close to the cathode). For signal-to-noise considerations, if we use a 1 or $2\,\mu s$ peaking time, the ballistic deficit is around 70% of the full signal at 100 keV for the deepest interactions. On the other hand, as significant physical charge trapping occurs in CdTe, mainly for holes, n and p are not constant in time. Thus the total collected charge at the anode dQ_L depends on the interaction depth too.

$$n = n_0 \exp\left(\frac{-t}{\tau_e}\right) = n_0 \exp\left(\frac{-(L-z)}{\mu_e \tau_e E}\right)$$

and

$$p = p_0 \exp\left(\frac{-t}{\tau_h}\right) = p_0 \exp\left(\frac{-z}{\mu_h \tau_h E}\right)$$

where L is the detector thickness, τ_e and τ_h are the electron and hole lifetime, z is the interaction depth, n_0 and p_0 are the initial amounts of photo-generated electrons and holes, respectively. For the same 2 mm thick CdTe crystal biased under 100 V,

Table 2
Typical values for charge transport properties and resistivity of CdTe and CdZnTe. μ is the mobility and τ the charge carrier lifetime. ρ is the apparent resistivity

Semiconductor	$(\mu\tau)_{electrons}$ $(cm^2\,V^{-1})$	$(\mu\tau)_{holes}$ $(cm^2\,V^{-1})$	Resistivity ρ $(\Omega\,cm)$
CdTe	$\sim (1-2) \times 10^3$	$\sim 1 \times 10^4$	$\sim 1 \times 10^9$
CdZnTe	$\sim (0.5-5) \times 10^3$	$\sim 1 \times 10^5$	$\sim (1-5) \times 10^{10}$

this leads to a maximum loss of 15% of the full photo-generated charge. The ballistic deficit in this example is the main contribution to the peak broadening at low energy, limiting the spectral resolution and the thickness of detectors. Almost all developments made with CdTe detectors consist in finding ways to get rid of the charge loss due to ballistic deficit spectral effects, either by applying corrections or discriminations for long rise-time pulses, or by modifying the weighting potential to try to induce the signal to the anode lately, which is equivalent to limiting the rise-time range.

2. (Bulk) pixel detectors

In this section, I will concentrate on applications involving bulk coplanar detectors. I emphasize the difference between segmented crystal arrays and arrays of pixels. I present below three approaches to improve the spectral performances: charge loss correction system, thin diodes and modified weighting potential systems.

2.1. CdTe charge loss correction systems

Charge loss correction devices are based on the principle of simultaneous pulse height and pulse rise-time measurements. The correlation between the two (cf. Fig. 3) allows computing a correction method in order to improve peak sensitivity [6 8]. It does not improve the spectral resolution but allows retrieving a symmetric line shape and improves drastically the peak efficiency, re-allocating each photon to its good energy position in the spectrum. This technique is applied to the *INTE-GRAL* Soft Gamma-ray Imager (ISGRI) on board *INTEGRAL* ESA's satellite and to the PEGASE medical gamma-ray camera.

2.1.1. ISGRI detectors

ISGRI is the first space instrument using good spectral resolution CdTe. ISGRI is made of 16384 CdTe THM grown, $4 \times 4 \times 2 \, \text{mm}^3$ [10,11], which represents a sensitive area of $2621 \, \text{cm}^2$. It is a hard X-ray spectro-imager mainly devoted to the detection and the precise measurement of celestial
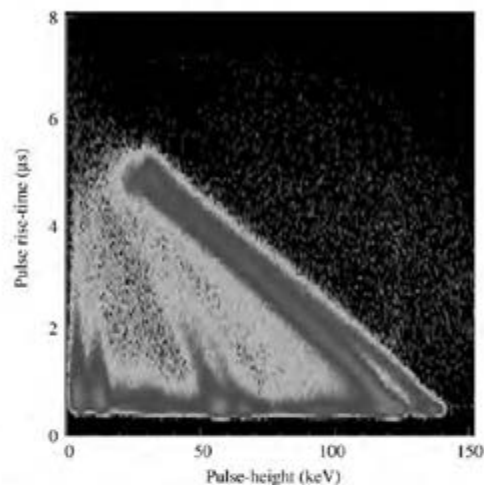
Fig. 3. Pulse rise-time vs. pulse height correlation obtained with a 2 mm thick CdTe detector biased under 100 V and irradiated with a collimated ^{57}Co source.

gamma-ray photons between 15 keV and 1 MeV. It will help studying violent processes involved near black holes, neutron stars or in supernovae for instance. This detector is the largest gamma-ray camera in the world at the moment and has illustrated the possibility to use a huge quantity of CdTe crystals in a space application. Each detector of ISGRI is read out by a four-channels ASIC dedicated to pulse height and rise-time measurements and hit pixels addressing. Fig. 4 illustrates the spectacular image quality obtained with 128×128 pixels array. The detector layer is shown on Fig. 5 where it appears in white. The pulse rise-time correction method applied to ISGRI leads to nice spectral performances (25% at 14.4 keV and 9% at 122 keV) and high narrow line sensitivity ($10^{-5} \, \text{photon s}^{-1} \, \text{cm}^{-2}$ for $10^6 \, \text{s}$ observation at 3σ). This corresponds to a peak-to-valley ratio improvement, thanks to the correction, by a factor of three at the left of a 122 keV ^{57}Co source line.

2.1.2. PEGASE medical gamma-camera

The gamma-ray medical imager PEGASE (Projet d'Etude de GAmma camera à Semi-conducteurs), developed by CEA/LETI [12], is devoted to
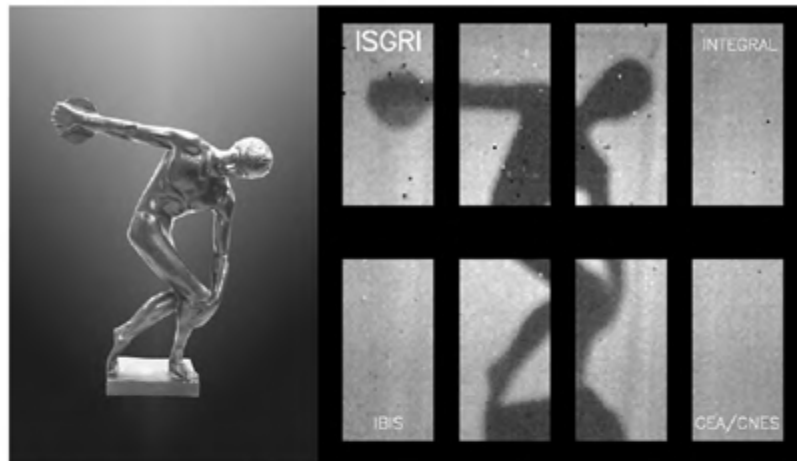
Fig. 4. Gammagraphy of a discobole statuette recorded by ISGRI detector array during test in CEA-Saclay.
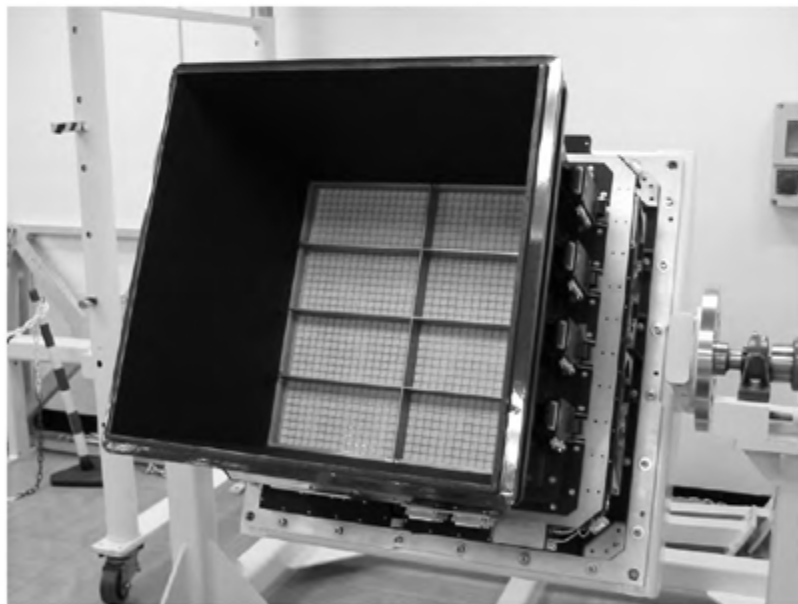

Fig. 5. Photograph of the IBIS telescope equipped with ISGRI (white detector layer in the foreground).

nuclear medicine. The aim of the project is to overcome the fundamental spatial and spectral limitations of medical Anger-cameras by using semiconductors instead of scintillator crystals. In addition, the use of semiconductors also offers other advantages including improved system count

rate performances, compactness, light weight, live edges, and the flexibility to construct camera of various shapes. PEGASE is based on the same correction principle as the ISGRI array, but adapted to the electron charge losses in thick CdZnTe crystals. PEGASE (cf. Fig. 6) is made of 1920 CdZnTe crystals, $4 \times 4 \times 6 \, mm^3$, with poor hole transport properties so that their contribution to the signal is negligible. Only the electron signal is exploited measuring simultaneously pulse height and pulse rise-time. The measurement is operated by a 16 channels front-end electronics including an ASIC. The camera is designed to work at the ^{99m}Tc line (140 keV) with a maximum efficiency. The spectral resolution of the camera is close to 9% at 140 keV.

2.2. High-resolution Schottky In–CdTe–Pt detectors

Since CdTe spectral performances are limited by the ballistic deficit due to poor hole transport properties, one possibility to increase the energy resolution is to accelerate charge carriers inside the detector. Thus, the transit time of carrier is reduced and can become shorter than the currently used shaping time of spectroscopic amplifiers. To accelerate charge carriers, it is necessary to increase the applied electric field inside the crystal. In order to avoid an excessive rise of the dark current, the basic idea is to use indium as the anode electrode on the Te-face of a p-CdTe wafer with $(1, 1, 1)$ orientation [13–15]. In this case, a high Schottky barrier is formed on the In/CdTe interface which limits the dark current value to 0.7 nA with a bias voltage of 400 V at 20°C for a $2 \times 2 \times 0.5 \, mm^3$ detector. The transit time of holes in this configuration is ~100 ns. The residual widening of peaks in this case is only due to the modest charge trapping and no ballistic deficit occurs. The spectrum shown on Fig. 7 illustrates the very high energy resolution achievable in such a device (830 eV FWHM at 60 keV for a diode biased under 1400 V at −40°C). These are extreme conditions but the same device currently gives 1.5 keV FWHM at 60 keV for 400 V bias voltage at 20°C.
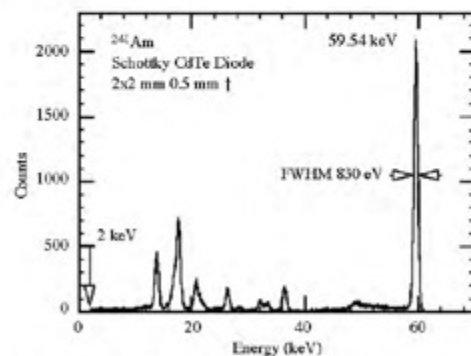

Fig. 6. Photograph of the PEGASE medical imager. Top: PEGASE 6mm thick CdZnTe assembly. Bottom: PEGASE module ready to receive the 1920 pixels array.

Fig. 7. ^{241}Am spectrum obtained with a Schottky CdTe diode $2 \, mm \times 2 \, mm \times 0.5 \, mm$ thick biased under 1400 V at −40°C. A resolution of 830 eV (FWHM) has been measured at 60 keV with a shaping amplifier time constant of 2 μs.

The main difficulties encountered using Schottky CdTe diodes are due to the polarization effects [16] (reduction of the sensitive volume as time is running) and the limited thickness of the device (necessary condition to maintain short transit time and small ballistic deficit). The first problem is overcome by pushing up the bias voltage and lowering the temperature to slow down the polarization process. The second is overcome using stacked detectors in order to increase the efficiency (edge-on geometry) [17].

Finally, as the transit time of charge carriers in thin Schottky devices becomes very short for sufficiently high bias voltage, we can envisage high timing-resolution applications, which could not be considered up to now. A 5.8 ns FWHM timing-resolution with $2 \times 2 \times 0.5\,mm^3$ Schottky diode has been reported [18]. Thanks to these results, the way opens to medical Positron Electron-Tomography applications, based on the coincident detection of back-to-back 511 keV gamma rays emitted after positron electron annihilation in a patient.

2.3. Modifying the weighting potential

As mentioned before, one way to get rid of the ballistic deficit is to induce the signal lately by modifying the weighting potential. In this section, I show three kinds of detector geometry based on this principle. According to their design, these devices act like single carrier charge collection detectors, ignoring the hole contribution to the signal.

2.3.1. eV_Products CAPture technique

Recently, eV-Products Company have commercialized a two asymmetric-electrodes device called *CAPture* [19], which can be classified as a hemispherical detector. This detector is based on the weakening of both applied and weighting fields near the cathode in order to homogenize pulse shapes induced at the anode. This is done by extending the cathode electrodes on the lateral faces of the device. The weighting potential inside the *CAPture* system distribution is represented in Fig. 8. The height of the lateral screening cannot be too high to avoid dead zones near the cathode.
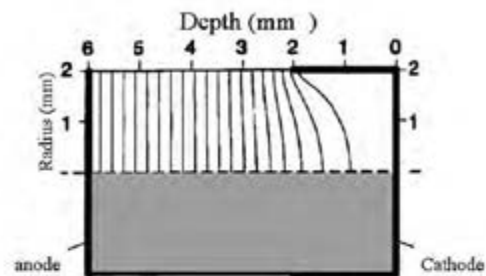

Fig. 8. Weighting potential profile in eV-Product CAPture device. Diagram from Ref. [9].

This detector works fine at low energies where interactions occur near the cathode. At higher energies, when energy deposits are distributed in the entire volume of the crystal, the device almost acts like a coplanar detector and leads to residual tailing of gamma-ray lines. Good performances have been demonstrated with a $5 \times 5 \times 5\,mm^3$ detector. Significant reduction of low energy tailing has been reached and the measured spectral resolutions were <3 keV FWHM at 60 keV, <5 keV FWHM at 122 keV and <13 keV FWHM at 662 keV.

2.3.2. CZT coplanar-grid device

Among all the techniques invented to circumvent energy resolution and low efficiency problems in CdTe/CdZnTe, some are based on the use of the effect of the Frisch grid used in gas and liquid detectors. The coplanar-grid technique [20] consists of a detector anode equipped with a pair of interleaved grid electrodes (shown in Fig. 9) and a full area electrode on the cathode side. A negative high voltage is applied on the full-area in such a manner that the grid electrodes collect electrons generated in the crystal. A separate smaller bias voltage is applied across the two interleaved grids so that the electron signal is induced lately only on the grid with the highest potential. Signals from the two grids are processed independently with two charge sensitive preamplifiers and subtracted one from the other, removing the hole depth-dependent component of the induced signal. The coplanar-grid detector is a single charge carrier device. Fig. 10 shows the assembly of a 1 cm³

CdZnTe crystal equipped with coplanar-grid electrodes, connected to its readout electronics for an application in environmental control. This
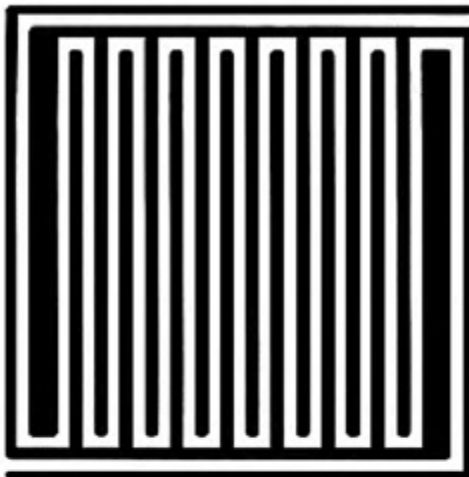

Fig. 9. Electrode pattern of the CZT coplanar-grid device [20].

detector gives very spectacular spectra like the one shown in Fig. 11, where a resolution of 13.9 keV FWHM at 662 keV has been measured. The line shape is almost symmetrical and the tiny residual tailing only results from the material quality.

2.3.3. Capacitive Frisch grid structure

We have seen previously that the modification of the weighting potential can lead to good spectral performances in CdZnTe, even for thick detectors. But on the one hand, the applied field is modified and the screening effect is limited to a small portion of the detector (cf. *CAPture* design) and on the other hand, the anode electrode is quite complex and two readout channels per crystal are needed (coplanar-grid structure). Recently, the new concept of *Capacitive Frisch Grid Structure* has been presented [9,21]. The device is based on a coplanar CdZnTe detector with two standard electrodes. The lateral faces are surrounded with a metal screen, which is isolated from the crystal by a thin dielectric film. The metal screen is connected to the cathode. Therefore, the applied electric field is not modified while the transient
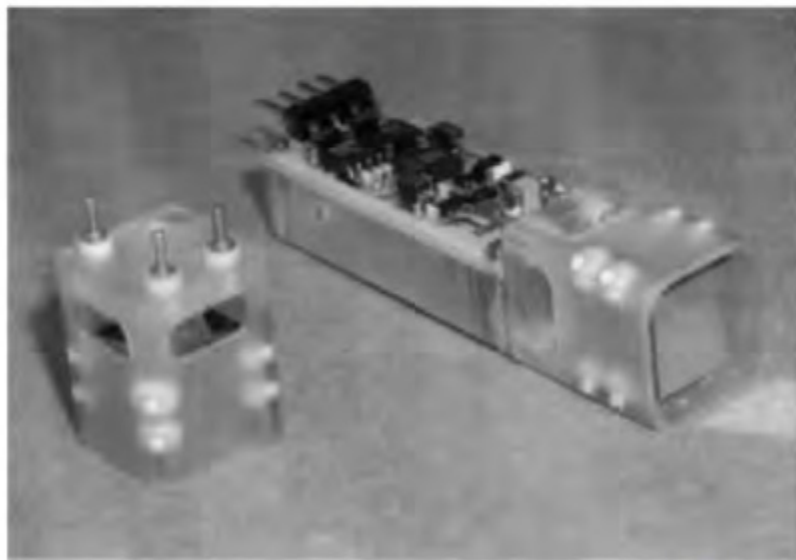
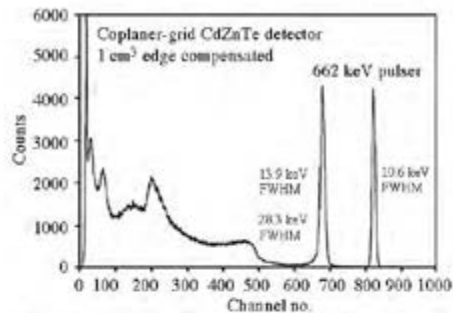Fig. 10. One cm^3 CZT coplanar-grid device coupled to its readout electronics [20].

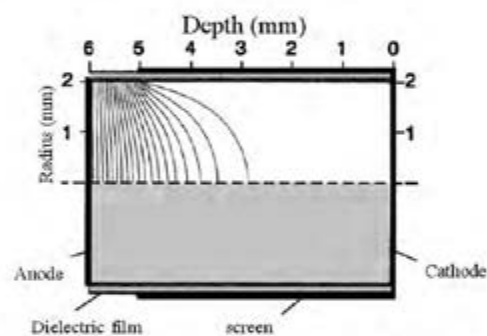Fig. 11. ^{137}Cs spectrum recorded with a CZT coplanar-grid device [20].

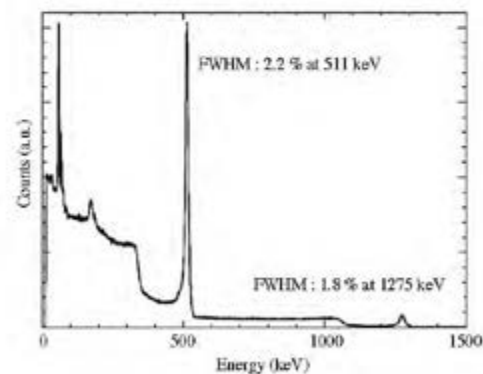Fig. 12. Weighting potential profile in a capacitive electrode device. Diagram from Ref. [9].

Fig. 13. ^{22}Na spectrum recorded with a 6 mm thick CZT Capacitive Frisch Grid Structure at 21°C, 400 V.

behavior of the detector changes through the new weighting field distribution (cf. Fig. 12). Moreover, the isolated lateral metal screen can be placed very high, and thanks to this design, the hole-tailing phenomenon is considerably reduced. Very promising performances have been obtained: 2.2% at 511 keV and 1.8% at 1275 keV (Fig. 13). Theoretically, this principle can be used with very thick detectors. Spectral performances will be limited by the charge transport uniformity in the bulk and the applied electric field distribution. Optimizing the screen geometry, a 1% resolution at 662 keV is expected in the near future.

3. Pixel arrays

Nuclear medicine, astrophysics and other fields need semiconductors detectors based on CdTe and CdZnTe compounds to become real direct spectro-imaging systems with both high spatial resolution and high energy resolution. Current technologies allow the use of large single crystals ($\sim 1\,cm^3$) with small segmented-electrodes realized by photolithography processes inherited from microelectronics technologies. The electrodes are connected to the readout chip by indium bump bonding. According to the application, either the spectral resolution or the spatial resolution can be emphasized. For instance, in medicine application *Medipix-2* [22,23], spatial resolution is challenging (55 μm pixel size) and spectral resolution (photon counter) is not mandatory. On the other hand, the two following application examples in astrophysics illustrate both simultaneous needs of spatial and energy resolution. At the end of the section, I will briefly explain why such devices can lead to excellent spectral performances and what are the new trends in CdTe/CdZnTe pixel arrays field, especially for thick sensors.

3.1. Fine pixel arrays: InFOCμS example

InFOCμS [24] is a balloon-borne instrument incorporating recent breakthroughs in focusing optics and detectors to achieve orders of magnitude improvements in both hard X-ray sensitivity ($\sim 100\,\mu$Crabs in 12 h) and imaging resolution

Fig. 14. Compact hybrid package CdZnTe/ASIC for the InFOCµS experiment. Gold coplanar contact on the cathode of the detector is visible on top with wire attached. The readout ASIC is underneath the detector [25].

($\sim$1 arcmin), with high resolution spectroscopy ($\sim$2 keV FWHM). This focussing telescope is working in two energy bands (20–40 and 65–80 keV) thanks to an X-ray grazing incidence mirror system placed 8 m from the focal plane. The focal plane is made of an assembly of four fine pixels CdZnTe arrays. Each one is a $26.9 \times 26.9 \times 2$ mm^3 detector equipped with 330 µm^2 pixel size anodes (4096 pixels) and a wide guard ring surrounding all the pixels (Fig. 14). These detectors are the largest devices ever made with this material at this time. Each channel is indium bumped and read out by a 64×64 channels ASIC that reaches a spectral resolution close to 2.3 keV FWHM at 22.1 keV as shown in Fig. 15. Each CdZnTe is embedded in an anticoincidence shield in order to reduce the background and therefore to optimize the instrument sensitivity. We have to mention that the background is also reduced thanks to a data analysis system, which is able to reject events depending on

their penetration depth into the material. This spectacular detector illustrates the possibility of using high pixel density CdZnTe arrays for applications with both spectroscopic and imaging high performances.

3.2. Medium size pixel arrays: HEFT example

In some applications, very small pixel sizes are not mandatory to reach scientific objectives. Nevertheless, spectral performances can constitute a priority. This is the case in the *High Energy Focusing Telescope* (HEFT) example proposed here. Once again, this example is taken from the CdTe/CdZnTe development for astrophysics instruments.

HEFT [26–28] is a hard X-ray telescope, which uses the focusing imaging technique with multilayer coatings mirrors. HEFT requires position-sensitive hard X-ray detectors (20–100 keV) with less than 1 mm spatial resolution, and good energy resolution. A room-temperature solid-state
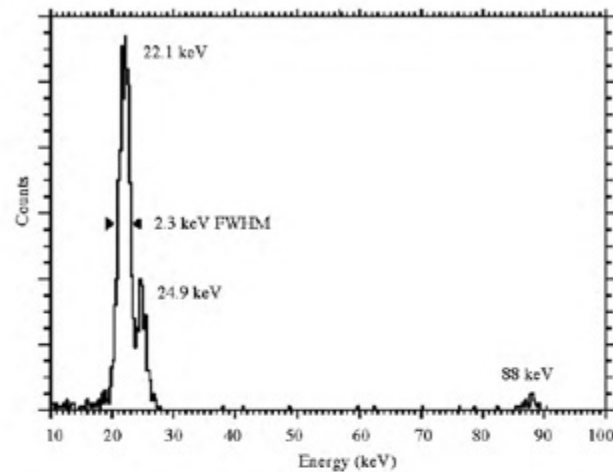
34   *O. Limousin / Nuclear Instruments and Methods in Physics Research A 504 (2003) 24–37*

Fig. 15. InFOCμS 1 pixel spectrum of ^{109}Cd source. The detector was biased at 200 V and cooled to 0°C [24].
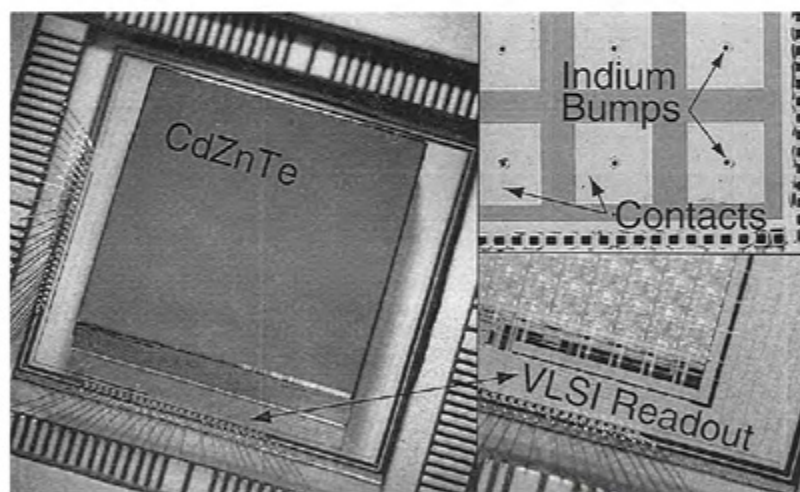

Fig. 16. Pixel array of the HEFT focal plane [29].

CdZnTe pixel detector has been chosen. The CdZnTe sensor has one monolithic contact, with the other (anode) segmented into pixels. Each pixel contact is indium bump bonded to a custom readout chip, with one complete pulse processing chain for each pixel. Fig. 16 shows the HEFT 8×8 pixels prototype detector: 600 μm pixel size, 680×650 μm pixel pitch, $8 \times 7 \times 2$ mm^3 single
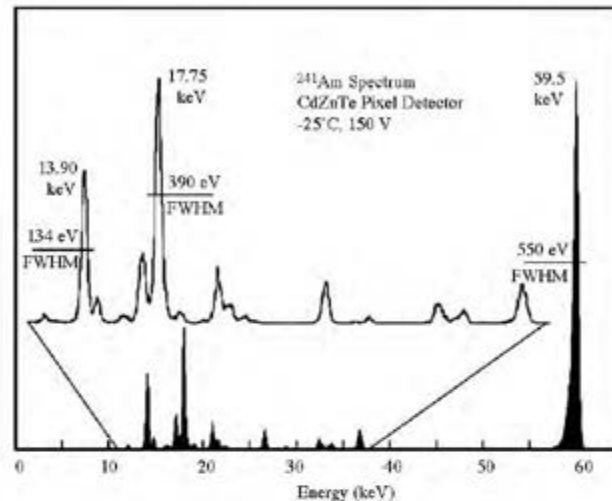
Fig. 17. HEFT Pixel performances [29].

crystal [29,30]. Excellent spectral performances have been demonstrated with this detector set-up including its very low noise front-end electronics (<40 electrons RMS [27]) as shown in Fig. 17, where 550 eV FWHM at 60 keV ^{241}Am line have been measured at −25°C (and 780 eV FWHM at 60 keV at +18°C).

3.3. Small pixel effect and thick pixel arrays

As demonstrated before, pixel arrays of rather large dimensions, equipped with small pixel size patterns are capable of impressive spectral performances. The segmented anode pattern is well adapted to charge collection in CdTe/CdZnTe. Actually, in segmented detectors, contrary to "bulk" detectors, the induced charge no longer only depends on the distance that carriers travel (penetration depth), but also on their proximity to the sensing electrode (anode) [31–33]. This is the "near field effect" (or "small pixel effect") and it can be exploited to define segmented anode geometry with small pixel in order to distribute the weighting potential close to the anode. This helps to remove the hole contribution to the signal. When a charge packet is generated in such a device, it induces a surface charge on any nearby

electrode. As the packet drifts along the applied electric field lines, the influence of carriers motion is equally distributed on every pixel until the packet moves very close to the one in front of it, where the weighting potential is strong. When charge carriers move within a hemispherical region around the pixel, approximately of the size of the lateral pixel size, a strong signal formation occurs in the pixel electrode. This small pixel geometry is good for signal formation because the signal is induced lately and no ballistic deficit takes place. The device works like a single carrier detector if the pixel size is less than a quarter of the detector thickness. On the other hand, the benefit of very fine pixel size is that the total crystal dark current and capacitance is shared over many channels and very low noise can be achieved.

For once, the "near field effect" encourages to use small pixel and thick detectors conjointly, i.e. to use high spectral and spatial resolution on high efficiency detectors.

One example of a thick segmented detector has been demonstrated with large size pixels (2×2 mm^2) implemented on an $8.4 \times 8.4 \times 5$ mm^3 CdZnTe crystal [34]. This device allowed obtaining 1% to 1.5% FWHM energy resolution for the 356 keV line of a ^{133}Ba source at room tempera-

Fig. 18. 6 mm thick CZT array manufactured by eV-Products [photo from CEA-Saclay].

ture, combining the response of the 16 pixels. The best resolution is achieved by applying a specific off-line correction method to the measured data.

Another astrophysical application involving a focusing telescope sensor is under development in CEA/Saclay and is based on the "near field effect" in CdZnTe. We plan to study thick pixel arrays (6 mm at least) with pixel size less than 1 mm surrounded by a guard ring. Our aim is to reach 1% resolution at 662 keV, based on the crystal selection, custom electronics design and segmented geometry. Fig. 18 shows a $10 \times 10 \times 6 \, \text{mm}^3$ prototype of a thick segmented array manufactured by eV-Products. This type of detector will combine high spectral performances, high spatial resolution and high efficiency simultaneously. This is a new trend for CdTe/CdZnTe semiconductor detector developments.

4. Conclusion

Thanks to CdTe and CdZnTe material, it is now possible to dream of high spectral performances for nuclear spectroscopy, high spatial resolution for imaging and high efficiency for high-energy photon detection. These three aspects can be considered simultaneously in the same application. This is due to major improvements in material growth, tests and selection of high quality crystals. It is also due to the better understanding of the charge collection processes that have limited the spectral response until today. Of course, nothing would be conceivable without the major progresses made in ultra low noise microelectronics developments related to the CdTe/CdZnTe research field.

I have shown in this article many different kinds of detectors that appeared to me particularly promising. I retain, in the "bulk" pixel category, the very promising *Capacitive Frisch Grid Structure*, which has already shown high performances with thick devices (2.2% FWHM at 511 keV), up to 6 mm for the moment. It is a brand new technique based on a simple design that exploits the pure charge induction process on electrodes. It will probably progress a lot in the next few years (capacitive electrode optimization and weighting

potential engineering, detector thickness, etc.). This device opens the door for real room temperature spectrometric applications up to the MeV region and above. In the pixel arrays category, I retain the idea of using very thick detectors with a high pixel density on the segmented anode. For once, the natural distribution of the weighting potential in such devices, reinforced close to the anode pixels, is favorable for nuclear spectroscopy and allows approaching intrinsic performances of CdTe and CdZnTe, not so far from cooled germanium ones, but adding imaging capabilities. This is a real new trend, notably in the astrophysics field.

References

[1] T. Takahashi, S. Watanabe, IEEE Trans. Nucl. Sci. 48 (4,1) (2001) 950.

[2] J.E. Toney, et al., Nucl. Instr. and Meth. A 428 (1999) 14.

[3] M. Funaki, et al., Nucl. Instr. and Meth. A 436 (1999) 120.

[4] P. Fougeres, et al., Nucl. Instr. and Meth. A 428 (1999) 38.

[5] Z. He, Nucl. Instr. and Meth. A 463 (2001) 250.

[6] F. Lebrun, et al., Nucl. Instr. and Meth. A 380 (1996) 380.

[7] Ph. DeAntoni, F. Lebrun, J-P. Leray, French Patent: #95 10670 (1995).

[8] O. Limousin, et al., Nucl. Instr. and Meth. A 442 (2000) 244.

[9] G. Montemont, Thesis Université J.Fourier, Grenoble, 2000.

[10] O. Limousin, et al., Nucl. Instr. and Meth. A 471 (2001) 174.

[11] F. Lebrun, Proceedings of SPIE Conference Astronomical Telescopes and Instrumentation 2002, Hawaii, 2002.

[12] C. Mestais, et al., Nucl. Instr. and Meth. A 458 (2001) 62.

[13] T. Takahashi, et al., IEEE Trans. Nucl. Sci. 49 (3,2) (2002) 1297.

[14] T. Takahashi, et al., Nucl. Instr. and Meth. A 436 (2000) 111.

[15] C. Matsumoto, et al., IEEE Trans. Nucl. Sci. NS45 (1998) 428.

[16] R.O. Bell, et al., Nucl. Instr. and Meth. A 117 (1974) 267.

[17] S. Watanabe, et al., IEEE Trans. Nucl. Sci. 49 (3,2) (2002) 1292.

[18] Y. Okada, et al., IEEE Trans. Nucl. Sci. 49 (4,1) (2002) 1986.

[19] K.B. Parnham, et al., SPIE 3768 (1999) 49.

[20] P.N. Luke, et al., Nucl. Instr. and Meth. A 458 (2001) 319.

[21] G. Montemont, et al., IEEE Trans. Nucl. Sci. NS48 (3,1) (2001) 278.

[22] S.R. Amendolia, et al., Nucl. Instr. and Meth. A 422 (1999) 201.

[23] http://www.nikhef.nl/pub/experiments/atlas/pixel/Medipix/.

[24] http://infocus.gsfc.nasa.gov.

[25] C.M. Stahle, et al., Nucl. Instr. and Meth. A 436 (1999) 138.

[26] http://www.srl.caltech.edu/HEFT/results.html.

[27] B.D. Ramsey, Proceedings of the 12th International Workshop on Room Temperature Semiconductor X- and Gamma-Ray Detectors, 2001.

[28] W.R. Cook, et al., IEEE Trans. Nucl. Sci. NS47 (4) (2000) 1454.

[29] A.E. Bolotnikov, et al., Nucl. Instr. and Meth. A 458 (2001) 585.

[30] C.M. Hubert Chen, et al., IEEE Trans. Nucl. Sci. NS49 (1) (2002) 270.

[31] J.D. Eskin, H.H. Barrett, H.B. Barber, J. Appl. Phys. 85 (2) (1999) 647.

[32] Y. Nemirovsky, M. Ifraimov, A. Ludwig, J. Appl. Phys. 88 (9) (2000) 5388.

[33] M.R. Squillante, et al., Nucl. Instr. and Meth. A 458 (2001) 288.

[34] A. Shor, Y. Eisen, I. Mardor, Nucl. Instr. and Meth. A 458 (2001) 47.

Erratum

Erratum to "New trends in CdTe and CdZnTe detectors for X- and gamma-ray applications" [Nucl. Instr. and Meth. A 504 (2003) 24–37]☆,☆☆

O. Limousin*

CEA/DSM/DAPNIA Service d' Astrophysique, CEA/Saclay, Gif-sur-Yvette Cedex 91191, France

The publisher regrets some misprints in Table 2 of the above article. The correct Table 2 should read as follows:

Table 2
Typical values for charge transport properties and resistivity of CdTe and CdZnTe. μ is the mobility and τ the charge carrier lifetime. ρ is the apparent resistivity

Semi-conductor	$(\mu\tau)_{Electrons}$ (cm² V⁻¹)	$(\mu\tau)_{Holes}$ (cm² V⁻¹)	Resistivity ρ (Ω cm)
CdTe	$\sim(1-2) \times 10^{-3}$	$\sim 1 \times 10^{-4}$	$\sim 1 \times 10^{9}$
CdZnTe	$\sim(0.5-5) \times 10^{-3}$	$\sim 1 \times 10^{-5}$	$\sim(1-5) \times 10^{10}$

1.2. Trend update 13 years later

In the last decade, astronomical missions, namely Nustar (and its precursor Infocus Balloon experiment), SIMBOL-X (up to phase B) and ASTRO-H, pushed most of the high-performance CdTe detector developments in the world in terms of performance, both spatial and spectroscopic. In parallel, other teams have created advanced concept such as the CdTe Rutherford Appleton Lab team in UK who created the HEXITEC design.

In the following, I briefly describe the highest performance designs that compare well to our own development strategy and results, leaving intentionally many other promising developments in the world like the one proposed by the Medipix collaboration at CERN, INFN PISA team, DTU, XPAD team, Radiation Measurements Group at Univ. of Michigan and so many other key players:

- ASTRO-H is making use of a fine pitch configuration stack of silicon DSSD and Schottky DS-CdTe detectors in a double sided strip configuration on HXI, a hard X-ray imager using a 250 µm pitch pattern covering 32 mm large single crystal. The energy resolution of 2 keV FWHM at 60 keV has been obtained. Two HXI imagers are form part of ASTRO-H, illuminated by the HXR mirrors placed 12 meters away [3.8, 3.24 and 3.29]
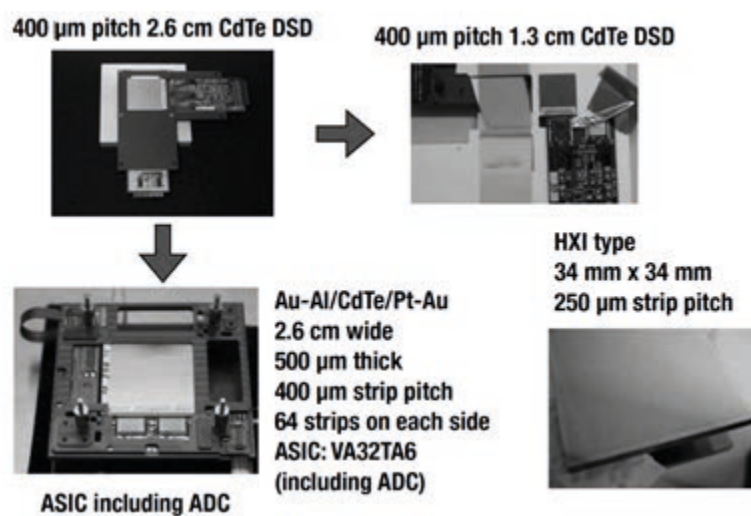

Figure 8. HXI prototypes from 400µm pitch to 250µm pitch strip CdTe detector readout with VATA ASICs.

- ASTRO-H is also using pixel CdTe detectors (In Schottky type, 3.2 mm pixel pitch) on the SGD (Soft Gamma Ray detector). SGD is a pair of large Compton gamma cameras. It offers a high sensitivity thanks to its intrinsic low background in addition to unprecedented polarization measurement capability. It demonstrates an energy resolution of 10 keV FWHM at 662 keV (compared to 26 keV for ISGRI at the same energy) [3.7].
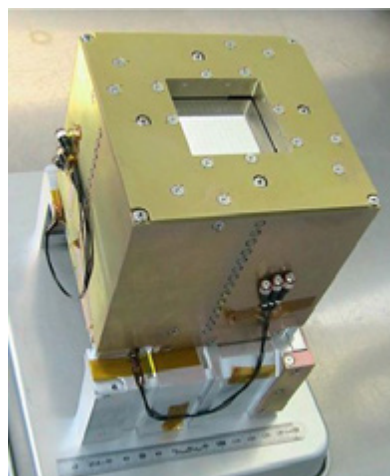

Figure 9. View of one of the six Compton camera of SGD. The bright front detector layer is one of the 32 Silicon pixel layers superimposed to 8 CdTe layers. A double stack of CdTe surrounds the stack as well.

- On board Nustar (NASA), a CZT array is placed at the focal plane of a 10 m long hard X-ray mirror. It consists of an assembly of four quadrants, buttable on 2 sides. Each quadrant is a hybrid made of 32x32 pixels of 600 µm pitch, the CZT being flip-chiped to a ultra-low noise readout ASIC. The energy resolution is measured in flight to be 400 eV at 6 keV and 900 eV at 60 keV. In my opinion, this development is certainly the most advanced worldwide. The detector is performing very well in space since 2012 [8.7 and 8.8].
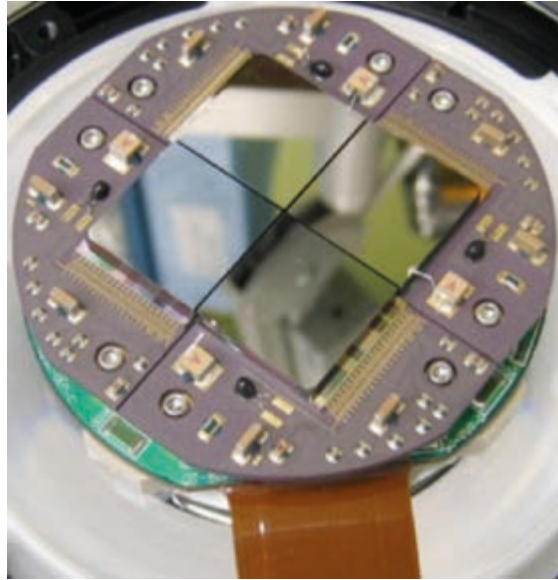

Figure 10. NuStar focal plane made of 4 modules of CZT flip-chiped onto the NuASIC with 605 µm pitch pixels.

- HEXITEC team in UK is also making use of pixel arrays with a 250 µm pitch in a hexagonal configuration. Similarly to NuStar, the CdTe detector is flip-chiped on top of an ultra low noise readout ASIC. The energy resolution has been found to be 1.6 keV FWHM at 60 keV over the 160,000 channels. It is important to note that the detector is readout by frames. Recently, the team achieved a mosaic of 10x10 cm^2 array for [8.9]. The team is now proposing a focal plane for Solar Physics at NASA [8.10].
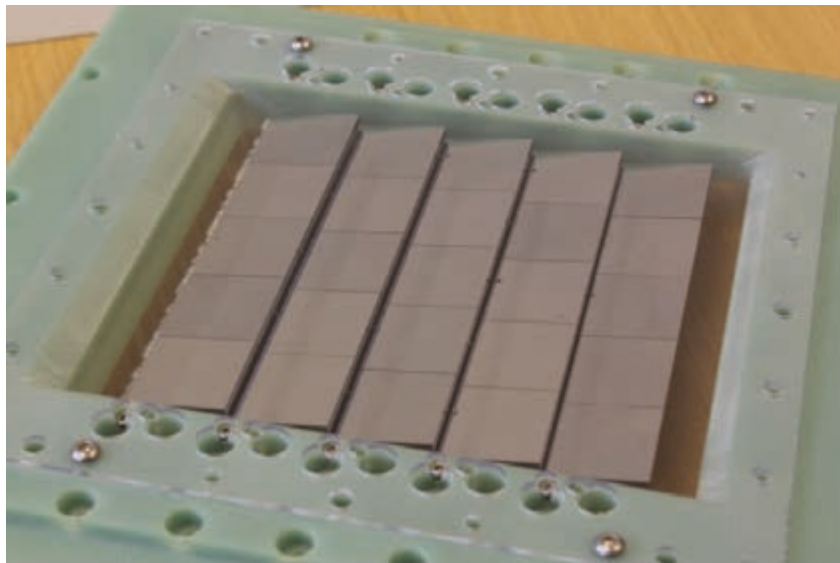

Figure 11. HEXITEC Configuration of 250 µm pitch buttable arrays in 10x10 cm^2 geometry.

2. Development strategy

The successful use of a very large amount of CdTe detectors in space with ISGRI was a strong motivation to further develop CdTe based space gamma camera at CEA.
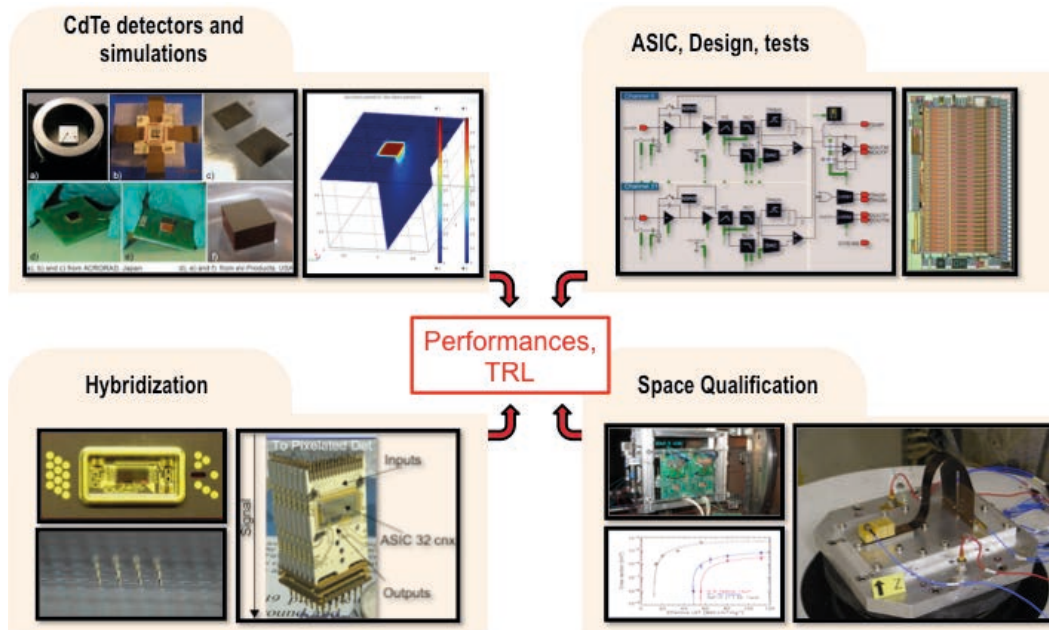

Figure 12. R&D strategy and axis of developments of detectors for space borne applications.

CdTe based detectors for astrophysics must obviously comply with current space manufacturing and reliability rules. For instance, from their conception, devices must be tolerant to radiation (dose and single events latch-up or upsets) and must survive the launch phase.

The new development of Caliste micro-gamma camera takes into account all these requirements simultaneously, from the early phases of developments, making sure process and materials are developed directly to fulfill demanding space qualification. This is the reason why simulation and experimental studies of detectors, microelectronics developments, packaging and hybridization as well as technological evaluations are performed in the frame of the R&D programs I lead, as shown in Figure 12.

5. Caliste, a new pixelated and high performance CdTe detector

1. Caliste basic concept

From the year 2004, an R&D program based on CdTe semiconductor detectors was set up in France by CEA-Irfu (Saclay, France) with the support of CNES (French national space agency) to build large focal planes for hard X-ray astronomy telescopes using focusing optics from 5 to 100 keV, with high spatial and spectral resolution. The performance of such arrays relies on the quality of the Cd(Zn)Te sensors, the noise performance of the front-end electronics and the hybridization technique that interconnects one to the other.

Several approaches have been considered worldwide to realize CdTe-based hybrid detectors with imaging spectroscopy capability as shown before for Nustar and ASTRO-H HXI.

The concept presented here is based on truly 3D integration technique. Caliste hybrid detectors have been thought as elementary modular units, buttable on their four sides to populate a mosaic focal plane. Thanks to that concept, the focal plane application can meet any shape of any size limited only by system resources.

The main drivers for the design of these devices are:
- The CdTe single crystal is 1 cm^2 to maximize the production yield and crystal uniformity;
- The front-end electronics is comprised of several one-dimensional ASICs placed perpendicularly to the CdTe pixel plane. This presents the advantage of a uniform and low stray capacitance at the ASIC inputs;
- The electrical interface is fully implemented underneath the right cylinder defined by the CdTe crystal surface. Such a way, the hybrid component is 4-side buttable.

Several generations of Caliste devices based on these statements were designed, produced and tested to reach step-by-step optimal performances [4.19, 4.20, 4.22, 3.37, 3.38 and 3.43]. In the next paragraphs, I describe the first prototype we issued in 2007: Caliste-64. This device hosts a square array of 64 pixels with 1mm pitch. Further, I will introduce a higher density prototype; Caliste-256 and I will refer and copy a paper I wrote in 2011 reporting on this innovative micro camera. This device closed the first phase of our R&D program with CEA and CNES. Behind that, I will show our most advanced version of Caliste, an improved version of Caliste-256 that we integrated into a prototype of focal plane: MACSI.

2. Pixelated CdTe detectors

2.1. CdTe properties
Despite our huge experience on CdTe with INTEGRAL, I revisited the different options to select the most appropriate sensing material for Caliste. Due to their high density (5.85) and high Z (50 on average), CdTe and $Cd_{0.1}Zn_{0.9}Te$ remain to be the unique mature candidates to meet our requirements for hard X-ray spectroscopy.

CdTe is a compound semiconductor material of type II-VI (with Cd in group II and Te in VI in Mendeleev's Periodic Table), having a mixed covalent and ionic bonding between Cd and Te. It has a Zinc Blend crystaline structure. CdTe shows a direct band-gap with an energy of 1.51 eV. Its electron-hole pair creation energy is ε = 4.42 eV/pair.

The CdTe crystals used in my research are produced by ACRORAD in Japan, which also provided the detectors for the ISGRI camera on the INTEGRAL satellite. The company developed a crystal growth technology based on the travelling heater method (THM) to produce single crystal ingots. ACRORAD can grow the world's largest CdTe crystals – 4-inch in diameter – with a high uniformity and excellent yield [8.11 and 8.12]. The production is based on the following pro-

cess: pure cadmium and tellurium are mixed and melted together to form a rough pre-synthesised ingot. This serves as starting material for the THM. The ingot is vertically injected into a heating zone where additional chlorine in the form of $CdCl_2$ is added to compensate for the Cd vacancies acting as acceptors sites and created during the process. These are however not completely compensated, keeping the material slightly of P-type. The compensation is adjusted to optimize both the resisitivity and the charge carrier's mobilities. After the THM process, the mix re-crystalises to form a highly resistive monolithic CdTe crystal with excellent purity.

During B. Dirks's PhD [8.13], we demonstrated that CdTe, equipped with Schottky contacts (In or Al), was still the most promising material for our purpose thanks to its excellent crystal quality, industrial availibility, and high production yield with procurement procedures compliant to space standards. Moreover CdTe is much cheaper than CZT, which in addition, is hard to procure in Europe, especially considering small quantities with only the very best quality.

Consequently, the detection materials used to design Caliste has always been based on CdTe in priority even if we experienced CZT as well. Our CdTe crystals are grown and processed by *Acrorad* (Japan). Our CZT samples were grown by the former *eV-Products* company in the US and patterned by *Brucker Baltic* in Latvia.

Main properties of CdTe and $Cd_{0.1}Zn_{0.9}Te$ are shown in Table 2. CdTe has a lower resistivity than $Cd0.1Zn_{0.9}Te$. However, CdTe crystals can be equipped with blocking contacts at the anode, from metals that have low work functions like indium, aluminum, or nickel. The use of blocking contact enables extremely low dark current, very competitive with the high resisitivity of CZT.

Metals, whose work functions are close to those of CdTe and CdZnTe, such as platinum or gold, are used to form quasi-ohmic contacts.
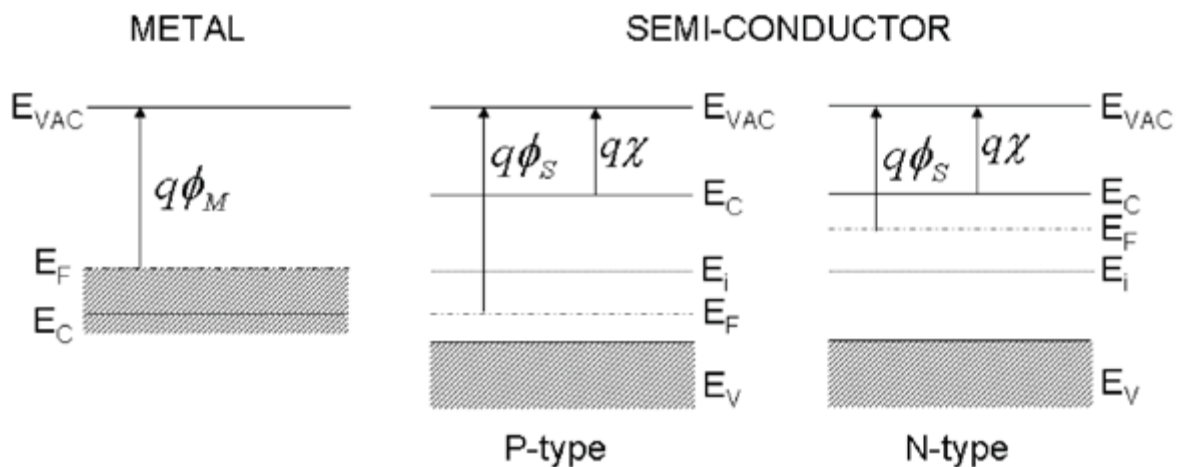

Figure 13. Band diagram of a metal and P- or N-type semiconductor (after B.P.F Dirks PhD thesis).

For a better understanding of the interface between metal and semiconductor, a schematic representation of the different energy bands at the contact is shown in Figure 13. The first figure represents the band diagrams for metal-P-type semiconductor junction. The energy difference between the vacuum and Fermi-level is defined as the work function: ϕ_M for a metal and ϕ_S for a semiconductor. Since the Fermi level in the semiconductor is dependent on the doping concentration it is more convenient to use the electron affinity χ, defined as the difference in energy between vacuum E_{VAC} and conduction band E_C.
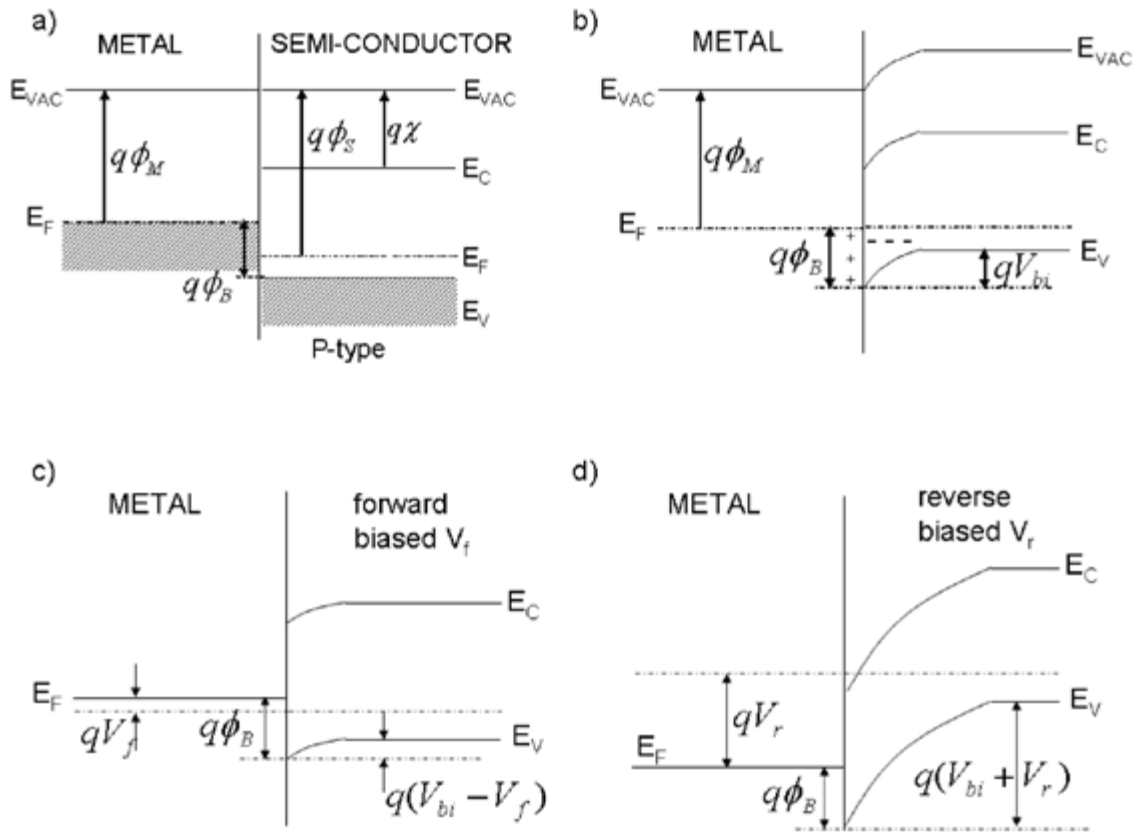
Figure 14. Band diagrams for a P-type semiconductor in contact with a metal. a/ The metal and the semiconductor are brought together – b/ thermodynamic equilibrium – c/Forward biased – d/ Reverse biased (after B.P.F Dirks PhD thesis).

Putting the metal and the semiconductor in contact, the different energy levels rearrange. Figure 15-a shows the situation directly after the connection and Figure 15-b a few moments later. At the thermodynamic equilibrium the Fermi levels of both materials align. This is achieved by the transport of charge carriers from one material to the other. In an N-type semiconductor the majority charge carriers are electrons. They will diffuse into the metal leaving behind a positive space charge near junction and creating a negative surface charge on the metal. In P-type materials, such as our CdTe, holes diffuse into the metal, leaving behind a negative space charge and creating a positive surface charge on the metal electrode. The space charge region is called the depletion zone and is free of carriers thus, highly resistive. Another consequence of the charge carrier diffusion is the appearance of an intrinsic voltage working against the diffusion and compensating it. The result is equilibrium between diffusion to the metal and the drift from the metal to the semiconductor. In a band diagram a bending of valence and conduction bands represents this effect. I show this effect for a P-type material in Figure 14.

The potential barrier, which appears between metal and semiconductor, has a height ϕ_B expressed as:

$$\phi_B = \frac{E_g}{q} + \chi - \phi_M \qquad \text{(Eq. 1)}$$

With E_g the band gap energy. The barrier is also known as a Schottky barrier. Charge carriers that would like to enter the semiconductor from the contact side see this barrier and first need to gain enough energy to pass it. This is possible by diffusion, thermal emission or quantum mechanical tunnelling through the barrier. Charge carriers, which exit the semiconductor toward the metal, see another potential wall, namely the built-in voltage ϕ_{bi} with a height of:

$$\phi_{bi} = \chi + \frac{E_C - E_{F,p}}{q} - \phi_M \qquad \text{(Eq. 2)}$$

By a applying an external voltage, the equilibrium is disturbed:
- A negative voltage increases the Fermi level in the metal, as shown in and Figure 14-c. The Schottky barrier, ϕ_B, remains unchanged while the built-in voltage ϕ_{bi} becomes smaller. More holes diffuse to the metal and the depletion region gets smaller. The junction biased in the forward direction.
- A positive voltage layer increases too and makes the junction more electrically isolating. The function is reverse Biased.

Table 2. CdTe and CZT material properties.

Semiconductor	Cd0.9Zn0.1Te [eV-Products]	CdTe (THM) [Acrorad]
Atomic numbers	48, 30, 52	48, 52
Density ρ (g/cm³) (300K)	5.78	5.85
Band gap Eg (eV) (300K)	1.57	1.51
Relative permittivity	10.9	10.3
Pair creation energy (eV/pair) (300K)	5	4.42
Resistivity (Ω.cm) (300K)	3.10^{10}	10^9
Electron mobility μe (cm²/V.s)	1350	950
Hole mobility μh (cm²/V.s)	120	73
Electron lifetime τ_e (s) (293K)	3×10^{-6}	1.2×10^{-6}
Hole lifetime τ_h (s) (293K)	1×10^{-6}	4.6×10^{-6}
Fano factor	0.14	0.2
Charge carrier concentration ni (cm⁻³) (300K)	2×10^5	6.9×10^5

A detector with a Schottky contact has several advantages:
- Operating the detector in reverse bias mode and applying a sufficiently high external voltage leads to a completely depleted detector region with high effective resistivity.
- Even at high voltages the leakage current stays low.
- Charge carriers created by radiation are quickly collected with little charge loss, even for holes.
- Low current means low noise.
- A strong electric field means quick charge collection and little ballistic deficit or charge loss.

Therefore a Schottky contact helps to reach very good energy resolution. The main drawback is that a CdTe- Schottky diode is unstable in time (cf. 4.5.2.4), especially if not sufficienlty cooled down.

Table 3 contains work functions values and theoretical Schottky barriers heights for several families of Cd(Zn)Te detectors, as well as typical dark current levels obtained in our laboratory by B. Dirks. Dark current was measured for each individual pixel of a 64-pixel array, 1 mm pitch, mounted on a substrate in our lab (see Figure 17-(b)). Current levels were measured with an accuracy of ~0.1 pA with Keithley 6517A ammeters.

Schottky CdTe detectors have the key advantage of showing a very low dark current at room temperature. Moreover, the dark current is distributed in each individual pixel and may reach values far below 10 pA at -15°C/200V for a 1 mm thick sample.

Table 3. CdTe and CZT contact properties and measured dark currents on 1 mm thick samples.

Detector	Supplier	Type	Semi-conductor work function	Metal work function	Theoretical Schottky barrier height	Typical dark current at 0°C, -200V/mm	Typical dark current at -15°C, -200V/mm
Au-Ni-Au//Cd$_{0.9}$Zn$_{0.1}$Te //Au	eV-products Bruker-Baltic	Ohmic n-type	4.4 eV	5.1 eV (Au)	0.5 eV	1.7 nA.cm^{-2}	0.5 nA.cm^{-2}
Pt//CdTe//Pt	Acrorad	Ohmic p-type	5.75 eV	5.35 eV (Pt)	-0.4 eV	125 nA.cm^{-2}	50 nA.cm^{-2}
In//CdTe//Pt	Acrorad	Diode p-type	5.75 eV	4.08 eV (In)	-1.67 eV	2.5 nA.cm^{-2}	1.0 nA.cm^{-2}
Al-Ti-Au //CdTe//Pt	Acrorad	Diode p-type	5.75 eV	4.28 eV (Al)	-1.47 eV	0.9 nA.cm^{-2}	0.3 nA.cm^{-2}

2.2. CdTe charge transport and signal induction, charge loss, charge sharing and small pixel effects

• Charge creation

When a photon hits the detector and interacts with it by photoelectric effect or Compton effect, an electron is ejected from a crystal atom and releases its energy by creating a number of electron-hole pairs in the semi-conductor. The number of pairs is proportional to the energy deposited by the impinging photon. The number of electron/hole pairs, N_0, created in the semicondcutor is simply propotional to the photon of energy E_γ:

$$N_0 = E_\gamma / \varepsilon \qquad \qquad \text{(Eq. 3)}$$

A photon of 59.54 keV coming from 241-Am source will therefore create about 14000 e–/h+ pairs in CdTe.

The number of electron-hole pairs created by the interaction of a photon with the semiconductor is statistically fluctuating because of the discrete character of the charge carriers. This process is approximated by a modified Poisson statistics named Fano limit. While Poisson proposes the number of created charge to spread with a deviation of $\sqrt{N_0}$, in reality the electrical charges are not strictly independent from one to the other. Therfore, the deviation is corrected to $\sqrt{F \cdot N_0}$, where is the Fano factor. A typical value for F in a semiconductor is close to 0.10 and in the case of CdTe, a value of 0.15 is expected.

Consequentlly the energy resolution (FWHM) of a perfect semiconductor detector chain, assuming no electronic noise at all, is limited to:

$$R_{\text{Stat}} = 2.35 \cdot \varepsilon \cdot \sqrt{E_\gamma \cdot F / \varepsilon} = 2.35 \cdot \sqrt{E_\gamma \cdot F \cdot \varepsilon} \qquad \text{(Eq. 4)}$$

At 59.54 keV, the ultimate energy resolution is expected to be 467 eV FWHM. My goal is to get as close as possible to this value.

• Charge transport

Once the electron-hole pairs are created in the bulk, the charge carriers are moved in the volume by drift motion under the influence of the electric field applied externally to the semiconductor or by diffusion due the charge concentration gradient. If no field is applied to the semiconductor, the net displacement of charge carriers will be null. However, if an electric field is applied, the electrons and holes are accelerated in between random collisions in the direction of anode and cathode respectively. The average drift velocities are given by:

$$\vec{v_n} = -\frac{q \cdot \tau_c}{m_n} \cdot \vec{E} = -\mu_n \cdot \vec{E} \qquad \qquad \text{(Eq. 5)}$$

$$\text{and} \qquad \vec{v_p} = -\frac{q \cdot \tau_c}{m_p} \cdot \vec{E} = -\mu_p \cdot \vec{E} \qquad \qquad \text{(Eq. 6)}$$

Where q the unit charge, τ_c the mean free time in between two scattering events on the crystal lattice imperfection, m_n and m_p the effective electron and hole masses, μ_n and μ_p the electron and hole mobilities and $\vec{E}$ the applied electric field. According to Table 2, one can easily derive the typical electron and hole velocities for a 1 mm thick CdTe biased under 400 V for instance and finds 3.10^6 cm.s^{-1} and 3.10^5 cm.s^{-1} respectively. The corresponding transit time, equivalent to the duration of the induce signal are t_n = 30 ns and t_p = 340 ns respectively.

Along the field direction, diffusion is nearly negligible in the induction process. On the other hand diffusion cannot be ignored when the characterisitic size of the charge cloud becomes comparable with the detector pixel pitch as the charge cloud extends by diffusion. Assuming the initial charge distribution to be punctual, the width of the electron and clouds extended by diffusion after they travel across the detector during t_n and t_p transit time respectively is written:

$$\sigma_n = \sqrt{2\frac{kT}{q}\mu_n \cdot t_n} \qquad \text{(Eq. 7)}$$

$$\text{and} \quad \sigma_p = \sqrt{2\frac{kT}{q}\mu_p \cdot t_p} \qquad \text{(Eq. 8)}$$

Considering a charge cloud created at the surface of a 1 mm thick detector biased under 400 V, the electron cloud would be enlarged by 3 μm, negligeable. Conversely, an interaction deep in the detector would cause an extension of the hole cloud up to 65 μm, which is no longer negligible.

The extension adds to the fact the initial charge cloud size is naturaly non-zero. A rule with the thumb gives a charge cloud size in the order of 1 μm/keV in diameter.

These effects are detailed in Bob Dirks and in Sebastien Dubos PhD thesis and are not further discussed here.

• Signal induction
As long as the charge carriers move into the bulk semiconductor along the electric field lines, a mirror surface charge is formed on the electrodes. The mirror charge build-up starts immediately after the photon interacted and last as long as the electrons and holes reach their respective electrodes. It is improper to talk about "collecting" electrodes, which is often used. The electrons and holes having significantly different mobilities, the signal structure is pretty complex and depends on the depth of penetration of the photon into the bulk.
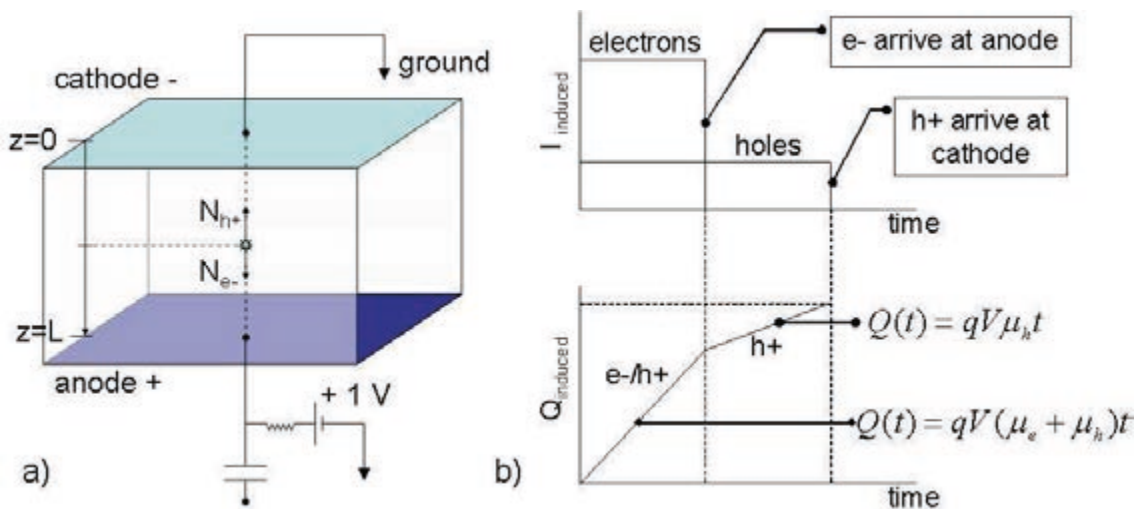

Figure 15. Schematic view of a signal induction in a simple planar structure and corresponding signal shape
(after B.P.F Dirks PhD thesis).

The induced charge is the integral of the electrons and hole current flows during the charge carrier transit times. The total induced charge Q_{induced} (and the correspoonding current flow I_{induced}) is also the integral of the weighting field $\overrightarrow{E_w}$ along the charge carrier trajectories; as proposed by Shockley and Ramo:

$$Q_{\text{induced}} = \int_{x_{\text{initial}}}^{x_{\text{final}}} q \cdot \overrightarrow{E_w} \cdot d\vec{x} \qquad \text{(Eq. 9)}$$

$$\text{and} \qquad I_{\text{induced}} = q\overrightarrow{E_w} \cdot \vec{v} \qquad \text{(Eq. 10)}$$

$\overrightarrow{E_w}$ is computed solving the Poisson equation $\nabla^2 \varphi = -\rho/\in$, where φ is the potential when the applied voltage is 1V, ρ the space charge density and $\in$ the dielectric constant in the semiconductor.

Considering a simple planar detector configuration, the weighting field is collinear with the trajectory of the carriers. Thus, it turns out that the signal is induced as described in Figure 16 and the induced current and charge are:

$$Q_{\text{induced}} = qN_0 \qquad \text{(Eq. 11)}$$

$$\text{and} \qquad I_{\text{induced}} = qV/L^2(\mu_n + \mu_p) \qquad \text{(Eq. 12)}$$

Where V is the applied voltage and L the thickness of the detector.

• Charge loss and Hecht relation

In reality electrons and holes also have a limited lifetime and a fraction of the charge is lost during their trajectory toward the electrodes. The charges are trapped by the native structural defects in the CdTe crystal and may recombine as well. Hecht's relation expresses the effect of charge loss (*i.e.* trapping) assuming that no charge detrapping happens during the signal induction:

$$Q_{\text{induced}} = qN_0 \cdot V/L^2 \left[\mu_n\tau_n\left(1 - e^{-t_n/\tau_n}\right) + \mu_p\tau_p\left(1 - e^{-t_p/\tau_p}\right) \right] \qquad \text{(Eq. 12bis)}$$

Where t_n and t_p are the electron and hole lifetimes. In this expression, the product mobility times lifetime appears as factor of merit of the quality of the inducved signal. This product is very popular in the CdTe community and often compared from one crystal technology to another, simply because a planar configuration allows its measurement easily. It is highly desirable that this product has the highest achievable value.

• Small pixel effect

Computing the weighting field, or the « sensing field » one could say, in a pixelated detector instead of a planar configuration, it turns out that the field is no longer colinear with charge carrier velocity vectors. When the pixel is small with respect to the detector thickness (< ½ thickness approx.), the weighting field is concentrated near the pixel. In other words, the charge induced on the pixel is mirrored when the carriers trajectory intercept the pixel neighboring region. This is generally called « small pixel effect ». The key advantage here is to screen the carrier that move to a direction opposite to the pixel. The pixel being an anode, the holes are screened. The detector becomes a single carrier system and is no longer sensitive to poor hole transport properties.

Figure 18 illustrates the small pixel effect. The left figure illustrates that in the case of planar configuration, the potential is linear which means that the signal induction is continuous all along the charge carrier transport in the bulk. Conversely, when the pixel-to-thickness tends to be small, the weighting potential is no longer linear and raises rapidly near the anode. This means that the signal on the pixel is induced when the charge is getting close to the pixel region.
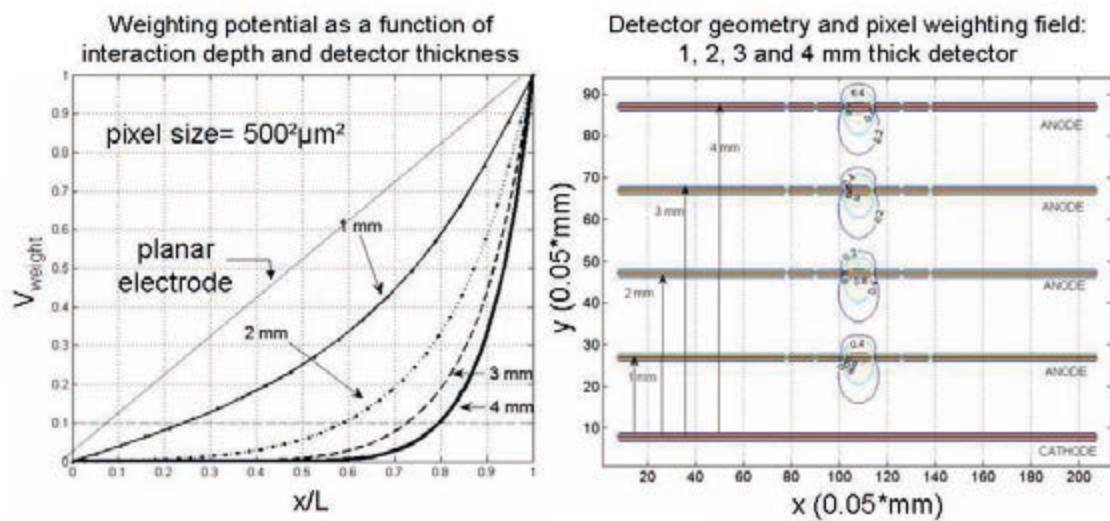
Figure 16.
Left – the weighting potential as a function of the position for different detector thicknesses. As the thickness,
L, increases, the small-pixel-effect becomes stronger.
Right – the numerically obtained weighting potentials. The pixels have a size of 500 μm
with a large guard ring surrounding them. (after B.P.F Dirks PhD thesis).

Optimization of a CdTe pixel detector therefore requires a **careful simulation** of signal induction that starts with a clean estimation of the weighting field and carrier velocities fields. This type of mathematical simulation of the detectors has been conducted by Dirks and Dubos with homemade models for different generations of Caliste detectors.

• Other benefits of small pixels
Apart the "small pixel effect" which reduces the degradation of the induced signal by hole trapping in the bulk, the use of small pixels is a natural advantage for:
– spatial resolution,
– dark current limitation and reduction of stray capacitance, *i.e*, noise.

Moreover, the improvement of the dark current is so important, especially with Schottky contacts at the anode that the applied field can be stronger than in coplanar configuration. This helps to speed up the charge transport, reducing again the trapping probability and improving the signal rise time, avoiding balisitic deficit for instance.

It is a exceptional situation where improving the pixel pitch will result in natural improvement in spectrsocopy as well. The only complication comes from the hybridization process described later in the text.

2.3. Promising spectroscopy in 2003
During B. Dirks's thesis, we extensively and fully modeled[1] the CdTe Schottky diode trying to anticipate our design performance and reach the best achievable energy resolution in our lab. Our goal was 1 keV FWHM at 60 keV. In 2003, I considered this analysis phase to be critical to define accurately the geometry of our forthcoming Caliste prototype.

---

1. Our CdTe model includes Monte Carlo Photon-CdTe interaction, 3D field calculation, 3D weighting field calculation, charge transport and loss, electronics shaping and noise.
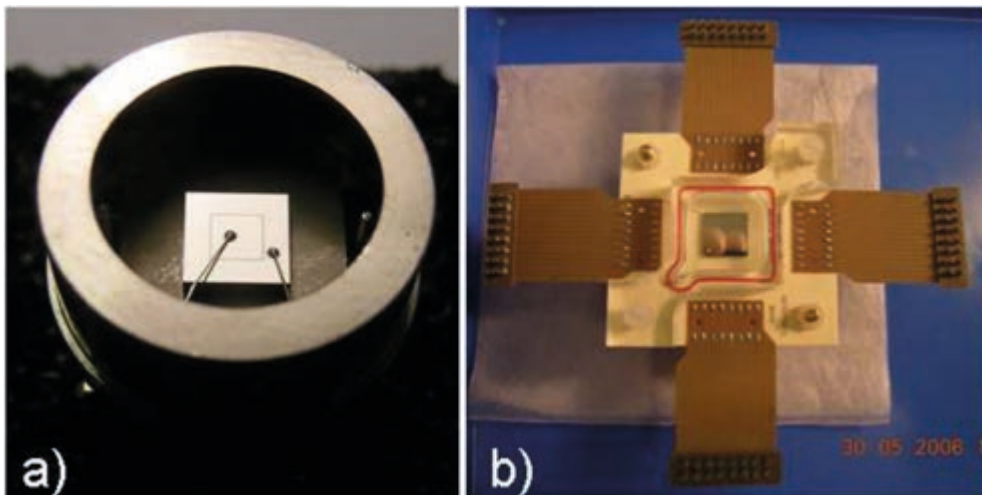
Figure 17.
(a) – Single Schottky CdTe pixel surrounded by a guard ring (2003) in a TO package.
(b) – 64 pixel array flip chip a flat carrier at CEA/Irfu.

We finally obtained our first sub-keV resolution spectrum in 2005 as shown on Figure 18. We obtained 700 eV FWHM at 14 keV on a 500 µm thick Al type Schottky diode equipped with a guard ring at the Ohmic side. The operating temperature was 22°C and the depletion voltage set to 350V. The model satisfactorily fits the data and allows exptrapolation for the future development according to Figure 19. This readout chip used was IDeF-X V1.0 described further in the text.
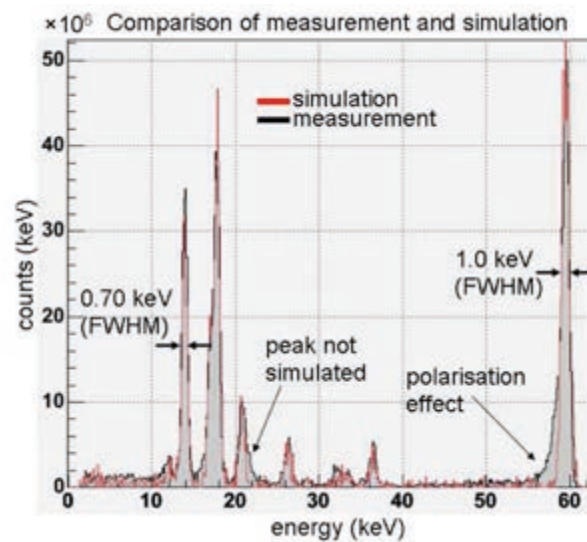
Figure 18. Single pixel spectral response superimposed with our model. Our first sub-keV energy resolution results in the lab in 2005 by B. Dirks.
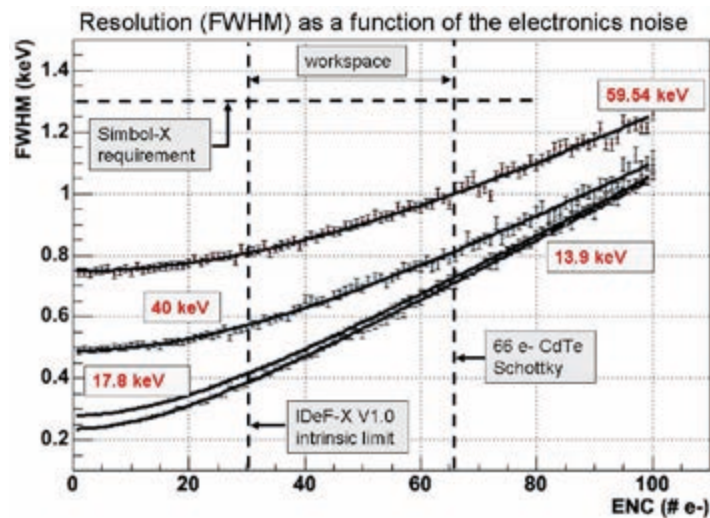
Figure 19. Simulation of the expected energy resolution against the electronics noise performance of the front-end.
After this work we envisioned a sub keV performance for an array of pixels trying to identify a process where the electronic noise is maintained below 60 e- rms. This value came to be our specification for Caliste.

2.4. Stability in time and "polarization effect"

Despite their promising dark current and high energy resolution capability, Schottky detectors suffer an embarassing instability in time, effect initially called improperly the « polarization effect »[2]. As a matter of fact, depending on temperature, voltage, detector geometry and detector crystal quality in terms of the density of deep trap levels in the bandgap, the effective Schottky barrier height at the anode decreases with time, causing a continuous rise of dark current. The consequence is that the energy resolution constantly degrades with time since it's is directly realted to the current flow at the front of the charge sensitive preamplifier. The physical interpretation of this instability relies on a continuous and progressive detrapping of holes in the whole crystal volume where an electric field is applied. Thus, deep acceptor levels ionization creates a space charge region in CdTe that modifies the distribution of the internal electric field. After a certain time, the field turns to be almost zero at the cathode near the ohmic contact, *i.e.* the entrance window of the sensor. As a consequence, the detector is no longer sensitive on its front side. It translates in the spectra by the extinction of low energy lines for instance. Because the field distribution is altered, *i.e.* compressed at the anode side, by the deep acceptors ionization, the equivalent thickness of the detector is thinner and the entrance side covered by insensitive absorbing material where charge transport is almost limited to diffusion. Thus the gain is also continously reducing with time as the detection efficiency.

Recovering Polarization effect is easy: turn off the high voltage, wait and start again.
One question remains: how long should we wait for? Naturally, both ionization and de-ionization of acceptor levels are thermal processes in semiconductors. This already reveals that the polarization time and recovery time are exponentially depending on temperature. On the other hand, when the field turns to zero, the number of available holes in the volume to neutralize the acceptors is very high. Consequently, by chance, the recovery time is much faster than the polarization time at any temperature.

While a Schottky CdTe diode is almost no longer a spectrometer in a tens of minutes time frame (see Figure 20) when the temperature is about +20°C, it can run stable for months when moderately cooled down at -20°C.

---

2. Note that Sieffert in 1976 mentionned in [5.8.14] that CdTe cannot be a good spectrometer du to this effect.
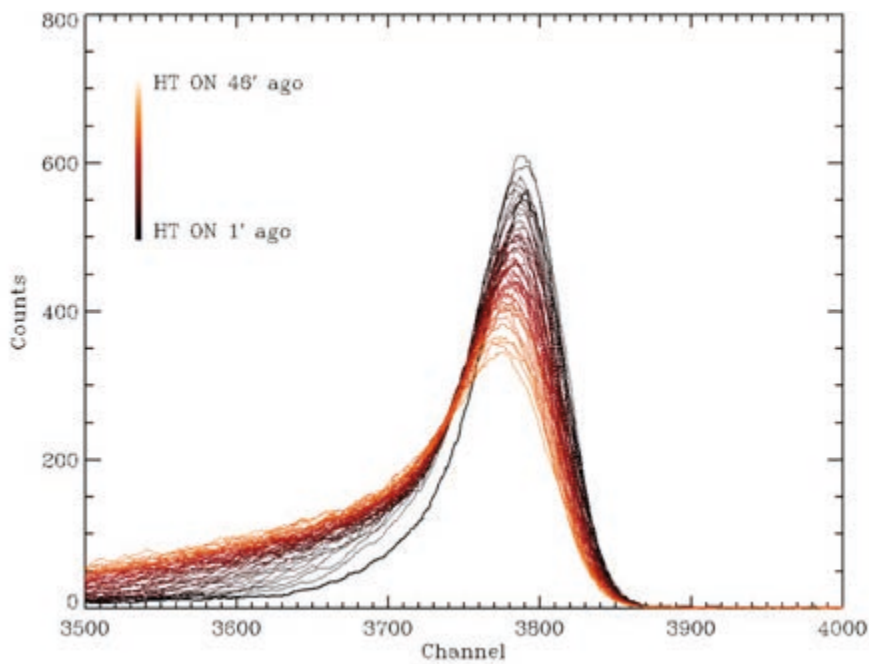
Figure 20. "Polarization effect" as seen in 2005 on a single pixel Schottky diode at room temperature.
The 60 keV line shifts towards the low energy in tens of minutes.

Concluding, if an application can afford a detector cooling, CdTe can really be a good spectrometer.

2.5. Paper #2 [4.18]: Chracterization of Polarization Phenomenon in Al Schottky CdTe Detectors using a spectroscopic analysis method

These unstability characteristics of Schottky type CdTe deserve a detailed understanding because we cannot fly unstable detectors in space. This risk must be mitigated by a perfect control of the detector behavior. During Aline Meuris PhD [8.15], we have extensively studied the polarization using our first Caliste prototype and the results are finally reported in 2011, in the following paper attached in the next section and published in *Nuclear Instruments and Methods in Physics Research A*.

In 2015, we are still working on the recovery time dependence with temperature and complete understanding of the polarization process.

Contents lists available at ScienceDirect

Nuclear Instruments and Methods in Physics Research A

journal homepage: www.elsevier.com/locate/nima

Characterization of polarization phenomenon in Al-Schottky CdTe detectors using a spectroscopic analysis method

Aline Meuris*, Olivier Limousin, Claire Blondel

CEA/Irfu, Orme des Merisiers, bât. 709, 91191 Gif-sur-Yvette Cedex, France

ARTICLE INFO

ABSTRACT

CdTe radiation detectors equipped with Schottky contacts are known to show spectral response degradation over time under biasing. Nevertheless, they can be used as high-resolution spectrometers for X-rays and gamma-rays with moderate cooling and high voltage. Spectroscopic long-term measurements have been performed with Al/CdTe/Pt pixel detectors of 0.5, 1 and 2 mm thicknesses and ^{241}Am source from -13 to $+16$ °C to evaluate how long they can be operated. Experimental results are confronted to simulations using the charge accumulation model for electric field. Activation energy for collection efficiency stability and peak shift was measured at 1.0–1.2 eV although deep acceptor levels responsible for hole detrapping during polarization were evaluated by other methods at $E_V + 0.6$–0.8 eV. The difference is probably due to a thermal effect of pre-polarization before biasing the detector.

© 2011 Elsevier B.V. All rights reserved.

1. Introduction

1.1. Motivations

Because of their high density and good charge transport properties, CdTe and CdZnTe semiconductor detectors are among the best materials for X-ray and gamma-ray imaging spectroscopy. Schottky-type metal contacts result in diode detectors with very low leakage current at room temperature and thus, excellent spectrometers for hard X-rays, operated since the end of the 1990s [1]. However, the development of such detectors is limited because of performance degradation with time, reported since the 1970s [2]. Loss in detection efficiency has been observed, all the more rapidly as the temperature is high, but recovery to initial performance can be achieved turning off the bias voltage of the detectors. Understanding and predicting this so-called polarization effect is crucial to provide astronomy, medical, industrial or homeland security applications with high energy resolution solid-state detectors in hard X-ray and gamma-ray range at room temperature or with moderate cooling. In 2014, the Astro-H mission led by JAXA will integrate a hard X-ray imager (HXI) and a soft gamma-ray detector (SGD) made of stacks of silicon and Schottky Al/CdTe/Pt strip detectors [3]. In 2015, the Sino-French SVOM mission will use 6400 crystals of In/CdTe/Pt detectors for the ECLAIRs gamma camera [4]. Other projects

proposed to the ESA Cosmic Vision program like IXO and COSPIX contemplate to use Schottky CdTe detectors [5,6]. Operating conditions and calibration methods have to be optimized with respect to the polarization phenomenon.

1.2. State of the art

Physicists agree that polarization effect in Schottky CdTe detectors is due to ionization of deep acceptors in the semiconductor due to the fact that the Fermi level cross the deep acceptor level (DAL) close to the rectified contact in Schottky-type detectors [7–9]. During time under polarization, the deep levels progressively release holes that drift towards electrodes and leave a negative space charge in the bulk, resulting in a modification of the electric field. The detrapping time constant τ in given by the following equation: (1):

$$\tau = \frac{1}{N_V \sigma v} \exp\left(\frac{E_T - E_V}{kT}\right) \tag{1}$$

where N_V is the effective density of states for the valence band, σ is the acceptor capture cross-section, v is the thermal velocity of a hole, E_T is the energy of the deep acceptor level and E_V is the energy of the top of the valence band. The temperature dependency of τ was evaluated in p-type CdTe detectors from Acrorad by two independent methods: current measurements to estimate the Schottky barrier lowering evaluate the energy level at $E_V + 0.69$ eV [10] and electric field measurements to estimate space charge concentration at the anode evaluate the energy level at $E_V + 0.62$ eV [11]. Deep energy levels can be directly
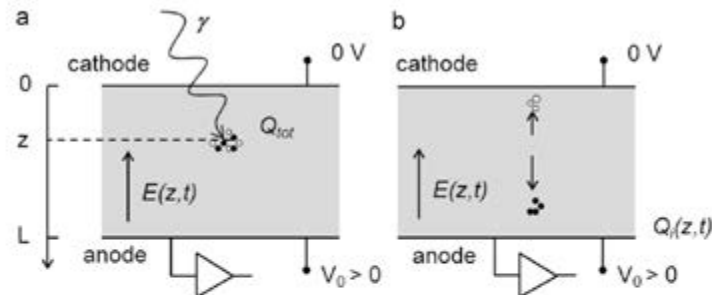
Fig. 2. Model to compute charge collection in CdTe Schottky detectors. Interaction position z is refered towards the cathode ohmic contact (contrary to x in Fig. 1). (a) The total absorption of a photon by photoelectric effect produces Q_{tot} charge of electron–hole pairs. (b) Drift of holes towards the cathode and electrons towards the anode induces a charge signal Q_i at the collecting electrode that can be measured with appropriated front-end electronics.
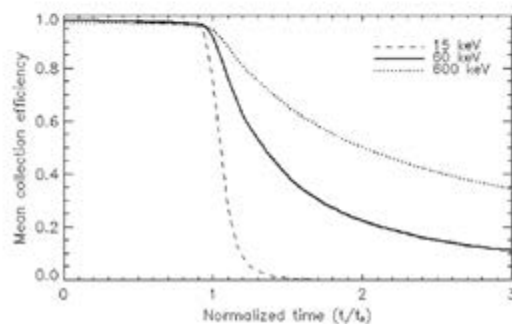

Fig. 3. Simulated change over time of mean collection efficiency at 15, 60 and 600 keV with a CdTe planar detector illuminated at the cathode and equipped with a Schottky contact at the anode. Only photons interacted by photoelectric effect are considered; absorption is assumed total and charge cloud is assumed punctual. Time scale starts when the bias voltage is turned on and is normalized with respect to the polarization time that depends on temperature and voltage conditions and detector thickness. The detector cannot be operated after the polarization time because of an efficiency drop, which is all the more dramatic as the incident energy is low. This effect is the mix of a weak electric field at the cathode and a small product $\mu\tau$ (mobility-life time) of holes in CdTe.

According to Eqs. (7) and (8), a change in η_{E_0} with time indicates a change in drift times, i.e. a change in electric field in the bulk. Mean collection efficiency was computed for 15, 60 and 600 keV photons interacting in CdTe material. At a given energy, all curves are identical if time scale is normalized with respect to the polarization time t_p defined in Eq. (5) whatever may be the voltage, the thickness and the temperature. Fig. 3 shows normalized curves for the three energies. Before t_p, mean collection efficiency is maximal and constant. The absolute value is close to 1 since we only consider total absorption events; it is slightly lower than 1 because of charge loss phenomenon. From t_p, mean collection efficiency drops. Efficiency loss is more dramatic for X-ray photons (<20 keV) because they all interact in the region where electric field is null. Consequently, X-ray lines vanish at first. But the efficiency drop is also critical for gamma-rays (>200 keV). The polarization time thus defines the maximal time of operation of CdTe Schottky detectors. It is a key parameter for all applications with this kind of radiation detectors. It depends on the detector (material properties and geometry, temperature and voltage conditions) but not on the source. However, other energy-dependent effects have to be taken into

account to determine the operational phase: i.e. energy resolution degradation and peak shifts.

2.3. Peak shift computation

Peak shifts can be critical for some spectroscopic applications, in case of real-time histograming in particular. Two approaches can be contemplated to tackle this issue: what data corrections should be applied for given operation conditions? Or which operational conditions should be used in order to keep good spectral performance without data correction? It is important to characterize and predict the trend in both cases. Spectra were simulated to reproduce the observed phenomenon. We chose the case of the main [241]Am line at 59.54 keV because it is the most relevant one to experimentally study polarization phenomenon. As a matter of fact, it is an isolated line that can be monitored even after the polarization time because it doesnot vanish as rapidly as the 14 keV line. Above 200 keV, our model is limited to build gamma-ray lines because it assumes that the photon is fully absorbed and the Compton peak cannot be reproduced, although Compton scattering starts to be the predominant interaction process. Events of 59.54 keV photons absorbed in CdTe were generated by the Monte-Carlo method. Each event induces an amount of charge depending on time and position of interaction and defined by the $Q(z,t)$ quantity previously computed. Histograms built by intervals of time and peak positions are evaluated. Assuming an energy calibration at initial time only, the first peak position is associated to 59.54 keV energy and the following positions can be expressed in apparent energy unit, as shown in Fig. 4. Curves of peak position are similar to mean collection efficiency curves with a break that coincides with the polarization time (see Fig. 4a). Moreover, looking into the detail to the operational phase before t_p, the model of electric field predicts a peak shift as soon as the detector is biased. To describe the phenomenon in a synthetic way, we model the peak position before t_p with a linear fit and we call *peak shift* the slope expressed in eV/h (see Fig. 4b). This unit is independent of the acquisition system; it is the convenient parameter for calibration issue and performance monitoring.

Peak shift was evaluated in different conditions of voltage, temperature and detector thickness. Fig. 5 demonstrates that peak shift can be modeled by a Boltzmann factor with an activation energy of 0.69 eV. This is precisely the energy of DALs assumed in our model. In other words, if our model is correct, it predicts that peak shift of the main Am line follows the same exponential temperature law as detrapping time and polarization time.

determined by photo-induced current transient spectroscopy (PICTS) [12], thermo-electric emission spectroscopy (TEES) [13] or surface photovoltage spectroscopy (SPS) [14]. Deep acceptor levels in Cl doped CdTe have been measured at $E_V + 0.60$–0.63 eV [15,16], $E_V + 0.71$ eV [17] or $E_V + 0.76$–0.77 eV [16–19]. They are interpreted as hole traps due to native defects, cadmium vacancies in particular. Higher energy levels measured at 1.1 and 1.4 eV have been identified as donor levels [17,19] due to telluride vacancies.

The present paper proposes in Section 2 a new method based on spectroscopic measurements to evaluate the energy level E_T–E_V and reports in Section 3 experimental results with Schottky Al/CdTe/Pt pixel detectors.

Toyama proposed in 2006 new hypothesis of initial concentrations of ionized acceptors to analytically explain the observed loss of detection efficiency [20]. The author assumes that deep acceptor levels in a λ-thin region close to the Schottky contact are already ionized before applying a voltage. As a consequence, from a characteristic time, electric field becomes null underneath the cathode, in a wider and wider volume. The electric field measured by Cola using Pockels effect also showed a break from a certain time and a region with constant weak field at the cathode where charge collection is less effective [21]. However, the field at initial time is not constant in the bulk and suggests the presence of a negative space charge uniformly distributed in the volume before biasing the detector. Section 4 is a discussion about polarization effect modeling from our experimental data.

2. Simulation of the polarization effect

2.1. Modeling

The goal of the simulation was first to predict changes over time of observable parameters, in order to compare the model of polarization effect in Schottky CdTe detectors with measurements in laboratory. If we assume that holes drift to electrodes and cannot be captured when the detector is biased, the concentration N_T^- of ionized deep acceptors is given by the dynamics of the hole release process:

$$\frac{dN_T^-}{dt} = \frac{(N_T - N_T^-)}{\tau} \qquad (2)$$

where N_T is the total concentration of deep acceptors (characteristic of the semiconductor material). Assuming a zero-temperature approximation, initial concentrations are

$$\begin{cases} N_T^-(x,0) = N_T & 0 \le x < \lambda \\ N_T^-(x,0) = 0 & \lambda \le x < L \end{cases} \qquad (3)$$

where x is the depth position from the Schottky interface, L is the detector thickness, λ is the intersection position of the deep acceptor level E_T and the Fermi level E_F (characteristic of the Schottky metal–semiconductor contact), as shown in Fig. 1. The concentration of ionized deep acceptors with time can be computed from Eqs. (2) and (3):

$$\begin{cases} N_T^-(x,t) = N_T & 0 \le x < \lambda \\ N_T^-(x,t) = N_T(1 - e^{-t/\tau}) & \lambda \le x < L \end{cases} \qquad (4)$$

The solving of the Poisson equation with Eq. (4) and the boundary voltage conditions ($V(x=0) = V_0 > 0$ for a backward polarization of the Schottky diode) allows determining the characteristic time t_p, referred to as the *polarization time* afterwards, when the electric field becomes null at the cathode as given
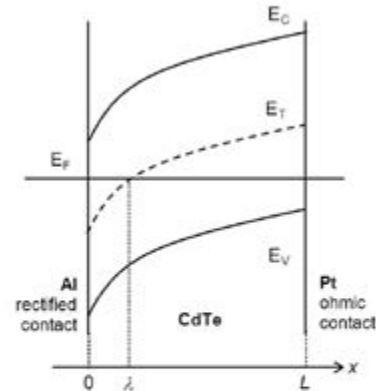

Fig. 1. Model of energy band diagram of an L-thick Al-Schottky CdTe detector in zero-bias conditions. The deep acceptor level E_T crosses the Fermi level E_F at a distance λ from the rectified (Schottky) contact.

below:

$$E(L, t_p) = 0 \Leftrightarrow t_p = \tau \log\left(\frac{L^2 - \lambda^2}{L^2} \left[1 - \frac{2\varepsilon V_0}{qN_T L^2} \right]^{-1} \right). \qquad (5)$$

Using numerical values extracted by Toyama ($\lambda = 87$ μm and $N_T = 4.56 \times 10^{12}$ cm^{-3}), Eq. (5) can be approximated by Eq. (6):

$$t_p \approx \frac{\tau}{L^2} \left(-\lambda^2 + \frac{2\varepsilon}{qN_T} V_0 \right) \text{ if } \frac{V_0}{L(mm)^2} \ll 10^3. \qquad (6)$$

Eqs. (1) and (6) clearly show that polarization time depends on temperature in an exponential way (with an energy E_T–E_V), on detector thickness in a quadratic way and on the bias voltage in a linear way.

2.2. Charge collection computation

Fig. 2a shows the interaction of a photon in a CdTe planar detector at depth z that produces a charge Q_{tot}. The cathode is the entrance window and the anode is the collection electrode made with a Schottky contact. Total charge induced $Q(z,t)$ at the anode of Fig. 2b is computed with the model of electric field $E(z,t)$ derived from the Poisson equation solving with the conditions of Eq. (4). Charge loss is described by the Hecht relation [22]:

$$\frac{dp}{dt} + \frac{p}{\tau_p} = 0; \quad \frac{dn}{dt} + \frac{n}{\tau_n} = 0 \qquad (7)$$

where p and n are the concentrations in holes and electrons, τ_p is the hole life-time of holes (3 μs in the model) and τ_n is the electron life-time (1 μs in the model). Filtering time of the front-end electronics is supposed to be long enough to neglect ballistic loss. The fraction of collected charge $Q(z,t)/Q_{tot}$ does not depend on the incident energy if we assume that the interaction always comes from photoelectric effect and creates point charge (Compton scattering of gamma-rays is ignored). For a photon of energy E_γ fully absorbed, the probability to have interacted at a depth z is defined as $f_{E_\gamma}(z)$. We introduce the *mean collection efficiency* η_{E_γ} as the fraction of induced charge at the depth z convoluted with this probability the following:

$$\eta_{E_\gamma}(t) = \int_0^L \frac{Q(z,t)}{Q_{tot}} f_{E_\gamma}(z) dz. \qquad (8)$$

The criterion quantifies the effect of the polarization phenomenon. Incomplete charge collection is due to charge loss.
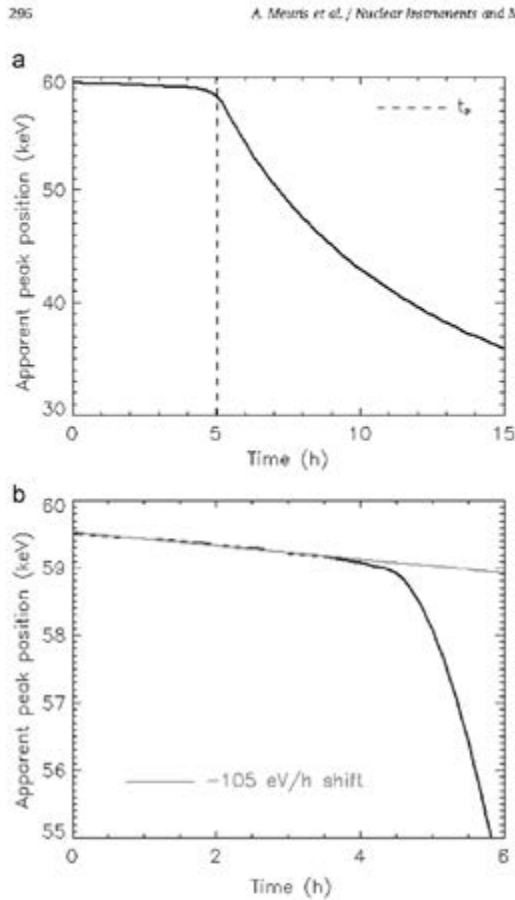
a

b

Fig. 4. Simulated change over time of peak position of the main ^{241}Am line at 59.54 keV with a 2 mm-thick CdTe Schottky detector biased at 800 V at 0 °C. The position is expressed in energy unit, independent of any acquisition system, assuming a unique energy calibration at starting point (detector biasing): (a) Development over 15 h, i.e. 3 times the polarization time; position break appears at the polarization time. (b) Development over the operation phase (before t_p); peak shift can be observed from the starting point and can be modeled with a linear fit to extract a slope in eV/h.

2.4. Conclusions on the proposed method

Some parameters observable with spectroscopic measurements can be used to extract parameters of the polarization effect model:

- Breaks in efficiency curves and in peak position curves must be observed synchronously; these are two independent ways to evaluate the polarization time and confirm the influence of temperature, voltage and detector thickness predicted by Eq. (5).
- Polarization time and peak shift evaluations at different temperatures are two independent ways to estimate the energy level of deep acceptors responsible for the polarization effect, according to Eq. (1).
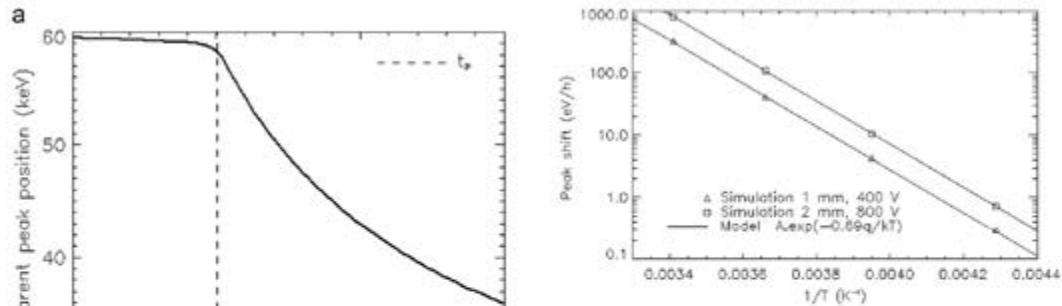

Fig. 5. Simulation of peak shifts for 2 operation configurations (1 mm-thick detector biased at 400 V and 2 mm-thick detector biased at 800 V) and 4 temperature points. Data can be modeled by a Boltzmann law with an energy level of 0.69 eV corresponding to the deep acceptor level assumed for the electrical field model. For a given voltage to thickness ratio (400 V/mm), peak shift is ~2.5 times faster with 2 mm-thick detectors than with 1 mm-thick detectors.
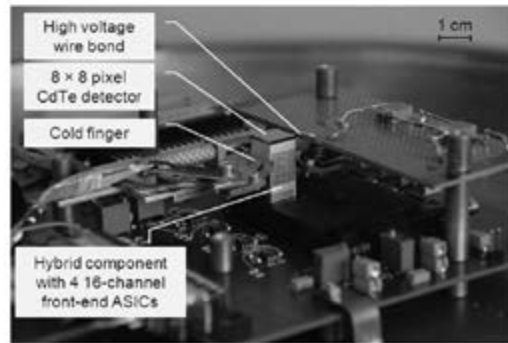

Fig. 6. Picture of the set-up used to study polarization effect. The Caliste microcamera is composed of an Al-Schottky CdTe pixel-detector with analog front-end electronics integrated in a hybrid component. The high voltage is supplied by a gold wire bonded on the planar Pt cathode. The hybrid is squeezed between cold fingers in order to cool the detector down to −15 °C.

The method based on spectroscopic measurement is not only a new method to study the polarization effect in Schottky detectors but also the only way so far to practically determine how these detectors must be operated for long-time spectroscopic applications.

3. Experimentation of the polarization effect using spectroscopy

3.1. Setup and data analysis method

Polarization of Al Schottky detectors was studied with Caliste 64 microcameras [23]. This device is the hybridization of an 8×8 pixel detector with 4 front-end ASICs of 16 channels called IDeF-X 1.1 [24]. Pixels are 900 µm-size and 1 mm-thick, and surrounded by a 900 µm-wide guard ring. The microcamera is placed in a thermal enclosure with a ^{241}Am source (see Fig. 6). To properly estimate the detector temperature, thermal tests were performed with the front-end electronics part of the Caliste camera and a PT100 sensor on top of it. Temperature measurement precision is
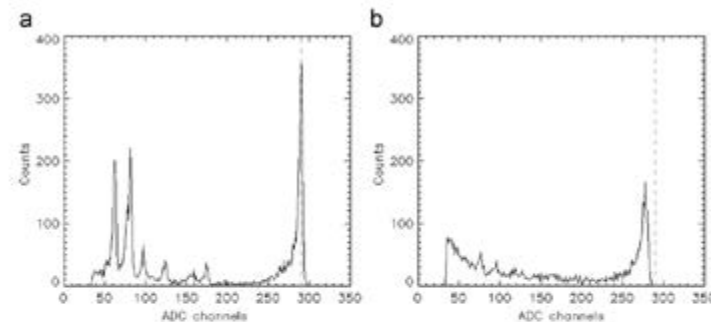
Fig. 7. ^{241}Am raw spectra obtained with a 900 μm-size pixel of a 1 mm-thick 64-pixel Al/CdTe/Pt detector cooled down to −7 °C and biased at 200 V without correction of energy or split events. (a) Spectrum just after biasing the detector; energy resolution is 0.9 keV at 59.54 keV. (b) Spectrum after 15 h; low-energy lines have vanished and the 59.54 keV line is shifted to the left.
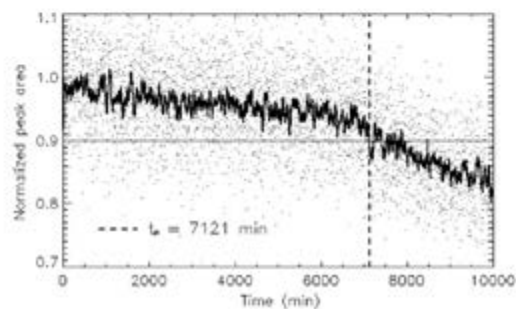

Fig. 8. Change over time of the area of main ^{241}Am line with a 0.5 mm thick detector cooled down to 0 °C biased at 150 V. Raw data (count rates in the peak) are normalized with respect to the initial value and filtered with a moving average to get the solid line. Polarization time is defined as the time from which the curve goes below the 0.9 limit and is evaluated to 7121 min (119 h) in this case.
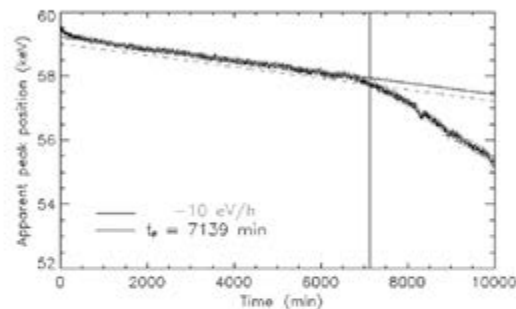

Fig. 10. Polarization times experimentally evaluated with 2 CdTe Schottky pixel detectors cooled down from −13 to +16 °C and biased at 2 voltages (200 and 300 V for the 1-mm thick detector and 400 and 600 V for the 2-mm thick detector). Error bars correspond to standard deviations over the 22 pixels studied. Data can be modeled by Boltzmann laws with energies between 0.9 and 1.0 eV.

Fig. 9. Change over time of peak position of the main ^{241}Am line measured with a 0.5 mm thick detector cooled down to 0 °C biased at 150 V. 2 min-histograms calibrated in energy and peak positions are estimated from Gaussian fits. A linear fit (gray solid line) in the operational phase is used to evaluate the peak shift (10 eV/h in this case). The polarization time is defined as the time from which the measured position is inferior to the linear fit by more than 200 eV, i.e. when the curve crosses the dotted gray line; it is here evaluated to 7139 min (119 h) synchronously with the efficiency break.

better than 1 °C. Outside the vessel, the high bias voltage can be controlled and the digital electronics board is in charge of readout sequencing and data formatting in packets of events. Data
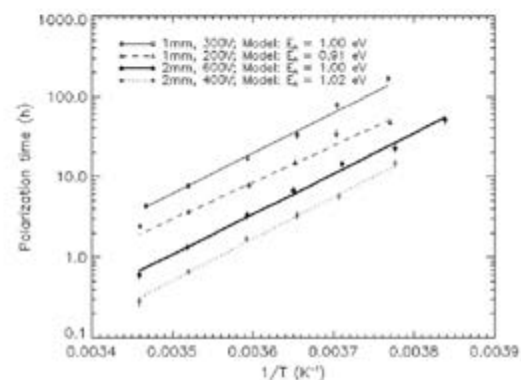
acquisition was continuously performed from high voltage turning-on until Am low-energy lines vanish (at 14 and 18 keV). Fig. 7 shows typical spectra obtained at the starting point and the at end of the measurement. Experiment was reproduced for various conditions of temperatures, voltages and detector thicknesses. For data storage and computing time issues, data are recorded for 22 pixels out of 64; they are chosen along a diagonal of the matrix in order to study both pixels in the center and in the borders of the crystal. Data processing consists of building histograms every 2 min for these 22 pixels in order to determine peak positions and peak areas (numbers of counts) of the main Am line as a function of time. Peak area is proportional to total efficiency at 60 keV. Since quantum efficiency depends on the material and not on the electric field, a break in peak area can only occur when mean collection efficiency at 60 keV starts dropping, i.e. at the polarization time according to our model. Apparent peak position in energy unit is also computed using initial energy calibration. Results at 0 °C are shown in Figs. 8 and 9. A break in the peak area curve was observed for all pixels of the matrix and in all conditions (see Fig. 8). Moreover, breaks were synchronously observed on the peak position curves (see Fig. 9). Polarization times t_p were extracted considering the time from which

detector is not null and is given by the Fermi–Dirac distribution F:

$$F(x) = \frac{1}{1 + e^{(E_{TD}(x) - E_F)/kT}} \qquad (9)$$

where E_{TD} is the deep acceptor level in zero-bias conditions, which depends on the x position in the detector because of the energy band curvature in the Schottky diodes (see Fig. 1). This effect of "pre-polarization" cannot be neglected since the electric field observed by Cola at initial time is not flat in the bulk [11,21]. As a consequence, the polarization phenomenon is all the more advanced before applying a voltage as the temperature is high. The initial conditions are no longer given by Eq. (3) but by Eq. (10) as follows:

$$N_T^-(x,0) = F(x)N_T \quad 0 \le x < L. \qquad (10)$$

If we still assume that the dynamic of N_T^- is only driven by the hole release process, a better expression of the concentration of ionized deep acceptors from Eqs. (2) and (10) would be

$$N_T^-(x,t) = N_T(1 - e^{-t/\tau}) + F(x)N_T e^{-t/\tau}. \qquad (11)$$

The x-dependency makes the Poisson equation complex to solve. Fermi–Dirac distribution law tends to increase the influence of temperature on Schottky detector spectral stability and could explain activation energies of polarization time and peak shift higher than 0.7 eV. Leakage current is directly connected to charge detrapping and DAL ionization at one position (at the anode for instance) also depends on detrapping time only; this explains why Toyama and Cola could measure the activation energy of the detrapping time with these methods [10,11]. Spectroscopic response of the detector integrates cumulated effects over a range of interaction depths and doesnot depend on detrapping effect only.

5. Conclusions

We have studied polarization phenomenon in Schottky CdTe detectors for four samples of Al/CdTe/Pt thin pixel detectors from Acrorad mounting on top of Caliste 64 microcameras. Performance degradation over time has been characterized with spectroscopic measurements using a ^{241}Am source in various conditions of temperatures, voltages and detector thicknesses. To operate Schottky CdTe detectors as spectrometers and predict their change over time, it is convenient to observe spectral parameters like peak area, peak shift or energy resolution. With this method, we have showed that stability of spectral response exponentially depends on temperature with an activation energy of 1.0–1.2 eV. This value can be interpreted as the combination of two thermal effects: the detrapping of holes by deep acceptor levels at $E_V + 0.6$–0.8 eV during the detector biasing (bulk effect) and a pre-polarization state before biasing due to the crossing of the DAL with the Fermi level close to the rectified contact (surface effect).

As an important consequence of this result, a moderate cooling strongly stabilizes a detector: a 1 mm-thick CdTe Schottky detector biased at 400 V and cooled down to $-20\,^{\circ}$C can be operated without efficiency loss for more than 1000 h. For high-resolution spectroscopy, the strongest constraints can come from peak shift and energy resolution degradation that are observed as soon as

the detector is biased. These parameters are channel-dependent and electronic-dependent because of dark current dispersal. With Caliste 64 camera (pixels of 1 mm pitch) equipped with Al–CdTe–Pt detectors from Acrorad and IDeF-X ASIC from CEA, peak shift of the 59.54 keV line is slower than 1 eV/h for all pixels for a 1 mm-thick detector biased at 300 V below $-8\,^{\circ}$C. Energy resolution was not the object of this study; this parameter is more difficult to model than peak position because trends can vary a lot from one pixel to another. At a given temperature, spectral stability varies in V/t^3 in first approximation; high voltages on thin detector ($L < 1$ mm, $V/L > 300$ V/mm) can be even more favorable. The current model of electric field explains well all the observable polarization phenomena in CdTe Schottky radiation detectors but is not accurate enough to be used to predict detector stability. It has to be refined taking into account both spectroscopic measurements and electric field measurements with Pockels effect. Next issue to tackle is the depolarization phase from the voltage switching off. Measurements in laboratory are on-going to properly describe the recovery phase and to propose in fine optimized scenarii of voltage cycling and annealing.

References

[1] T. Takahashi, K. Hirose, C. Matsumoto, K. Takizawa, R. Ohno, T. Ozaki, K. Mori, Y. Tomita, SPIE Proc. 3446 (1998) 29.
[2] R.O. Bell, G. Entine, H.B. Serreze, Nucl. Instr. and Meth. A 117 (1974) 267.
[3] T. Takahashi, R. Kelley, K. Mitsuda, H. Kunieda, R. Petre, N. White, the NeXt team, SPIE Proc. 7011 (2008) 701100-1.
[4] D. Götz, J. Paul, S. Basa, J. Wei, S.N. Zhang, J.L. Atteia, D. Barret, B. Cordier, A. Claret, J. Deng, X. Fan, J.Y. Hu, M. Huang, P. Mandrou, S. Mereghetti, Y. Qiu, B. Wu, IAP Conf. Ser. 1133 (2009) 25.
[5] K. Nakazawa, T. Takahashi, O. Limousin, M. Kokubun, S. Watanabe, P. Laurent, H. Tajima, SPIE Proc. 7732 (2010) 7732.
[6] P. Ferrando, A. Goldwurm, P. Laurent, O. Limousin, V. Beckmann and the COSPIX team, PoS (Texas 2010) 254, ⟨http://pos.sissa.it/⟩.
[7] H.B. Serreze, G. Entine, R.O. Bell, F. Wald, IEEE Trans. Nucl. Sci. NS-21 (1974) 404.
[8] H.L. Malm, M. Martini, IEEE Trans. Nucl. Sci. NS-21 (1974) 322.
[9] P. Siffert, J. Berger, C. Scharager, A. Cornet, R. Stuck, R.O. Bell, H.B. Serreze, F.V. Wald, IEEE Trans. Nucl. Sci. NS-23 (1976) 159.
[10] H. Toyama, A. Higa, I. Owan, M. Yamazato, T. Maehama, R. Ohno, M. Toguchi, IEEE Nucl. Sci. Symp. Conf. Rec. NS-6 (2006) 3694.
[11] A. Cola, I. Farella, Appl. Phys. Lett. 94 (2009) 102113.
[12] M. Taperio, N. Benjelloun, J.P. Zielinger, S. El Hamd, C. Noguet, J. Appl. Phys. 64 (1988) 4006.
[13] J. Kubát, H. Elhadidy, J. Franc, R. Grill, E. Belas, P. Höschl, P. Praus, IEEE Trans. Nucl. Sci. NS-56 (2009) 1706.
[14] L. Kronik, Y. Shapira, Surf. Sci. Rep. 37 (1999) 1.
[15] M.D. Kim, T.W. Kang, T.W. Kim, Solid State Commun. NS-99 (1996) 117.
[16] M. Ayoub, M. Hage-Ali, J.M. Koebel, A. Zumbiehl, F. Klotz, C. Rit, R. Regal, P. Fougères, P. Siffert, IEEE Trans. Nucl. Sci. NS-50 (2003) 229.
[17] A. Cavallini, A. Castaldini, D. Cavalcoli, B. Fraboni, IEEE Trans. Nucl. Sci. NS-54 (2007) 1719.
[18] A. Castaldini, A. Cavallini, B. Fraboni, J. Appl. Phys. 83 (1998) 2121.
[19] A. Cavallini, B. Fraboni, J. Appl. Phys. 94 (2003) 3135.
[20] H. Toyama, A. Higa, M. Yamazato, T. Maehama, R. Ohno, M. Toguchi, Jpn. J. Appl. Phys. 45 (2006) 8842.
[21] A. Cola, I. Farella, N. Auricchio, E. Caroli, J. Opt. A: Pure Appl. Opt. 8 (2006) 5467.
[22] K. Hecht, Z. Phys. 77 (1932) 235.
[23] A. Meuris, O. Limousin, F. Lugiez, O. Gevin, C. Blondel, F. Pinsard, M.C. Vassal, F. Soufflet, I. Le Mer, Nucl. Instr. and Meth. A 610 (2009) 154.
[24] F. Lugiez, O. Gevin, P. Baron, E. Delagnes, O. Limousin, IEEE Nucl. Sci. Symp. Conf. Rec. NS-2 (2006) 841.
[25] G. Sato, T. Fukuyama, K. Hagino, H. Ikeda, S. Ishikawa, J. Katsuta, M. Kokubun, K. Nakazawa, H. Odaka, M. Ohta, S. Saito, T. Sato, T. Takahashi, S. Takeda, T. Tanaka, S. Watanabe, IEEE Nucl. Sci. Symp. Conf. (2010) talk R09-3.

normalized peak area becomes inferior to 0.9 and the time from which apparent peak position is more than 200 eV below the linear trend observed in the operational phase before the break. Standard deviations on polarization time values are estimated to be ~10% over the 22 pixels, including errors of estimation with the defined criteria.

3.2. Results

Fig. 10 shows influence of temperature on polarization time for 3 series of measurements. The exponential trend is confirmed; however, the activation energy of polarization time, interpreted as the energy level of deep acceptors, is equal to ~1.0 eV. This mean value is the result of full characterizations of 44 pixels from 2 different samples in 2 voltage conditions and 6 temperature conditions. This value is much higher than the 0.6–0.7 eV values reported by Toyama and Cola [10,11]. It is nevertheless in good agreement with spectroscopic results from Sato et al [25]. Fig. 11 shows influence of temperature on peak shifts. We demonstrate here that peak shift during the operational phase (before efficiency loss) follows the exponential trend predicted by our simulations. Error bars correspond to standard deviation over the 22 studied pixels. The peak recorded by one pixel can shift
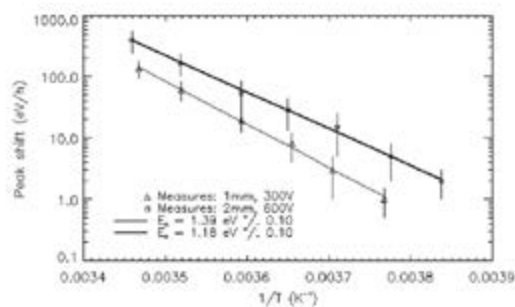
with time twice faster as the peak of another pixel of the same matrix, leading to an important dispersal of the peak shift values. The activation energy measured for peak shift is 1.2 ± 0.2 eV. Practically, these results underline that thin CdTe detectors moderately cooled can be remarkably stable: peak shift at 60 keV with a 1 mm-thick detector is less than 1 eV/h for temperatures lower than $-8\,^{\circ}$C and bias voltage higher than 300 V. If data of Fig. 10 are extrapoled to lower temperatures, we can assert that this detector can be continuously operated at 300 V below $-20\,^{\circ}$C during at least 1 month.

Fig. 12 shows influence of voltage on polarization time for 1 and 2 mm-thick detectors cooled down to 0 °C. The linear trend predicted by Eq. (6) is confirmed for the 2 mm-thick detector; it is also valid for the 1 mm-thick sample up to 250 V. It can be also noticed that, with a 200 V voltage, the 1 mm-thick detector is stable for 14 h whereas the 2 mm-thick detector is stable for less than 1 h; this is not compliant with the predicted quadratic dependency of polarization time with thickness. According to Figs. 10 and 11, a 2 mm-thick detector is around 4 times less stable than a 1 mm-thick detector for a given voltage to thickness ratio. This trend was confirmed with a 0.5 mm-thick detector; applying 200 V/mm at 0 °C results in polarization times of 50, 14 and 3.3 h for 0.5, 1 and 2 mm-thick detectors, respectively. Stability of Schottky CdTe detectors is better explained by an L^{-3} law. As a consequence, a stack of thin detectors is much more favorable from a stability point of view than thick detectors for gamma spectrometry. From a system point of view, that requires less cooling power but that increases complexity of electrical architecture.

4. Discussions

Experimental results question the expression of the polarization time and thus, the model of electric field. The activation energy of polarization time and peak shift is not compliant with measurements of detrapping times by other authors [10,11]. Another thermal effect has to be taken into account to explain spectral response of Schottky CdTe detectors. The concentration of ionized deep acceptors N_T^- of Eq. (4) is based on the assumption that levels are empty if they lie above the Fermi level. This zero-temperature approximation makes it possible to solve the Poisson equation analytically; in reality, the probability for deep acceptor levels to be ionized i.e. occupied by electrons before biasing the
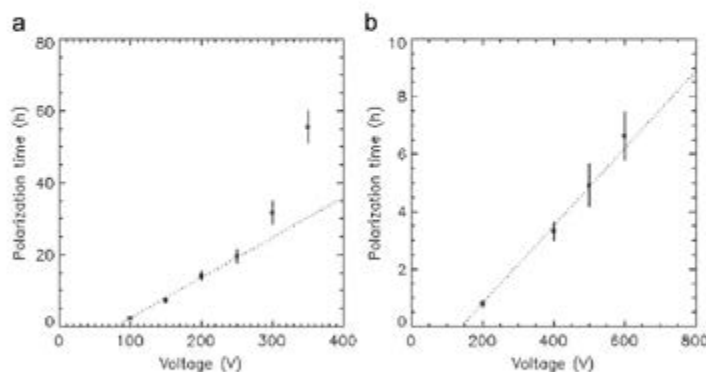

Fig. 11. Peak shifts experimentally evaluated with 2 CdTe Schottky pixel detectors cooled down from -13 to $+16$ °C and biased at 300 V/mm. Error bars correspond to standard deviations over the 22 pixels studied. Data can be modeled by Boltzmann laws with energies between 1.2 and 1.4 eV.

Fig. 12. Influence of bias voltage on detector stability for 2 CdTe Schottky pixel detectors cooled down to -7 °C. Error bars correspond to standard deviation over the 22 pixels studied: (a) Polarization time values for a 1 mm-thick sample. Data can be approximated by a linear law for voltages lower than 250 V (dotted line). (b) Polarization time values for a 2 mm-thick sample. Data can be approximated by a linear law over the full tested voltage range (up to 600 V).

3. IDeF-X: CdTe detectors dedicated front-end microelectronics

3.1. IDeF-X family, from V0 to HD

In parallel to CdTe detectors studies, we initiated in 2003 the development of dedicated microelectronics front-end circuits series for Cd(Zn)Te detectors, taking into account the specific characterisitics of our diodes as described in the previous section, and the need to use these circuits in a harsh environment. Thus, radiation hardness and reliability were central preoccupations in this phase of the development work. We created the IDeF-X circuit family, IDeF-X standing for Imaging Detector Front-end for X-rays.

The main requirements for the circuit were defined as follows:
- Low noise charge sensitive preamplifier (CSA) adapted to low dark current in the range of ~10 pA or below, scaled for low stray capacitance at the input in the range of 2-5 pF in total.
- Self triggered system.
- Integrated filters.
- Individual spectroscopy channels.
- Multiplexing output system.
- Fully programmable.
- Use of a commercially available sub-micron technology, analog design oriented.

The first design we made was IDeF-X V0. It is a test chip realized using the AMS[3] 0.35 μm CMOS standard technology. It consists of a set of CSAs based on a classical "folded cascode amplifier" structure, with NMOS or PMOS input transistors of different sizes and shapes. The CSA is designed to be DC coupled to the input of a detector pixel. The CSA integrates the incoming charge into a feedback capacitor and converts charge into a voltage. The feedback capacitor is discharged by a continuous reset system achieved with a PMOS transistor that can source the leakage current of the detector. The optimized CSAs are connected preferably to the anode of a detector.

The goal of this preliminary circuit was to explore the noise performance, realize first spectroscopic measurements with CdTe samples and choose the most appropriate design for a more advanced version of the circuit. The first chip was realized in my R&D team by Olivier Gevin and Francis Lugiez (Irfu/SEDI) and gave promising results that enabled the following versions. In particular, we demonstrated that the most suited CSA could reach a 33 e- rms noise floor, *i.e.* without any detector connected at the input. This result appeared promising as it was already far below the 60 e- rms limit defined above. In addition, we immediately tested the Total Ionizing Dose tolerance of the CSAs up to 200 krad. We demonstrated that the design was robust to radiation and we identified the noise degradation was solely due to the input pads protection diodes of the circuit, the unique feature used from the standard library.

The results obtained with this test chip were published in IEEE Transaction on Nuclear Sciences in 2005 in the paper "IDeF-X ASIC for Cd(Zn)Te Spectro imaging Systems". The paper is attached to the next section [4.32].
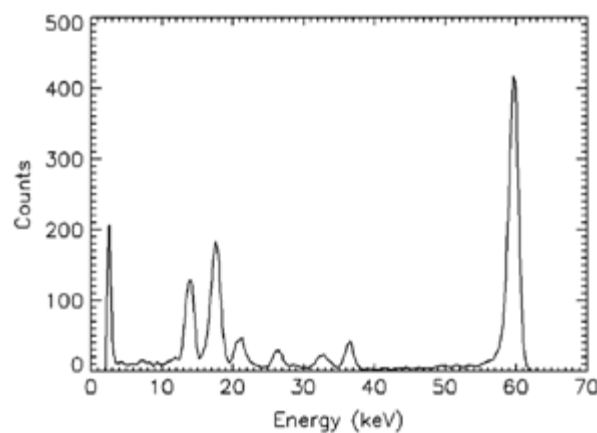

Figure 21. Spectrum of CdTe Schottky diode connected to CSA#3 of IDeF-X V0, illuminated with a Am-241 source. The energy resolution is found to be 1.6 keV FWHM at 60 keV at room temperature. The threshold is measured at 3 keV.

---

3. Austria Micro Systems.

Providing good results, we developed right after a more sophisticated version of the circuit. IDeF-X V1.0 [3.50 and 4.27] is a non-programmable analog circuit without any logic inside but 16 parallel miniature spectroscopy channels. The structure of the circuit is 1D, *i.e.* all channels positioned parallel side by side. The channels share the power rails. One input and one output pad per channel.

After our favorite PMOS CSAs suited of 2-5 pF detectors, the second stage of the chain is a pole zero cancellation stage (PZC). Placed after the CSA, it avoids long duration undershoots at the output. It is also used to amplify the signal and minimizes the influence of the leakage current on the transfer function of the whole channel. The two very front-end stages are followed by a filter stage. A fourth order shaper optimizes the signal to noise ratio; it is achieved by two second order Sallen and Key low pass filters (S&K) in series with variable shaping times. Thus the peaking time is programmable from 1 to 10 μs. This parameter allows the user to set the best filter according to the input capacitance (hybrid and detector geometry) and the real detector leakage current, depending on the operating temperature, detector geometry and applied voltage.

The noise performance was found to be uniformly excellent as evidenced by the spectrum of Figure 19. Apart the excellent energy resolution of 1 keV FWHM at 60 keV and 700 eV FWHM at 14 keV at room temperature, one can notice the low threshold value down to 2 keV. This major result was remarked by Jacques Paul who immediately thought to use such a technology in a Space hard X-ray camera for Gamma Ray Burst detection at cosmological distances. As a matter of fact, extending a hard X-ray instrument from few keV up to 250 keV was innovative. This property of our circuits is still valid today.

Behind that, we further developed the circuit to include some preliminary system logic, but not yet programmable, such as a discrimination system, a peak detector and a multiplexer at the analog output. In this version of the circuit, the low threshold discrimation level is set in common for all the 16 channels by tuning an external reference voltage. This design is affordable because we demonstrated the excellent uniformity of our CdTe pixel arrays in parallel. On this ASIC version, we ran our first latch-up evaluation at UCL with the support of CNES (F. Malou) to determine the LET threshold of the digital part of the circuit. We found the chip slightly sensitive with a threshold about 10 MeV.cm^2.mg^{-1}. IDeF-X V1.1 [3.42 and 3.48] used precisely the same filtering stage as V1.0 but could be integrated in a multi-chip design for Caliste-64.

During the integration of Caliste-64 demonstrated further in the text, we pursued our development to a 32 channels circuit: IDeF-X V2. This time, the discrimination threshold is programmable (6-bit DAC) for each individual channel. A global trigger is built from the logical OR of the outputs of all the 32 individual discriminators. If at least one channel is hit, a trigger signal is sent out of the chip and wakes up the sequencer to initiate the readout sequence. IDeF-X chip responds with a serial digital pattern corresponding to the hit channel addresses. Then, the energy readout starts for hit channels only or any desired channel according the readout mode: the outputs of the peak detectors are successively multiplexed on the analog output via the common output buffer.

We payed a lot of attention to the sensitivity to latch-up and redesigned the circuit accordingly. This version will be integrated later in Caliste-256. A corrected version of the chip was specially realized for the ECLAIRs telescope and the production was realized in 2007. We demonstrated at this occasion the improvement of the SEL threshold above 56 MeV.cm^2.mg^{-1}; very encouraging but not yet SEL free. This circuit has been completely space qualified and will fly in 2023 on board SVOM/ECLAIRs. In the meantime, we have developed a new version of our chip in order to be able to readout silicon diodes by the cathode, inverting the input signal. The resulting circuit IDeF-X BD is also space qualified and has flown on CINEMA trio nanosat program (collaboration with SSL/UCB) and will fly on Solar Orbiter on the EPD/STEP instruments in 2018.

Table 4. Main properties of IDeF-X V1.1 and IDeF-X V2.

Parameter	IDeF-X V1.1	IDeF-X V2
Chip size	3000 μm x 4000 μm	2800 μm x 6400 μm
Number of channel	16	32
Power supply	3.3 V	3.3 V
Power consumption	2.8 mW/channel	3 mW/channel
Gain	200 mV/fC	200 mV/fC
Dynamic range	60 ke-	50 ke-
Peaking times	0.9-9.6μs	0.9-9.6μs
Discrimination threshold	0 to 5 ke- (Common to all channel)	210 e- to 4 ke- (LSB = 65 e-)
Radiation hardened design	No	Yes
SEL LET	12 MeV.cm^2.mg^{-1}	56 MeV.cm^2.mg^{-1}
Noise	37 e- + 7 e-/pF	33 e- + 7 e-/pF

Characteristics of IDeF-X V1.1 and IDeF-X V2 are summarized in Table 4.
The best Equivalent Noise Charge (ENC) was found to be 33 electrons rms in all chip versions. In a complete detection system, the ENC increases with as formalized in Eq. 14:
  • The dark current of the detector in each pixel: The latter contributes to parallel noise
  • The total stray capacitance at the ASIC CSA input: Including detector and interconnections. Stray capacitance contributes to series and 1/f noise.

The ENC characteristics of IDeF-X can be modeled as follows:

$$ENC^2 = C_{\text{tot}}^2 \cdot \left(\frac{\alpha_s}{\tau} + \alpha_f \right) + \alpha_p \cdot I_L \cdot \tau \qquad \text{(Eq. 14)}$$

where:
α_s, α_f, α_p are ASIC parameters characterizing the series noise, the 1/f noise and the parallel noise respectively.
  • τ is the peaking time.
  • I_L is the leakage current.
  • C_{tot} is the total input capacitance. In a complete detector, C_{tot} is the sum of three terms: C_{int}, the input capacitance of the chip estimated to be ~4 pF, C_{body} the stray capacitance of the routing from the ASIC to the detector interface and C_{det} due to the detector capacitance (bulk and neighboring pixels) and the bump bonding interface.

The dark current may vary according to operating conditions (voltage and temperature) while capacitances are fixed once the design of the hybrid is done (track length, routing and materials). That has to be minimized in the hybrid component definition.

In the section 4.5.3.3, I will describe in detail the latest and ultimate version of our circuit family: IDeF-X HD.

3.2. Paper #3: IDeF-X ASIC for Cd(Zn)Te Spectro-imaging Systems

IDeF-X ASIC for Cd(Zn)Te Spectro-Imaging Systems

O. Limousin, O. Gevin, F. Lugiez, R. Chipaux, E. Delagnes, B. Dirks, and B. Horeau

Abstract—Progress in the fields of Cd(Zn)Te detector development, microelectronics, and interconnection technologies open the way for a new generation of instruments for physics and astrophysics applications in the energy range from 1 to 1000 keV. Cd(Zn)Te based instruments operating in the range between −20 and 20 °C will offer high spatial resolution (pixel size ranging from $300 \times 300 \ \mu m^2$ to few mm^2), high spectral response, and high detection efficiency. To reach these goals, reliable, highly integrated, low-noise, and low-power consumption electronics is mandatory. Our group is currently developing a new full custom ASIC detector front-end named IDeF-X, for modular spectro-imaging systems based on the use of Cd(Zn)Te detectors. We present here the first version of IDeF-X that consists of a set of ten low-noise charge sensitive preamplifiers (CSA). It has been manufactured using the AMS 0.35 μm CMOS technology. The CSAs are designed to be DC coupled to detectors having low dark current at room temperature. We have optimized the various preamplifiers to match detector capacitances in the range from 0.5 to 30 pF.

Index Terms—CdTe, Cd(Zn)Te, analogue front-end, ASIC, X- and gamma-ray spectroscopy, .

I. INTRODUCTION

SINCE our previous development, the IBIS/ISGRI gamma-ray camera [1] on board the INTEGRAL Satellite, we have demonstrated that it is possible to reliably use a large number of CdTe detectors associated with microelectronics front-end in space. On the other hand, progress in the manufacturing of CdTe detectors in terms of crystal quality and volume size and progress in the field of microelectronics and interconnection technologies open the way for a new generation of 1 to 1000 keV photon energy detectors for physics and astrophysics. The next generation of instruments based on these technologies will have high spatial resolution (pixel size: $\sim 300 \times 300 \ \mu m^2$ to few mm^2), high spectral response, and high detection efficiency operating in the range between −20 and 20 °C. To reach these goals, reliable, highly integrated, low-noise, and low-power consumption electronics is mandatory.

Our group is currently developing a new modular spectro-imaging system based on CdTe detectors coupled to a dedicated full custom readout ASIC, named IDeF-X for Imaging Detector Front-End. This device will be used in large area cameras (100 to 1000 cm^2) for space borne astrophysics, either on focusing

TABLE I
IDeF-X CSAs CHARACTERISTICS

CSA #	Input transistor type	Input transistor size W/L ($\mu m/\mu m$)	Input capacitance range (pF)	Detector application
0	PMOS	310/0.5	0.5	NA (no pad)
1	PMOS	1000/0.5	2 to 5	Cd(Zn)Te
2	PMOS	1550/0.35	5 to 10	Cd(Zn)Te
3	PMOS	1600/0.5	5 to 10	Cd(Zn)Te
4	PMOS	1400/0.75	5 to 10	Cd(Zn)Te
5	NMOS	1550/0.35	5 to 10	Cd(Zn)Te
6	NMOS	1600/0.5	5 to 10	Cd(Zn)Te
7	NMOS	1400/0.75	5 to 10	Cd(Zn)Te
8	PMOS	4000/0.5	30	cooled Ge
9	PMOS	2700/0.75	30	cooled Ge

telescope (e.g., SIMBOL-X [2] and MAX [3]), operating in hard X-rays (4 to 150 keV) or gamma-rays (511 and 847 keV), or on a large area detector for coded aperture instruments (4 to 600 keV) (e.g., ECLAIR's [4]).

This paper is structured as follows: Section II presents the IDeF-X ASIC design. Section III discusses its performance in terms of noise measurements, and the spectral response of one of the charge sensitive preamplifiers (CSAs) connected to a set of moderate capacitance CdTe detectors (<5pF). Finally, Section IV is devoted to the results of Total Ionizing Dose tests performed on the chip with a ^{60}Co source up to 224 krad.

II. IDeF-X ASIC DESIGN

The development of the IDeF-X front-end ASIC will include several steps from its first version as a set of stand-alone preamplifier prototypes to a complex multichannel (32 to 256) circuit for high-pixel density CdTe readout. We present here the very first version of IDeF-X.

The goal of this first prototype is to evaluate the AMS 0.35 μm CMOS technology capabilities for low-noise and low-power consumption analog design (less than 60 electrons noise rms for 50 μW per CSA). Therefore, we have built a set of ten low-noise CSAs, well suited to high-energy detectors.

The CSAs are designed to be DC coupled to detectors with a low dark current (<5 nA). The geometry of the input transistors (W/L) has been optimized for detector capacitances in the range of 0.5 to 30 pF (see Table I). Most of the CSAs (#1 to #7) are designed for low-capacitance detectors like Cd(Zn)Te small crystals or pixels. Nevertheless, we have also designed two CSAs (#8 and #9) matching larger detector capacitance (e.g., cooled germanium). CSAs were defined to study the $1/f$ noise behavior with respect to the type (NMOS and PMOS) and gate length (L) of the input transistor. In order to secure the tests, the input pads are equipped with anti-ESD protections.
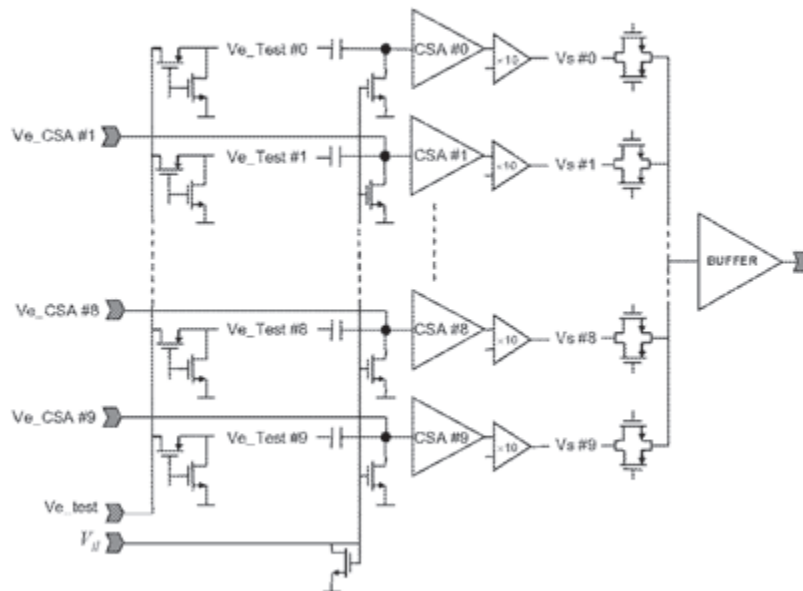
Fig. 1. IDeF-X synoptic: Ten CSAs are placed before a gain amplifier, a multiplexer directed to a low-impedance output buffer. At the input, each CSA has its own test capacitor. All CSAs are connected to a pad except CSA #0.

The CSA electrical design is based on a "folded cascode amplifier" [5], [6] with either a PMOS or a NMOS input transistor. The value of the feedback capacitance is 300 fF for CSAs #0 to #7, and 500 fF for CSAs #8 and #9. The DC feedback is done by a PMOS transistor biased by the detector leakage current. Each CSA output is connected to a $10\times$ voltage gain stage.

These stages are multiplexed toward a low-output impedance buffer. All channels are connected to an input pad except CSA #0. Inputs can be connected to a test input Ve_test with an individual 300 fF and 500 fF on-chip injection capacitor, respectively for CSAs #0 to #7 and CSAs #8 and #9.

On the other hand, in order to simulate a detector current or to compensate a reverse detector current, each channel includes a tunable current source il driven by the gate voltage V_{il} (Fig. 1). The IDeF-X layout is represented in Fig. 2.

III. RESULTS

A. Equivalent Noise Charge Measurements

The first characterization of the circuit consists in measuring the Equivalent Noise Charge (ENC) of each channel as a function of the peaking time when the CSA is placed at the input of a tunable $CR–RC^2$ or $CR–RC$ filter. To perform the measurements, the circuit is packaged into a standard JLCC chip-carrier and mounted on a standard printed circuit board (PCB) into the setup described below.

1) ENC Measurements Test Bench: The JLCC carrier is mounted on a test board allowing biasing, configuration, injection, and response measurements. This board is inserted in an automatic ENC versus peaking time test bench shown in Fig. 3,
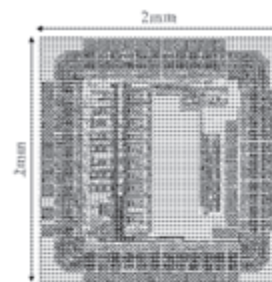

Fig. 2. IDeF-X layout. Ten preamps are placed on the left-hand side of the 4 mm^2 circuit.

[7]. This setup includes a $CR–RC^2$ filter with tunable peaking times ranging from 20 ns up to 10 μs. It also includes a wave form generator. The pulse shapes and the noise are alternately recorded on a digital oscilloscope for the various filtering time-constants and analyzed with a computer. ENC measurements for larger peaking times (up to 1 ms) are done manually with a $CR–RC$ filter but are not performed systematically.

2) Main ENC Results for All of the CSAs: A significant part of the noise is due to the setup itself (JLCC parasitic capacitance, connectors, PCB parasitic capacitance, and dielectric losses). Therefore, we have performed two types of ENC measurements.

In the first, the inputs were totally disconnected from the setup—no bonding on the inputs—in order to measure the intrinsic performances of the circuit, i.e., the floor noise of each CSA.
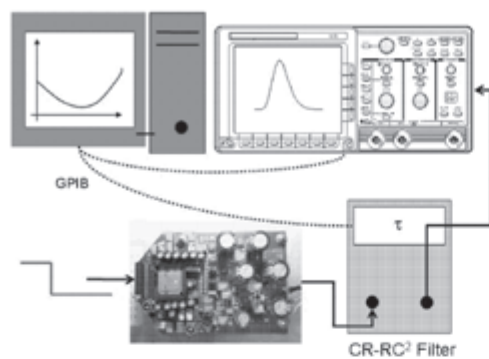
Fig. 3. Setup for ENC measurement is operated with an external programmable *CR–RC²* shaper.

In the second, the inputs were connected to the JLCC carrier with wire-bonding thus allowing the chip to be used with a detector. Nevertheless, the JLCC input pads were not connected to the PCB nor to the connector. Detectors were installed directly on the JLCC by wire soldering.

Note that forthcoming ENC evaluation on new IDeF-X versions will be done using a ceramic board (or another type of low dielectric loss factor material), to maximize the chip's performances.

We measured the ENC for each of the ten CSAs without bonding, the results of which are shown in Table II. These measurements illustrate the intrinsic performances without assumption on the setup quality. Depending on the input transistor type and size, the floor noise was found to be between 29.2 and 49.3 electrons rms. In this set of tests, the CSAs were polarized with 1 mA/3.3 V to reach the very best performances.

We have estimated the influence of additional parasitic capacitances on the noise of each CSA. The measurements were taken with a 9 μs peaking time for PMOS type CSAs and 4.5 μs for the NMOS type (values for minimizing the noise level when no detector is connected). We obtained 3 to 5 electrons/pF for PMOS type CSAs and 5 to 6 electrons/pF for NMOS type.

In the following sections, we will concentrate on the PMOS type CSA #0 and CSA #3, and on the NMOS type CSA #6, to analyze their performance in greater detail. Those were chosen for the following reasons:

—CSA #0 does not have any input pad and thus can be used as a reference for the design noise behavior (not sensitive to external noise sources).

—The PMOS CSA #3 has the least noise among the CSAs of the same type optimized for the range from 5 to 10 pF (see Table I). This preamplifier best matches the typical CdTe pixel detector capacitance.

—The NMOS CSA #6 was used to test the NMOS type and because it has the same input transistor dimensions as CSA #3.

3) ENC Versus Peaking Time for CSA #0, #3 and #6: We have measured the ENC versus peaking time characteristics with the CSAs input pads bonded to the JLCC chip carrier without connecting any detectors. The minimum noise level in

TABLE II
IDeF-X CSA Main Performances

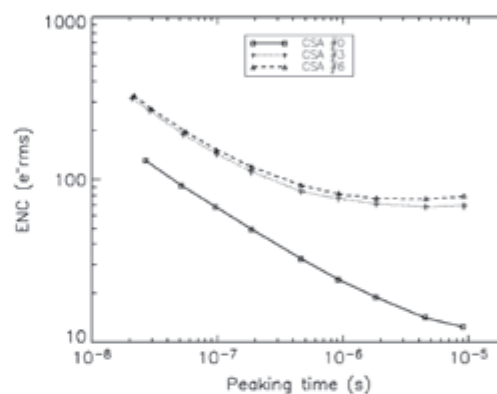| CSA #	Min ENC (electrons rms)	Peaking time at ENC min (μs)
0	12.4 (no pad)	8.9
1	31.5	9.1
2	33.1	9.1
3	32.3	9.1
4	34.1	9.1
5	44.8	4.5
6	49.3	4.5
7	47.6	4.5
8	30.4	4.5
9	29.2	4.5

Fig. 4. ENC versus peaking time measurement results for CSA #0, CSA #3, and CSA #6. The CSA #0 has no input pad. On CSAs #3 and #6, the inputs are connected to the JLCC chip carrier but no detector is present. CSAs are biased with 1 mA current through the input transistor.

the ENC versus peaking time characteristics was 69 electrons rms at 9.1 μs for the PMOS type input transistor (CSA #3) and 76 electrons rms at 4.5 μs peaking time for the NMOS input transistor (CSA #6). In NMOS type CSAs, injection of a current *il* is required for proper response. This current compensates the reverse current from the anti-ESD input diodes but adds a parallel noise contribution to the ENC versus peaking time characteristics. This is the reason why the minimum value of the noise occurs for shorter peaking times than in the PMOS case where no additional current is necessary. On CSA #0, without input pad, we can measure intrinsic performances and limits of the design. Its minimum noise level is 12.4 electrons rms for a 9.1 μs peaking time. ENC versus peaking time characteristics are plotted for CSA #0, CSA #3, and CSA #6 in Fig. 4.

4) ENC Behavior With Different Biasing Conditions: Until now, our tests were performed under conditions of high power consumption—3.3 mW, i.e., 1 mA. The power consumption can be reduced by limiting the total current I_0 passing through the input transistor. We have recorded the noise behavior of the CSA #3 as a function of I_0 (200 μA, i.e., 660 μW, and 50 μA, i.e., 165 μW) and present the results in Fig. 5. As expected, when the total current I_0 in the CSA is reduced, the series noise increases. The series noise is inversely proportional to the square root of the input transistor transconductance g_m (see (1)), and roughly inversely proportional to the square or fourth root of I_0 ((2) and
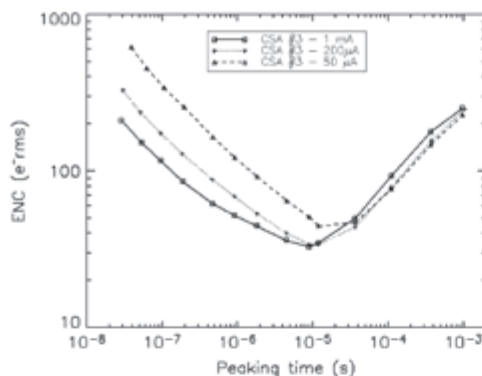
Fig. 5. ENC versus peaking time as a function of the bias current in the CSA #3 input stage of IDeF-X. The ENC are obtained on a chip without input bonding to avoid noise due to the setup conditions (PCB, JLCC, connector contributions).

(3)) depending on the input transistor regime (weak, moderate, or strong inversion).

$$\mathrm{ENC}^2_{\mathrm{series}} \propto \frac{C_t^2}{g_m} \qquad (1)$$

$$g_m \text{ strong inversion} = \sqrt{2\mu C_{\mathrm{ox}} \frac{W}{L} I_0} \qquad (2)$$

$$g_m \text{ weak inversion} = \frac{I_0}{n} \frac{q}{kT} \qquad (3)$$

where :

For instance, the PMOS CSA #3 operates in weak inversion when $I_0 = 50 \,\mu A$ and $I_0 = 200 \,\mu A$ and operates in strong inversion when $I_0 = 1$ mA.

For long peaking times (above 8 μs), the parallel and $1/f$ noise contributions begin to dominate and the influence of the bias condition on the ENC drops significantly.

We conclude that our design can be easily used in a low-power input stage if large peaking times (> 8–$10 \,\mu$s) are applicable. This requires detectors with leakage current as low as possible. This current has to be lower or equal to the chip internal leakage currents we found to be primarily due to the anti-ESD diodes of the input pads. The dark current has to be less than few picoamperes, as shown in Section IV. A moderately cooled—around 0 °C—Schottky CdTe detector or pixel CdZnTe detector can reach such values.

B. Spectroscopy Measurements

These promising results allowed us to consider a direct application for spectroscopy. We connected the PMOS CSA #3 of IDeF-X biased with $I_0 = 200 \,\mu A$ (660 μW) to a set of CdTe detectors at room temperature (21–24 °C). The detectors were DC coupled to the input of the CSA, whose output was connected to a Canberra 2025 amplifier with an adjustable Gaussian shaping time in the range of 0.5 to 12 μs, corresponding to a peaking time of 1.5 μs to 36 μs.

First, we plugged a $2 \times 2 \times 2$ mm^3 Travelling Heater Method grown (THM) CdTe detector (Eurorad) equipped with quasi-ohmic platinum electrodes. This detector showed a dark current
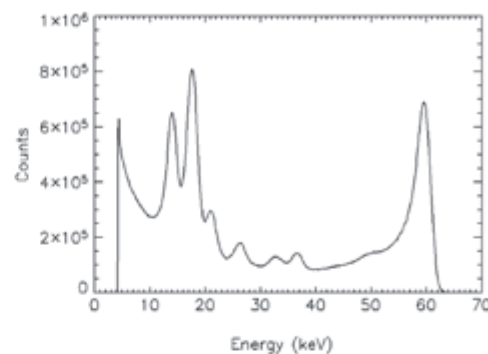

Fig. 6. Spectrum of a ^{241}Am source obtained with a $2 \times 2 \times 2$ mm^3 CdTe detector equipped with Pt contacts on both electrodes (EURORAD, France) plugged on CSA #3, biased with 200 μA. The detector is biased under 100 V at 24 °C. The spectral response is good (3.5 keV FWHM at 59.5 keV). The broadening on the left-hand side of the 59.5 keV line is mainly due to the charge loss and ballistic deficit in the 2 mm thick CdTe.

of 5 nA when biased at 100 V (24 °C). The intrinsic capacitance of the CdTe detector is $\sim$0.2 pF. However, this value is negligible compared to the other parasitic and interconnection capacitances of the setup that amount to $\sim$5 pF. The lowest noise was obtained for a 0.5 μs shaping time. As a matter of fact, the parallel noise increases rapidly with the shaping time because the current is not negligible. The series and $1/f$ noise are moderate thanks to the low input capacitances. We obtained satisfactory lines with a 3.5 keV FWHM at 59.5 keV and 2.2 keV FWHM at 17.8 keV (see Fig. 6).

Using the same setup, we connected CSA #3 to a $4.1 \times 4.1 \times 0.5$ mm^3 THM grown CdTe (ACRORAD) equipped with a Schottky contact at the anode and a guard ring at the cathode (1 mm guard ring surrounding the 2×2 mm^2 pixel). The reverse dark current of the CdTe diode is very low (<10 pA under 200 V bias voltage at 21 °C) and the capacitance of the pixel is 0.7 pF. The spectrum shown in Fig. 7 illustrates the results with 2 μs shaping time: 1.6 keV FWHM at 59.5 keV and 1.4 keV FWHM at 13.8 keV.

In the ISGRI CdTe gamma camera equipped with mixed analog and digital ASIC [1], [8], [9], 2.8 mW power consuming per channel, the best spectral resolution measured during the ground calibration phase, with $4 \times 4 \times 2$ mm^3 THM CdTe crystals (ACRORAD), biased under 100 V at 0 °C, was 5.6 keV FWHM at 60 keV.

IV. IRRADIATION WITH ^{60}Co

Since the development of the IDeF-X ASIC is intended for future space-borne application in astrophysics, it was necessary to evaluate our first prototype's sensitivity to radiation. We irradiated two IDeF-X circuits with a 589 GBq ^{60}Co source during 224 hours. The ASICs were placed 13 cm from the source and were thus subjected to a 1 krad/h dose rate. We performed a set of nine irradiation tests starting from 10 up to 224 krad of accumulated dose.

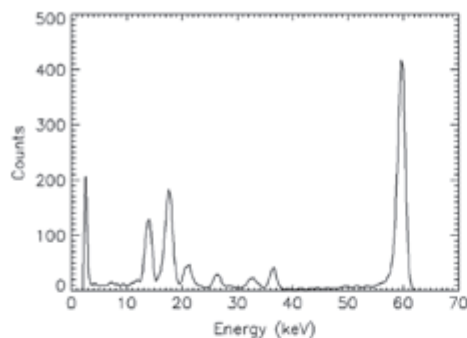One chip was used to analyze the behavior of the PMOS type CSA #3 and another for the NMOS type CSA #6. Both CSAs

Fig. 7. Spectrum of a ^{241}Am source obtained with a $4.1 \times 4.1 \times 0.5$ mm^3 CdTe detector equipped with a Schottky contact at the anode (ACRORAD, Japan) plugged on CSA #3, biased with 200 μA. The cathode is 2×2 mm^2 pixel surrounded by a 1 mm guard ring. The detector is biased under 200 V at 21 °C. The spectral response is very good (1.6 keV FWHM at 59.5 keV and 1.4 keV FWHM at 13.8 keV). The very low threshold value around 3 keV is noticeable.
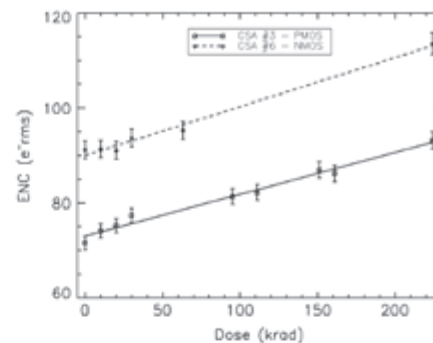

Fig. 8. Minimum of the ENC versus peaking time characteristics as a function of the absorbed dose in PMOS CSA #3 and NMOS CSA #6. Both CSAs are polarized under 200 μA /3.3 V conditions. A linear function fits both sets of data.

were correctly biased to ensure their functionality during the runs with a 200 μA current in the input transistor. All other CSAs in the chip were also biased but not multiplexed to the output and, therefore, not systematically monitored. During the irradiation runs, the injected current il in the reset transistor of the NMOS type CSA#6 was raised high enough to compensate a potential shift of the internal leakage current, minimizing the effect of this shift on the preamplifier that could cause it to stop working. The spectral response of the two circuits was monitored during each irradiation stage. A calibrated injected signal was sent to the ASIC inputs and we recorded the response using a 3 μs shaping time amplifier (ORTEC DUAL SPEC 855) and a standard acquisition chain. Between irradiation runs, the two CSAs #3 and #6 were fully characterized (ENC, gain, rise-time, and fall-time, polarization currents) with the test bench described in Section III-A-1. During fine characterization, the compensation current il of the NMOS CSA #6 was readjusted to its optimal minimum value.

A. Results

1) Amplification Gain: We monitored the amplification gain of the CSAs throughout the irradiation, and measured the output voltage level directly after the output buffer. No shift was found in either the PMOS or the NMOS type CSAs. The amplitude was found to be constant at 37 mV and 35.5 mV respectively for the CSA #3 and #6 when a 4 mV square signal was injected through the 300 fF internal injection capacitor.

2) Output Signal Rise-Time and Fall-Time: The signal output rise-times were also found to remain constant in both CSAs at 35 ns and 38 ns for the CSA #3 and #6. However, we noticed that the irradiation caused slight changes in the output signal fall-times in both preamplifiers:

—CSA#3: For this type of preamplifier, the current through the reset transistor is very low in nominal conditions ($\sim$380 fA). Consequently, the output signal fall-time is long ($>$ 35 ms). Fall-time decreased to 13 ms after

95 krad, and dropped to 10 ms after 224 krad. This effect is typically associated with an increase in the current I_R through the reset transistor that acts as a feedback resistor R_R, inversely proportional to I_R (see (4)). After 224 krad, the current through the reset transistor was found to be $\sim$1.5 pA.

$$R_R = \frac{1}{I_R} n \frac{kT}{q} \qquad (4)$$

—*CSA #6:* For this type of preamplifier, we had to tune the compensation current il after each run in order to reach fall-time values as long as possible. Therefore, the evolution of the fall-time is not directly related to the effects of irradiation. We will detail this point later in the paper.

3) Power Consumption: At the end of the campaign, we measured the power consumption (current level in the 3.3 V power supply) and we concluded it was not affected by the irradiation. The measured current is the total current of the circuit (ten CSAs, amplifiers, multiplexer, and output buffer). It is not possible to distinguish the NMOS from the PMOS CSAs in this case.

4) ENC Measurements: We systematically measured the ENC versus peaking time characteristics of the CSA #3 and CSA #6. As shown in Fig. 8, the minimum ENC increases linearly with increasing dose. Furthermore, the two CSAs appeared to be slowly degrading at a similar rate (0.09 and 0.1 electrons rms/krad respectively for PMOS and NMOS type CSA). The minimum ENC values were found to be between 1.8 and 4 μs peaking time for the NMOS CSA. This short peaking time was constrained by the compensation current il, unfortunately causing a strong parallel noise structure. But for the PMOS CSA, the minimum ENC values occurred at 9 μs peaking time until 111 krad. For higher doses, the minimum ENC occurred at 4.5 μs peaking time which is typically associated with a progressive increase of the parallel noise contribution.

In order to monitor the evolution of the CSAs response following the irradiation campaign, these were annealed for two
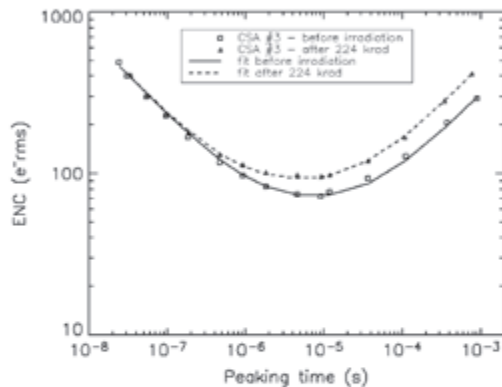
Fig. 9. ENC versus peaking time for the CSA #3 before and after 224 krad of irradiation. CSA #3 is polarized with 200 μA current through the input transistor. Lines represent the noise model that fits the data.
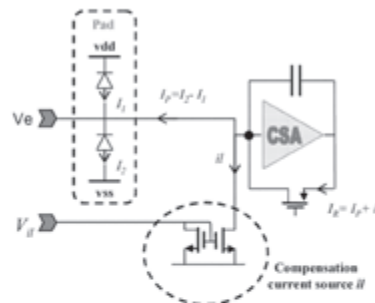

Fig. 10. Scheme of the CSA. Definition of the currents: I_1 and I_2 are the reverse bias diode currents of the pad, il is the compensation current (or residual current when $V_{il} = 0$ V), I_R is the current through the reset transistor.

months at room temperature. No further postirradiation degradation or recovery was observed, and the circuit characteristics remained remarkably stable.

B. Discussion

In this section, we focus on the analysis of the noise structure for the PMOS and NMOS CSAs, before and after the 224 krad irradiation dose. Results and parameters are derived by fitting the following (5)–(8), [10] to the ENC versus peaking time characteristics data:

$$\text{ENC}^2_{\text{series}} = A \times \frac{C_t^2}{g_m} \times \frac{1}{\tau_P} \qquad (5)$$

$$\text{ENC}^2_{//} = B \times 2q(il + Ip + I_R) \times \tau_P \qquad (6)$$

$$\text{ENC}^2_{1/f} = C \times \frac{C_t^2}{WL} \qquad (7)$$

$$\text{ENC}^2 = \text{ENC}^2_{\text{series}} + \text{ENC}^2_{//} + \text{ENC}^2_{1/f} \qquad (8)$$

where:

$\text{ENC}_{\text{series}}$	equivalent series noise charge;
$\text{ENC}_{//}$	equivalent parallel noise charge;
$\text{ENC}_{1/f}$	equivalent $1/f$ noise charge;
I_p	total current from the pads as defined in Fig. 10;
A and B	constants that depend on the filter order;
C	constant that depends on the filter order as well as technological parameters;
τ_P	peaking time.

1) Noise Structure in PMOS Input CSA: Fig. 9 illustrates the ENC versus peaking time characteristics for the PMOS CSA #3, before and after irradiation. The shape of the curves clearly reveals the high-frequency series noise, the low-frequency parallel noise, and the base level $1/f$ noise. Using the AMS CMOS technology parameters, we have fitted the data and derived the total capacitance C_t at the CSA input, the transistor transconductance g_m, the total parallel noise, and the $1/f$ noise level.

We found that the series noise was not affected by the irradiation which means that the transconductance of the input transistor (3.2 mS for 200 μA) remained unchanged with the dose. The total capacitance was estimated to be 6.1 pF. At very low frequencies, the noise is totally dominated by the parallel noise contribution that increases with the dose. This is consistent with the decreasing of the output signal fall-time as it was presented in Section IV-A-2. The total current I_{tot}, responsible for the parallel noise, includes the following contributions (see Fig. 10 for current definitions):

- the pad leakage current $I_1 + I_2$ (two reverse bias diodes);
- the compensation current il driven by V_{il};
- the reset transistor noise, depending on $I_R = I_2 - I_1 + il$.

The total current I_{tot} is defined by the following relation:

$$2q \cdot I_{\text{tot}} = 2q \cdot (I_1 + I_2 + il + I_R). \qquad (9)$$

The current I_R is derived from the CSA output signal fall-time. The current il is derived from the CSA #0 output signal fall-time. In fact, since CSA #0 has no pad, I_R is equal to il. When $V_{il} = 0$V in the PMOS case, we found $il \sim 200$ fA before irradiation and ~ 1 pA after being subjected to 224 krad. This increase is probably due to the threshold voltage shift of the NMOS current mirror transistors. As mentioned before, the current through the reset transistor I_R increases and goes from 380 fA to 1.5 pA. The model fitting of the parallel noise allowed extracting the total current I_{tot}. It was found to be 8.7 pA before irradiation and increased to 17 pA after 224 krad.

At this point in our analysis, we can conclude that the reverse current of the anti-ESD pad diodes is by far the main parallel noise contribution, even if the current through the reset transistor increases more rapidly with the dose.

We also concluded that the ENC versus peaking time characteristics showed a 30% increase of the $1/f$ noise with the dose.

2) Noise Structure in NMOS Input CSA: Fig. 11 illustrates the ENC versus peaking time characteristics for the NMOS CSA #6, before and after irradiation. We find that the series noise was not affected by the 224 krad irradiation dose. Therefore, the transconductance appeared to be stable at ~ 3 mS for 200 μA polarization. Note that the CSA #6 NMOS has exactly the same
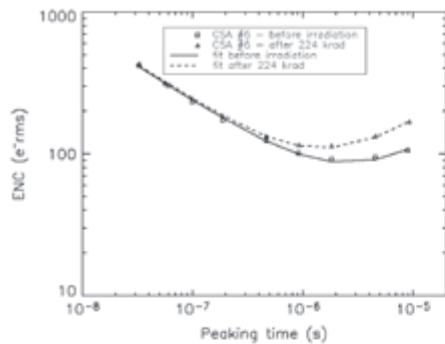
Fig. 11. ENC versus peaking time for the NMOS type CSA #6 before and after 224 krad of irradiation. CSA #6 is polarized with 200 μA current through the input transistor. Lines represent the noise model that fits the data.

dimensions as the CSA #3 PMOS input transistor. We saw a similar value of the transconductance g_m for both CSAs, as expected in weak inversion regime.

At very low frequencies, the noise is dominated by the parallel noise. It increased with the dose because the compensation current il had to be raised to ensure CSA #6 proper response. Note that NMOS or PMOS CSAs need the current $I_R = I_P + il$ to remain positive for proper operation. The necessity to enforce a positive il current in the NMOS CSA seems to demonstrate that the current I_P is negative. In the PMOS CSA, since no adjustment of il is necessary, I_P must be positive (see Fig. 10 for current sign definition). The current I_P is negative in the NMOS CSA probably because the gate of the input transistor (Ve) has a much lower voltage (typically 0.5 V) than in the PMOS CSA (typically 2.8 V).

The gate of the compensation current mirror (see Fig. 10) was set to $V_{il} = 198$ mV prior to irradiation and drifted upwards to reach 235 mV after 224 krad. In order to determine the corresponding values of the compensation current il, we measured I_R using the output signal fall-time of the CSA #0 for which $I_R = il$. Since all CSAs have the same compensation current source, they all have the same il. As mentioned before, the fall-time is directly linked to the current I_R through the reset transistor. We found that il was ~40 pA before irradiation and ~80 pA after.

Model fitting of the ENC versus peaking time characteristics for CSA #6 give us the total current responsible for the parallel noise. This total current includes the pad contribution, the compensation current level il, and the reset transistor noise. We found $I_{tot} \sim 80$ pA before irradiation and ~160 pA after 224 krad. Finally, measuring the output signal fall-time on the CSA #6, we found the current through the reset transistor I_R decreased from 35 pA before irradiation to 2.5 pA after. From all those estimations, we derive $I_1 + I_2 \sim 5$ pA for the pad current before irradiation and ~80 pA after irradiation.

The ENC versus peaking time characteristics shows a 20% increase of the $1/f$ noise.

We make the following conclusions for the NMOS type CSA #6.

- The main noise source is probably the anti-ESD pad leakage current $I_1 + I_2$.
- This pad current generates a negative I_P which obliges us to use a strong compensation current il, leading to an even more important parallel noise.
- The pad current is strongly sensitive to the radiations.

V. Conclusion

IDeF-X is the very first version of our analog front-end electronics mainly devoted to Cd(Zn)Te spectro-imaging systems in space where low-noise, low-power consumption, and radiation tolerance are essential design requirements.

We have designed and tested a set of ten very-low-noise charge sensitive preamplifiers manufactured using the standard AMS 0.35 μm CMOS technology. Depending on the type and size of the input transistors, we could obtain a floor noise ranging from 31 to 49 electrons rms using 3.3 mW of power in the CSA. However, we can obtain almost the same floor noise with a much lower power consumption of 165 μW.

We have identified the PMOS type input CSA as the best candidate for future use in a fully integrated spectroscopic chain. As a matter of fact, its noise level is lower than the NMOS type design and works properly without making use of any compensation current source, limiting intrinsically its parallel noise. Hence, it is well adapted to low current applications with CdTe detectors at room or moderately low temperatures.

Inspired by these results, we used this chip for hard X-Ray spectroscopy at room temperature with CdTe detectors, and obtained a spectral resolution of 1.6 keV FWHM at 59.5 keV with only 660 μW to the CSA. Compared with the ISGRI detectors and ASIC, this represents a spectral resolution improvement of more than a factor of 3.

We irradiated the circuit with a ^{60}Co source up to 224 krad at 1 krad/h dose rate and demonstrated the good tolerance of the design submitted to the Total Ionizing Dose test. We observed a slow increase in the noise level (~30%) for irradiation doses much higher than those of typical space conditions for high-energy astrophysics experiments (~1 krad/year). We believe that this increase is primarily due to the standard AMS pads and not to the CSA design itself. We did not expect such a high leakage current in the anti-ESD pads. Future designs will need specific pads with lightened anti-ESD protections to limit their contribution to the parallel noise.

We conclude that the AMS 0.35 μm CMOS technology appears to be well adapted to a low-noise and low-power consumption analog front-end design devoted to high energy spectroscopy with CdTe. Furthermore, our irradiation tests show that this technology is also tolerant to gamma-rays irradiation.

REFERENCES

[1] F. Lebrun, J. P. Leray, P. Lavocat, J. Crételle, M. Arquès, C. Blondel, C. Bonnin, A. Bouère, C. Cara, T. Chaleil, F. Daly, F. Desages, H. Dzitko, B. Horeau, P. Laurent, O. Limousin, F. Mathy, V. Manguea, F. Meignier, F. Molinié, E. Poindron, M. Rouger, A. Sauvageon, and T. Tourrette, "ISGRI: The INTEGRAL soft gamma-ray imager," *A&A<AUTHOR: Please provide first initial of Rouger—ed.>*, vol. 411, pp. L141–L148, 2003.
[2] P. Ferrando, M. Arnaud, B. Cordier, A. Goldwurm, O. Limousin, J. Paul, J. L. Sauvageot, P. O. Petrucci, M. Mouchet, G. Bignami, O. Citterio, S. Campana, G. Pareschi, G. Tagliaferri, U. Briel, G. Hasinger, L. Strueder, P. Lechner, E. Kendziorra, and M. Turner, "SIMBOL-X: A new generation hard x-ray telescope," in *Proc. SPIE Conf.*, vol. 5168, 2003, pp. 65–76.
[3] P. V. Ballmoos, H. Halloin, G. K. Skinner, R. K. Smither, J. Paul, N. V. Abrosimov, J. M. Alvarez, P. Astier, P. Bastie, and D. Barret, "MAX: A gamma-ray lens for nuclear astrophysics," in *Proc. SPIE Conf.*, vol. 5168, 2003, pp. 482–491.
[4] S. Schanne, J.-L. Atteia, P. Goldoni, A. Klotz, O. Limousin, P. Mandrou, R. Mochkovitch, S. Paltani, J. Paul, P. Petitjean, R. Pons, and G. Skinner, "The space-borne multi-wave-length gamma-ray burst detector ECLAIRs," in *Proc. IEEE NSS-MIC Conf. Rec.*, 2004.
[5] B. Razavi, *Design of Analog CMOS Integrated Circuits*. New York: McGraw-Hill Higher Education, 2001.
[6] V. Radeka and P. O'Connor, "IC front ends for nuclear pulse processing," presented at the IEEE NSS Conf. Short Course, Toronto, ON, Canada, Nov. 8–14, 1998.
[7] C. D. L. Taille, "Automated system for equivalent noise charge measurements from 10 ns to 10 μs" by Orsay," in *Nucl. Phys. Proc. Suppl.*, vol. 32, 1993, pp. 449–459.
[8] O. Limousin, J.-M. Duda, F. Lebrun, and J.-P. Leray, "The basic component of the ISGRI CdTe gamma-ray camera for space telescope IBIS on board the *INTEGRAL* satellite," *Nucl. Instrum. Methods Phys. Res. A*, vol. 428, pp. 216–222, 1999.
[9] F. Lebrun, J.-P. Roques, A. Sauvageon, R. Terrier, P. Laurent, O. Limousin, F. Lugiez, and A. Claret, "INTEGRAL: In flight behavior of ISGRI and SPI," Nucl. Instrum. Methods Phys. Res. A, vol. 541, pp. 323–331, 2005, to be published.
[10] Z. Y. Chang and W. M. C. Sansen, *Low Noise Wide-Band Amplifiers in Bipolar and CMOS Technologies*. Norwell, MA: Kluwer, 1991.

3.3. IDeF-X HD, the latest version

IDeF-X HD [3.30 and 4.17] is the last generation of low-noise radiation-hard front-end ASICs designed by CEA/Irfu for spectroscopy with CdTe or CdZnTe detectors. It has been specially designed to be integrated in Caliste-HD (see section 5.6). The circuit includes 32 analog channels to convert the impinging charge into an amplified pulse shaped signal, and a common part for slow control and readout communication with a controller. The first stage of the analog channel is again a charge sensitive preamplifier (CSA) based on a "folded cascode amplifier" with an inverter input amplifier. The feedback capacitor is discharged by a continuous reset system realized with a PMOS transistor. The increase of drain current in this transistor during the reset phase is responsible for a non-stationary noise; to reduce the impact of this noise on the equivalent noise charge, a so-called non-stationary noise suppressor was implemented for the first time in this chip version using a low pass filter between the CSA output and the source of the reset transistor to filter this noise. The second stage is a variable gain stage to select the input dynamic range from 10 fC (250 keV with CdTe) to 40 fC (1 MeV in CdTe). The third stage is a pole zero cancellation (PZ) circuit. The next stage of the analog channel is a second order low-pass filter (RC^2) with variable shaping time. To minimize the influence of the leakage current on the signal baseline, a so-called baseline holder (BLH) was implemented by inserting a low pass filter in a feedback loop between the output of the RC^2 filter and the output of the PZ stage. The DC level at the output is stabilized for leakage currents up to 7 nA per channel. The output of each analog channel feeds, on one hand, a discriminator that compares the amplitude with an in-pixel reference low level threshold to detect events, and on the other hand a stretcher made of a peak detector and a storage capacitor to sample and hold the maximum of amplitude of the signal which is proportional to the integrated charge and hence to the incident energy. In addition, each channel can be switched off by slow control programming to reduce the total power consumption of the ASIC when using only few channels of the whole chip.

The slow control interface was designed to minimize the number of command signals and to allow connecting up to 8 ASICs and address them individually. This optimization has allowed reducing the electrical interface to 16 pins. When an event is detected by at least one channel, a global trigger signal (TRIG) is sent out of the chip. The controller starts a readout communication with 3 digital signals (DIN, STROBE and DOUT) to get the address of the hit ASIC and then the hit channels. The amplitudes are stored in the peak detectors. The hit channels are multiplexed using a differential output buffer (AOUT). The whole readout sequence lasts between 5 and 20 μs, according to the reset delays and clock frequencies and the number of channels to read out. The main paramaters of the chip are summerized in Table 5.
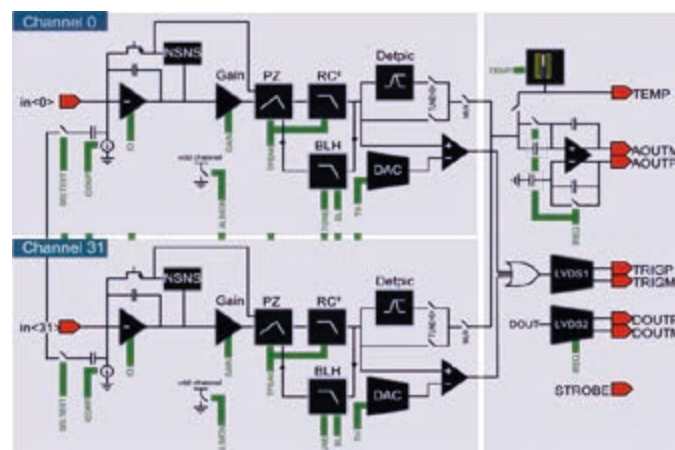

Figure 22. Architecture of IDeF-X HD front-end ASIC including 32 analog channels and one digital part for slow control and readout communication and one temperature sensor.

Table 5. Main features of IDeF-X HD front-end ASIC.

Parameters	IDeF-X HD
Die area	3.5 mm x 5.9 mm
Technology	Austriamicrosystems 0.35 μm CMOS 3.3 V
Number of analog channels	32
Input stage	DC coupling, negative polarity (for connection to detector anode), optimized for 2-5 pF input capacitance, 1 pA to 7 nA dark current (CdTe small pixels)
Peaking time	0.7 to 10.7 μs (16 possible settings)
Dynamic range	10 to 40 fC (4 possible gain settings)
Output stage	Single-ended or differential output buffer
Typical power consumption	27 mW in total, *i.e.* 0.8 mW per channel
Radiation hardness	Latch-up free, tolerant to total ionizing dose > 200 krad

- Noise performance
  Figure 24 shows the noise characteristics of IDeF-X HD, expressed in equivalent noise charge (ENC) refered to the input. The noise at short peaking times is dominated by series noise, which depends on the main charge preamplifier features (power and geometry), on the input capacitance and the temperature. The small pixel area and the hybridization technique limit the input capacitance to 1 to 2 pF. Without dark current, noise at long peaking is dominated by 1/f noise, which depends on geometry and technology of the charge preamplifier and on the input capacitance also. With dark current, it is the parallel noise that dominates. Dark current in small pixels can be limited to a fraction of picoamps in CdTe Schottky diode when the crystal is cooled down below 0°C. The expected best performance in Caliste-HD configuration is an equivalent noise charge between 50 and 60 electrons rms, as required. That corresponds to an energy resolution between 550 eV and 650 eV FWHM at 14 keV with a CdTe Schottky detector array.
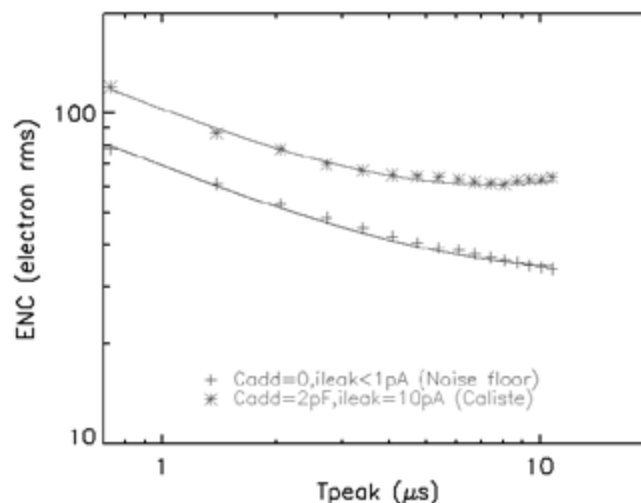

Figure 23. Equivalent noise charge characteristics of IDeF-X HD versus peaking time for two input capacitances and leakage currents values.

- Radiation tolerance of IDeF-X HD

  The IDeF-X family has been designed to be radiation hard. Radiation hardness of IDeF-X HD was evaluated during irradiation campaigns:

  – Heavy ion tests were performed at the UCL/HIF cyclotron facility of Louvain-la-Neuve (Belgium)/ no latch up was mesaured up to a linear energy transfer of 110 MeV.cm^2.mg^{-1}. This is the result of the special design of the digital circuitry of the chips.

  – Single Event Upsets have been evaluated too. Heavy ions tests revealed a slight sensitivity above 8 MeV.cm2.mg-1. No upset was observed at all under proton beam up to 200 MeV.

  – Total ionizing dose tests were performed with a ^{60}Co source at the CoCase facility (Saclay, France) and circuit parameters were monitored including noise performance during the campaign. Results are reported in Figure 24. Up to 40 krad total ionizing dose, the noise remains unchanged which is typically sufficient for typical orbital conditions for hard X-ray missions. The chip can actually work properly upt to at least 200 krad total ionizing dose, with very satisfactory performance and no modification of the power consumption.
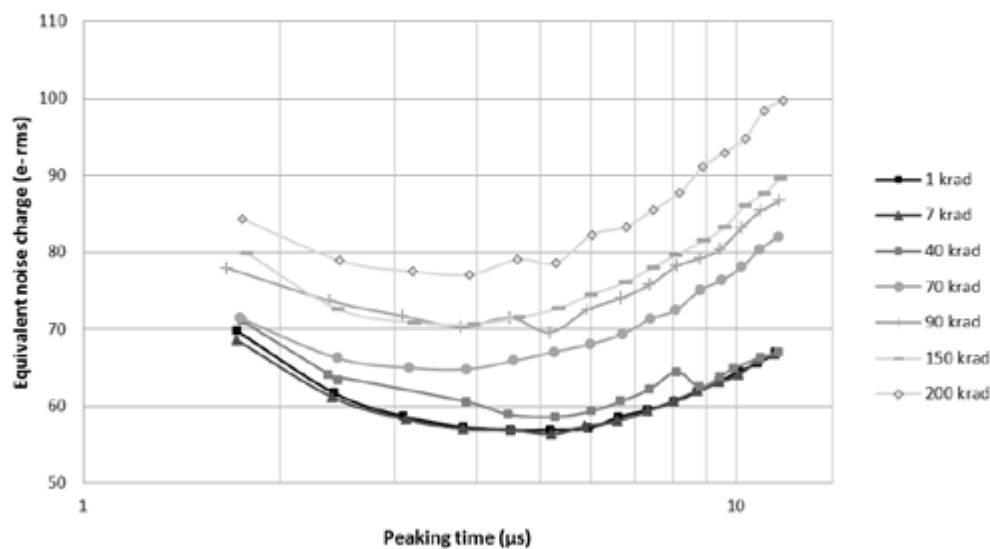

Figure 24. Equivalent noise charge characteristics of IDeF-X HD versus Total Ionizing Dose (TID).

4. 3D hybridization technique

Hybridization is a technological process that allows the interconnection of the CdTe sensor and its front-end electronics, resulting in a modular detection system. The hybrid is then handled as a part to be installed on a motherboard. In our case, our goal was to realize a 3D packaging in order to keep the detector four sides clear of any material. In 2004, we had in mind to use the 3D Plus technology to do so. 3D Plus is a French company, expert in plastic packaging of memories for space applications. Their "System in Package" technology is based on the stacking of known good dies. The parts are tested, stacked and molded into an epoxy resin. The latter is diced, metallized and laser ablated to interconnect the circuits together. Our idea was to implement this technology into an imager design where the IDeF-X ASIC could be stacked, up to 8 circuits in a single module, and interconnected to the sensor using one side of the module. The principle of the 3D Plus System in Package technology is illustrated on Figure 25.
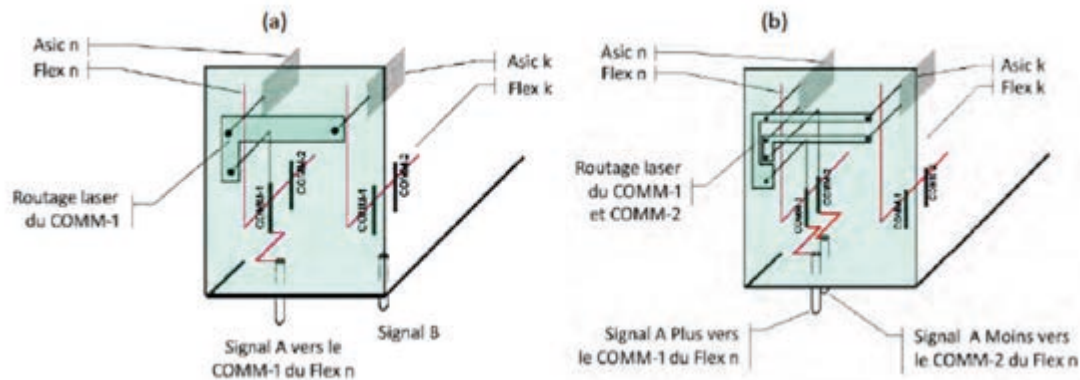
Figure 25. Schematic view of the 3D Plus System in Package technology. ASIC circuits are stacked and molded.
The I/O's are routed to the module surface where interconnect is achieved by a metallization process.
Common signals are short-circuited. Signals are routed in and out the module from the interface to the application.

5. First prototypes, Caliste-64 and Caliste-256

5.1. Caliste-64, a first step towards CdTe based high resolution pixelated detector

Caliste-64 is the first prototype of our hybrid assembly. It is a 1 cm^2 by ~2 cm height elementary detection unit devoted to large area space applications. Caliste-64 design integrates 64 pixels read out by means of four 16 analog-channel IDeF-X V1.1. The electrical interface is optimized to fit into a 7×7 pin grid array 1.27 mm pitch connector at the opposite side of the detector. Caliste-64 fulfills requirements for space-qualified components with respect to power consumption, radiation hardness and environmental constraints (including reliability, thermal cycles, vibrations and shocks).

The solution to integrate the ASIC chips below the detector is to put the chips perpendicular to the detection surface. Each ASIC is responsible for reading out two rows of pixels. The design and the fabrication of Caliste-64 device is a collaborative effort between CEA/Irfu and 3D Plus (France). The ASICs are mounted using classical wedge wire bonding on mini Printed Circuits Boards (PCB) substrates. The latter must have good dielectric properties to avoid excess of noise due to dielectric losses. The drawing at the front is done such a way to limit parasitic capacitances and consequently, series and 1/f noise. The residual parasitic capacitance is estimated to be near 1 pF, without the Cd(Zn)Te pixel self capacitance. The latter depends on the detector pitch and thickness but is clearly negligible with respect to other capacitances on the input path. The four PCB substrates are stacked and molded inside an insulating epoxy resin according to the 3D Plus technology. The resulting block is diced and metallized. The top surface of the block is prepared by laser ablation to receive a 1 cm^2 matrix of 8 x 8 pixels. Each pixel pad is connected to an IDeF-X input. An interconnection stack drives signals from the main block to the bottom electrical interface. Finally, a 1 cm^2 Cd(Zn)Te detector of 0.5, 1 or 2 mm thick, is fixed using a polymer bump bonding technique at a moderate curing temperature, to obtain the complete Caliste-64 camera. Figure 26 illustrates the resulting device.
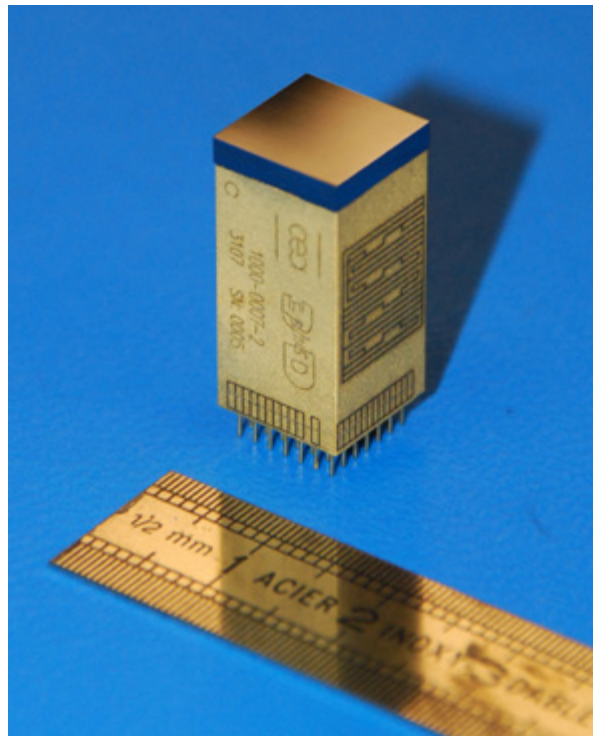
Figure 26. Caliste-64. The hybrid component hosts 4 IDeF-X ASICs installed perpendicularly to the CdTe sensor. In this version, the CdTe Schottky detector is 2 mm thick, 64 pixels, 1 mm pitch.

The bottom interface comprises 49 pins for power lines, ground, analog and digital signals. This design allows easy routing of an array of Caliste-64 units placed side by side. The common ASIC signals are routed together on the laser-ablated sides of Caliste-64. Ten prototypes of cameras were realized with different kinds of detectors (CdTe Al Schottky, CdTe Ni Schottky or CdZnTe) with different thicknesses (1 or 2 mm).
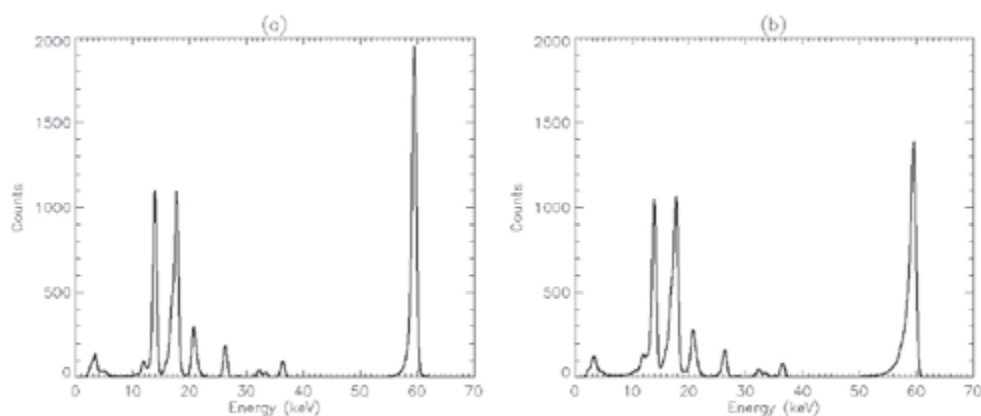

Figure 27. Caliste-64 Spectroscopic perfomances. (a) Caliste-64 equipped with a 2 mm thick CdTe Schottky diode array. The spectral resolution is found to be 905 eV FWHM at 60 keV. (b) Caliste-64 equipped with a 2 mm thick CdZnTe detector. The spectral resolution is found to be 1066 eV FWHM at 60 keV – In both cases, the detectors were cooled down to -15°C, biased under 800V.

Figure 27 shows the sum spectra obtained from single events only, with 2 mm thick Al Schottky CdTe and $Cd_{0.1}Zn_{0.9}Te$ detectors. Cooling the sensor down to -15°C, Caliste-64 equipped with a 2 mm thick CdTe Schottky diode biased under 800 V offers a spectral resolution of 905 eV FWHM at 60 keV. Under the same conditions, a CdZnTe offers 1066 eV FWHM instead.

Using a 1 mm thick CdTe Schottky diode brings the spectral response to a better result: we found 842 eV FWHM at 60 keV and 664 eV at 14 keV.

This innovating technology was published in 2007 in I*EEE Transaction on Nuclear Sciences* [3.38, 3.43, 4.20 and 4.24].

5.2. Caliste-256, 4 times higher pixel density

After the validation of the hybridization concept with Caliste-64, a new generation of micro-camera called Caliste-256 was designed. This time, the device integrates in the same volume four times more channels in the same volume. Caliste-256 is based on the same principle: eight 32-channels IDeF-X V2 chips are stacked perpendicularly to the detector plane to read out two rows of pixels. The bottom interface is also reduced to 49 connection pins for power lines, ground, command signals and analog outputs. The fabrication process is basically the same. A new aspect taken into account in Caliste-256 design is heat dissipation because power consumption is also four times higher in the same volume (816 mW instead of 188 mW). Routing on PCB and on lateral modules sides have been optimized in order to reduce the thermal gradient between the bottom of the camera and the detector using an extra copper layer beneath the gold metallization. To operate the modules in a focal plane in space with an efficient cooling system, we need to drastically reduce the power consumption of Caliste devices. This goal was achieved with Caliste-HD, two years after Caliste-256. The power has been reduced by at least a factor of ~5. This will bring the power consumption back to Caliste-64 level for 256 channels. This will be achieved on Caliste-HD.
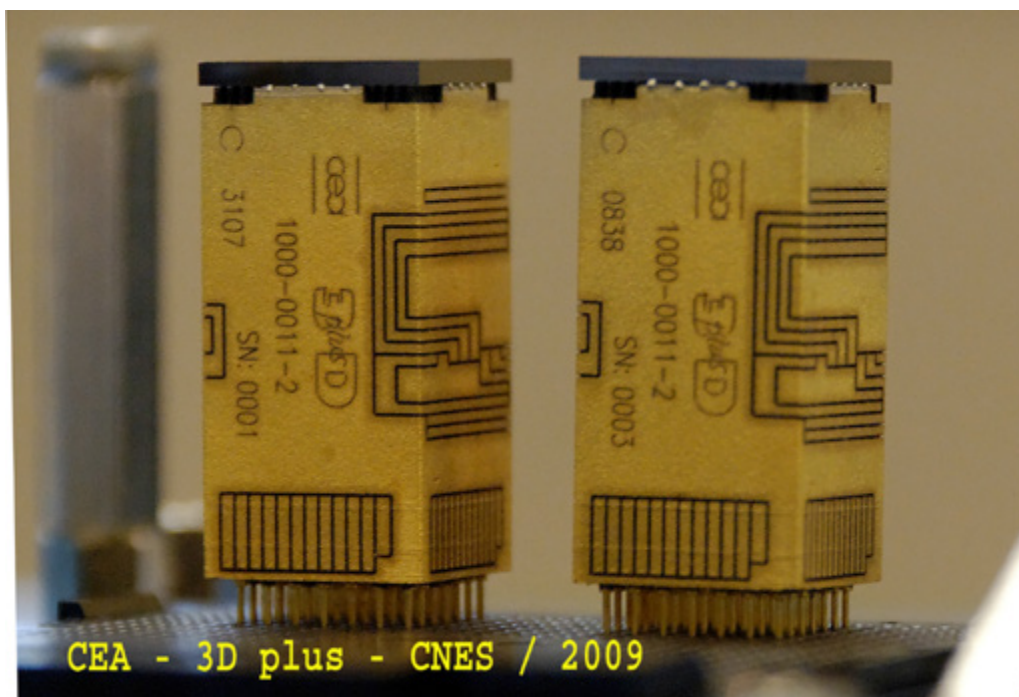

Figure 28. Caliste-256 equipped with a 1 mm thick CdTe Schottky diodes.

One of the most challenging fabrication steps for Caliste-256 with respect to Caliste-64 is related to the detector mounting. Similarly to Caliste-64, the interconnection technique to provide electrical contacts between all detector electrodes and ASIC entries is based on Laser assisted polymer bump bonding technology that I patented together with Fabrice Soufflet at 3D PLUS. This time, the detector pitch is 580 μm instead of 1000 μm. It obviously requires much more precise alignment of the electrodes when the flip-chip process is performed. Such alignments are very usual with indium bump bonding on silicon chips for instance, thanks to self-alignment of the pads when indium reflows, but it becomes more difficult using conductive polymer bump contacts. Furthermore, the glue spots must be high enough to absorb the mechanical strength due to differential thermo-elastic coefficient between the stiff crystal and the high CTE electrical body in epoxy resin; otherwise the detector could break when the device is cooled down. The bonding pads are ~220 μm high in the present design.

In 2009, we realized the first prototypes of Caliste-256 cameras, shown in Figure 28. They are equipped with eight chips stacked to readout the 16x16 array of independent pixel with a pitch of 580 μm. This is the smallest pitch we consider reasonable with our current flip-chip technology.
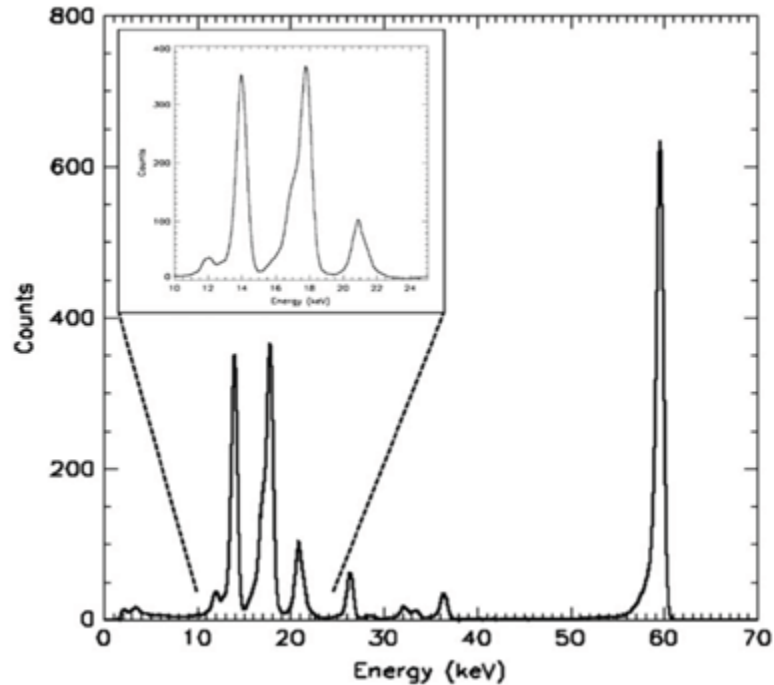

Figure 29. Spectral response of Caliste-256 equipped with a 1 mm thick CdTe Schottky diodes.
The detector was cooled down to 0°C and biased under 300V.

The modules are performing extremely well and show an energy resolution between 700 eV and 850 eV FWHM at 60 keV depending on sample number. We also managed to keep the low threshold value of the whole module as low as 1.5 keV. These results represent a record at that time, up to my knowledge, in such an integrated micro camera. A spectrum is shown on Figure 29.

Note that Caliste-256 has undergone many qualification tests, which bring its TRL to 5, the highest achievable TRL for such a standalone component. This realization concludes our R&D work with CNES on Caliste prototyping.

The results have been published [4.19] in *Nuclear Instruments and Methods in Physics Research A* in a paper named Caliste-256: A CdTe imaging spectrometer for space science with a 580 μm pixel pitch.
The paper is attached in the next section.

5.3. Paper #4 [3.4.19]: Caliste-256: A CdTe imaging spectrometer for space science with a 580 μm pixel pitch

Contents lists available at ScienceDirect

Nuclear Instruments and Methods in Physics Research A

journal homepage: www.elsevier.com/locate/nima

Caliste 256: A CdTe imaging spectrometer for space science with a 580 μm pixel pitch

O. Limousin [a,*], F. Lugiez [b], O. Gevin [b], A. Meuris [a], C. Blondel [a], E. Delagnes [b], M. Donati [a], I. Le Mer [a], J. Martignac [a], F. Pinsard [a], M.C. Vassal [c], R. Bocage [c], F. Soufflet [c]

[a] CEA/Saclay, DSM/Irfu/Service d'Astrophysique, F-91191 Gif-sur-Yvette, France
[b] CEA/Saclay, DSM/Irfu/Service d'Electronique Détecteurs et Informatique, F-91191 Gif-sur-Yvette, France
[c] 3D Plus, 641 rue Hélène Boucher, F-78532 Buc, France

ARTICLE INFO

ABSTRACT

Caliste project aims at hybridizing 1 cm² CdTe or CdZnTe pixel detectors with low-noise full custom front-end electronics, in a single component standing in a $1 \times 1 \times 2$ cm³ volume. Caliste device is 4-side buttable and can be used as elementary detection unit of a large mosaic to form a hard X-ray focal plane of any size and shape. Caliste is especially designed to match astronomical space mission requirements and its design takes into account environmental constraints, radiation environment in particular. This new imaging spectrometer for hard X-rays detection offers high spectral and spatial resolution together with accurate time-tagging capability and low dead time. Caliste concept relies on a 3D hybridization technology that consists in stacking full custom ASICs perpendicular to the detection surface into a single component. This technique simultaneously permits to realize a buttable imager and to enhance performance and uniformity response. Our last prototype is called Caliste 256 and integrates 16×16 pixels array, 580 μm pitch and 256 corresponding independent spectroscopy channels. This paper presents Caliste 256 design and properties. We emphasize spectral performance and demonstrate spectral resolution capabilities better than 1 keV FWHM at 60 keV.

1. Introduction

Future hard X-ray astronomical space missions mostly rely on promising focusing optics, which enables breakthrough in this energy domain. New telescopes with extremely high sensitivity and unequaled angular resolution will be built to reveal the physics of the violent Universe. IXO (ESA/NASA/JAXA) [1], Astro-H (JAXA) [2], NuStar (NASA) [3] or Cospix [4] and NHXM [5] (both proposed in the frame of the ESA third "Cosmic Vision" call for M-class science space missions) are all recent examples of space instruments making use of this grazing incidence mirror technologies. As a consequence, direct imaging is achievable above 10 keV and development of entirely new position sensitive spectrometers is mandatory. In the energy domain ranging from few keV up to 250 keV or more, CdTe (or CdZnTe) crystals are extensively used for their attractive performance in terms of stopping power and spectral response, when associated to advanced readout electronics. Moreover, CdTe is well suited to electrode patterning process to create pixel detectors. Unfortunately, due to crystal growth complications, CdTe based devices cannot be as large as required to cover large field of views where imagers must show up to 8 cm by side. We tackled this issue by creating Caliste 256, a new imaging spectrometer developed by CEA and using

industrial means of 3D Plus, in the frame of a research and development program supported by CNES, the French national space agency. The program is now concluded by this report on the properties and performance of this complete detection unit. The specs for the development inherit from Simbol-X program science requirements [6]: pixel pitch less than 625 μm, 64 cm² and less than 1.3 keV FWHM at 60 keV (in the point spread function, i.e. the sum response of tens of pixels). In order to raise our chance to succeed, we firstly decided to prove our Caliste concept creating Caliste 64 [7], using 1 mm pitch CdTe sensors and IDeF-X V1.1 [8]. After successful operation of this first prototype, we finally designed, realized and tested Caliste 256. The paper presents in Section 2 the Caliste 256 concept, design and associated test setup. In Section 3, we will demonstrate Caliste 256 performance in detail, emphasizing noise and spectral response.

2. Caliste 256 concept

2.1. Design and fabrication

Caliste 256 is a tiny hybrid camera fitting into an approximately 2-cm³ volume. This elementary detection unit consists of a pixilated CdTe or CdZnTe detectors mounted on top of a hybrid module supporting a dedicated front-end electronics based on full custom

* Corresponding author.
E-mail address: olimousin@cea.fr (O. Limousin).

ASICs IDeF-X V2 [9] developed at CEA. This low-noise and radiation-hard chip is processed with the standard AMS 0.35 µm CMOS technology. The detector itself is made of a CdTe monolithic single crystal. Its surface is 1 cm² and its thickness can be chosen arbitrarily from 0.5 up to 10 mm. In the present design, we experienced 1 and 2 mm thick crystals, which are convenient for detection in the hard X-ray range we are interested in. The top surface of the detector is fully covered by a quasi-ohmic electrode, negatively biased. On the contrary, the bottom anode electrode is segmented in 256 pixels, 500 µm by side, square shape, 580 µm pitch and distributed in a 16 × 16 array. Note that the pixel pattern is surrounded by a 200 µm guard ring, used to drive the leakage current from the non-metalized surface to the ground in order to avoid excess noise especially in the side pixels. The pixel detector is flip-chipped on a receiving pattern prepared on the Caliste 256 electrical body (Fig. 1), where each individual pixel is connected to its input channel. The Caliste 256 electrical body beneath the crystal is approximately 2 cm in height and is not larger than the detector surface. It hosts the entire analog readout electronics, which consists of a stack of eight micro printed circuit boards, called flex (Fig. 2), wherein IDeF-X ASICs are bonded. The flex stack is presented perpendicularly to the detector surface, which offers uniform response since the routing at the input differs only slightly from one pixel to the other. The flex stack is molded into an epoxy resin according to a technology developed and patented by 3D Plus (France) [10]. In Caliste 256, each of the eight ASICs has 32 individual inputs and corresponding spectroscopy chains and is consequently responsible for reading out two rows of the matrix. Thus, eight circuits are necessary to read out the full array. Common signals are distributed all along the sides of the modules towards the bottom interface made of a 1.27 mm pitch 7 × 7 pin grid array. The interface is designed to plug the hybrid component in a zero-insertion-force test socket for screening and calibration or to solder it on a printed circuit board leaving its sides clear. This design enables to put several Caliste cameras side by side to realize a large detection plane, as required.

Caliste 256 is finally a standalone and fully integrated pixels 580 µm pitch CdTe camera and its design makes it intrinsically uniform and well adapted to high spectral resolution applications. Its main characteristics are shown in Table 1.

The main technological challenges for Caliste 256 are the integration of the 8 ASICs inside a 1 cm large module and the
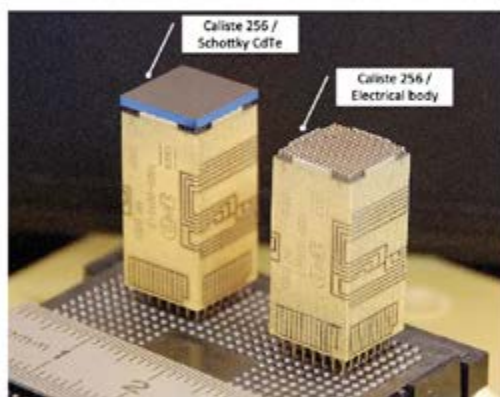

Fig. 1. Caliste 256 macro camera. Left device is equipped with a 1 mm thick Schottky CdTe detector, 256 pixels and a surrounding guard ring. Right sample is the Caliste 256 electrical body, ready to receive a CdTe or CZT crystal on top. The electrical body consists of a stack of 8 IDeF-X V2 full custom ASICs packaged into a 3D module according to the 3D Plus patented technology [10].
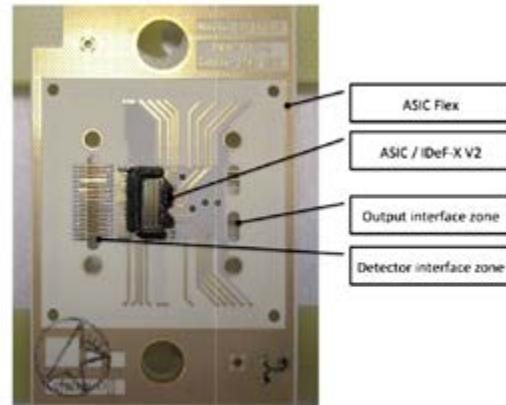

Fig. 2. View of a Flex circuit equipped with a IDeF-X V2 ASIC. Inputs are the left hand side where one sees the detector interface zone, to be revealed during the 3D Plus stacking process.

Table 1
Caliste 256 main characteristics.

Physical properties	
Dimensions of the Caliste 256 electrical body (3D block) (mm³)	10 × 10 × 20.7
Number of pixels/channels	256 (16 × 16)
Pixel pitch (µm)	580
Inter-pixel gap (µm)	80
Guard ring (µm)	200
Crystal size (mm²)	10 × 10
Number of IDeF-X V2 ASICs	8
Interface (mm pitch)	Pin Grid Array 7 × 7, 1.27
Electrical properties	
Controller frequency (slow control & readout) (MHz)	20
Low-level threshold	Individual setting (6-bit DAC/channel)
Shaper peaking time (µs)	Adjustable from 0.6 to 9.6
Test input	200 fF on-chip switchable capacitor
Power consumption	816 mW 3.18 mW/channel
Power Supply	3.3 V/Integrated low voltage filters
Operating conditions	
Temperature range (°C)	−45/+55
High Voltage (V)	Up to 1000

detector flip-chip. Nine samples have been produced. One of them is not equipped with a detector and is used as a reference for electrical properties such as noise, power or timing evaluation using external waveform generator. One device is equipped with a 2 mm thick CZT crystal (prepared by BSI, Latvia, from raw material by eV-products, USA) while all others are equipped with 1 mm thick CdTe Schottky diodes [11] (Al type, Acrorad, Japan). Two of the samples have undergone thermal cycling tests to evaluate the technology robustness and reliability.

2.2. Test setup and configuration

Caliste 256 may be operated at room temperature, with or without detector installed on top. Nevertheless, detector response is always better when the sensor is cooled down below 0 °C, first because leakage current starts to be negligible with respect to

noise in our pixels geometry and second, because the detector is more stable in time in case we use a Schottky type diode [12]. Alternatively, Caliste 256 equipped with CZT crystal operates with a remarkable stability in time even if overall spectral response is a bit worse as demonstrated in Section 3. In our space science applications, Caliste is planned to be used in a temperature range starting from − 40 up to 0 °C. Only functional tests and verification tests are supposed to be done at room temperature. Performance evaluation needs to justify that Caliste 256 is installed into a thermal enclosure under vacuum conditions capable of bringing the device in the nominal operating range (Fig. 3). Caliste 256 is mounted on a test board, placed on a zero-insertion-force plastic socket fitting the PGA interface geometry. The board itself is screwed on a cold plate and thermal straps are used to control precisely Caliste temperature. Thermal probes are used to monitor and regulate the temperature of the setup. In addition to the device under test, the test board hosts the necessary local passive parts (power supplies and filters mainly), LVDS drivers for digital signals and connectors. The board distributes the necessary low voltages (3.3 V) to Caliste 256 ASICs and high voltage (down to − 1000 V) to Caliste 256 CdTe sensor. The acquisition is controlled outside the vessel by a second board equipped with a FPGA, multiplexers, drivers and analog-to-digital converters. The FPGA is used for ASICs programming (peaking time, low threshold, internal bias, injection test mask, etc.) and readout sequencing, event time tagging, synchronization with analog-to-digital converters and data packet preparation. The readout sequence mode can be chosen among full-frame, hit pixels or hit pixels plus their neighbors. The FPGA-embedded Spacewire protocol [13] is used to communicate with the acquisition computer. The interface is accessible by a C++ real time software. In the data packet, photon-by-photon information is recorded, including trigger time tag as well as hit pixel address and pulse height amplitude. Note that in the hit pixel mode, multiple event acquisition is managed. In case of a multiple hit, only one trigger date is delivered but all hit pixel addresses and corresponding amplitudes are transmitted for analysis. Precise sequencing operations are described further in Section 3.3. The dataset is analyzed off-line using an IDL code and allows construction of spectra, calibration or imaging for instance.

2.3. Caliste 256 test flow

2.3.1. Manufacturing
During manufacturing process, each ASIC is fully tested before stacking. For instance, power, slow control commands and analog parameters such as gain and noise performance are measured precisely on 100% of the channels. To do so, voltage steps are injected through an on-chip 200 fF capacitance. It permits to simulate charges generated by the interaction of a photon within the semiconductor detector without any detector. Dark current of the detector is simulated by a programmable current source in the ASICs. This exhaustive test is required to raise our chances to build a fully functional Caliste 256 electrical body by grouping ASICs with similar parameter values or rejecting suspicious chips if any. In addition to the electrical tests, visual inspections are performed in clean room conditions.

Once the ASIC stack and 3D process are completed by 3D Plus, new sequence of electrical tests and inspections is performed at Caliste electrical body level. At this stage, the top surface is ready to get a 256-pixel detector but the crystal is not yet mounted.

2.3.2. Final performance tests
After completion of the electrical test sequence, the detector is mounted and bias interconnection is installed at the cathode. The module is ready for performance tests and final inspections and metrology.

During data acquisition, Caliste 256 samples are illuminated by an uncollimated radioactive source (Am 241, Co 57 or others). Spectro-imaging performance is derived after calibration.

2.3.3. Technological evaluation
During Caliste development program we have continuously taken care of the adequacy of Caliste design and fabrication process with applicable rules of the art for space instrumentation. Consequently, many tests have been performed on Caliste devices along the development to evaluate the technology readiness level and to anticipate critical points with respect to the space environment constraints. Main technological evaluation test and results are summarized in Table 2. We experienced vibrations and shocks to simulate lift-off operations, extreme temperature storage (− 60 °C) to test worst cold case, life-test on ASICs during 2000 h at 125 °C to simulate electronics aging, radiation tests (single event upset, single event latch-up and total ionizing dose up to 1 Mrad) to simulate cosmic rays effects on electronics parts, static temperature/humidity/bias (THB) tests and thermal cycling between − 55 and + 100 °C to simulate life cycle of the devices, both on ground and in flight. After some process corrections, all tests have been passed successfully and we can estimate the Caliste 256 Technology Readiness Level up to 5 according to the ESA scale [14]. This level is considered to be the
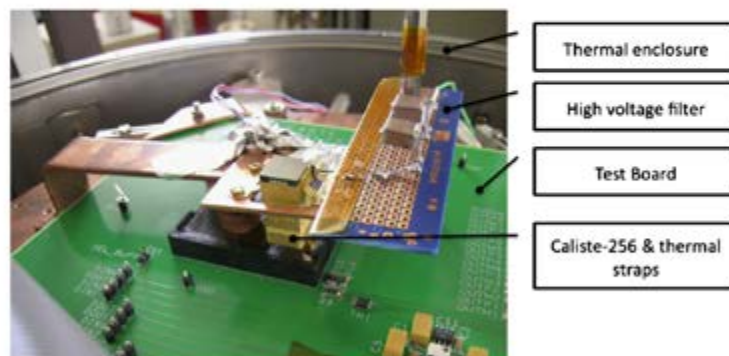

Fig. 3. View of a Caliste 256 test bench. Caliste sample is mounted onto a ZIF socket and connected to cold fingers, used for thermal regulation. Once the vacuum chamber is closed, a radioactive source is installed vertically to illuminate the sample.

Table 2
Caliste 256 technological evaluation.

Technological evaluation	Standard	Details	Result
IDeF-X Total ionizing dose	ESCC detail specification No. 22900	Co-60 500 rad/h up to 1 Mrad 50 rad/h up to 100 krad	> 1 Mrad
IDeF-X SEL	ESA SCC basic specification No. 25100	Heavy ions	> 65 MeV cm² mg⁻¹
IDeF-X SEU	ESA SCC basic specification No. 25100	Heavy ions	> 9 MeV cm² mg⁻¹ (SEU detection signal on-chip)
Life test*	MIL-STD-883H, Method 1005	125 °C/2000 h	Passed**
Sine vibrations	MIL-STD-883H Method 2007.A	20–2000 Hz peak acceleration 20g Three axis 4 mn	Passed*
Shocks	MIL-STD-883H Method 2002.B	1500 g–0.5 ms	Passed*
Thermal cycling*	MIL-STD-883H Method 2007.A	50 cycles −55 to +55 °C +50 cycles −55 to +100 °C	Passed
THB*	MIL-STD-202 Method 103. A JESD22-A101	240 h+85 °C/85% RH	Passed*

* Stresses are applied on test-vehicles that are representative of Caliste 256 technology and process (qualification would require a dedicated Caliste 256 lot).
** Tests are performed at IDeF-X ASIC level. → Standards are used as guidelines for technological evaluation purpose.

most advanced technological readiness level achievable for such a device. Next level requires sub-system level qualification process, generally specific of a particular mission profile.

3. Caliste 256 performance characterization

3.1. Gain and ENC distribution

By virtue of techniques described in Section 2.3.1, calibrated charge injection tests have been done on Caliste 256 to derive gain and equivalent noise charge (ENC) maps. Typical results are illustrated in Figs. 4 and 5 (Caliste 256, SN2—this device was kept without detector as a reference for the electrical body). For a peaking time and a leakage current set 4.8 μs and ~20 pA, respectively, gain and noise responses are uniform over the 256 pixels. Mean (m_{256}) and standard deviation (σ_{256}) are found to be $m_{256} = 189.2$ mV/fC ($\sigma_{256} = 3.8$ mV/fC) for the gain and $m_{256} = 78.3$ el. rms ($\sigma_{256} = 4.5$ el. rms) for the noise. No pixel appeared out of global statistics. We experienced various conditions of shaping times and leakage currents and the uniformity maps permanently appeared flat. On one hand, this high uniformity of gain is expected after individual testing of ASICs and sorting by group of gain in each module. On the other hand, once the gain is uniform, excellent uniformity of the noise is achieved thanks to the original architecture of Caliste 256. As a matter of fact, the vertical position of the chips on flexes makes the input stray capacitance dispersion very low by design. For instance, tracks length between the Caliste 256 surface to IDeF-X from one input pad to the other only varies by approximately 1 mm. Used with a highly uniform CdTe detector, the micro camera must have flat response, which is obviously very attractive for calibration, camera tuning and on board science data calculation.

3.2. Noise performance

Caliste 256 noise is characterized versus peaking time in Fig. 6. The minimum achievable noise was found to be 64 electrons rms in average over the 256 channels. This result is obtained for a peaking time of 9.6 μs (largest programmable value) and no leakage current.

Setting the IDeF-X V2 programmable current source to 20 pA, we can simulate the effect of detector leakage current. The effect

Fig. 4. Equivalent noise charge map for Caliste 256 SN2.

on the noise at low frequency is clearly visible on Fig. 6 while, ENC at high frequency remains independent of the current.

According to theoretical expression of Eq. (1) [15] of the ENC at the output of the shapers and assuming that IDeF-X model parameters are determined independently, we can derive the properties of the assembly in terms of additional noise.

$$ENC = C_{tot}^2 \left(\frac{\alpha_d}{\tau_{peak}} + \alpha_{1/f} \right) + \alpha_{f/} i_{leak} \tau_{peak} \tag{1}$$

where

- C_{tot} is the sum of the total capacitance into the chip at the input of the CSA, the capacitance on the ASIC board and the additional soldered capacitance.
- α_d, $\alpha_{1/f}$ and $\alpha_{f/}$ are parameters related to IDeF-X V2 design (input transistor of the CSA and filter order).
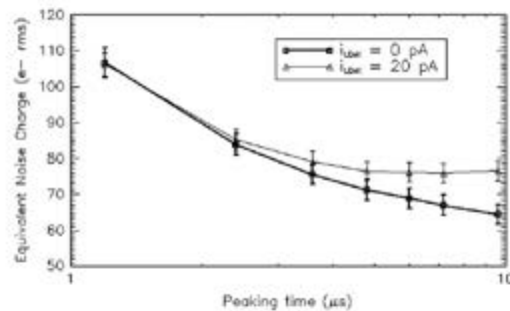
Fig. 5. Gain map for Caliste 256 SN2.

Fig. 6. Equivalent noise charge (ENC) measurement on Caliste 256 SN2 (no detector on top) against the peaking time value. Error bars illustrate standard deviation of ENC over the 256 channels. Large line is obtained without dark current while thin line is obtained imposing a ~20 pA current from on-chip current source.

● i_{leak} is the leakage current injected at the input of the CSA. Several values are accessible starting from 0 up to 100 pA.

According to this model, we can derive the stray capacitance level at the input to be approximately 2 pF and the simulated dark current to be 20 pA in average (it spreads from 10 to 30 pA depending on channel number and from chip to chip). Slight dispersion is measurable and depends on the routing at flex level. However, whatever the channel number, the noise level remains low, i.e. in the range of 70 ± 5 electrons rms. More details on Caliste 256 noise performance are published in one of our previous papers [16].

As the dark current in the CdTe Schottky detectors is generally extremely low (in the order of only few pA per pixel at -15 °C [7]), we estimate the energy resolution from the noise measurement to be 0.76 keV FWHM at 14 keV and 0.86 keV at 60 keV, assuming a Fano factor of 0.15 and a mean electron–hole pair creation energy of 4.42 eV (CdTe).

3.3. Low-level threshold

Noise characterization also enables to predict low-level threshold value. Assuming that low threshold can be set at 5σ of the noise distribution, we expect the low threshold to be close to 1.4 keV in the optimal conditions (low leakage, largest peaking time). This value is generally very difficult to reach, especially into an integrated device where analog and digital electronics coexist because digital glitches are likely to trigger the analog chain through small capacitive coupling to the inputs.

In Caliste 256, low-level discriminator threshold can be set for each pixel individually. Sixty-three values per pixel are available, ranging from 0 up to 18 keV, by steps of ~285 eV. In addition, a 64th value helps to disable a malfunctioning pixel if any. Using this functionality, we measured the low threshold value at 9.6 μs, globally setting the same discrimination level for all the pixels. Decreasing the level step by step down to 1.4 keV (or 1.7 keV) without dark current (with 20 pA dark current resp.) does not cause any self-triggering issues. These values are consistent with noise measurements and no digital coupling has been detected. These low threshold values have been confirmed by spectroscopic measurements, illustrated in Section 3.5 and visible in Fig. 7 and Fig. 8 (Am 241 spectrum).

3.4. Dead time

When at least one channel reaches its low-level threshold, a global trigger signal rises and locks the whole Caliste 256 device during a short time to achieve the readout sequence. This dead time depends on the latency time $\tau_{latency}$ between the trigger and the peak detectors freezing, the hit pixel address readout time τ_{arg} to get the position of triggered pixels and to compute the pixels to be read, the readout time $\tau_{readout}$ to receive and encode one pixel data and the duration τ_{reset} of reset operation.

Each IDeF-X has its own analog output in Caliste 256. Therefore, multiple hits inside a chip are readout successively by multiplexing output buffer while multiple hits in different ASICs are readout in parallel if the acquisition board houses one analog to digital converter
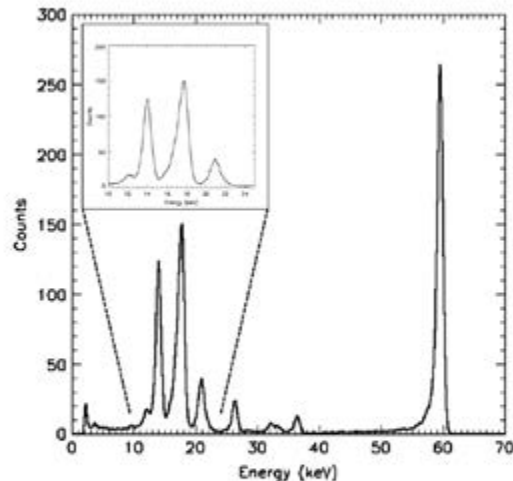

Fig. 7. Am 241 spectrum obtained with Caliste 256 SN4 equipped with a CZT detector summing the 256 individually calibrated spectra (–15 °C, 800 V, 6.0 μs peaking time). Energy resolution at 59.54 keV is 1.09 keV FWHM. Zoom in the 10–25 keV band emphasizes the energy resolution revealing the triangle shape of the 17.75 keV triplets.
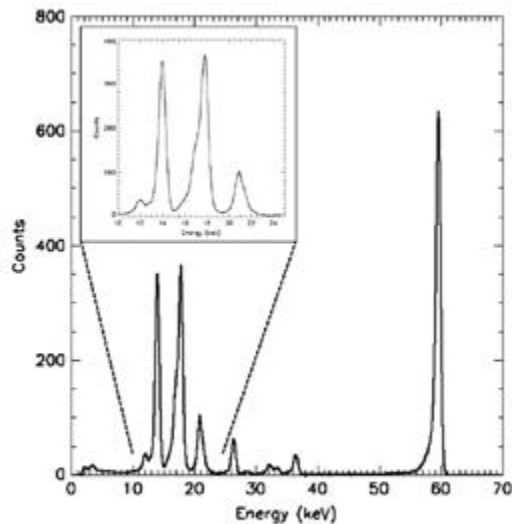
Fig. 8. Am 241 spectrum obtained with Caliste 256 SN5 equipped with a CdTe Schottky diode summing the 256 individually calibrated spectra (0 °C, 300 V, 9.6 μs peaking time). Energy resolution at 59.54 keV is 0.85 keV FWHM. Zoom in the 10–25 keV band emphasizes the energy resolution revealing the structure of the 17.75 keV triplets.

per ASIC. In this configuration, the duration of the encoding sequence depends on the maximum number N of hit pixels per ASIC to read out ($N \leq 32$). As a result, Eq. (2) gives dead time.

$$\tau_{deadtime} = \tau_{latency} + \tau_{rfle} + N.\tau_{readout} + \tau_{rest}$$ (2)

We measured that dead time can be as low as 17 μs to read one hit pixel when the peaking time is 9.6 μs. Any additional hit pixel causes one more μs readout time ($\tau_{readout}$).

Typical count rates in hard X-ray astronomy space mission is expected to be in the order of few hundreds of counts per second in typical point spread function of 3 mm in diameter, in case of a bright source such as the Crab pulsar. Assuming that 10 pixels are hit at the same time in the PSF, contained entirely in one Caliste 256 area, the camera is disabled during 26 μs, which induces a dead time fraction of ~0.5%.

3.5. Spectral response

We have realized and tested 9 Caliste 256 samples: One remained without detector as a reference, one equipped with a 2 mm thick CZT crystal and seven other equipped with a 1 mm thick CdTe Al Schottky type array. All Caliste 256 electrical bodies were fully functional and satisfactory. After detector mounting, two modules had one pixel misconnected, two modules had more than two pixels improperly connected and all other four devices had 100% properly connected pixels, leading to a yield of approximately 60% admitting than one pixel failure is acceptable for an imager.

In this section, we will focus on results obtained with sample #4 and #5. The first one (SN4) is equipped with a CZT crystal while the second one (SN5) equipped with a CdTe crystal showed the best performances of the lot. In the next, we will summarize other device results to show good repeatability of the spectral performances.

3.5.1. SN4 (CZT) spectral response

We found the optimal conditions for a 2 mm thick CZT pixel detector on top of Caliste 256 to be an operating temperature of −15 °C and a bias voltage of 800 V. In these conditions, dark current is low enough to set a peaking time as long as 6 μs. Assuming an input stray capacitance of ~2 pF in average, we derive the dark current to be in the range 20– 30 pA per pixel. In principle, lower current is achievable at lower temperature but, unfortunately, performance of the Caliste 256 current version does not improve in this situation (see next paragraph). Using such a voltage, we find a comfortable compromise between charge collection and spreading and low dark current. Increasing the voltage could eventually arrange the line shapes at the expense of parallel noise.

Fig. 7 illustrates the spectrum obtained by summing all individual contributions of the 256 pixels, previously calibrated individually using a linear function. The energy resolution is found to be 0.91 keV FWHM ($\sigma_{256} = 0.16$ keV FWHM) and 1.09 keV FWHM ($\sigma_{256} = 0.13$ keV FWHM) at 13.94 and 59.54 keV. Note that the low energy threshold is approaching 2 keV. However, at least one of the pixels has its threshold set a bit too low causing a line structure between 2 and 3 keV. The threshold has been set to the same value for every channel in this dataset. Fine individual tuning of the pixel threshold should help to get rid of this structure. Zooming into the 10–25 keV energy band allows revealing the 17.8 keV multi-line structure.

In addition to the spectral response, one must notice that the Caliste 256 SN4-CZT is remarkably stable as the operating temperature is regulated within a degree.

3.5.2. SN5 (CdTe Schottky) spectral response

Considering now a Caliste 256 equipped with a Schottky type CdTe diode (Al type), we found the best energy resolution to be 0.73 keV FWHM ($\sigma_{256} = 0.10$ keV FWHM) at 13.94 keV and 0.85 keV FWHM ($\sigma_{256} = 0.09$ keV FWHM) at 59.54 keV (Am 241 lines) reached at 0 °C, 300 V reverse bias voltage with a shaper peaking time set 9.6 μs. As the shaper time can be set to a long value, we derive that the dark current level is pretty low in average in the pixels. Even with an intrinsic bulk resistivity significantly higher for CdTe than CZT, the use of a blocking contact brings the dark current to a suitable value for very good spectral performance on CdTe. According to our model, expecting a ~2 pF average stray capacitance at the input of the IDeF-X chips, we conclude that dark current is certainly below 10 pA in our case. Unfortunately, the use of a blocking contact causes unstable spectral response in time due to the so-called "Polarization effect", as reported in Ref. [12]. Nevertheless, using the sensor below 0 °C allows performing comfortably for days without significant degradation of the spectral response in these conditions.

Note that 100% of the pixels contribute to the sum spectrum shown in Fig. 8. In this dataset, the low energy threshold value is close to 1.5 keV. Zooming into the 10–25 keV energy band of the spectrum reveals the three-lines structure of the 17.75 keV Am line, which illustrate the very promising results obtained with Caliste 256 equipped with the CdTe Schottky diodes. From the spectral resolution, we derive the noise to be approximately 73 electrons rms ($\sigma_{256} = 5$ electrons rms) assuming a Fano factor of 0.15. This extraction matches with noise measurements as reported in Section 3.2. Moreover, the low energy threshold value is also measured as expected in Section 3.3, which demonstrates that Caliste 256 low energy range is not limited by digital coupling to the analog inputs. Note again that all pixel thresholds are set to the same value in this dataset even if an individual tuning is possible.

Exploring a higher energy domain with a Co 57 source, we measured the energy resolution to at 122.06 keV and found it to be 1.38 keV FWHM, with a standard deviation of $\sigma_{256} = 0.27$ keV FWHM over the pixels. Corresponding spectrum is shown in Fig. 9. Even if

this result is attractive, the energy resolution was expected to be ~1 keV FWHM assuming a Fano factor of 0.15. Energy resolution results against energy are plotted in Fig. 10, where diamonds are measurements while dashed-line represents the energy resolution as expected from our model. We interpret this result as follows.

Using the linear calibration laws for each pixel, derived from Am 241 spectra, results in a wrong energy evaluation at 122.06 and 136.47 keV. This is due to a small integral non-linearity of the pixel response estimated to be ~0.5% in average. Such an uncorrected integral non-linearity, randomly distributed from one chain to the other, will cause a degradation of the sum spectrum energy resolution by more than 1 keV FWHM. Using a second order polynomial calibration law improves the situation for Co 57 sum spectra but still an improvement of calibration analysis may arrange the performance result a little. Another reason for degrading the 122.06 keV line resolution can be found in the front-end design. As a matter of fact, we suspect the continuous reset function architecture to play a role: the charge sensitive amplifier (CSA) hosts a feedback-reset transistor to perform the continuous reset function. The current of the detector goes through this transistor contributing to the parallel noise. This noise source remains constant, as the dark current is stable in time for a given temperature. But in addition to that, when the charge signal is generated, the output voltage of the CSA "opens" the reset transistor causing a slightly lower feedback equivalent resistance. This generates an additional noise source on the signal itself. We call it non-stationary noise. This noise is approximately proportional to the induced charge, causing a degradation of the spectral response, as the energy gets higher. Initially, we designed the reset feedback this way to take advantage of a fast reset when the chain is saturated after a high-energy cosmic ray in space (most of the events) deposits its energy in a pixel. Another motivation was to avoid active reset architecture to facilitate the very low threshold capability of our device.

In order to overcome this problem, we have designed an entirely new IDeF-X CSA that will be gainful for next generations of Caliste [17].
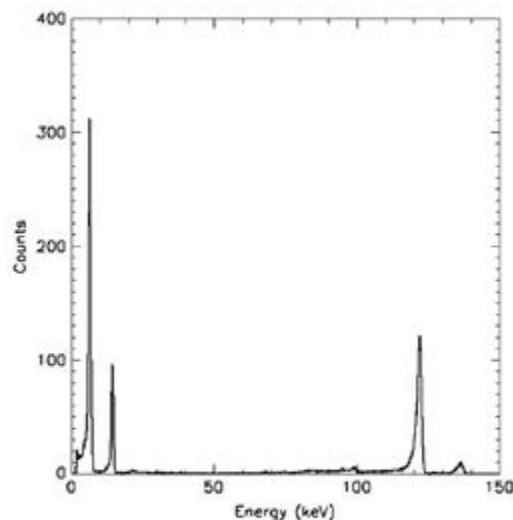

Fig. 9. Co 57 spectrum obtained with Caliste 256 SN5 equipped with a CdTe Schottky summing the 256 individually calibrated spectra (0 °C, 300 V, 9.6 µs peaking time). Energy resolution at 122.06 keV is 1.38 keV FWHM.
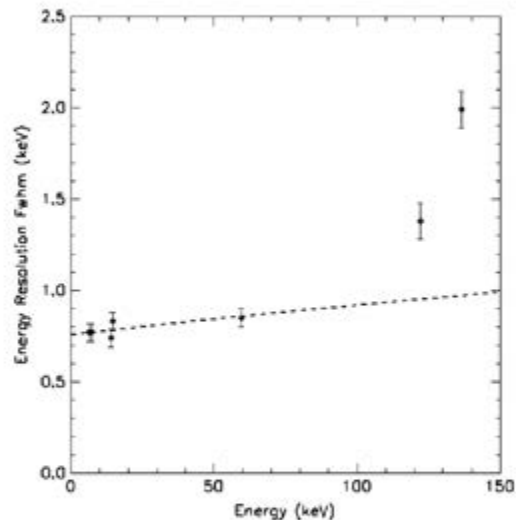

Fig. 10. Energy resolution against energy measurement results obtained with Caliste 256 SN5, from Am 241 and Co 57 sum spectra (CdTe Schottky, 0 °C, 300 V, 9.6 µs peaking time, 100% pixels active).

3.5.3. Thermal behavior

Dark current decreases exponentially with temperature in semiconductors. Cooling down the CdTe or CZT sensors must improve performance until the dark current reaches a value where its associated parallel noise contribution becomes negligible with respect to $1/f$ noise at low frequency. Consequently, we have explored Caliste 256 performance down to −32 °C where we expect dark current to be negligible in a pixel but found a degradation of spectral performance instead of an improvement. The reason for that is linked to the low voltage bias circuitry of IDeF-X CSA. As a matter of fact, the CSA current surprisingly gets higher when the temperature goes down. Using series resistors in the CSA bias circuitry from the 3.3 V power supply to get intermediate voltages required in the design, causes a voltage drop that put the CSA out of its low-noise operation range. Depending on the samples, the optimal temperature for spectroscopy has always been found to be the lowest functional temperature (when all pixels operate), between −15 and 0 °C. Fig. 11 illustrates the spectral performance evolution of Caliste 256 SN5 against temperature where the effect is clearly visible. New design of IDeF-X will permit to get rid of this issue by regulating the CSA biases on-chip.

3.5.4. Summary of performance results

Keeping the Caliste 256 samples in their operating range, we have explored performances over our eight samples illuminated by an Am-241 radioactive source. Table 3 summarizes these results. The most remarkable result is the good uniformity of response between similar samples. Apart SN1 (157 pixels on) and SN4 (CZT), all of our devices could perform well with a sub-keV spectral resolution at 59.54 keV. In addition, best results have been obtained for various samples in similar operating conditions of temperature and high voltage. It illustrates the good maturity of CdTe and CZT manufacturing process on one hand as well as the good maturity of the electronics and hybridization process on the other hand. This result is extremely important in prospect
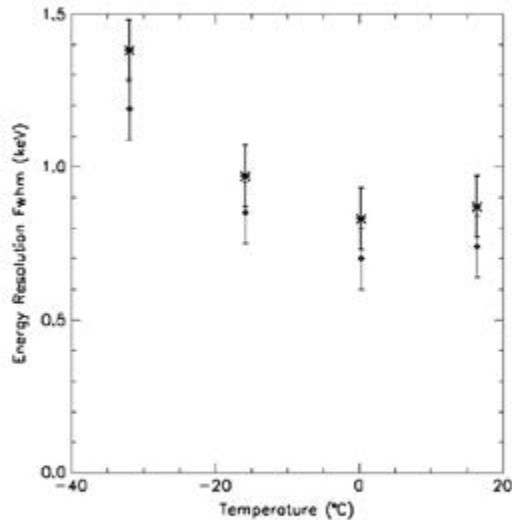
Fig. 11. Spectral performance of Caliste 256 SN6 equipped with a Schottky CdTe diode versus operating temperature (300 V, 9.6 μs peaking time). Diamond and star symbols stand for energy resolution FWHM at 13.94 and 59.54 keV, respectively.
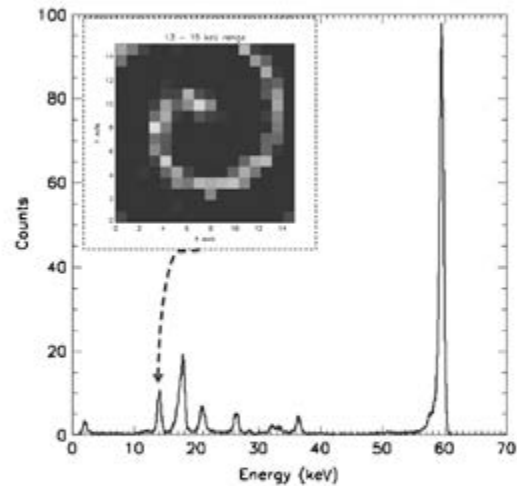

Fig. 12. Image of a spiral mask placed vertically to Caliste 256 SN6 and illuminated by an Am 241 radioactive source. The mask is 1 mm thick and is made of Al. The shadowgram is built from the selection of photons in the 13–16 keV band. Spectrum is built summing all pixels data and shows 0.78 keV FWHM energy resolution at 59.54 keV (Schottky CdTe diode 0 °C, 300 V, 6 μs peaking time).

Table 3
Caliste 256 performance table – Optimal conditions and performance results for Am 241 lines for each sample.

Caliste 256 sample number	Optimal conditions	ΔE FWHM at 14 keV	ΔE FWHM at 60 keV	Comments
1	6 μs, 300 V, 0 °C	0.88	1.03	157 pixels on
3	6 μs, 300 V, −15 °C	0.83	0.98	253 pixels on
4	6 μs, 800 V, −15 °C	0.91	1.09	CZT crystal 256 pixels on
5	9.6 μs, 300 V, 0 °C	0.73	0.83	256 pixels on
6	6 μs, 300 V, 0 °C	0.80	0.93	255 pixels on
7	6 μs, 300 V, 0 °C	0.77	0.86	247 pixels on
8	6 μs, 300 V, 0 °C	0.79	0.96	256 pixels on
9	6 μs, 300 V, 0 °C	0.74	0.87	255 pixels on

of assembling Caliste 256 into a mosaic array to form a large focal plane.

3.6. Imaging spectrometry

We have completed our Caliste 256 performance evaluation recording an image resolved in energy using Caliste 256 SN6 installed right below a spiral shape mask made of Al, 1 mm thick. The open spiral width is 1 mm. A radioactive Am-241 source has been placed on-axis, vertically to the setup. From photon–photon acquisition, we could build spectrum and image as illustrated in Fig. 12. The spectral response in this dataset is 0.70 keV FWHM at 13.94 keV and 0.78 keV FWHM at 59.54 keV. The low energy threshold is set to ~1.5 keV.

Selecting events belonging to an energy range of 2 keV wide, centered on the 13.94 keV Am 241 line (13–15 keV), we built a shadowgram with appreciable contrast: for a total number of 940 events in the 13–15 keV band acquired in 3600 s, darker pixels have recorded 1.2 event/pixel in average in total while the ~30% brightest pixels (open fraction of the mask projected on top of the detector surface) have recorded 10 events/pixel in average in total. At the contrary, the mask is 97% transparent at 59.54 keV. The image remains flat in this energy band.

4. Conclusion

We successfully completed design, fabrication and tests of a new micro hard X-ray camera called Caliste 256. The prototypes have been completed nine times with a promising yield. Caliste 256 is equipped with CdTe Schottky diodes or CdZnTe detectors having a 16×16 pixels array, 580 μm pitch. The sensor is mounted on top of an electrical body that hosts eight full-custom ASICs IDeF-X V2. Caliste 256 is made such a way it can be installed in mosaic forming an arbitrary large camera minimizing dead zones. Caliste 256 is an imaging spectrometer capable of high-resolution performances in the hard X-ray energy range: 1.09 keV FWHM and 0.85 keV FWHM energy resolution at 59.54 keV have been measured on CZT or CdTe samples, respectively, derived from the sum spectra, in the best configuration slightly cooled down in the range from −15 to 0 °C. Caliste 256 also proves its very low threshold performance and has been operated successfully down to ~2 keV.

Caliste 256 has been designed and optimized to face demanding space environment constraints and we could demonstrate its high technological maturity through extensive reliability and performance tests.

In the near future, new evolutions of Caliste 256 will be issued. The goal is mainly to adjust the design for better performance in a

larger energy range and modify the electrical interface using a more advanced communication protocol enabling 16-pin interconnection PGA instead of 49. Finally, the new generation of IDeF-X ASIC will facilitate Caliste 256 cooling thanks to its lower power consumption.

Acknowledgment

References

[1] K. Nakazawa, T. Takahashi, O. Limousin, et al., The hard X-ray imager onboard IXO, in: Proceedings of the SPIE Conference, vol. 7732, 2010.

[2] T. Takahashi, et al., The ASTRO-H Mission, in: Proceedings of the SPIE Conference, vol. 7732, 2010.

[3] F. Harison, et al., The Nuclear Spectroscopic Telescope Array (NuSTAR), in: Proceedings of the SPIE Conference, vol. 7732, 2010.

[4] P. Ferrando, et al., The COSPIX mission: focusing on the energetic and obscured Universe, in: Proceedings of the 25th Texas Symposium on Relativistic Astrophysics, Heidelberg Dec. 6–10, 2010, PoS(Texas 2010) 254, 2011.

[5] G. Tagliaferri, et al., NHXM: a new hard X-ray imaging and polarimetric Mission, in: Proceedings of the SPIE Conference, vol. 7732, 2010.

[6] P. Ferrando, M. Arnaud, U. Briel, et al., Simbol-X: mission overview, in: Proceedings of the SPIE Conference, vol. 6266, 2006.

[7] A. Meuris, et al., IEEE Trans. Nucl. Sci. NS-55 (2) (2008) 778.

[8] F. Lugiez, et al., IDeF-X V1.1: Performances of a New CMOS 16 Channels Analogue Readout ASIC for Cd(Zn)Te detectors, in: Proceedings of the IEEE NSS-MIC Conference Record, pp. 841–844, 2006.

[9] O. Gevin, et al., IEEE Trans. Nucl. Sci NS-56 (4) (2009) 2351–2359.

[10] C. Val, M. Leroy, Patent 90 15473, 3D Plus, Dec. 1990.

[11] S. Watanabe, et al., Jpn. J. Appl. Phys. 46 (2007) 6043.

[12] A. Meuris, O. Limousin, C. Blondel, Characterization of polarization phenomenon in Al-Schottky CdTe detectors using a spectroscopic analysis method, accepted for publication.

[13] F. Pinsard, C. Cara, High resolution time synchronization over SpaceWire links, in: Proceedings of the IEEE Aerospace Conference, paper #1158, 10.1109/ AERO.2008.4526462, 2008.

[14] ⟨http://sci.esa.int/science-e/www/object/index.cfm?fobjectid=37710⟩.

[15] V. Radeka, P. O'Connor, IC Front Ends for Nuclear Pulse Processing, IEEE NSS98 Short Course, Toronto.

[16] A. Meuris, et al., IEEE Trans. Nucl. Sci. NS-56 (4) (2009) 1835.

[17] O. Gevin, et al., IDeF-X HD: a Low Power Multi-Gain CMOS ASIC for the Readout of Cd(Zn)Te Detectors, in: Proceedings of the IEEE NSS-MIC Conference Record, Knoxville, October 2010.

6. Caliste HD, the ultimate version

The Caliste-HD [3.23] detection system consists in hybridizing eight 32-channels IDeF-X HD chips with a 256-pixel CdTe sensor of 1 cm² surface and 1 or 2 mm thickness. The ASIC are mounted on micro printed circuit boards, tested then stacked by 8 with high alignment precision and molded into epoxy resin, according to the technology of the 3D-Plus company. The channels of an ASIC are connected to two adjacent rows of 16 pixels in a similar manner as Caliste-256. The resulting block is cut and metallized with a Cu-Ni-Au coating. The thick copper layer is added to facilitate heat load evacuation to the ground metal layers. Laser routing is applied on the lateral sides to make electrical connections between the 8 ASICs that share all supply voltages, input and output signals. Each ASIC has an individual address to enable chip select during I/O operations. The bottom interface includes a filtering stage for power supplies and a grid array of 16 pins only (49 in Caliste-256). The top interface of the so-called Caliste body is then prepared by a CEA/3D PLUS patented technology of laser-assisted polymer bump bonding technique [2.1] to realize a matrix of 16 x 16 conductive epoxy bumps with a pitch of 625 µm and two extra bumps at the periphery for the connection of the guard ring. The CdTe pixel detector is epoxied to the Caliste body by a flip-chip technique using stencil printing on the previously forms epoxy pads. This full hybridization process was optimized for CdTe, with operations at a relatively low temperature (80°C) and bumps high enough to withstand thermal cyclings for space qualification keeping a good adherence force without any underfill. The resulting device with a 1 mm-thick detector has a volume of 10 mm x 10 mm x 17.5 mm for a total weight of ~6 grams (see Figure 30). Performances results are presented in paragraph 4.5.6.2.
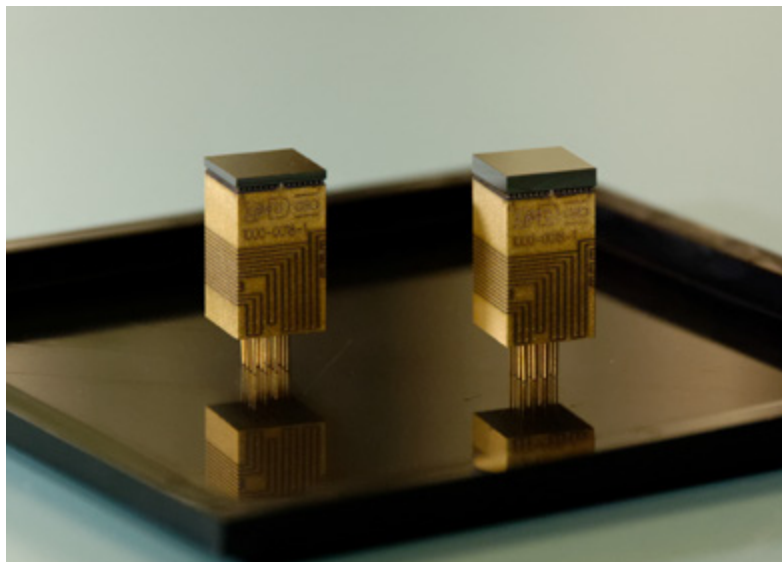

Figure 30. Picture of 2 Caliste HD units, with 1 mm-thick (left) or 2 mm-thick (right) CdTe detector, fitting in a volume of 10 mm x 10 mm x 17.5 (left) or 18.5 (right) mm.

6.1. MACSI, a mosaic of Caliste-HD to cover large focal planes

By design, Caliste-HD is a 4-side buttable imaging spectrometer device with 1 cm² CdTe sensor and can be used to build large cameras. A prototype of 8 cm² detection plan called MACSI (standing for Modular Assembly of Caliste Spectro-Imagers) was designed and realized with an array of 2 x 4 Caliste-HD units. This geometry was chosen in the prospect of the realization of a 64 cm² CdTe focal plane with 8 MACSI detection sectors for astronomy in orbit. In this context, the only way to cool down the CdTe sensors is by thermal conduction from the base plate and through the Caliste bodies. To optimize it, the printed circuit board hosting the Caliste units is a flex circuit realized with thick ground planes and glued to a mechanical drain made of aluminum. The 20 cm long flex lid allows a routing into a focal plane enclosure surrounded with an anticoindence shielding; it is terminated with a small printed circuit board integrating power supply regulation parts and filtering SMD[4] components and could possibly include amplifier buffers and LVDS drivers and receivers for other applications. All components and processes were chosen to be compliant

---

4. SMD: Surface-Mount Device.

with space quality standards. After manufacturing this assembly presented in Figure 31 (a), the Caliste-HD units are placed with a dedicated alignment tool and manually soldered, with a gap of ~400 μm between each other. In this way and using an electrode pattern of the CdTe detector anode with only 20 μm-wide guard ring, we can guarantee with this assembly a dead zone no larger than one pixel pitch between two pixels of adjacent Caliste-HD units. The high voltage is connected by wire bonding between the high voltage filtering stage and the platinum planar cathodes of the two closest Caliste-HD units; wire bonds coming from adjacent Caliste-HD bias the other neighbour units, as shown on Figure 31 (b). The wire bonding is performed on a gold pad epoxied to the crystal platinum electrode.
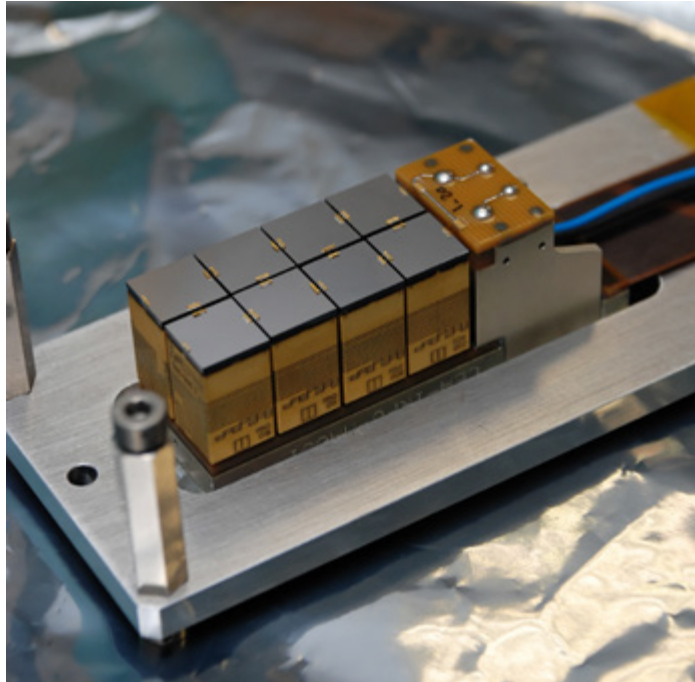

Figure 31. Picture of the first MACSI realization. Close-up view on the 8-cm^2 CdTe detection plane with 2048 individual spectroscopic channels made of 8 Caliste-HD units placed side by side.

The MACSI ends with two 37-pin micro-D connectors that can be connected to the warm electronics, including the controller and analog-to-digital converters (ADC). The first prototype was tested in the vacuum chamber using an interface board with LVDS drivers and receivers and test points. The acquisition board was placed outside the vessel and includes a field programmable gate array (FPGA) that controls the configuration and the readout of the 8 Caliste-HD units (64 ASICs), controls the encoding of the amplitudes with one 12-bit ADC, generates event frames and sends them to the computer through a Spacewire link. When a photon interacts in one CdTe crystal, all the ASICs of the corresponding Caliste-HD are disabled for the readout of the event but the other Caliste-HD can be in observation mode.

6.2. Caliste-HD performances
• Spectral response
  Caliste-HD units were tested individually before being integrated in a MACSI system. 25 Defect-free units were fabricated, with excellent spectral performance. Figure 32 shows the Am-241 spectrum obtained after calibrating the 256 pixels of a sample and summing the 256 histograms by energy bins of 50 eV. The resulting energy resolution is 562 eV FWHM at 14 keV and 666 eV FWHM at 60 keV. That corresponds to a mean ENC of 50 electrons rms. This performance can be obtained thanks to the low noise IDeF-X HD ASIC, the hybridization principle that minimizes the input capacitance of the CSA and the Al-Schottky CdTe diodes from Acrorad that have extremely low leakage current (typically 1 nA.cm^{-2} at –5°C, 300 V). The pixel configuration compared to the double-sided strip detectors is favorable for imaging spectroscopy because the capacitance and the leakage current that drive the ASIC performance are proportional to the electrode area.
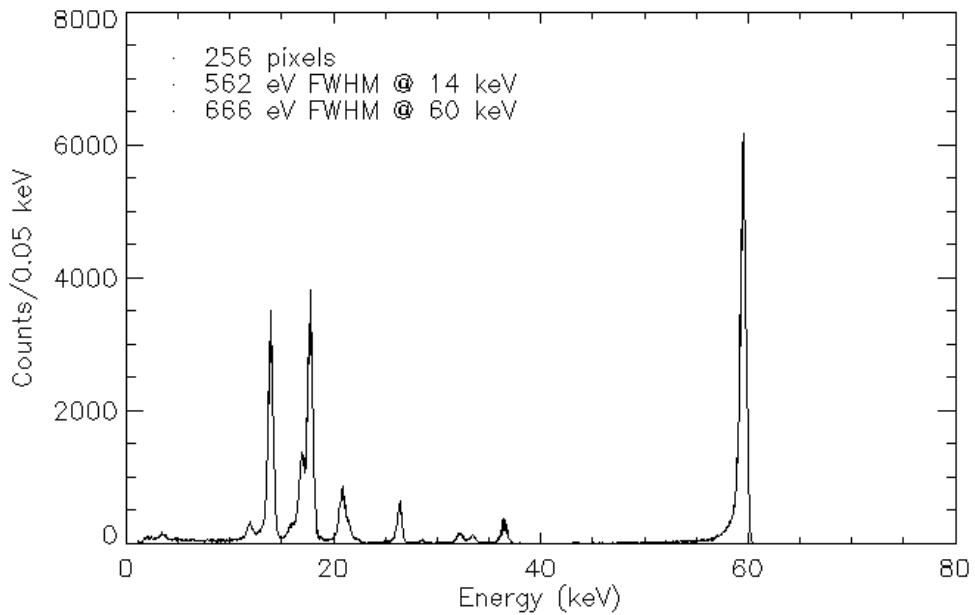
Figure 32. Americium 241 spectrum obtained by summing the 256 calibrated spectra of the Caliste-HD matrix,
when the device is cooled down to –5°C. The 1 mm-CdTe detector is biased at –300 V.
The energy resolution is 0.56 keV at 14 keV and 0.67 keV at 60 keV. The triplet at 17 keV is getting separated.
The low-level threshold is 1.5 keV.

• Low threshold

The architecture of the discrimination channel in IDeF-X HD with individual settings enables us to reach low-energy thresholds as low as 1 keV for the best channels and 1.5 keV on the sum spectrum of a Caliste-HD unit. This capability was exploited to determine the real detection efficiency of the CdTe detectors at low energy with a platinum electroless planar cathode. Caliste-HD was placed in the SOLEX facility (LNHB, CEA-Saclay, France) that generates a flux-calibrated monoenergetic X-ray collimated beam from 2 to 12 keV. Images and spectra were obtained down to 2.2 keV with Caliste-HD (cf. Figure 33-Left). The energy resolution at this energy was found to be 441 eV FWHM for single events and 560 eV a (F5 3-R.
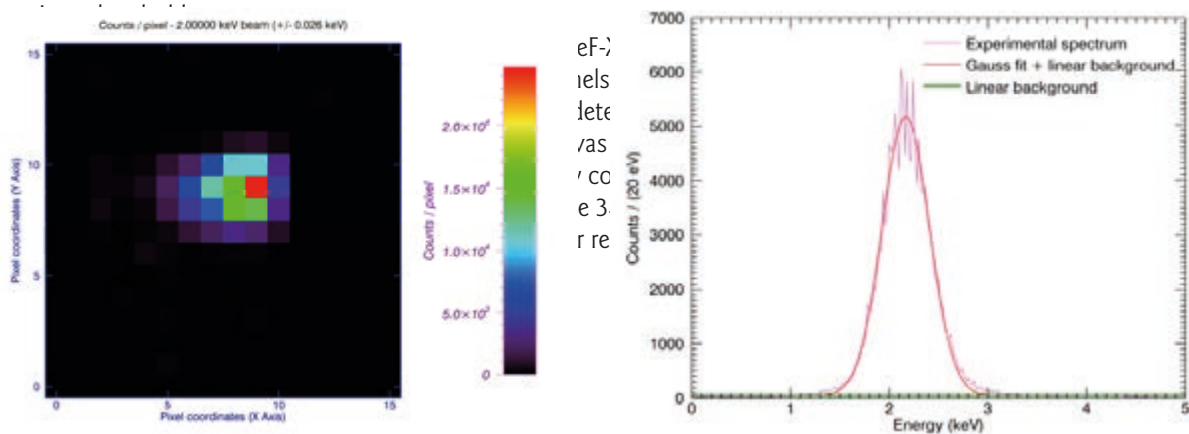

Figure 33. Left – Image obtained with CALISTE-HD of a collimated spot at 2.137 keV at SOLEX facility.
With a pitch of 625 micrometers, we can estimate the spot size to a maximum of 3.75 mm (X axis)
and 2.5 mm (Y axis). The color scale represents the counts in a pixel.
Right – Example of sum-spectrum obtained with the 2.137 keV beam. The energy resolution is found
to be 560 eV FWHM. The photopeak can be fitted by a Gaussian function.

To compute the ratio between detected photons and incoming photons, the incident count rate on Caliste-HD was determined by measuring time intervals between two events and fitting a Poisson-law distribution (typically 1000 count/s). Taking into account single events and double events, double event deficit due to the energy threshold cutting, Pt, Cd, and Te K-edges, the total X-ray efficiency was evaluated and modeled at low energy.
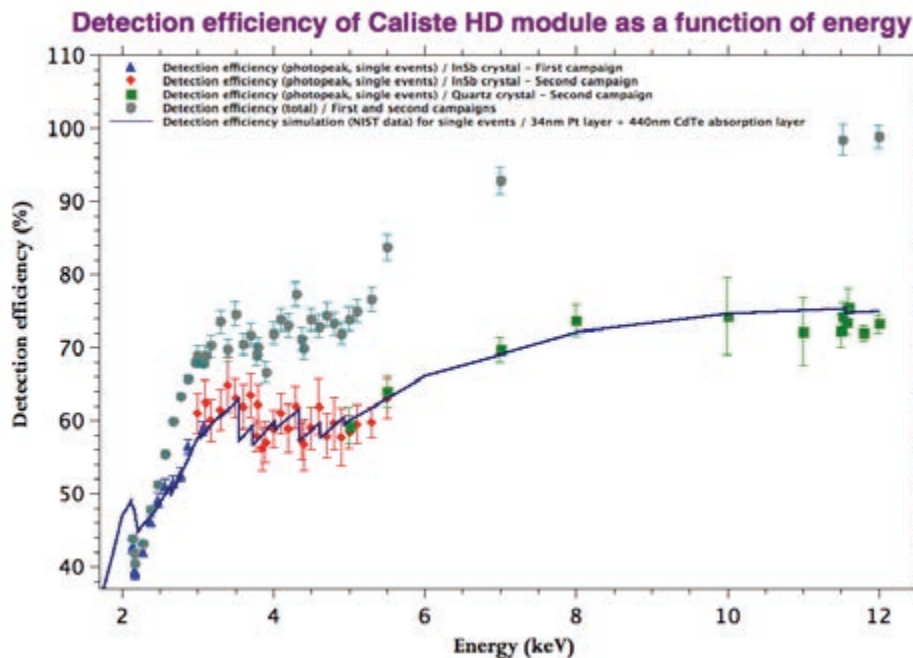

Figure 34. Detection efficiency measured and simulated for single events, between 2.137 and 12 keV.
Two series of runs were represented, for different monochromators used in SOLEX facility.

Figure 34, total efficiency is 40% at 2 keV and 84 % at 3.6 keV. The model is compliant with a platinum thickness of 34 nm and an interface layer between Pt and CdTe of 440 nm, which would be insensitive to X-rays. Such entrance window with a monopixel crystal (no charge sharing effect) would lead to a total X-ray efficiency of 60 % at 2 keV. Further investigation on the nature of this dead layer allowed identifying, with RBS[5], a TeO_2 layer underneath the electrode of 396 nm thick [3.12, 4.13 and 8.16]. This detailed analysis of the surface allows us to understand the response at low energy and consolidating our real senstivity at low energy with Caliste. We conclude that Caliste is an X-ray and hard X-ray spectrometer.

- High-energy response
  The nominal dynamic range of Caliste-HD is optimized from 2 keV up to 250 keV. However, we engineered an adjustable gain (4 different settings) by switching the feedback capacitor of the IDeF-X HD CSA to set the dynamic range up to 1 MeV (40 fC). This parameter is simply set by telecommand. No change is required to Caliste electronics body but a thick enough CdTe or CdZnTe crystal could be used. We equipped one of our Caliste-HD prototypes with a 2 mm thick CdTe crystal to raise the stopping power keeping good crystal quality and low noise. Despite the pretty thin CdTe crystal placed on top of Caliste-HD, we recorded the response to high-energy radioactive sources like Cs-137 with a line 662 keV with 4% photopeak efficiency. A typical sum spectrum, from all the channels, free of any correction but a linear energy calibration of individual channels, is shown in Figure 36 where the spectrum was recorded using between 2 keV and 700 keV. The dynamic range was set to 1 MeV but no line is available above 662 keV with this particular radioactive source. With different sources at higher energies (Co-60 for instance), we confirmed the 1 MeV dynamic range. The detector was cooled down to -16°C and biased under -600V.

---

5. RBS is standing for Rutherford Backscattering Spectrosopy. This technique makes use of a 3.2 MeV alpha particles impinging the material to be analysed. The spectrum of backscattered particles is dependent of the composition of the material and is compared to a model. The composition of the layer is derived.
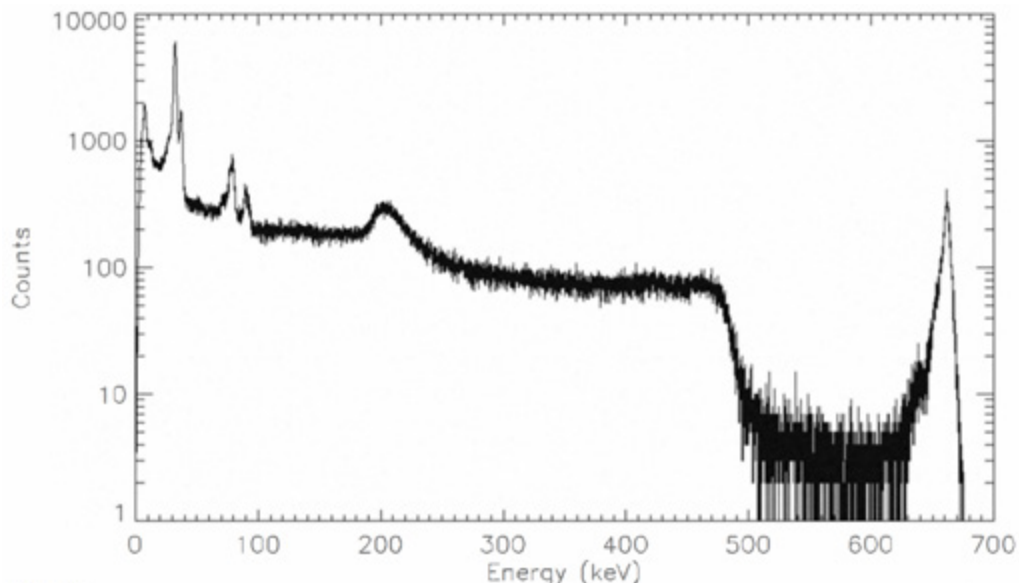
Figure 35. Cs-137 spectrum obtained with Caliste-HD. The spectrum is the sum of all calibrated channels single events spectra. In this configuration, Caliste-HD is equipped with a 2 mm thick CdTe (Schottky). The energy resolution is 4.1 keV at 662 keV and the low energy threshold is set at 2 keV.

The Cs-137 spectrum shows an excellent energy resolution at 662 keV with 4.1 keV FWHM (0.6%). This result is obtained keeping the low-threshold value as low as 2 keV. This result is pretty unique. Zhong He group at University of Michigan, using 3D sensitive thick CZT obtain a higher energy resolution, typically of 0.5% at 662 keV with an energy cutoff at 10 keV or more [8.17]. The energy resolution of the 32 keV line is found to be ~1.1 keV FWHM.

Caliste-HD has not been experienced with thicker CdTe crystals than 2 mm. As a matter of fact, the Schottky type detector instability is getting worse and worse with the CdTe thickness and would require us to to operate the detector even colder, in the range of -40°C. Improving the efficiency at this energy suggests the use of thick CdZnTe instead, up to 10 or 15 mm, free of polarization effect.

- Dead time

    Caliste-HD is self-triggered. When at least one photon hits a pixel, a trigger is generated and time-tagged with an accuracy of approximately 100 ns with time-walk correction (off line). The modules are frozen after a latency time set equal or higher than the selected peaking time. After that period, the FPGA controller records the hit pixel addresses and the analogue outputs are multiplexed. Single photon readout takes approximately 5 to 20 µs readout in total depending on the selected peaking time.

    With a focusing technique for hard X-ray imaging, the count rate expected for bright astronomical sources is of the order of 100 to 1000 counts/s in the point spread function of few millimeters half energy width. Despite this rather low count rate requirement, CdTe detection planes based on Caliste hybridization with IDeF-X front-end ASIC are well suited for high-count rate applications, due to the self-triggered architecture. Each Caliste of a detection array can be connected to an analog to digital converter and hence, can be operated fully independently from its neighbor. When the controller detects a trigger signal from a Caliste unit, it has to wait for a latency time at least equal to the time for the pulse to reach its maximal value, which is stored in the peak detector and is proportional to the incident energy. During this period, a second photon arriving in the same pixel would provoke a pile-up event, or a "misfit" event if it interacts in another pixel (good count estimate but bad energy estimate). Then the controller starts the readout sequence and the whole device becomes blind that corresponds to a dead time for the instrument: events occurring in this period in the same Caliste unit are missed. A simulation tool has been built to estimate the timing response of such a system. The input events are generated by Monte Carlo simulation of a monoenergetic bunch of photons interacting in a 1 mm-thick CdTe detector and 100 nm Pt entrance window, and time-tagged using a Poisson-law distribution. A basic model of induction in the semiconductor detector is assumed to take into account the charge sharing according to the pixel pattern of the anode: for Caliste-HD, only

interactions occurring in the 100 μm pixel gap provoke split events. The events are then processed sequentially using simulation data of the ASIC response; events are tagged as detected, misfit, in pile-up or missed. The results obtained after several simulation runs with different source count rate are shown in Figure 36 for a typical configuration of Caliste-HD. For a peaking time of 2 μs and a latency time of 2.5 μs (corresponding to the time to summit) and a low-level threshold of 3 keV, the fraction of misfit events including pile-up can be inferior to 2% until 10000 photons.s^{-1}.cm^{-2}. At that rate, the dead time is 9% of the observation time but the actual number of missed events due to the readout of the device is only 3%. It is however possible to operate the device up to 10^5 photons.s^{-1}.cm^{-2} and to correct the recorded counts knowing the dead time and using such simulation tools to properly estimate the incident flux. Another efficient way to estimate this flux is to study the statistics of time intervals between two events and to model it by a Poisson law.
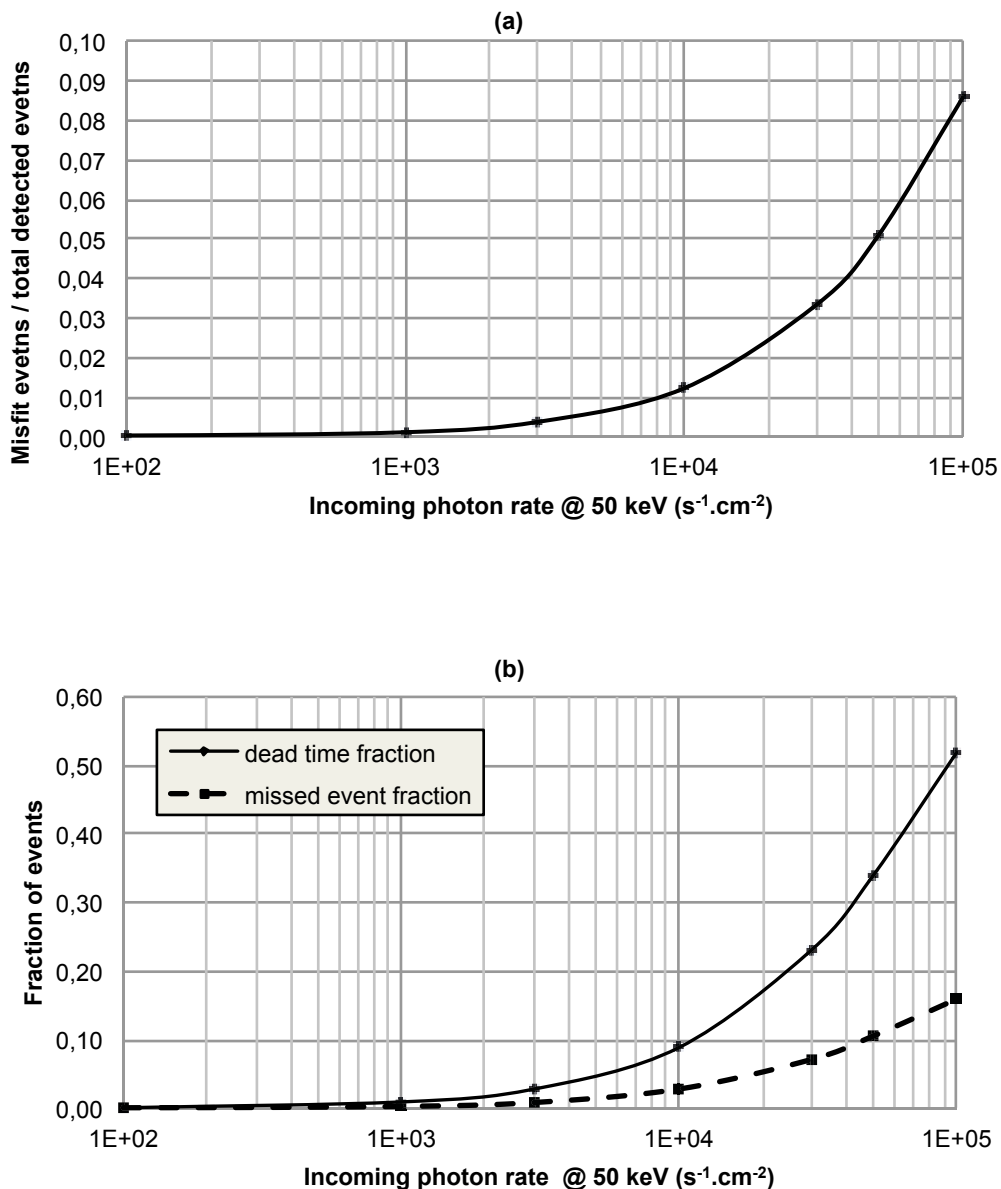
Figure 37. Simulation of timing properties of Caliste-HD for 50 keV photon beam, for a Poisson distribution of events, a shaping time of 2 μs, a readout time of 9 μs for single events and 10 μs for double events, a low-level threshold of 3 keV. (a) Pile-up fraction as a function of the source count rate (b) Fraction of dead time and missed events a function as the source count rate.

- Imaging

  To illustrate the imaging capability in X-rays, we illuminated MACSI [3.5.1] with a [241]Am source using a tungsten mask with a spiral-shaped aperture between the source and the detectors. The images are shown on Figure 38. Cooling the system down to 0°C, we successfully operated 2045 pixels out 2048. The pixels show a normal statistics count rate thanks to excellent uniformity of the sensing material. The dead zones of the camera, appearing in black in Figure 37, are due to the required space between two neighbor Caliste units on the MACSI design. This dead space is limited to the width of 1 pixel and appears every 16 pixels. For a 64-cm² focal plane made of 8 MACSI sectors, the total dead zone would correspond to 9% of the total surface. Thanks to impressive progress in Schottky CdTe production in terms of uniformity and yield, since 2005 it is now possible to design new space imaging spectrometers with 2 to 4 cm² CdTe detectors using the same hybridization concept to reduce the dead area fraction.

Despite the presence of dead region between Caliste modules, note that the entire volume of the pixelated CdTe crystal is sensitive to X-rays; when a photon interacts in a pixel gap (100 μm pixel gap for 525 μm pixel size in Caliste-HD geometry), the charge cloud induces charges in all the neighbor channels with very little charge loss (less than 1% at 60 keV) and creates split events. All MACSI channels are independent and include their own discriminator. Consequently, multiple hits are read out and associated in the data with a unique time-tag but distinct energy and position coordinates. Therefore, it is possible to analyze the data and efficiently correct the split events between neighbor pixels. The split events are mostly due to charge sharing (2, 3 or 4 pixels) between pixels or fluorescence escapes (double hits). Assuming the fact that a large majority of split events is caused by photons impinging into the inter-pixel gaps, their localization is assigned to a 100 x 525 μm rectangle between two triggered pixels for double hits (see Figure 37-b) or assigned to a 100 x 100 μm square at the center of 4 neighboring pixels in case of triple or quadruple hits. The flexibility of MACSI architecture allows selecting only single events to obtain a high-resolution image associated with excellent spectral performances, as well as the possibility to refine interaction areas by visualizing split events. In this case, the improvement of the spatial resolution comes at the expense of a slight degradation of the energy resolution. As matter of fact, the energy resolution results from the quadratic sum of the each channel electronic noise. Double hits degrade the energy resolution by $\sqrt{2}$.

Regarding the imaging refinement, it is not sufficient to compute the geometrical ratio of the interpixel gap surface to the total sensitive surface in order to estimate the fraction of multiple to single events. For instance, the image displayed in Figure 37-c, the fraction of split events is found to be 23% while the inter pixel regions represent 28% of the whole detection surface. Apart the fluorescence which plays a role when the impinging photon energy is high enough with respect to the Cd and Te K edges, the operating conditions must be taken into account as well: high-voltage and operating temperature affect the probability of charge-sharing to occur. Moreover the low-level discriminator threshold settings affect the capability to detect multiple events. In fact, a high discrimination level will cause the single event rate to be artificially higher than expected. Consequently, a rigorous image reconstruction, where singles and multiple events are properly assigned to pixels and inter-pixel areas respectively, requires some careful corrections. An "effective pixel surface", likely to be larger than the metalized surface, must be defined to flatten the images. The effective pixel surface is a correction coefficient matrix that depends on the photon energy (*e.g.* charge cloud size), the operating conditions and the detector geometry. Nevertheless, for simplicity and as a first approximation, Figure 37-c is obtained by weighting the pixels and inter-pixels counts to their respective geometrical surfaces and looks flat and uniform.
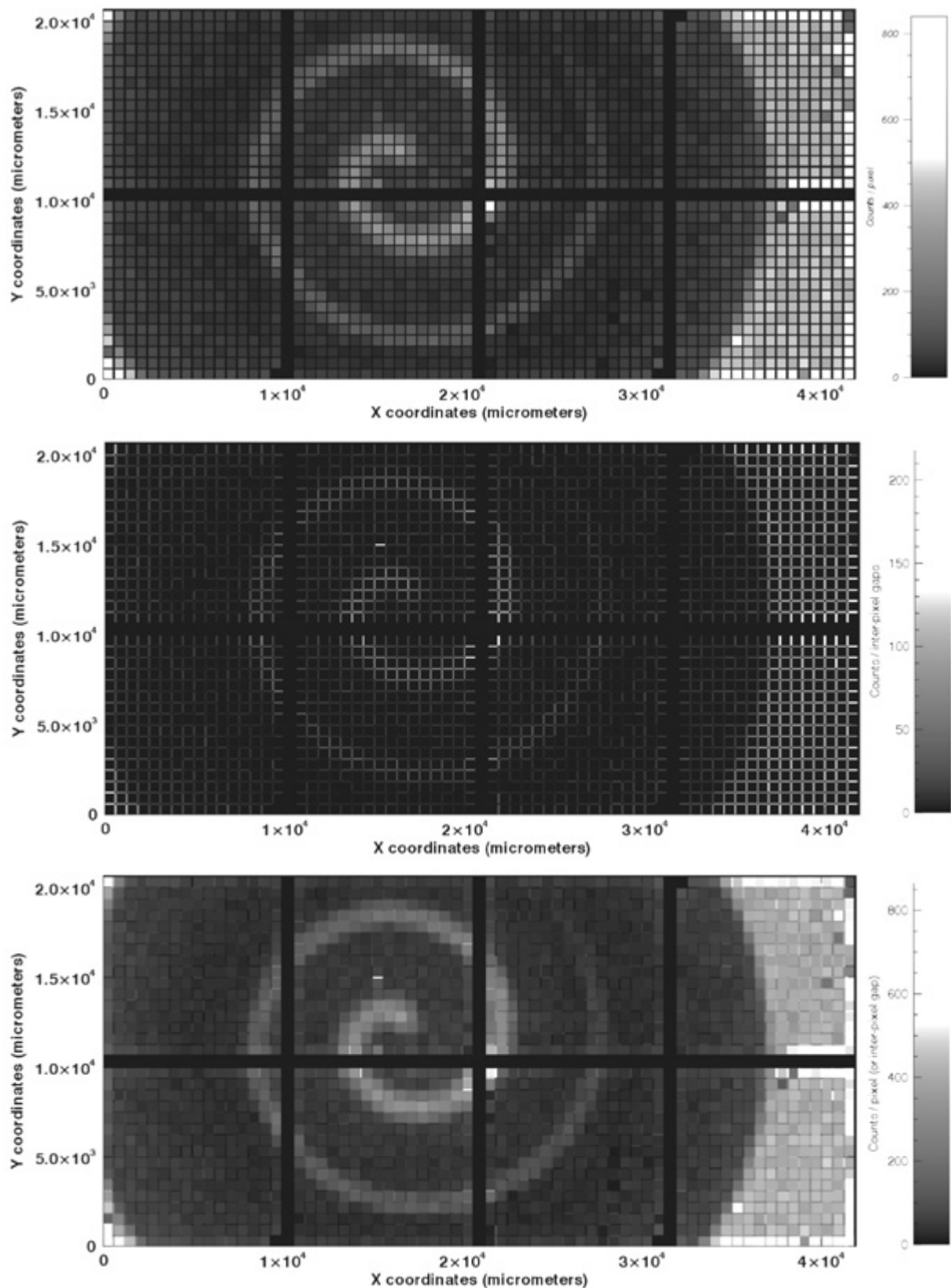
Figure 37. X-ray image of the first MACSI detection plane of 8 cm² CdTe (2048 pixels) by illuminating the matrix with a 241Am source through a 1 mm-thick tungsten mask. The round mask has a spiral-shaped opening. (a) Image of counts obtained for each single pixel. (b) Image of counts obtained by selecting only split events between two neighbor pixels, assuming the fact that incident photons impinged the inter-pixel gap. (c) Image of counts obtained for each single pixel and in inter-pixel gaps. Respective counts measured in inter-pixel gaps were weighted to their surface.

Concluding, MACSI deserves the name of hard X-ray Camera since it is able to make movies, recording hit position, energy and time of arrival with high accuracy.

- Polarimetry

   Caliste devices are not only imaging spectrometers resolved in time but can be used as a hard X-rays in Compton polarimeter. The polarimetric performance of our detector is primarily determined by the fundamental physics of the Compton scattering process for linearly polarized photons.

We tested Caliste-256 devices as a Compton polarimeter [4.4 and 4.9] at the European Synchrotron Radiation Facility (ESRF, Grenoble, France) where we exposed the detector to a highly polarized and mono-energetic beam at 300 keV, for different angles and fractions of polarization. At these energies, it is very likely that a Compton scattering process occurs in a CdTe detector. Deviating by 90°, the scattered photon energy is 189 keV and has a mean free path of 5.42 mm, well suited to the 1 cm^2 of Caliste. Figure 38-a shows an example of a map of the photoelectric absorptions in the energy range from 181 keV up to 197 keV, the beam — 300 keV, 98% linearly polarized with an angle of 0° – being focused in the middle of the bowtie figure. The data are corrected for fluorescence lines escape, charge sharing and detector alignment and the modulation curve is derived as shown on Figure 38-b. We find a modulation factor to be Q = 0.74 ± 0.02. Our model is superimposed to the data and the match is almost perfect.
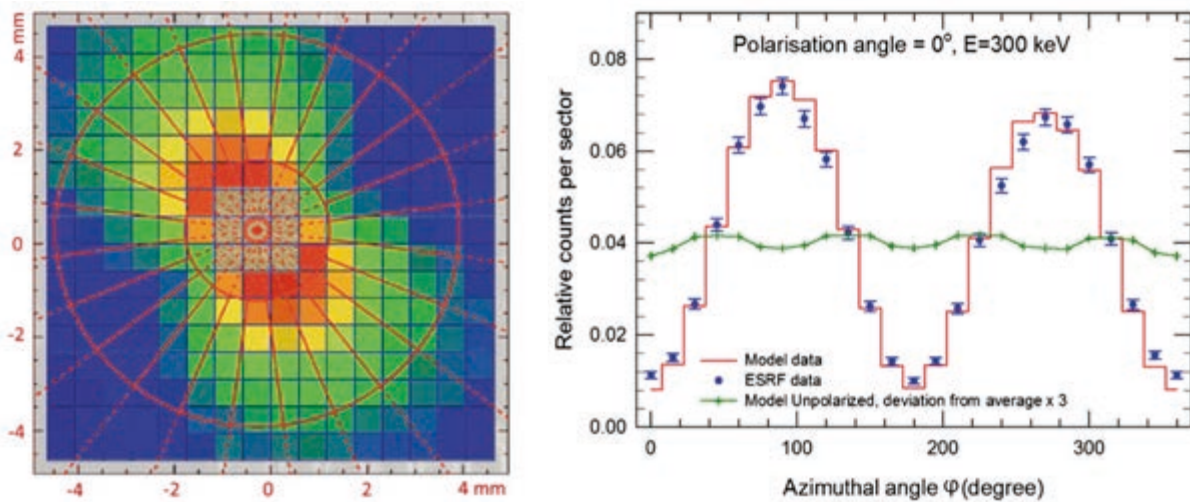

Figure 38. Polarimetry measurements realized at ESRF Grenoble by selecting Compton events in one Caliste-256 detector (scattering around 90°). (a) Compton photon distribution over the CdTe 256-pixel matrix with a 300 keV photon beam with 98% polarization at 0°. (b) Count rate modulation: comparison of experimental data and modeling (300 keV, 98% polarization). Q factor of 0.78 ± 0.02 can be obtained with this device (300 keV, 100 % polarization).

We published our results in Experimental Astronomy in a paper named "Hard X-ray polarimetry with Caliste, a high performance CdTe base imaging spectrometer. This paper has been realized in the frame of "Lapolcaliste" collaboration. I was the PI of this experiment.

6.3. Paper#5 [3.4.9]: Hard X-ray polarimetry with Caliste, a high performance CdTe based imaging spectrometer

ORIGINAL ARTICLE

Hard X-ray polarimetry with Caliste, a high performance CdTe based imaging spectrometer

S. Antier · P. Ferrando · O. Limousin · E. Caroli ·
R. M. Curado da Silva · C. Blondel · R. Chipaux ·
V. Honkimaki · B. Horeau · P. Laurent · J. M. Maia ·
A. Meuris · S. Del Sordo · J. B. Stephen

Abstract Since the initial exploration of the X- and soft γ-ray sky in the 60's, high-energy celestial sources have been mainly characterized through imaging, spectroscopy and timing analysis. Despite tremendous progress in the field, the radiation mechanisms at work in sources such as neutrons stars, black holes, and Active Galactic Nuclei are still unclear. The polarization state of the radiation is an observational parameter which brings key additional information about the physical processes in these high energy sources, allowing the discrimination between competing models which may otherwise all be consistent with other types of measurement. This is why most of the projects for

S. Antier (✉) · P. Ferrando · O. Limousin · C. Blondel · B. Horeau · P. Laurent · A. Meuris
CEA Saclay, DSM/Irfu/Service d'Astrophysique, 91191 Gif-sur-Yvette Cedex, France
e-mail: sarah.antier@cea.fr

E. Caroli · J. B. Stephen
INAF/IASF-Bologna, Via Gobetti 101, 40129 Bologna, Italy

R. M. Curado da Silva
LIP-Coimbra, Departamento de Física, Universidade de Coimbra, 3004-516 Coimbra, Portugal

J. M. Maia
Physics Department, University of Beira-Interior, 6201-001 Covilhã, Portugal

J. M. Maia
LIP-Coimbra, Physics Department, University of Coimbra, 3004-516 Coimbra, Portugal

R. Chipaux
CEA Saclay, DSM/Irfu/Service d'Électronique, des Détecteurs et d'Informatique, 91191 Gif-sur-Yvette
Cedex, France

V. Honkimaki
ESRF, 6 Rue J. Horowitz, BP 220, 38043 Grenoble Cedex 9, France

S. Del Sordo
INAF/IASF-Palermo, Via Ugo La Malfa 153, 90146 Palermo, Italy

the next generation of space missions covering the few tens of keV to the MeV region require a polarization measurement capability. A key element enabling this capability, in this energy range, is a detector system allowing the identification and characterization of Compton interactions as they are the main process at play. The compact hard X-ray imaging spectrometer module, developed in CEA with the generic name of "Caliste" module, is such a detector. In this paper, we present experimental results for two types of Caliste-256 modules, one based on a CdTe crystal, the other one on a CdZnTe crystal, which have been exposed to linearly polarized beams at the European Synchrotron Radiation Facility (ESRF). These results, obtained at 200 and 300 keV, demonstrate the capability of these modules to detect Compton events and to give an accurate determination of the polarization parameters (polarization angle and fraction) of the incoming beam. For example, applying an optimized selection to our data set, equivalent to select 90° Compton scattered interactions in the detector plane, we find a modulation factor Q of 0.78 ± 0.06 in the 200–300 keV range. The polarization angle and fraction are derived with accuracies of approximately 1° and 5 % respectively for both CdZnTe and CdTe crystals. The modulation factor remains larger than 0.4 when essentially no selection is made at all on the data. We also present in this paper a simple analytical model of the interactions for the detector geometry. We show that the experimental data compare very well with the simulation, and that simple geometrical effects explain some of the observed deviations between the data and the simulation. All of these results, both experimental and from simulations, prove that the Caliste-256 modules have performances allowing them to be excellent candidates as detectors with polarimetric capabilities, in particular for future space missions.

1 Introduction

Astrophysical studies of the γ- and X-ray universe are currently mainly based on imaging, spectral and timing analysis of high energy sources. Even though progress has been remarkable in these domains, thanks in particular to large dedicated space telescopes (such as Chandra, XMM, RXTE, INTEGRAL, SWIFT and Fermi); there still remain unsolved questions concerning high energy sources' physical processes. Source radiation emission polarization state (i.e. angle and degree of linear polarization) provide additional key information which can be used to address these questions and to distinguish between different models which are otherwise consistent when considering other source characteristics. In particular, polarimetric measurements provide information on the emission mechanisms at play, the emission region geometry, and the structure of the magnetic field in a wide variety of hard X- and γ-ray sources such as pulsars, solar flares, active galactic nuclei, galactic black holes or γ-ray bursts [24, 36].

Several theoretical models for these types of high energy sources predict the emission of fluxes with different levels of linear polarization, ranging from a few percent for AGN to several tens of percent for pulsars [16, 22, 26]. The complexity of making polarization measurements, coupled with the limited number of photons in the hard X- and γ-ray range have been the limiting factors that have kept this field

practically unexplored in space astrophysics. The only missions with dedicated polar-imeters ever flown are OSO-8 in the soft X-rays domain, with a successful measure-ment of the Crab nebula polarization [34, 35], and IKAROS, the small solar power sail demonstrator launched in 2010, in the gamma ray domain which carries the Gamma-Ray Burst Polarimeter [37]. Finally, in the gamma-ray domain, complex data analysis of the imaging spectrometers SPI and IBIS onboard INTEGRAL, have allowed to obtain pioneering on the Crab pulsar and Cygnus X-1 [3, 8, 11, 23], as well as on different GRBs [4, 14, 15, 19, 30] The interest in this field has generated a large number of proposals, advanced design projects, or even built but never flown instruments dedicated to polarimetry, and using non focusing optics. The will not be reviewed here as this is beyond the scope of this paper, but the interested reader is referred to [32].

Still in the context of the instrumental work presented here, another path is now also being followed based on the progress made in focusing optics in the hard X- and soft γ-rays domain. This allows designing missions with an increase of several orders of magnitude in sensitivity and angular resolution with respect to non-focusing telescopes. The NuSTAR mission [17] is the first flying mission of this type, and other missions with enhanced performances or different energy domains have been proposed e.g. COSPIX [10], PheniX [29], GRI [21], and DUAL [33]. In these focusing telescopes, the focal plane has a small size, and the detectors need to have a very good spatial resolution to ensure that the imaging performance satisfies the requirements on angular resolution, and a very good spectral resolution to deal with requirements rising from astrophysical questions for which a clear identification of lines is required. Devices fulfilling these requirements are imaging spectrometers based on segmented and pixelated detectors. Provided that proper coincidence logic is used to read out the pixelated sensor, then the sensitive volume can also be used as a scattering polarimeter, taking advantage of the Compton interaction properties. This detector configuration allows optimizing the trade-off between the scientific return and the instrument design complexity thanks to the development of a single focal plane array playing all the roles. This is with the main prospect of such a telescope configuration for a space mission that we are presenting the results on the Caliste-256 modules in this paper.

In the hard X-ray / soft gamma-ray domain, the use of high Z material is mandatory, and in order to optimize a focal plane instrument for the different missions envisioned, CdZnTe polarimeters prototypes have already been tested in a series of experiments [5–7], which allowed the evaluation of their polarimetric performance and the study of possible sources of errors and factors limiting the achievable performance.

As a further step for improving the performance of this type of scattering polarim-eter, we have decided to study the use of the fine pitch (580 μm), high energy resolution (~1 keV FWHM at 60 keV) and good time resolution imaging spectrometer developed at CEA, the Caliste-256 module [25]. In this paper, we quantitatively investigate such prototype detector performance, both from measurements performed under a linearly polarized beam at the European Synchrotron Radiation Facility (ESRF) in Grenoble (France), and from simulations dedicated to this detector configuration.

This paper is organized as follows. We first recall the measurement principle and describe the experimental setup configuration at the ESRF. We then detail the analytical model which has been specifically developed in this context, and which is used to generate simulation data in the same detector configuration as for the ESRF experi-ment. The next section presents the spectral analysis of the experimental data, including

corrections for charge splitting and escapes lines. This is then followed by the description of the polarization analysis procedure, common to both experimental and simulation data, and to the study of systematics effects. In the last section, before the conclusion, are presented all the experimental results obtained in this experiment, and its comparison with simulation data.

2 Scattering polarimetry principle

The possibility to measure polarization with spectro-imaging detectors such as that we are developing relies on the fundamental physics underlying the Compton scattering process for linearly polarized photons. This process presents a dependence on polarization direction given by the Klein and Nishina [20] differential cross-section for Compton scattering per unit of elementary solid angle $d\Omega$:

$$\frac{d\sigma}{d\Omega} = \frac{r_0{}^2}{2} \left(\frac{E'}{E}\right)^2 \left[\frac{E'}{E} + \frac{E}{E'} - 2\, sin^2\theta\, cos^2\varphi\right], \tag{1a}$$

where $r_0,2$ is the classical electron radius and E, E' are the energies of the incoming and scattered photons respectively. The scattered photon is deviated from its original direction by θ.

E, E' and θ are related by the following equation:

$$E' = \frac{E}{1 + \dfrac{E}{m_e c^2}\,(1-cos\theta)}, \tag{1b}$$

with $m_e c^2$ being the electron rest energy.

The azimuthal deviation angle φ corresponds to the angle formed by the scattering plane (defined by the initial direction and the scattered direction, see Fig. 1a) and the incoming photon polarization plane (defined by the photon direction and its polarization vector, i.e. the photon electric field component).

Considering linearly polarized photons, Eq. (1a) provides the azimuthal (φ) dependency for the Compton scattered photons. The Compton scattering of polarized photons generates non-uniformity in its azimuthal angular distribution (Fig. 1b). From the equation, fixing all parameters except the azimuthal angle φ, the probability of interaction reaches its minimum and maximum for orthogonal directions, $\varphi=0°$ and $\varphi=90°$ respectively.

The polar plot in Fig. 1b shows the probability distribution against the azimuthal angle φ for linearly polarized photons at 200 keV, after Compton scatterings at θ angles of 10, 50 and 90°. It is clearly apparent that the asymmetry of this distribution increases with the scattering angle. Note that the asymmetry is almost invisible at $\theta=10°$, while for $\theta=\theta_M=90°$, the probability of a photon to scatter perpendicularly to the polarization plane is roughly five times larger than that to scatter along the polarization plane, with the probability distribution looking like a bowtie (cf. Figs. 1 and 5).

The measurement of polarization consists in measuring, and characterizing the shape of this distribution. To do this, one has to identify both the location of the Compton
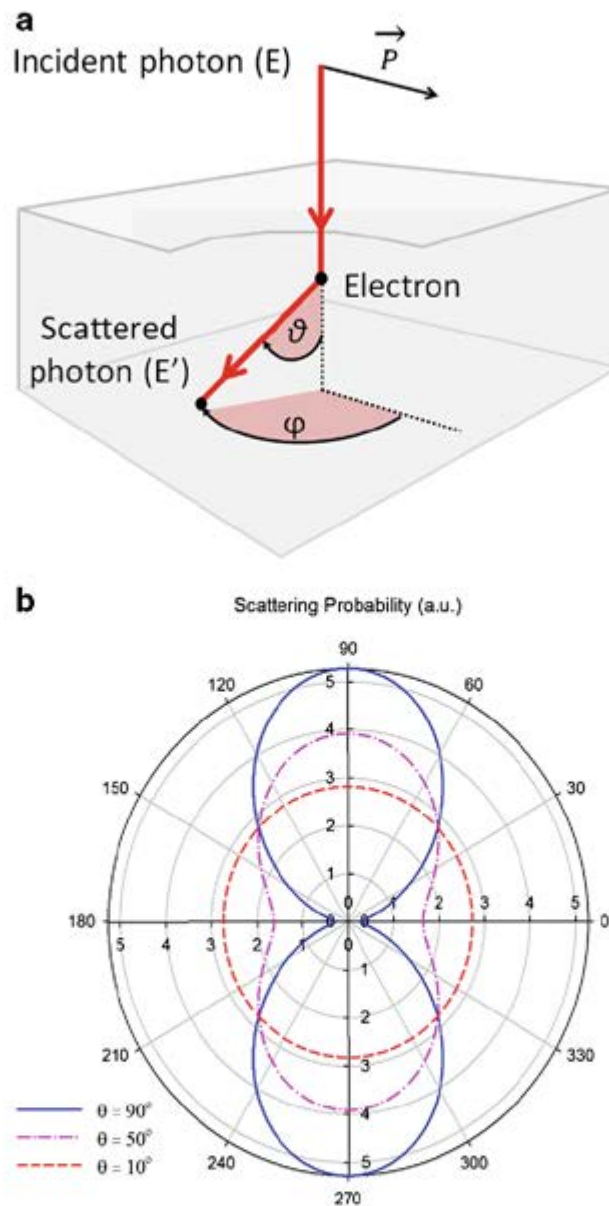
a

Incident photon (E)

$\vec{P}$

Electron

Scattered photon (E′)

ϑ

φ

b

Scattering Probability (a.u.)

$\theta = 90°$
$\theta = 50°$
$\theta = 10°$

Fig. 1 **a** Scheme of Compton scattering of a polarized photon; **b** Azimuthal angle (φ) probability distribution for a given Compton scattering angle (θ) of linearly polarized photons at $E=200$ keV. The direction of the polarization is parallel to the horizontal axis of the polar plot

interaction (the center of the bowtie distribution), and the direction of the scattered photon. This latter information can be obtained if the scattered photon interacts and this interaction location is measured. In the range of energies we are testing, this second interaction is usually a photoelectric absorption. A polarimetric measurement thus necessitates the measurement of two simultaneous events, one at the location of the Compton interaction, with an energy deposit in the pixel E_d, and one at the location of the photoelectric absorption with an energy deposit $E_p=E'$, with $E_d+E'=E$.

In practice, with a single thin detector, pixelated, the best configuration is for a perpendicular illumination of the detector, in the center of one of its central pixels. Photons scattered around $\theta=90°$, for which the polarization information is maximum, can then be stopped in the same detector, in one of the peripheral pixels, thanks to the large amount of matter provided in this configuration. By analyzing the spatial distribution of this second interaction position, for double events, which has the imprint of the bowtie shape, one can derive the degree of polarization and the polarization direction of the incident radiation.

At this point, it is possible to define the widely used figure of merit for a polarimeter: the polarimetric modulation factor Q. For a pixelated detector, Q is written as:

$$Q = \frac{1}{P} \frac{Nmax - Nmin}{Nmax + Nmin},$$ (2)

where N_{max} and N_{min} are the maximum and minimum of the angular azimuthal distribution of the scattered photons defined over the detector plane and P is the degree of polarization. Because of the nature of the scattering process, N_{max} and N_{min} are counted along two orthogonal directions.

3 Experimental setup

As explained in the previous section, the fraction and the angle of polarization of the incoming radiation are determined by measuring the azimuthal angular distribution of the scattered photons after the impinging photons Compton scatter into a position sensitive spectrometer detector: double-hit positions, arrival time and energy deposits are measured simultaneously and independently. The polarization of the source is derived from the data after a sufficient accumulation of events.

In May 2011, with the aim of evaluating the performance of CZT/CdTe based room temperature solid state pixel spectrometers as hard X ray scattering polarimeters, our collaboration set up an experiment at European Synchrotron Radiation Facility (ESRF Grenoble, France) using the ID15A high energy beam line: POLCaliste, i.e. POLarisation with Caliste-256.

3.1 The Caliste-256 detection module

In order to measure the two interactions, one corresponding to a Compton scatter, the other to the absorption of the scattered photon, a fine pixel and high spectral resolution detector, named Caliste-256 was employed [25]. Caliste-256 is a hybrid camera that integrates a 1 mm thick CdTe Schottky (or a 2 mm thick CZT) monolithic crystal pixelated detector mounted on top of a 3D module supporting the front-end electronics based on eight full custom ASICs IDeF-X [12] developed at CEA (Fig. 2). This detector module is able to detect photons between 2 and 280 keV. With a 580 μm pitch, arranged in a 16×16 pixels array, and 1 keV (FWHM) energy resolution at 60 keV, the Caliste-256 version has been specially developed for space missions taking into account environmental space constraints [9]. Its characteristics enable a straightforward selection of Compton events, and a good determination of the geometry of the photon interactions.
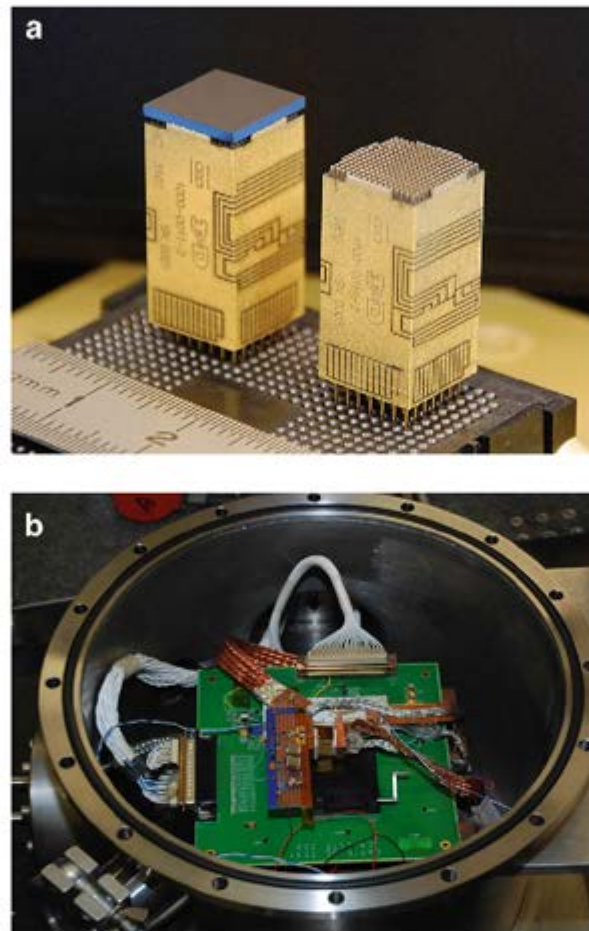
Fig. 2 a The 1 mm thick Schottky CdTe Caliste-256 module with 580 μm pixel pitch; **b** The Caliste module mounted on its electrical and mechanical interface inside the vacuum container (T≈−10 °C)

3.2 The ESRF experiment setup

The ID15 beam line at ESRF (Grenoble, France) provides high-energy and mono-energetic X-ray photon fluxes with a user selectable energy between 30 and 750 keV and a linearly polarized fraction up to about 100 %. As can be seen in Fig. 3a, the mono-energetic X-ray beam was directed onto the top surface of the Caliste-256 module, confined in a vacuum chamber, through a collimation system with adjustable tungsten slits. This collimator allowed the beam size to be set to 100×100 μm, significantly smaller than the 500 μm pixel size. We scanned the detector surface with beams of different energies in the dynamic range of Caliste-256 in order to perform a fine energy calibration of each individual pixel. We checked the detector response uniformity and evaluated the overall system performance prior to performing dedicated Compton runs for which we centered the beam spot onto one of the four central pixels.

Figure 3b shows, in the foreground, the X-ray beam collimation system, and in the background the flange of the vacuum vessel which has at its center a beryllium entrance
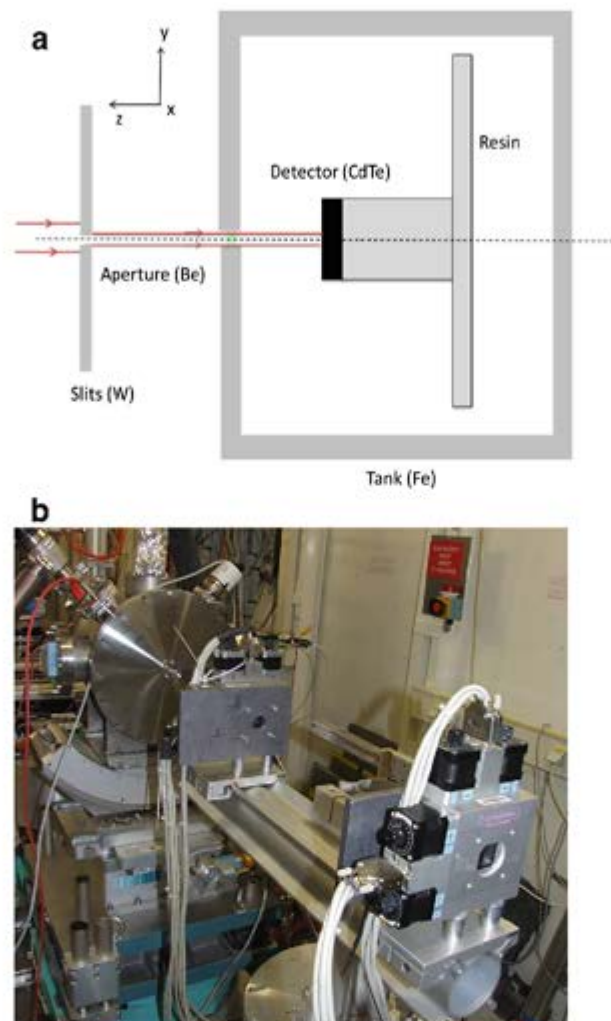
Fig. 3 Schematics (a) and picture (b) of the PolCaliste experiment set-up at experimental hutch of the ESRF ID 15A beam line in Grenoble (France)

window placed in front of the cathode side of the Caliste-256 module. The vacuum vessel hosts the Caliste-256 mounted on its test board, used to supply the voltages and data link and is cooled down to −10 °C. The whole setup is installed on a movable system. The micrometric precision translation and rotation stages allow the accurate positioning of the detector in the plane (X, Y), perpendicular to the beam axis Z, and its rotation around the direction of the beam itself.

Table 1 summarizes the set of measurements, which have been performed for both Caliste-256 samples (1 mm CdTe and 2 mm CZT) under different conditions: beam energies, degree and angle of polarization. Approximately 1 million events were recorded for each run defined by a unique experimental configuration. The data are time tagged photon-photon lists of events, which were then analyzed off-line: energy calibration, double event selection, spectra build up.

Table 1 Parameters tested with Caliste-256

Type of detector	CdTe/CZT
Thickness (mm)	1/2
Incident beam Energy (keV)	200–300
Degree of polarisation (%)	80-85-88-89-90-98
Angle of polarisation (degrees)	0-5-10-20-30
Model analysis	Yes

3.3 The Caliste-256 triggering logic for the ESRF experiment

Caliste-256 is an imaging spectrometer with fine timing resolution. Each of the 256 pixels is independent from the others. Each channel has its own preamplifier, pulse shaper, adjustable discriminator, and its own peak detector system. Note that Caliste-256 has no pile-up rejection system. Caliste-256 has no sample and hold circuitry but a peak detector (the peak detector records the maximum of the amplitude at each shaper output). The detailed architecture is described in [25]. Each of the eight IDeF-X ASICs inside Caliste-256 shares for all its 32 channels a common hit pixel register, an analogue memory, a multiplexing analogue output system, a slow control digital link and a triggering system. All discriminator outputs are routed to an OR logic system to deliver a unique trigger signal for one ASIC. Inside Caliste-256, the eight ASIC trigger outputs are routed again to a cabled OR logic. Thus Caliste-256 has a unique global trigger for the whole camera.

When a photon hits the CZT sensor and deposits an energy above the discrimination threshold, a trigger signal is generated and the address of the hit pixel is stored into the hit pixel register of the associated ASIC. The Caliste-256 global trigger signal rises when at least one channel of the camera has been hit. The Caliste-256 global trigger signal is sent to the FPGA controller to enable the readout sequence. The trigger is time tagged with a resolution of 20 ns. Note that the trigger resolution is not the sensor resolution, which is in the range of one microsecond. After a 10 µs latency time, the delay required to develop the pulse shape up to its maximum, Caliste-256 is locked. The latency time is set to 10 µs, which corresponds to the shaper peaking time value, enabling accurate pulse height measurement, free of ballistic deficit. During the latency time, pile-up may occur when the count rate is high. All peak detector outputs are held and the corresponding amplitudes are stored into each channel analog memory. Any new upcoming photon hit will be ignored. Once locked, Caliste-256 is ready to communicate with its FPGA controller to release the memorized data. At first, the FPGA reads the hit register of each ASIC to determine the addresses of the hit channels. It computes and starts the multiplexing sequence to present the analogue data of the corresponding channels to the system ADCs. The data packet is created as a list of events. The latter contains the global trigger date, hit pixel addresses and amplitude binary codes. The data packet is transmitted to the Data Acquisition System via a Space-Wire link. Because the channels are read in serial mode, the readout dead

time is dependent on the number of hit channels. The typical value is 17 μs plus 1 extra μs per channel to be read. When the readout sequence is completed, Caliste-256 is reset and the acquisition resumes.

For a Compton event, two hits arise into two distinct channels. In this case, one or two ASICs trigger exactly at the same moment but a single global trigger is set up, as depicted above. This event generates, for a unique time tag corresponding to the global trigger, a set of two addresses and two corresponding energies. The data packet has a list of two events having precisely the same date. Similarly, a photon hit accompanied with a photon escape in a neighboring pixel generates a similar kind of event in the list. Conversely, when two independent events hit the sensor in the duration of the latency time, the first of the two raises the trigger. Consequently, there is a chance that the second event energy is not recorded properly as its pulse height might not reach its maximum before being read out. The probability of such an event is related to the detector count rate and the 10 μs duration of the latency time, which can be seen as a coincidence window. At ESRF, where the beam was targeted onto a single pixel at a time, this probability was very low apart in the targeted pixel itself. Compton scattered energy in surrounding pixels is very likely to be measured accurately as shown in further.

Thanks to the architecture of the Caliste-256 electronics, it is possible to measure simultaneously the energy deposits in different pixels from the same impinging photon after it has Compton scattered. Consequently, the selection of Compton events in the photon list is straightforward, which facilitates an accurate construction of the bowtie figure.

The Caliste-256 trigger is very flexible. Due to the low probability of recording a Compton double event in the detector volume (~5 % of all events at 200 keV beam energy) we chose to set the trigger criterion so as to record only double and more hits in order not to saturate the telemetry with simply useless data. On the contrary, the rejection of the single events prevents us from measuring the Compton to photoelectric probability. The way to adjust the trigger system is as follows: The Caliste-256 global trigger works in current mode. In other words, the global trigger signal is the sum of the ASIC trigger signal currents. For instance, the trigger signal amplitude out of Caliste-256 when two chips are hit simultaneously, in at least one pixel each, is exactly twice the signal amplitude obtained with one single chip trigger. Discriminating on the trigger height forces the FPGA controller reaction only when at least two ASICs are touched. The drawback of this configuration is that there is no trigger generated for single interactions, in particular in the beam pixel and for Compton double hit when the two corresponding pixels are read by the same ASIC (two rows). The readout happens only when a second chip is hit. However, apart the central pixel information, no information is lost because the signal amplitude is kept in the chip memory until the next reset: all scattered photons interacting into the detector are accurately transferred (energy and position of interaction) to the acquisition system but the corresponding primary energy deposit into the central pixel is lost as it is almost immediately followed by a photon at the beam energy: due to the peak detector behavior which records the maximum signal in the latency time, the central pixel energy is almost always the beam energy. We checked that the bowtie figure is not biased by the trigger configuration until all multiplicities are taken into account. The model described further away supports this conclusion.

4 Numerical simulation of the polarimetric performance

In order to support the interpretation of the experimental results, and to assess the reliability of the Caliste-256 module polarimetric performance, we have developed a 3D numerical tool to calculate the expected polarization performance in the energy range of interest here, from 50 to 300 keV. Based on tabulated photon-matter interaction probabilities, the model allows the theoretical azimuthal distribution of Compton scattered photons to be constructed. The input parameters of this model are, on the detector side, the crystal composition (CdTe and CZT) and its geometry (number of pixels, pixel pitch, inter-pixel gap and detector thickness), and, on the incident photon beam side, its energy, its position and angle of incidence with respect to the surface of the sensor, and its degree and angle of polarization.

The model, implemented in IDL (Interactive Data Language), is based on the analytical expressions describing the following elemental process depicted in Fig. 4: a Compton interaction at depth z_{in} in the central pixel, with the scattered photon emitted with angles θ and φ, followed by a photoelectric absorption of this scattered photon after travelling a distance r_{in} without any interaction. These are given by:

$$dP_{Compton}(z_{in}, E) = e^{-\mu_T(E)\cdot\rho\cdot z_{in}}\cdot\mu_C(E)\cdot\rho\cdot dz, \tag{3}$$

$$dP_{Ph.El.}(r_{in}, E') = e^{-\mu_T(E')\cdot\rho\cdot r_{in}}\cdot\mu_{Ph.El.}(E')\cdot\rho\cdot dr, \tag{4}$$

$$P(\theta, \varphi) = \frac{1}{\sigma_{tot}}\frac{d\sigma}{d\Omega}. \tag{5}$$

where μ_C, $\mu_{Ph.El.}$, and μ_T are respectively the Compton, photoelectric and total mass attenuation coefficients, ρ is the density of the detector material, E is the incident photon energy and E' that of the scattered photon, and $d\sigma/d\Omega$ is the Klein Nishina differential cross section given in Eq. (1) with σ_{tot} its integral over the entire solid angle.
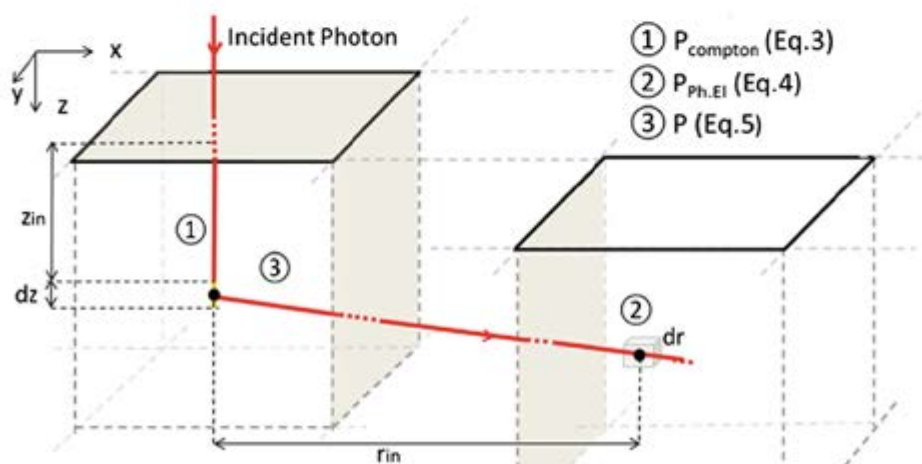

Fig. 4 The elemental process implemented in the simulation tool, with proper integration on the detector thickness and pixel location and volume

These equations are integrated over the relevant parameters for detector thickness and pixel location and volume. For a given Compton interaction position (z_{in}) and scattering direction (θ and φ) the integration over r_{in} is performed analytically for each pixel. The integration over z_{in}, θ and φ can be performed only numerically, which is performed with sufficiently small steps with respect to the interaction length (z_{in}) or the characteristic variation scales (θ and φ).

This model does not take into account more complex phenomena, as e.g. the Doppler broadening of the Compton interaction, or the energy resolution of the detector, or processes which could give rise to higher multiplicity events (such as a second Compton interaction or an escape line). This would necessitate a full Monte-Carlo simulation. However, as will be seen in the following sections, this analytical model is more than accurate for our purposes. It describes our observations very well, and allows simple and fast investigations regarding the different beam and detector parameters.

Figure 5 shows the theoretical distribution of double events generated by this model, a Compton scattering in the central pixel followed by a photoelectric absorption of the scattered photon in a peripheral pixel. In Fig. 5a, the distribution showing a bowtie shape is obtained by simulating a 100 % linearly polarized beam at 200 keV, normal to the detector surface with an angle of polarization of 30°. In this case, the main scattering axis of distribution is perpendicular to the polarization vector. In Fig. 5b, the same simulation is performed but the impinging flux polarization fraction is set to 0. In this case, no preferred direction is visible on the map.

5 Experimental data spectroscopic analysis

As the Compton scattered photon energy is related to its angle of deviation, a careful energy calibration and a detailed analysis of the observed spectral lines is mandatory before attempting to derive the Compton polarimeter performances. The typical spectra in the central pixel and the surroundings pixels are displayed in Fig. 6. They show complex features, and in particular include two phenomena that can be corrected for: fluorescence escape lines and charge sharing between adjacent pixels. These spectral analysis and corrections are described below.

We focus here on the analysis of spectra obtained at 200 keV with a 1 mm thick CdTe sample but an identical analysis has been performed at all beam energies and for both CdTe and CZT detectors. In order to achieve the full detector energy calibration, we scanned the surface with the beam, pixel by pixel. Figure 6a shows a spectrum from the target (central) pixel, after pulse-height calibration, while Fig. 6b is the spectrum from the sum of all the pixels of the detector, except for the central pixel and the eight adjacent ones (the "9 central pixels").

In the central pixel (Fig. 6a), where the beam is aimed, apart from the photoelectric peak at precisely 200 keV we can identify the following expected structures:

- Fluorescence lines from matter surrounding the detector, mainly W ($K_\alpha \approx 59$ keV and $K_\beta \approx 67$ keV) and Pb ($K_\alpha \approx 75$ keV and $K_\beta \approx 85$ keV). W is present in the slits located at the front of the detector, which are used to fine shape the beam. Lead is massively present on the ID15A hutch walls, facing the detector and used as
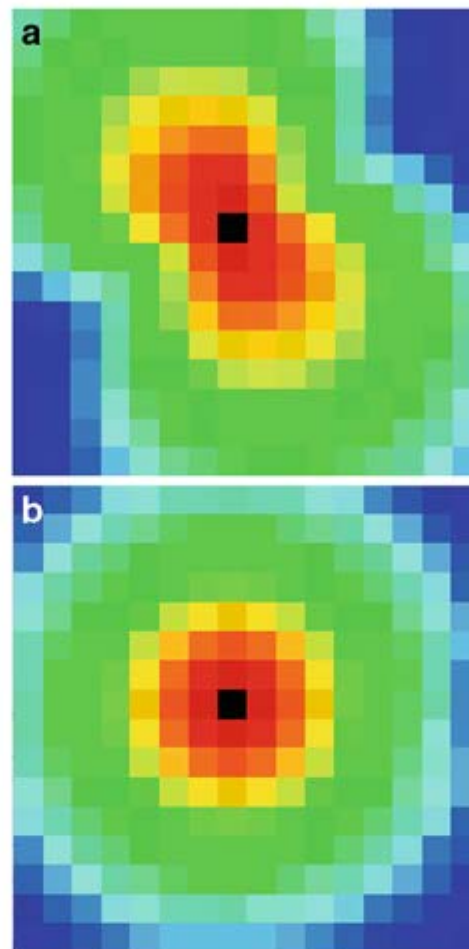
Fig. 5 Compton scattered photons distribution for a 200 keV incident energy beam predicted by the numerical model. The color code corresponds to the probability: *Red* is high while blue is faint. **a** 100 % linearly polarized beam with angle of polarization=30°; **b** un-polarized photon beam

shielding. Due to their position with respect to Caliste-256, the W and Pb fluorescence photons are rather uniformly distributed over the CdTe surface.

- The Compton edge at 87.8 keV.
- The backscatter peak at 112 keV, which is due to the interaction of photons with the electronic material behind the sensor.
- The Cd ($K_\alpha \approx 23$ keV) and Te ($K_\alpha \approx 27$ keV) fluorescence escape lines, respectively at 177 and 173 keV.
- Some combinations of piled-up events above 200 keV. Note that Caliste-256 has no pile-up rejection system and has no sample-and-hold circuitry but a peak detector. Thus, Caliste-256 is sensitive to pile-up when several photons interact into the same pixel during the latency time (time elapsed between the trigger and the internal hold signal commended 10 µs later by the FPGA sequencer).
- The saturation of the analogue front-end electronics for pulse heights approximately corresponds to 270 keV. The saturation is not sharp due to the readout chip design.
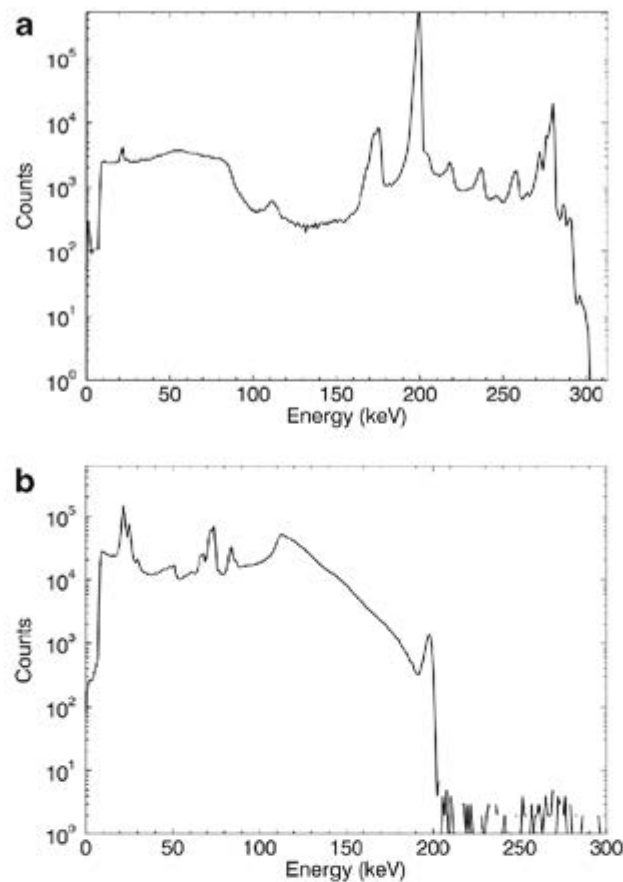
Fig. 6 Energy spectra of CdTe Caliste-256 detector, irradiated by 200 keV photons, (30° angle of polarization and 98 % degree of polarization) a spectrum of the central pixel b spectrum of the all pixels except for the nine at the center

The shape of the saturation is complex because the dynamic range of our readout electronics depends on the count rate. Usually, saturation appears as a peak ending the dynamic but it looks different in Caliste-256. One should consider that Caliste-256 response is no longer valid above 270 keV and events above must be ignored. However, such events are not discarded in our data set as they contribute to the dead time.

Regarding now the pixels around the central one (Fig. 6b), we identify the following expected structures:

- The Cd ($K_\alpha \approx 23$ keV) and Te ($K_\alpha \approx 27$ keV) fluorescence lines.
- The surrounding material fluorescence lines, mainly W ($K_\alpha \approx 59$ keV and $K_\beta \approx 67$ keV) and Pb ($K_\alpha \approx 75$ keV and $K_\beta \approx 85$ keV) as described previously.
- The Compton scattered photons from 112.2 keV up to the photo peak energy with a particular population of interest around 143.8 keV corresponding to the Compton scattered photons at exactly 90° with respect to the beam direction.
- The bump at 195 keV up to the photo peak energy of Compton photons scattering in front of the detector (probably with the beryllium window), corresponding a scattered angle between 0 and 20°.

- A continuous spectrum due to charge sharing between neighboring pixels. This type of event occurs when a photon hits the detector in between two pixels or when the charge spreads out a pixel and induces a fraction of the signal on a neighbor pixel.

Prior to build the modulation curve and to analyze the polarimetric performances of Caliste-256, we apply spectral corrections for split events (charge sharing) and CdTe X-ray fluorescence escapes. Such events are responsible for incorrect energy measurement in a pixel where a Compton scattered photon has interacted.

In case of Cd or Te X-ray fluorescence photon escape in neighbor pixels, the sum of the energies is reassigned to the primary pixel position.

Besides the fluorescence, 21 % of the Compton scattered photons have theoretically a chance to interact in between two pixels generating a charge sharing [18]. In our case (CdTe, 1 mm, 300 V −10 °C, 2 keV threshold) we measured a probability of 19.8 % to record a split event. This effect is corrected as well, by summing neighboring double events. The computing process is very similar to the X-ray fluorescence apart the energy distribution is continuous. We chose to reassign the location of the event to the pixel position where the highest charge has been detected. Finer corrections can be engineered. In the energy band from 19 to 31 keV, combining fluorescence and charge sharing, up 76 % of the photons are reassigned to a neighbor pixel.

This correction increases the Compton hump in the range from 112 up to 195 keV by more than 4 %. The remaining ~24 % uncorrected fluorescence and charge sharing events are essentially due to isolated events located at the vicinity of the guard ring. The 200 μm guard ring that surrounds the pixel array is not connected to a spectroscopic channel. Thus, a photon escape or split event with the guard ring cannot be reassigned to any pixel. The effect of the correction is illustrated on Fig. 7.

6 Scattering maps, modulation curve construction and polarization parameters determination

We build the modulation curve searching for the azimuthal distribution of Compton scattered events in the Caliste-256 sensor plane. A crude analysis, taking into account
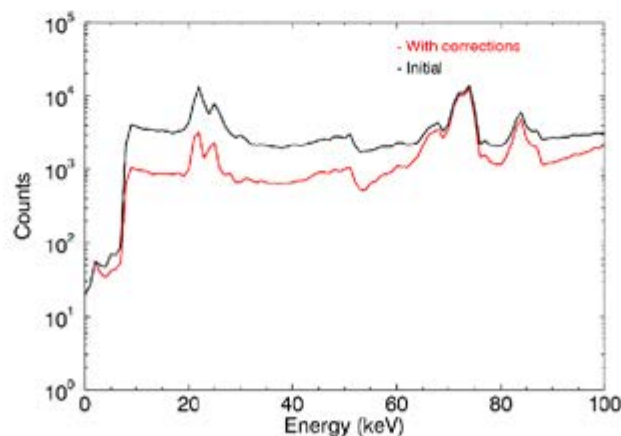

Fig. 7 Initial and corrected energy spectrum of the pixels around the nine central pixels of CdTe Caliste-256 detector, irradiated by 200 keV photons, (30° angle of polarization and 98 % degree of polarization)

all the photons detected in the pixels surrounding the central pixel (targeted by the X-ray beam), would result in a moderate modulation factor Q in the range of 0.4. Conversely, taking advantage of Caliste-256 fine resolution, spectral corrections as shown above and selection of events in narrow bands of energy are possible. We chose the energy bands to select Compton scattered photons strictly deviated by 90° in the detector plane. This approach allows a maximization of the modulation factor Q, up to ~0,8, at the expense of a lower efficiency.

In the following we chose to build the modulation curve by selecting the Compton scattered events corresponding to a scattering of the beam photons at the maximum modulation of around 90°. At 200 and 300 keV this corresponds to a scattered photon energy (which we will refer to as simply "energy" in the following) of 144 and 189 keV respectively. Accounting for Doppler broadening [38] and the detector energy resolution (1 keV FWHM), we decided to select events with energies in the 139–148 keV range for the 200 keV beam, and 181–197 keV range for the 300 keV beam. Note that in the case of an ideal detector and no Doppler broadening these energy ranges would theoretically correspond to a scattering at 90±6°. This is the only selection, which is applied to the data. A map of the corresponding counts in these ranges reveals the expected bowtie shape (see Fig. 8).

The final step of the data analysis is the extraction of the modulation curve. It consists of building the distribution of the Compton scattered photon count-rate with respect to the azimuthal angle. To do so, we superimpose a grid with 24 angular sectors, of 15° each, on the 2D Compton event distribution map as shown in Fig. 8. The inner and outer radii of the grid are set to 1.5 and 4.2 mm respectively. The inner value is chosen to exclude the nine central pixels, which give poor information on the angular direction of the scattered photons; the outer value is chosen so that the entire grid is included in the square shaped detector surface. The center of the grid coincides with the beam spot position on the central pixel.

The number of counts from a given pixel assigned to each sector is measured in the following way. If a pixel is fully included into the sector surface, the total number of counts of the pixel is added in the sector count. If only a part of the pixel is included in
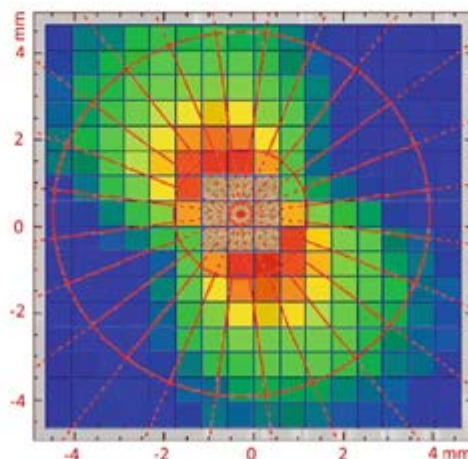

Fig. 8 A false color map of the CdTe Caliste-256 counts distribution of events with scattered energies in the 139–148 keV band. These data are for a 200 keV photon beam, 98 % linearly polarized and with 30° polarization angle. The nine central pixels are off scale. On top of the data are shown the sectors, with their inner and outer radii, and their angular limits, which are used to count the events for building the azimuthal distribution curves

the sector, then the number of counts, fractional, assigned to that sector is given by the total number of counts of the pixel weighted by the fraction of the pixel surface, which intersects the sector. This first order correction of the pixel-size effect allows the construction of a smooth modulation curve as a function of angle, as shown on Fig. 9.

The same method is applied to the data obtained from the simulation described in Section 4, which are organized as count maps, as for the experimental data. When compared to experimental data, the simulated data are normalized so that the total number of counts is the same for both sets. Figure 9 shows both experimental and simulated data for the case of a 300 keV, 98 % polarized beam with a 0° polarization angle. As expected, the first maximum is found at +90°. The modulation curve from the simulation is represented on Fig. 9 in a sinusoidal full line. The model almost perfectly matches the data. The experimental Q factor is 0.74±0.02.

Using the same simulation model, we have calculated the modulation curve for a non-polarized beam at the same energy, ie 300 keV. The corresponding modulation curve is pretty flat but not perfectly straight, as a perfect system would show. The response to a non-polarized beam is shown in Fig. 9, intentionally magnified by a factor of three to help the reader to appreciate the shape of the parasitic modulation structure. This parasitic modulation is a systematic error due to the square shape of the pixels sampling the bowtie figure. The effect will be one of the limiting factors of our Minimum Detectable Polarization (MDP) [36]. Although the paper aims at studying of the polarimetric performances of Caliste-256 in laboratory conditions and the reader must be aware that others systematics errors may contribute to the loss of polarimetric sensitivity in a given telescope configuration. For example, the reconstruction of the modulation curve will be affected by the continuous spectrum of a gamma sources and the pretty uniform beam impinging over the detector surface. In this case, other strategies are employed to control the systematics such as discussed by Muleri and Campana [27].

Finally, for fast fitting purposes of the experimental data, we have also used a simplified simulation of the modulation curve, in the 90° scattering conditions, based
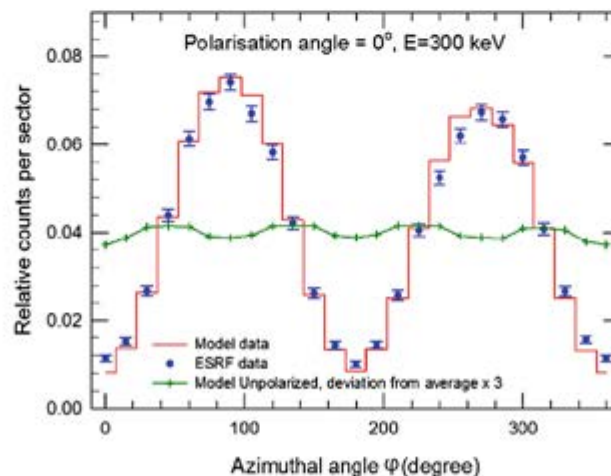

Fig. 9 Modulation of scattered photons distribution for a 300 keV incident beam with a 98 % linear polarization at an angle of 0°, for CdTe Caliste-256. A simulated modulation histogram is superimposed to the data taking into account the true incidence angle of the beam. The curve in green is the result of a simulation for a non-polarized irradiation: the fluctuations (with respect to average) are multiplied by 3

on the integration of Eq. 1a and b over the azimuthal range corresponding to the sectors, with parameters being the polarization angle φ_{obs} and the fraction of polarization P_{obs}. In this simplified model, the finite dimension of the pixels is not taken into account. Using the "curvefit" function of IDL, on can find the best parameters describing the data. In the case of Fig. 9, they are φ_{obs}=0.09±0.29° and P_{obs}=90.4± 0.7. The results for all measurements are listed in the Table 2 of Section 7.

6.1 Effect due to the inclination of the detection plane

Looking at the modulation curve maxima on Fig. 9, it is noticeable that the plot is asymmetric: the first peak is significantly higher than the second one. We call Δ_{max} the difference of the peak heights, as shown in Fig. 10. The curve will only be fully symmetric, i.e. Δ_{max}=0, if the incident beam is perfectly perpendicular to the detector. Any tilt of the detector surface causes a non-uniformity in the Compton scattered photon range: selecting the energy of the Compton scattered photons corresponding to a 90° scatter changes the effective thickness of the detector in each azimuthal direction, because the scattered photon direction is no longer in the detector plane. Consequently, this impacts the modulation curve by shifting the relative heights of the maxima, i.e. $\Delta_{max}\neq0$. The impact depends on the beam energy and the polarization angle. These results are consistent with the recent work published by Muleri et al. [28], devoted to the analytical calculation of a Compton polarimeter response when incident photons are impinging on the detector plane off-axis.

On Fig. 10, the modulation curve model superimposed to the data assumes a perfectly normal incidence for the beam and reveals a deviation to the data at the maxima positions. Δ_{max} is about 10 % of the modulation amplitude. Simulations have demonstrated that by tilting the detector surface with respect to the beam direction, one can account for this effect, as shown on Fig. 9 for the same data set.

In our experimental setup conditions, it is extremely difficult to precisely control the detector orientation. The detector is inevitably tilted with respect to (zOy) and/or (zOx) planes by δx and/or δy rotation angles respectively, as defined on Fig. 11a. The modulation curve symmetry is very sensitive both to the incidence angle and the polarization angle, as is shown in Fig. 11b. Simulating a 0° polarization angle at 300 keV, we see that a rotation angle δx along the x-axis in the range of ~1° will cause a maxima height separation by Δ_{max}≈0.006 counts fraction/sector, i.e. ~10 % of the modulation amplitude. The effect is non linear and increases with the tilt angle.

Fitting the angle δx is a measurement of the detector surface position with respect to the beam direction. From Fig. 11b, we find the detector surface tilt to be δx=1.5°. In this case, the fitting of the angle δy is not decisive because there are few counts recorded in the direction of polarization. The same analysis with 10/30°, 300 keV leads to a same fitting value of δx=1.5°.

7 Full experimental results, and polarimetric response and sensitivity of Caliste-256

From the data treatment and analysis described above, we have characterized the response of the Caliste-256 as a polarization detector, depending on the beam energy,
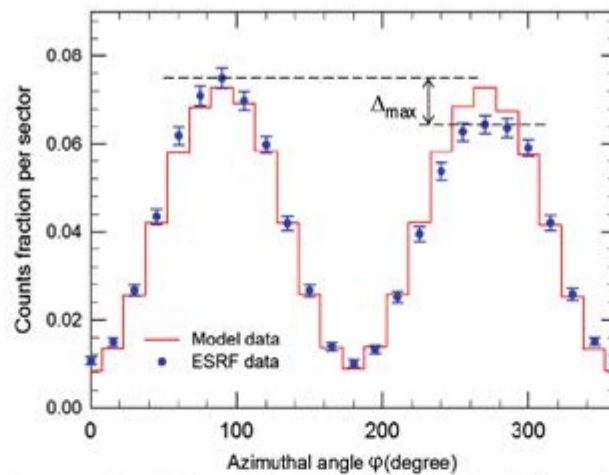
Fig. 10 Modulation curve obtained from real data at 300 keV, 98 % polarized beam, 0° polarization angle. Photons energy selection from 181 to 197 keV corresponds to 90° Compton scattered events only. A simulated modulation curve (histogram) is superimposed to the data and reveals an asymmetrical behavior when the beam is supposed to be strictly normal to the detector surface

the degree and angle of polarization, and the type of crystal. For each run, after the spectral corrections described in Section 5, we have built the modulation curve using only an energy selection criterion, 139–148 keV at 200 keV and 181–197 keV at 300 keV. From this modulation curve, we have on the one hand measured the Q factor, which has been reached in this configuration, and on the other hand derived the best fit for the polarization parameters (angle, fraction), using the method explained in the previous section. Table 2 summarizes the results for all the runs in our database.

Figure 12a shows the modulation curves obtained at 200 and 300 keV. The modulation factor at both energies is remarkably similar as can be seen by superimposing them on the same plot. Q values of 0.79 ± 0.02 and 0.76 ± 0.01 are found respectively. In Fig. 12b, we illustrate the effect of the angle of polarization on the modulation curve displacement at 200 keV. In this case the angles of polarization given by the fitting procedures are 4.84 ± 0.22 and 29.55 ± 0.20 for an expected value of 5° and 30° respectively. The corresponding Q factors are 0.80 ± 0.02 and 0.79 ± 0.02 respectively.

Comparing the 1 mm thick CdTe with the 2 mm CZT based Caliste-256 at 200 keV, with 98 % polarization and 0° polarization angle, we find Q to be 0.84 ± 0.05 and 0.79 ± 0.01 respectively. Looking at the combined data in all conditions, we conclude that within the error bars, both CdTe and CZT behave the same whatever the energy. This is what we would expect due to the fact that we are selecting almost the same subset of Compton scatters–those around 90°. Of course, the 2 mm thick CZT has the key advantage of a higher efficiency than the 1 mm thick CdTe, which increases the sensitivity but not the figure of merit.

Without any energy selection in our dataset, the modulation factor Q is found to be 0.47 ± 0.003 and 0.41 ± 0.003 for CdTe and CZT modules respectively. These results illustrate the advantage of the fine energy resolution of Caliste-256 to maximize the figure of merit, admitting the efficiency is affected. When compared with other CdTe-based single layer and planar polarimeters, we obtain a higher Q factor [6]. This is
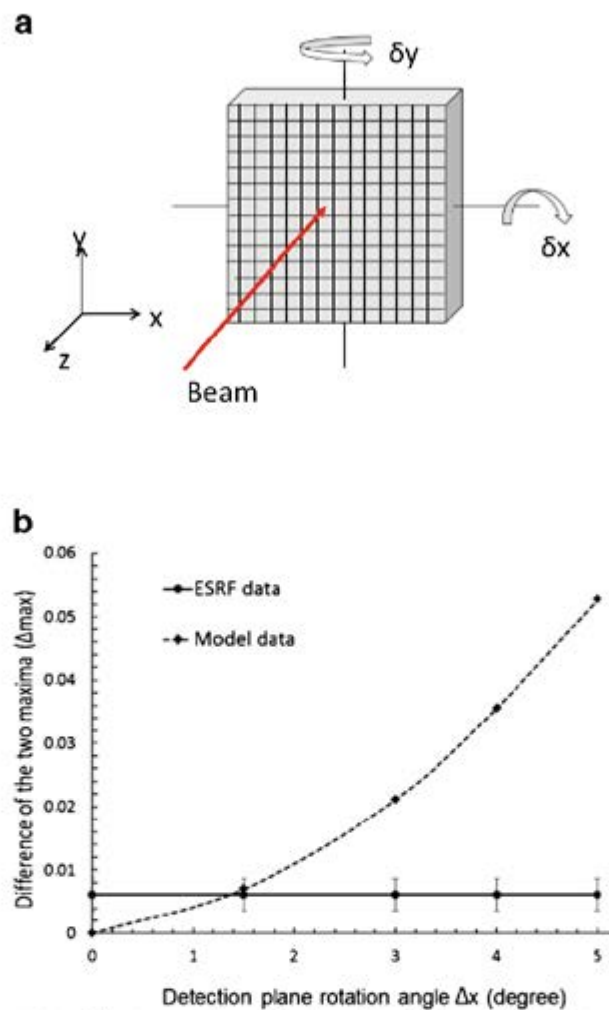
Fig. 11 a Representation of the two rotations angles δx and δy; b Δ_{max} against detector tilt along the x-axis. Δ_{max} is the absolute difference of maxima in the modulation curve, expressed in counts fraction per sector, for 24 sectors. A perfectly perpendicular incidence of the beam with respect to the detector surface gives $\Delta_{max}=0$. The plot is calculated for 300 keV, 0° polarization angle. The model is compared to the data

explained by Caliste-256 prototypes fine pitch, which allows better modulation resolution [2, 24], and the excellent energy resolution, which allows an optimal angular selection of Compton double events.

In Table 2, one can see that the fitted angles of polarization differ by less than 1° from the nominal angle of polarization of the beam. Figure 13 shows the linear correlation ($\varphi_{obs}=a+b\,\varphi_{beam}$) between the incident beam polarization direction φ_{beam} and the measured polarization direction φ_{obs}. The offset a is less than 1° (-0.5 ± 0.5), which is fully consistent with the alignment uncertainty of the system. The slope b is equal to unity within the uncertainty, (1.00 ± 0.04), which shows that despite the square shape of the pixels, there is no bias in the determination of the beam polarization angle. At all incident energies, the angular results are close to $\varphi_{obs}=\varphi_{beam}$. The small differences can moreover be explained by a small deviation of the beam incidence
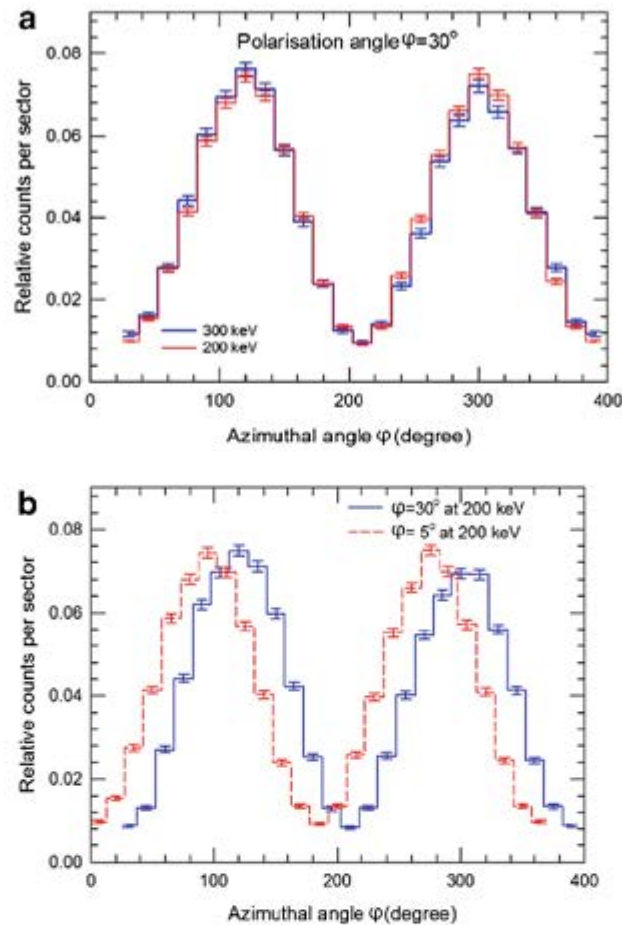
Fig. 12 a Angular azimuthal distribution of Compton scattered photons (histograms) for a 200 and 300 keV incident beam, angle of polarization $\varphi=30°$, 98 % polarization degree. Scattering angles close to 90° are discriminated by selecting the Compton scattered photon energies from 139 to 148 keV and from 181 to 197 keV for a beam energy of 200 and 300 keV respectively; (b) Angular azimuthal distribution of Compton scattered photons (histograms) for two different angles of polarization with a 200 keV incident beam, 98 % polarization degree. Scattering angles close to 90° are discriminated by selecting the Compton scattered photon energies from 139 to 148 keV

direction from the perpendicular to the detector surface. The fitting angle of polarization of a simulated modulation curve (with 200 keV, 98 % polarized, 0° of angle of polarization) where the detector surface is strictly orthogonal to the beam, is $-0.08°$, whereas with a $\delta x=1.5°$ detector surface tilt defined as Fig. 11a, the fitted angle of polarization is $-0.8°$.

Caliste's performance in resolving the degree of polarization of incoming radiation has been assessed by varying the polarization degree of the ID15A beam from its maximum value (98 %) to 80 % which is the lowest value achievable, due to beam flux reasons. Previous polarimetric analyses (simulations and measurements) have addressed the polarization degree [7] but in none of these was the instrument resolution to measure this parameter estimated. Figure 14 shows the linear correlation ($P_{obs}=a+b$

Table 2 Summary of the data configuration taken at ESRF ID15A for Caliste-256, corresponding to our data analysis results

Incident beam parameters				Measurements					
Crystal kind	Energy (keV)	Polarization		Q factor		Angle of polarization		Degree of polarization	
		Angle (°)	Degree (%)	Q	Error	Angle (°)	Error (°)	Fraction (%)	Error (%)
CdTe	200	0	98	0.84	0.05	−1.18	0.65	91.2	1.56
			90	0.79	0.01	−0.08	0.30	79.5	0.68
			89	0.79	0.02	0	0.30	79.1	0.85
			88	0.77	0.02	0.09	0.33	76.6	0.74
			85	0.80	0.02	−0.34	0.30	76.1	0.81
			80	0.78	0.04	0.27	0.50	70.1	1.07
		5	98	0.80	0.02	4.84	0.22	88.0	0.5
		10	98	0.80	0.02	9.7	0.21	87.9	0.5
		20	98	0.79	0.02	19.62	0.21	86.7	0.5
		30	98	0.79	0.02	29.55	0.20	86.1	0.05
	300	0	98	0.74	0.02	0.09	0.29	90.4	0.75
		5	98	0.76	0.01	4.81	0.20	91.2	0.53
		10	98	0.76	0.01	9.79	0.21	91.3	0.54
		20	98	0.76	0.02	19.91	0.21	90.6	0.55
		30	98	0.76	0.01	29.74	0.20	91.1	0.51
CZT	200	0	98	0.79	0.01	−0.6	0.09	86.2	0.2
			90	0.77	0.02	−0.48	0.07	77.6	0.16
			89	0.78	0.02	−0.23	0.23	77.0	0.52
			88	0.75	0.01	−0.59	0.22	74.4	0.5
			85	0.75	0.02	−0.54	0.09	72.0	0.19
			80	0.75	0.03	−0.27	0.40	67.6	0.85
		5	98	0.78	0.02	4.62	0.20	85.6	0.49
		10	98	0.78	0.01	9.36	0.05	85.0	0.13
		20	98	0.77	0.01	19.37	0.18	84.3	0.43
		30	98	0.77	0.01	29.66	0.18	84.3	0.44
	300	0	98	0.73	0.03	−1.07	0.37	88.1	0.95
		5	98	0.73	0.01	4.65	0.15	88.2	0.53
		10	98	0.72	0.01	9.93	0.22	87.6	0.55
		20	98	0.72	0.01	19.73	0.21	87.3	0.53
		30	98	0.73	0.01	30.05	0.19	88.5	0.5

P) between the actual degree of polarization of the beam (P) and that measured (P_{obs}). The slope b, being close to 1 (1.05 for CdTe and 1.15 for CZT), shows that both Caliste modules exhibit a good sensitivity over the full measured range. The Q factor and the associated error bars for polarization levels that differ only by 2 % is practically indistinguishable, as the polarization region between 88 % and 90 % illustrates. Both
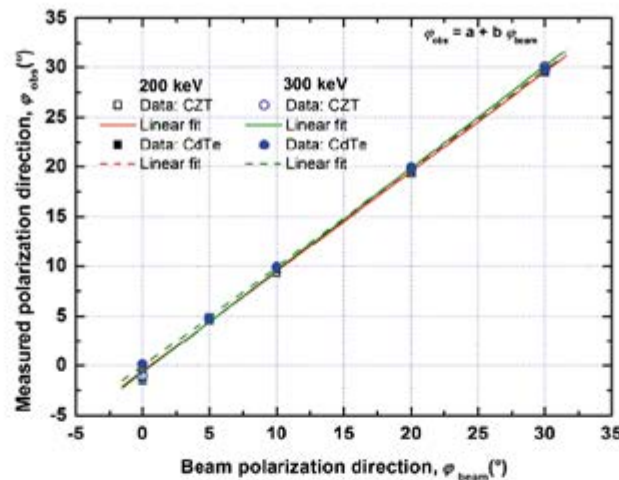
Fig. 13 The observed polarization angle (φ_{obs}) as a function of the ESRF beam polarization angle (φ_{beam}) at 200 and 300 keV, for both CdTe and CZT Caliste modules

detectors show an excellent potential to distinguish between polarization degrees different by less than 5 %, which is an acceptable performance for studying the different physical processes that generate polarized emissions levels e.g. astrophysical synchrotron about 65 % to 80 %, magnetic photon splitting: about 20 % to 30 %, Bremsstrahlung radiation up to 80 % [1, 13, 24, 31].

On the same Fig. 14 are shown the simulated values. They are fully matching for both Caliste modules, demonstrating that the sensitivity to polarization is not dependent on the thickness and absorption properties within the range tested here. The same conclusion can be drawn within errors from the
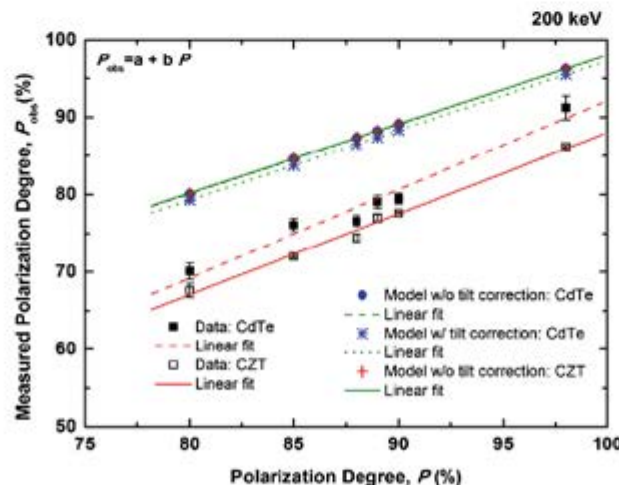

Fig. 14 The observed fraction of polarization (P_{obs}) as a function of the ESRF beam fraction of polarization (P) at 200 keV for both CdTe and CZT Caliste module. Two corresponding simulations at 200 keV for CdTe and CZT where the incident is strictly orthogonal to the beam detector (without correction) and one simulation with the CdTe with the surface detector slightly tilted by 1.5° (with correction)

experimental measurements. The difference between the experimental and simulated curves, which is relatively small, can be probably traced to several reasons. One is that the simulation does not take into account the detector energy resolution and the Doppler broadening, which if done would inevitably blur the polarization information. It might also be that despite this careful energy selection, there is still a small unidentified background component, homogeneous in azimuth, which contributes to lowering the apparent polarization fraction. Finally, as seen before, a modest surface tilt has an effect on the modulation curve, with an impact on the fitted parameters. Investigating these possibilities in more detail is beyond the scope of this paper.

8 Conclusions

Through a set of experiments performed at the ESRF, two Caliste-256 prototypes (CdZnTe and CdTe) have been tested in a configuration for determining the system performance when used as a polarization detector at 200 and 300 keV. Taking advantage of the excellent energy resolution of these devices, it is possible to perform a simple energy selection to extract the Compton events scattering close to 90° into the detector plane, where the modulation is the highest. Combined with the small size of Caliste-256 pixels, with respect to the interaction lengths at these energies, we have been capable to measure Q factors up to ~0.8, much higher than those achieved with the previous types of Cd(Zn)Te detectors. We have also shown that the beam polarization parameters can be measured with an accuracy better than 1° for the polarization angle and better than 5 % for the fraction of polarization. These results compare extremely well with a relatively simple analytical simulation model that we have developed, and which moreover, has enabled us to accounts for small geometrical setting effects seen in the data. Of course, a drastic selection in energy to extract the best events causes the efficiency to get lower, which hopefully could be compensated by the use of focusing optics and/or long exposure times, in a science payload. Eventually, the polarization capability of Caliste-256 is used without any compromise in the same acquisition mode than standard time resolved imaging spectroscopy.

The work presented in this paper demonstrates the excellent potential of Caliste-256 modules for being used as a detector for future missions with spectrometric capabilities in the hard X-ray domain.

References

1. Baring, M.G.: Photon splitting limits to the hardness of emission in strongly magnetized soft gamma repeaters. Astrophys. J. **440**, L69 (1995)
2. Caroli, E., et al.: Polarisation performances of CdTe pixel detector for Laue hard X-ray focusing telescopes. Exp. Astron. **20**, 353–364 (2005)
3. Chauvin, et al.: Polarimetry in the hard X-ray domain with INTEGRAL SPI. Astrophys. J. **769**, 137 (2013)
4. Coburn, W., Boggs, S.E.: Polarization of the prompt gamma-ray emission from the gamma-ray burst of December 2002. Nature **423**, 415 (2003)

5. Curado da Silva, R.M., et al.: Hard X- and soft gamma-ray polarimetry with CdTe array prototypes. IEEE Trans. Nucl. Sci. **51**, 2478 (2004)

6. Curado da Silva, R.M., et al.: Polarimetric performance of a Laue lens gamma-ray. J. Appl. Phys. **104**, 084903 (2008)

7. Curado da Silva, R.M., et al.: Polarization degree and direction angle effects on a CdZnTe focal plane performance. IEEE Trans. Nucl. Sci. **59**, 1628 (2012)

8. Dean, A.J., et al.: Polarized gamma-ray emission from the Crab. Science **321**, 1183 (2008)

9. Ferrando, P., et al.: SIMBOL-X: a formation-flying mission for hard X-ray astrophysics. Proc SPIE **5900**, 195 (2005)

10. Ferrando, P., et al.: The COSPIX mission: focusing on the energetic and obscured Universe. 25th Texas symp. on relativistic astrophysics, December 06–10, 2010 Heidelberg (Germany) PoS(Texas 2010) p. 254 (2010)

11. Forot, M., et al.: Polarization of the Crab pulsar and nebula as observed by the Integral/IBIS telescope. Astrophys. J. **688**, 29 (2008)

12. Gevin, O., et al.: IDeF-X ECLAIRs: a CMOS ASIC for the readout of CdTe and CdZnTe detectors for high resolution spectroscopy. IEEE Trans. Nucl. Sci. **56**, 2351 (2009)

13. Gluckstern, R.L., Hull, M.H.: Polarization dependence of the integrated bremsstrahlung cross section. Phys. Rev. **90**, 1030 (1953)

14. Götz, D., et al.: GRB 140206A: the most distant polarized gamma-ray burst. MNRAS **444**, 2776 (2014)

15. Götz, D., et al.: Variable polarization measured in the prompt emission of GRB 041219A using IBIS on board INTEGRAL. Astrophys. J. **695**, L208 (2009)

16. Harding, A.K.: Polarization characteristics of rotation-powered pulsars. In: Bellazzini, R., Costa, E., Matt, G., Tagliaferri, G. (eds.) X-ray polarimetry: a new window in Astrophysics. Cambridge University Press (2010)

17. Harrison, F.A., et al.: The Nuclear Spectroscopic Telescope Array (NuSTAR). Proc. SPIE **7732**, 27 (2010)

18. Iniewski, K., et al.: Modeling charge-sharing effects in pixelated CZT detectors. IEEE 2007 Nucl. Sci. Symp. Conf. Record, p. 4608 (2007)

19. Kalemci, E., et al.: Search for polarization from the Prompt Gamma-Ray Emission of GRB 041219a with SPI on INTEGRAL. Astron J Suppl Ser **159**, 75–82 (2007)

20. Klein, O., Nishina, Y.: Über die Streuung von Strahlung durch freie Elektronen nach der neuen relativistischen Quantendynamik von Dirac. Z. Phys. **52**, 853 (1929)

21. Knödlseder, J., et al.: GRI: focusing on the evolving violent Universe. Exp. Astron. **23**, 121 (2009)

22. Krawczynski, H., et al.: Scientific prospects for hard X-ray polarimetry. Astropart. Phys. **34**, 550 (2011)

23. Laurent, P., et al.: Polarized gamma-ray emission from the galactic black hole Cygnus X-1. Science **332**, 438 (2011)

24. Lei, F., Dean, A.J., Hills, G.L.: Compton polarimetry in gamma-ray astronomy. Space Sci. Rev. **82**, 309 (1997)

25. Limousin, O., et al.: Caliste-256: "A CdTe imaging spectrometer for space science with a 580 μm pixel pitch". Nucl. Instr. Meth. Phys. Res. A. **647**, 46 (2011)

26. Matt, G.: X-ray polarimetry and radio-quiet AGN. In: Bellazzini, R., Costa, E., Matt, G., Tagliaferri, G. (eds.) X-ray polarimetry: a new window in astrophysics. Cambridge University Press (2010)

27. Muleri, F., Campana, R.: Sensitivity of stacked imaging detectors to hard X-ray polarization. Astrophys. J. **751**, 88 (2012)

28. Muleri, F., et al.: On the operation of X-ray polarimeters with a large field of view. Astrophys. J. **782**, 28 (2014)

29. Roques, J.P., et al.: PheniX: a new vision for the hard X-ray sky. Exp. Astron. **34**, 489 (2012)

30. Rutledge, R.E., Fox, D.B.: Re-analysis of polarization in the gamma-ray flux of GRB 021206. MNRAS **350**, 1288 (2004)

31. Skibo, J.G., et al.: Is the high-energy emission from Centaurus a compton-scattered jet radiation? Astrophys. J. **426**, L23 (1994)

32. Soffitta, P., et al.: XIPE: the X-ray imaging polarimetry explorer. Exp. Astron. (2013). doi:10.1007/s10686-013-9344-3

33. Von Ballmoos, et al.: A DUAL mission for nuclear astrophysics. Exp. Astron. **34**, 583 (2012)

34. Weisskopf, M.C., et al.: Measurement of the X-ray polarization of the crab nebula. Astrophys. J. **208**, L125 (1976)

35. Weisskopf, M.C., et al.: A precision measurement of the X-ray polarization of the crab nebula without pulsar contamination. Astrophys. J. **220**, L117 (1978)

36. Weisskopf, M.C., et al.: X-Ray polarimetry and its potential use for understanding neutron stars, neutron stars and pulsars. Astrophys Space Sci Libr **357**, 589 (2009)

37. Yonetoku, D., et al.: Detection of gamma-ray polarisation in prompt emission of GRB 100826A. Astrophys. J. Lett. **743**, L30 (2011)
38. Zoglauer, A., Kanbach, G.: Doppler broadening as a lower limit to the angular resolution of next-generation Compton telescopes. Proc. SPIE **4851**, 1302 (2003)

7. Caliste-SO, our first ticket for space to observe Solar Flares

In 2010, I managed to enter the STIX consortium (Switzerland, whose Principal Investigator was A. Benz of ETHZ and now is Säm Krucker of FHNW). The consortium was searching for a low-noise and low-power ASIC to read 64 CdTe based detectors collecting the hard X-ray photons from Solar eruptions and modulated by a Fourier Transform imaging system. I proposed to provide an entirely new full custom version of Caliste, equipped with the IDeF-X HD ASIC and a pixelated CdTe crystal embedded into a space qualified component to populate the focal plane of the STIX telescope: Caliste-SO [3.3, 3.9, 3.10, 3.11, 3.16 and 4.16]. The use of a pixelated sensor allowed reducing the number of active devices aboard the instrument by a factor of 2, reinforcing the imaging performances and simplifying the low mass and low power system.

The maturity of Caliste technology and the availability of my team was a unique opportunity at that time to bring Caliste technology to space in a major ESA scientific program, with the support of CNES and CEA. We entered the program in phase B. After a six month period development phase supported by CNES, we demonstrated the ability of our team to procure high reliability and high performance detection units, able to meet the demanding scientific requirements, in particular we demonstrated the robustness of our concept to meet the 4 keV low-threshold value. In addition to that, we were also able to generate required and considerable documentation.

In the following lines, I will briefly describe the STIX telescope and focus on the Caliste-SO device, the first fully space qualified Caliste product. At the time of writing these lines, the manufacturing of the FM parts is completed and our team is now involved in the follow-up of the integration and qualification of the instrument.

7.1. STIX: Spectrometer Telescope for Imaging X-rays

The Spectrometer Telescope for Imaging X-rays (STIX) is part of the suite of 10 remote sensing and in-situ instruments on-board the ESA Solar Orbiter mission to be launched in October 2018. The time-resolved imaging spectroscopy of solar flares in the hard X-ray range (4-150 keV) will give new data on the intensity, the location and the energy of electrons accelerated in the heliosphere. A Fourier imaging technique, consisting in measuring the Fourier complex visibilities of the image using non-rotating collimators made of grid pairs, can achieve a 7-arcsec angular resolution at perihelion. The imager of STIX is composed of 30 collimators whose grids have a variety of slit spacings and orientations to sample the (u,v) plan of spatial frequencies at a variety of points, plus two collimators for Sun coarse location (pinhole system) and background monitoring (opaque system).

In the Detector Electronics Module (DEM) underneath the imager tube, X-ray photons are detected and events are processed to obtain on-board light curves, spectra and visibility measurements. The time resolution of the images is limited by the photon statistics and can be as low as 0.1 s for very bright events. A 4 arcsec pointing accuracy will be obtained using an aspect system made of a lens, a series of holes and photodiodes in the center part of the telescope to precisely measure the position of the solar limb with respect to the telescope optical axis. The telescope is protected from thermal load and straylight by X-ray windows placed in front of the imager in the feedthrough of the spacecraft.

Figure 39 is a 3D view of the STIX instrument showing the subsystems and their volume allocation to achieve a 6 cm^2 effective area. The instrument weight is 7 kg mass and the total electrical power is 6 W in normal operation mode, 8 W in case of intense solar flares.
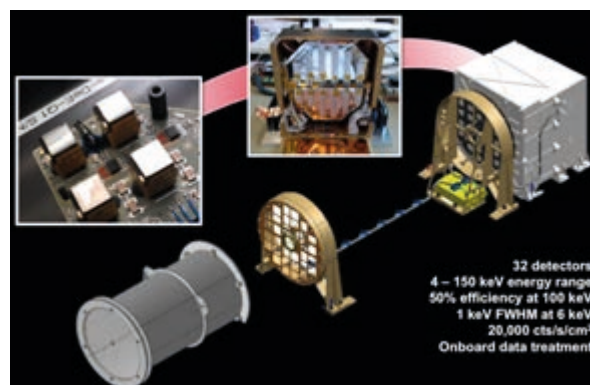

Figure 39. Overview of the STIX instrument on-board Solar Orbiter for solar flare observations in hard X-rays.

The front-end board of the DEM includes 32 detection units aligned behind each collimator of the imager to perform photon counting and spectroscopy in the hard X-ray range. The front grid and the rear grid of one collimator are slightly twisted with respect to each other to create a Moiré pattern on the detector as shown on Figure 41 – Left. In this manner, a coarse pixelating of the sensor to measure this pattern gives access to the real and imaginary parts of the Fourier complex visibility as described in references [5.8.18].
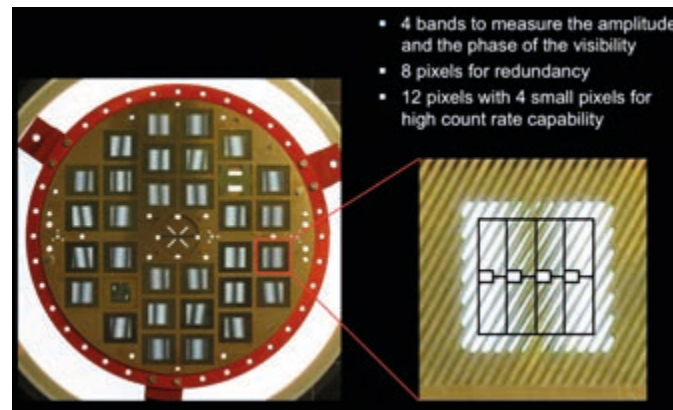
Figure 40.
Left – Superimposition of the grid collimators slightly twisted, creating a Moiré pattern when illuminated by a light source.
Right – Zoom of a particular grid where the Moiré pattern is superimposed to the specific pixel
pattern of Caliste-SO CdTe electrode.

The goal of Caliste-SO is to record the hard X-ray photon energies and the Moiré pattern created by accumulating the photons. A specific electrode pattern as shown on Figure 40 – Right, with a structure of parallel stripes, has been created for that purpose. Each pixel is connected to an individual readout channel. The top-level requirements for Caliste-SO are summarized in Table 6.

Table 6. Caliste-SO scientific requirements.

Parameter	Value
Energy range	4-150 keV 50% efficiency at 100 keV
Detection surface	1 cm^2
Count rate capability	2.10^4 counts/s (goal 10^5)
Energy resolution	1 keV FWHM @ 6 keV 15 keV FWHM @ 150 keV
Electrode pattern	4 bands or higher pixelating
Power consumption	20 mW

7.2. Caliste-SO Design
- **CdTe pixel sensor**

    Because the high-energy photons are required up to 150 keV for STIX science, CdTe was considered the most appropriate semiconductor thanks to its pretty high temperature operational range. The targeted operating temperature on-board STIX is -20°C to guarantee the spectral resolution all along the mission, despite the high proton flux which will inevitably degrade the sensor response. We chose Al-Schottky CdTe detector from Acrorad (Japan) for their high production quality, both in terms of growth and electrode deposition, resulting in extremely low leakage currents under bias. We also chose Acrorad for our successful 20-years of experience to build high

performance CdTe base detectors from astronomy. A 1 mm-thick detector has a total efficiency of 63% at 100 keV (resp. 30% at 150 keV) and a peak efficiency of 50 % at 100 keV (resp. 22% at 150 keV). The special electrode pattern defined for STIX instrument consists of four bands surrounded by a 300-μm large guard ring. Each band is divided in two large pixels and one small pixel as illustrated in Figure 41. The subdivision has the advantage of optimizing the input capacitance and the leakage current of the pixels, which are the two main limiting factors of the spectral response, keeping minimized power consumption by using only 12 channels and the guard ring. The small pixels have been proposed to face the super intense solar flares. In that case of an event, the large pixels are turned off. The pile-up is therefore limited and the electronic activity (dead time and on board computation time) is reduced to avoid data overflow.
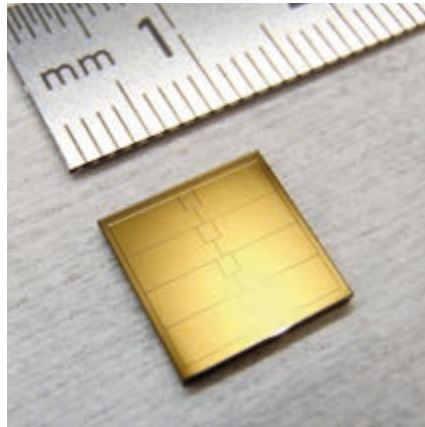
Figure 41. Picture of a pixelated Al-Schottky CdTe detector for STIX. Four bands divided in two large pixels and one small pixel are used to sample the Moiré pattern from the grids in a large dynamic range of Solar flare intensities.

From the full surface Al-Ni-Au Schottky electrode deposited in Japan, PSI processes the pixelated electrode pattern by photolithography and lift-off techniques. The process is completed after plasma etching, dicing and cleaning. In addition, the leakage current and the spectral capability of each individual pixel is measured at +20°C and -20°C with soft temporary contacts on the electrodes created at CEA. This test is crucial to guarantee the assembly of good CdTe detectors on Caliste and to guarantee 100% good pixel aboard, with the best achievable response uniformity.

- **Front-end electronics**
  Caliste-SO is equipped one IDeF-X HD circuit (see §5.5.5.3) and one pixelated detector. While IDeF-X is able to handle up to 32 channels, only 12 are used in the particular case of Caliste-SO, the other channels being simply shut down by telecommand.

- **Hybridization**
  Caliste-SO directly inherits from the previous versions of Caliste product line, using precisely the same technology as described earlier. The force of the 3D technology in this particular implementation, even with a small number of channels per device, relies on the limited surface of the component and on the limited length of the route from the pixel to the ASIC inputs, saving noise. The chip is again placed perpendicular to the CdTe surface. In addition to the ASIC, we used the available space into the module core to integrate three other PCB with passive parts for supply filtering, local decoupling and high voltage routing. The four PCB are stacked and molded into an epoxy resin according the 3D Plus process. The architecture of Caliste-SO is shown on Figure 42.

The resulting block is metalized and laser ablated on the sides to create electrical connections between the internal circuits. The bottom electrical interface is a 20-pin Small Outline Package for a surface mounting in the STIX DEM boards. The ASIC channels are connected to the top surface of the block with "flying leads". A dedicated process of laser assisted bump bonding is applied on the top surface to attach the pixel sensor. The resulting device is called Caliste-SO electrical body and is fully functional. Electrical performance is fully characterized all along the process. The numerous technology process steps include visual inspections, metrology and screening tests, bake-out, thermal cycles and test to ensure a flight quality of the final device. Approximately 200 technological steps are required to build up a Caliste-SO unit.
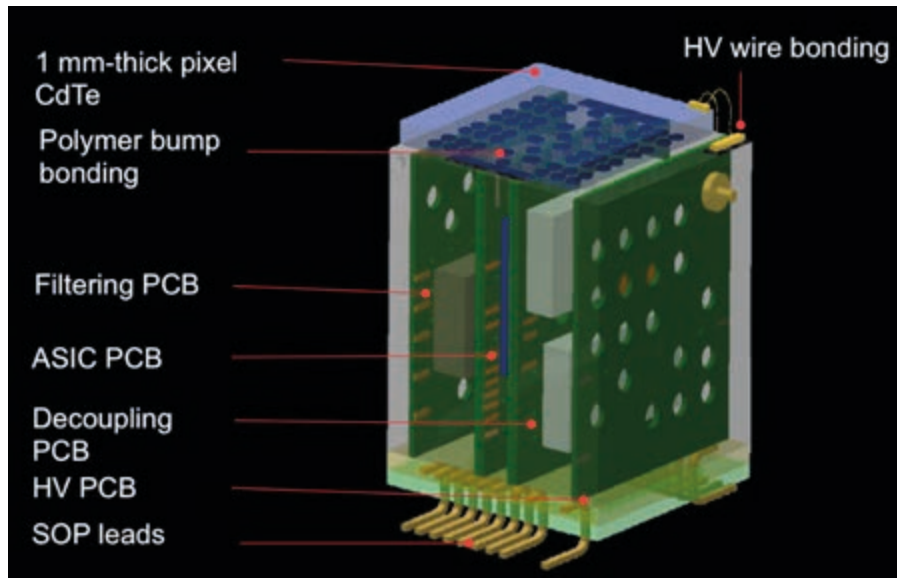
Figure 42. Architecture of Caliste-SO.

The body is slightly larger (12 mm x 14 mm) than the crystal (10 mm x 10 mm) and includes a wire-bonding pad on the side to connect the high voltage provided by the Caliste-SO bottom interface up to the CdTe planar cathode (see Figure 43 – Right). For each Caliste-SO production batch, samples are produced for "Lot Acceptance Tests" and undergo "Destructive Process Analysis" to monitor the manufacturing quality according to space standards. Both mounting processes were jointly invented by CEA and 3D-PLUS for Caliste devices.
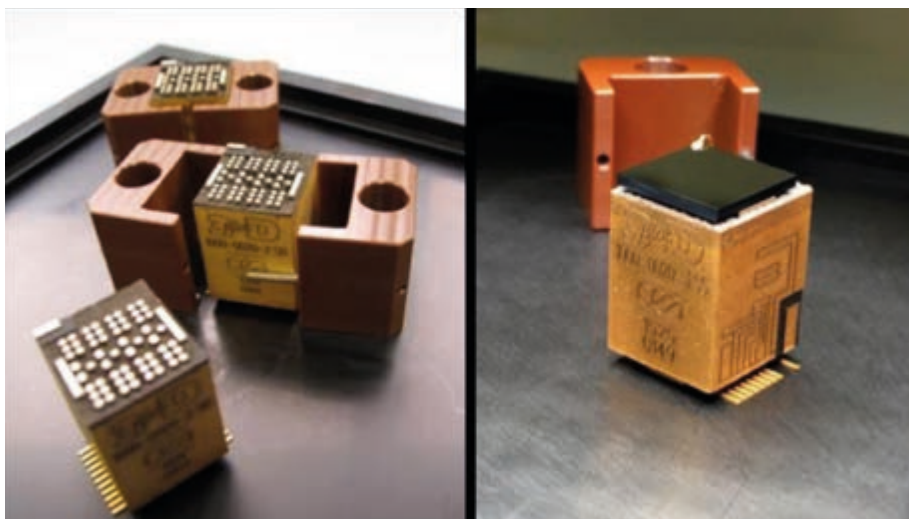
Figure 43. Left – Caliste-SO body (no detector). Right – Caliste-SO full device.
The final device is 12 mm large, 14 mm long and 18 mm high, has a mass of 6 grams and has a total power
consumption of 20 mW for 12 spectroscopy channels + guard ring.

The final Caliste-SO modules are electrically characterized by 3D-PLUS (noise measurements with different parameter settings), transferred to CEA for spectral characterization at -10°C, -20°C, -30°C with radioactive sources (Am-241 and Co-57) at different bias voltages. The best Caliste-SO units are inspected, measured, cleaned, packed and transferred to Switzerland for integration into the STIX focal plane. Caliste-SO performances

- **Performance of stand-alone detectors**

  According to the noise characteristics of IDeF-X HD and sensitivities to current and capacitance (Eq. 15 and 17), we estimated that a leakage current below 60 pA allows reaching the spectral performance with Caliste-SO of 1 keV FWHM at 6 keV, *i.e.* ~100 e- rms equivalent noise charge. The devices produced for the Caliste-SO flight models have a current much lower than required at -20°C, -300V; most of them show no pixel with a leakage current higher than 10 pA. This demonstrates the high quality of the raw CdTe material and the successful patterning process. With the set-up developed by PSI and ETH, it is also possible to connect the pixels of the stand-alone detectors to an IDeF-X ASIC mounted on a printed circuit board. This configuration is not fully representative of the final performance since the connection between the two is not optimized as in Caliste-SO but this is a unique way to verify the spectral capability of each individual pixel, in order to mount on top of Caliste-SO defect-free crystals. The leakage current performance seems to be pretty uniform and within the specifications over the entire series (see Figure 44 – Left). A typical energy resolution value of 1.1 keV FWHM is measured at 31 keV with this test bench on the sme series of crystals (see Figure 44-Right).
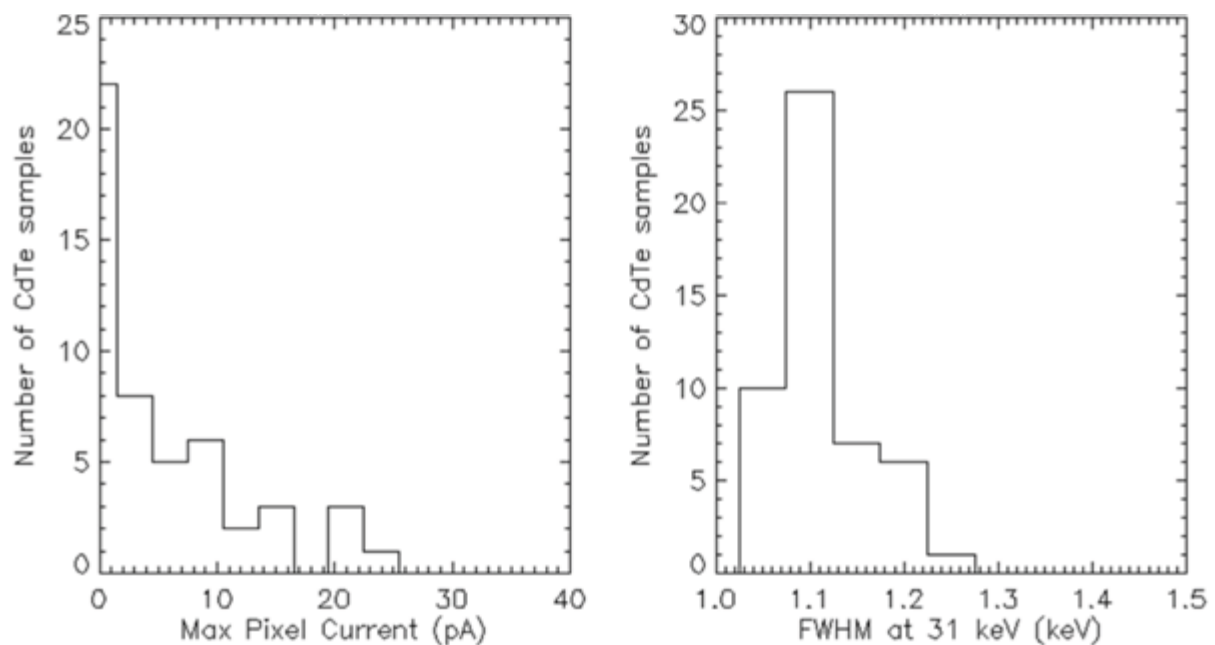

Figure 44.
Left – Results of leakage current measurements on a series of 50 CdTe pixel sensors at -20°C, -300V.
The histogram represents the worst pixel current value of each sensor is included in the histogram.
Right – Results of energy resolution at 31 keV on the same series of 50 CdTe pixel sensors at -20°C, -300V,
exposed to a Ba-133 radioactive source. For each sensor, the mean energy resolution of the 8 large pixels
is represented in the histogram.

- **Electrical performance**

  Electrical performances are measured just before the CdTe mounting on top of Caliste-SO. The measurements are repeated rigth after. These tests are performed using a test pusler brought to the dedicted Caliste-SO input where a series of calibrated charges are applied to derive the gain, the offset and the ENC. The operation is repeated at different peaking times to extract the ENC characteristics for each channel.

  When the detector is not present, or when no high voltage is applied to the detector, the internal current source of the ASIC is set to ~20 pA and simulate the dark current of the detector.

From ENC model of Eq. 14, we derive two interesting parameters to characterize Caliste-SO:
The sensitivity of the ASIC to the input capacitance, in particular at low peaking time (1.4 µs):

$$\left.\frac{\partial ENC}{\partial C}\right|_{\tau=1.4\mu s} = 15\, el \cdot /pF \qquad \text{(Eq. 15)}$$

The relationship between the optimal peaking time, which minimizes the ENC, the leakage current and the input capacitance:

$$\frac{\alpha_p \cdot I_L \cdot \tau_{opt}^2}{\alpha_S \cdot C_{tot}^2} = 1 \qquad \text{(Eq. 16)}$$

$$I_L(pA) = \left(\frac{3.78 \cdot C_{tot}(pF)}{\tau_{opt}(\mu s)}\right)^2 \qquad \text{(Eq. 17)}$$

In Caliste-SO body, among the 32 ASIC channels, 12 channels are routed for the pixels and 1 for the guard ring, to the top surface. 19 channels of IDeF-X HD are not used nor routed at all. Because they are functional, it is expected they give excellent noise figures and diagnostics on the hybrid performance.

From connected routed channels to unused channels, the noise difference is only 15 electrons rms at 1.4 µs (see Figure 45 – Top), which implies according to Eq. 15 that Cbody is limited to 1 pF whatever the pixel position is. This remarkable value is really low and results from the hybridization principle of Caliste devices where the ASICs are placed perpendicular the detection surface: the distance between the ASIC input pads and the bump pads for the crystal can be limited to few mm for all connected channels.

With the detector in place, noise increases by ~10 e- rms for small pixels (see Figure 45-Top with high voltage) and increases by ~30 e- rms for the large pixels (see Figure 45-Bottom, with high voltage).

From these measurments, we derive C_{det} and we found ~0.7 pF for the small pixels and ~2 pF for the large pixels. Summing, all parasitics, we found the total stray capacitance affecting the noise to be:

$$\begin{cases} C_{tot}(small\ pixel) \approx 5.7\,pF \\ C_{tot}(large\ pixel) \approx 7\,pF \end{cases} \qquad \text{(Eq. 18)}$$
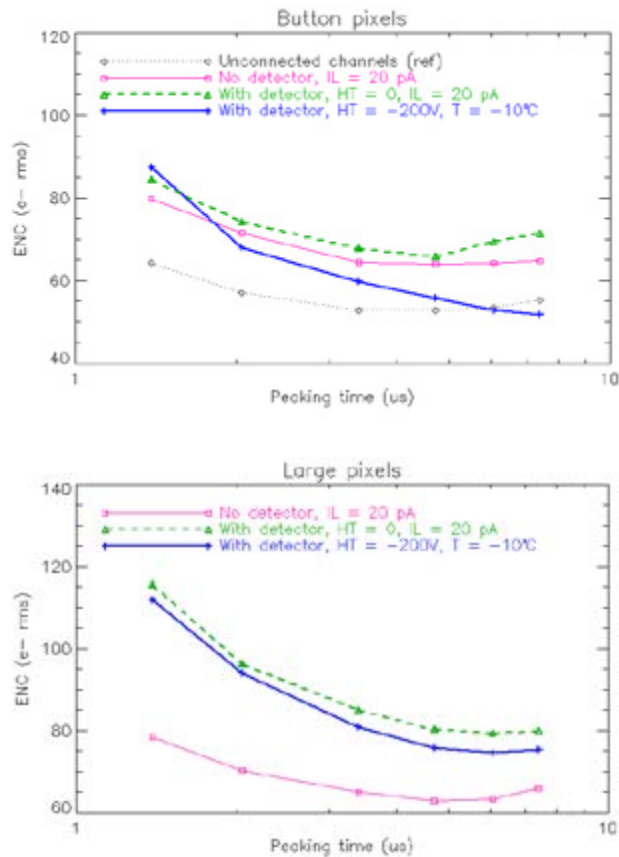
*Figure 45. Top – Typical equivalent noise charge characteristics of the small pixels in Caliste-SO versus peaking time.
Bottom – Typical equivalent noise charge characteristics of the large pixels in Caliste-SO versus peaking time.
All data were taken by 3D-PLUS at different steps of the production.*

The optimal peaking time for small pixels at -10°C, -200V is greater than 10 µs, which implies according to Eq. 17 and Eq. 18 a dark current lower than 5 pA.

The optimal peaking time for the large pixels in the same, at ~6 µs, corresponding to a dark current of ~20 pA. These results are coherent with leakage current measurement on stand-alone detectors.

A similar anlysis can be made on the guard ring since it is connected to an ASIC channel: we found a capacitance Cdet around 5 pF and a leakage current around 350 pA at -10°C and 150 pA at -30°C whereas its electrode surface is only 20% bigger than a large pixel. This underlines the effect of surface currents on the cutting edges and the key role of a guard ring to obtain optimal pixel performance.

Combining the Fano limit of CdTe (Eq. 4) and the ENC measured on the Caliste-SO, we easily predict a spectral performance at 6 keV using Eq. 19:

$$\Delta E = 2.35 \cdot \sqrt{(\varepsilon \cdot ENC)^2 + F \cdot \varepsilon \cdot E_\gamma} \qquad \text{(Eq. 19)}$$

Where:
• ε is the pair creation energy in CdTe (4.42 eV),
• F is the Fano factor in CdTe (0.15).

Applying Eq. 14 to photons with an energy of $E\gamma$ = 6 keV we find that the Fano limit is pretty low compared to the electronic noise (63 eV), so the equation can be simplified as in Eq. 20:

$$\Delta E(eV \ FWHM) \approx 10.8 \cdot ENC(el \cdot rms) \quad \text{(Eq. 20)}$$

Given the ENC measurements on Caliste-SO of Figure 46 and Eq. 20, we expect at -10°C an energy resolution of 1 keV FWHM (resp. 1.2 keV) for a peaking time of 2 μs. (resp. 1.4 μs) with the large pixels.

At lower temperature, the performances remain the same simply because the main noise contribution at short peaking time is the input capacitance so that a reduction of the dark current does not benefit drastically to the resolution.

An energy resolution better of 0.95 keV can be achieved with the small pixels.

- • Spectral performance
  Spectral characterizations were performed on each Caliste-SO device with an Am-241 source and a Co-57 source, as illustrated in Figure 46 and Figure 47.
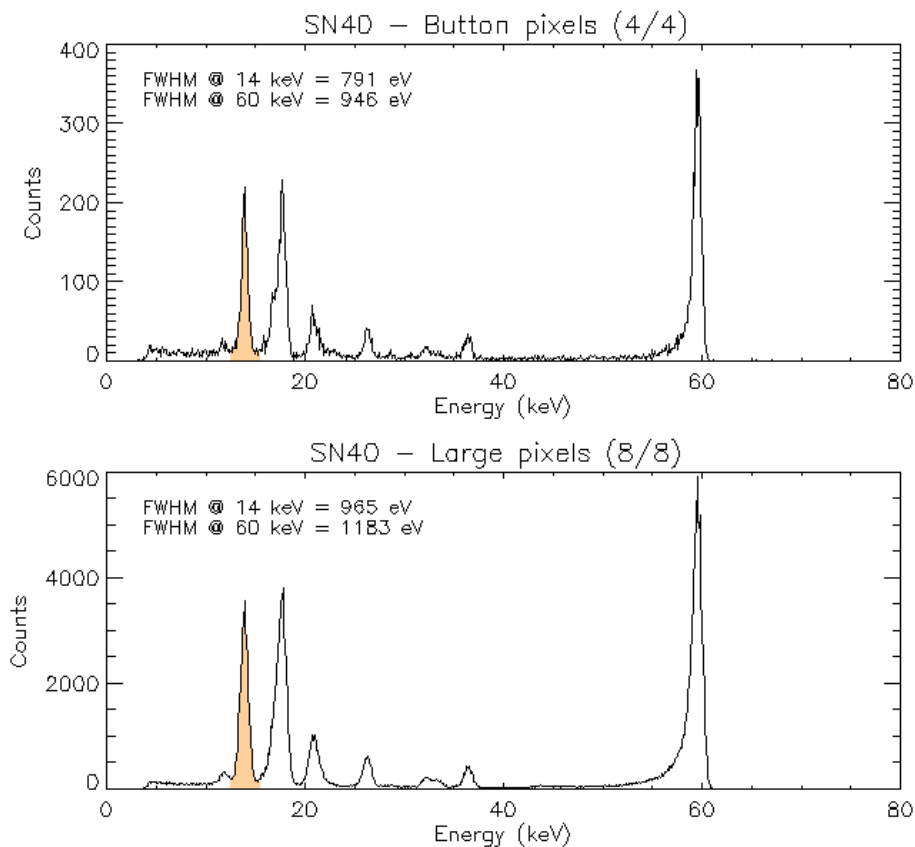

Figure 46. Am-241 spectra at -20°C, -300V. Individual pixel spectra are calibrated in energy
and summed up to build the sum spectrum of small pixels (top figure) and the sum spectrum of large pixels
(bottom figure). Energy resolution is found to be better than 1 keV FWHM at 14 keV as required in the specification.

Figure 48 presents the energy resolution vs the peaking time for Caliste-SO. The results match the electrical measurements: energy resolution between 1.1 and 1.2 keV was anticipated for a peaking time of 1.4 μs in the large pixels and 0.9 keV for the small pixels.

The STIX scientific requirement of 1 keV FWHM at 6 keV is achieved for τ = 2 μs or longer peaking times.

The peaking time results in a latency time between the Caliste-SO trigger and the beginning of the readout sequence. A second photon occurring in this time window and into the same pixel will cause pile-up. Simulations performed with an event generator and the Caliste-SO geometry predicts a pile-up fraction lower than 1% for 2 μs peaking time setting with a maximal count rate of 10^5 counts/s/cm^2.

From this set of spectral measurements, we also confirm that the low-level thresholds of individual channels are always better than 3 keV (even 2 keV for the small pixels), far better than the 4 keV specifications.
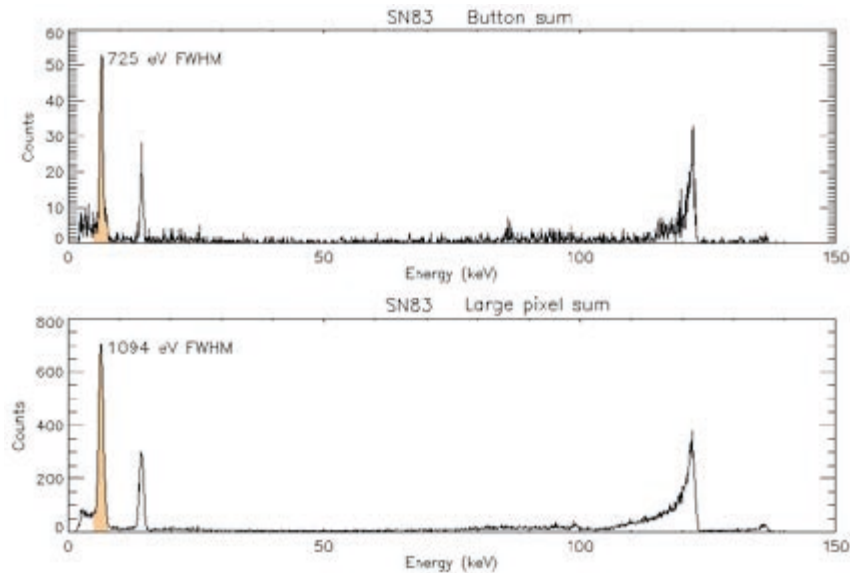

Figure 47. Co-57 spectra at -20°C, -300V. The energy resolution od 1.1 keV FWHM at 6 keV corresponds to an energy resolution of 1 keV by the spectrometer because the line at 6 keV is actually a multiple line of Fe K_α and K_β X-ray transitions at 6.4 and 7.10 keV respectively.
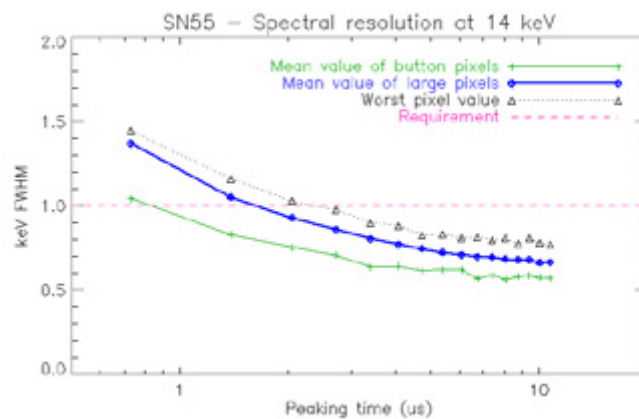

Figure 48. Spectral resolution of Caliste-SO pixels versus peaking time measured on the 14 keV line of the ^{241}Am source (-20°C, -300V).

- **Caliste-SO Flight models production results overview**
  In 2015, my group completed the manufacturing of 98 Caliste-SO, flight models. The modules were produced in five runs between 2014 and mid-2015. Delivery to STIX consortium started immediately after the fabrication was completed.

A figure of merit of the success of the manufacturing is shown on Figure 49 where the envelop of the energy resolutions recorded in each channel is presented against the Caliste-SO number. This number is the chronological order of arrival (not the sample number).

In this envelop, the best pixel is always a small pixel while the worst is a large pixel as expected. All these modules are compliant with the specification or they would have been discarded, thus not presented here.

The improvement and stabilization of the production is pretty obvious even if the envelope keeps tight all along the manufacturing period. The improvements are due to continuous effort in the selection of CdTe, ASICs and Caliste-SO body with a refinement of criteria to reach the very best units for the STIX focal plane flight model and its complete spare unit.

All these devices are associated with sacrificed units (not accounted here), which guarantee the qualification for Space use, as required in the standards.
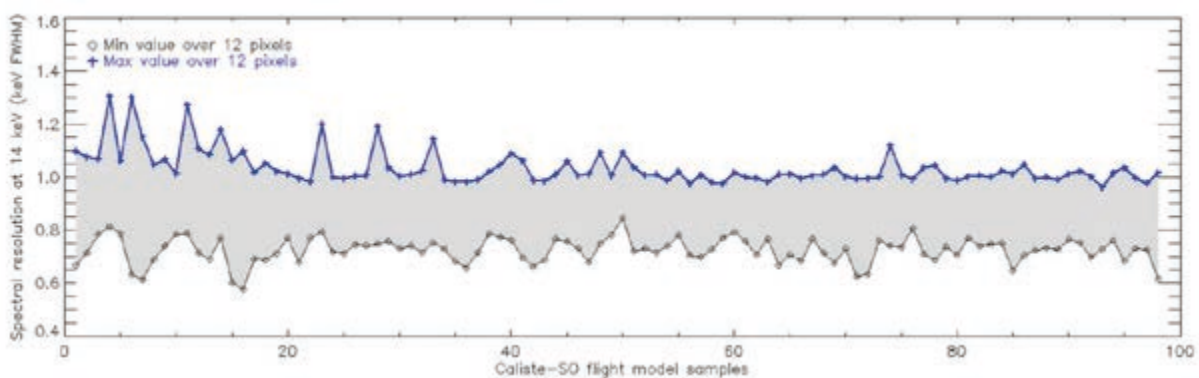

Figure 49. Performance of the 98 Caliste-SO flight models. Energy resolution is measured on each pixel with Am-241 source at -20°C, -300V, 2 μs peaking time. Most pixels have an energy resolution between 0.8 and 1 keV FWHM at 14 keV.

8. Conclusion: Summary of Caliste product line

During the last decade, I have created with my group a new concept of miniature imaging spectrometer resolved in time, offering excellent spectral response in the range of the hard X-ray photons and an extremely low energy threshold for such kind of CdTe based devices. At the time of INTEGRAL/ISGRI, we were able to measure the 60 keV line of Am-241 with an energy resolution of 5.6 keV FWHM on a 4 mm pitch CdTe detector with a low threshold of 15 keV. I brought these parameters down to 666 eV FHWM, 580 μm and 1.3 keV respectively (see Figure 50).

The different versions offer to users a wide range of configurations fitting different scientific needs according to pixel pitch and pattern or system requirements keeping the energy resolution better than 1 keV FWHM at 60 keV and a low threshold lower than 4 keV, a recurrent specification in the last few years.

I demonstrated that the true 3D techonolgy enables creating many full-custom versions compliant with the demanding space qualification standards.

I emphasize also the fact that IDeF-X ASICs are eventually used in other applications than Caliste. For instance, they have been used for the ECLAIRs imager [3.35, 3.39, 3.40, 3.44 and 4.23] for instance or for EPD/STEP instrument on board Solar Orbiter.
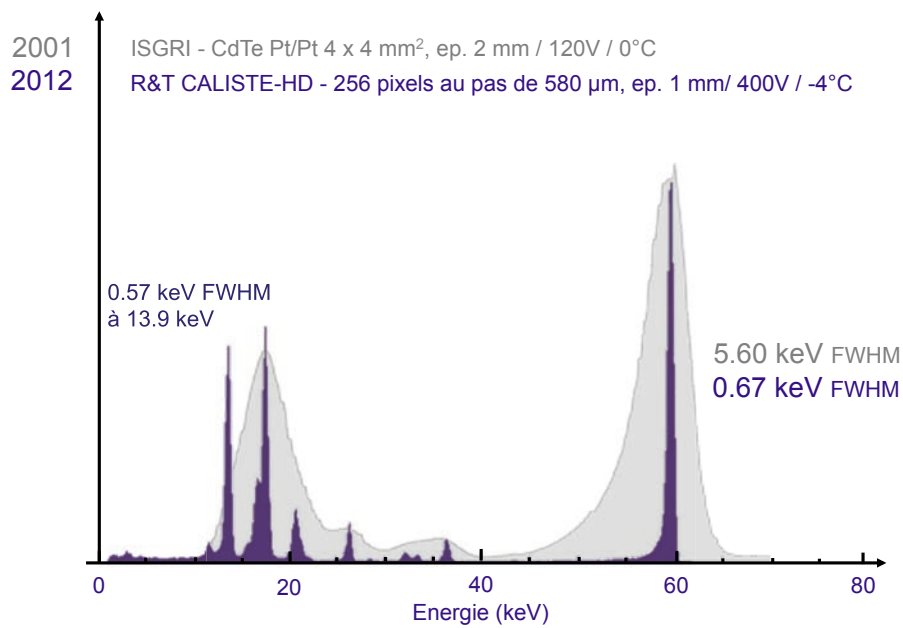
Figure 50. Progress in hard X-ray spectroscopy from INTEGRAL/ISGRI to Caliste-HD.

The different parameters of the Caliste product line are summarized in Table 7.

Table 7. List and features of Caliste devices designed and produced from 2005 to 2011 for hard X-ray imaging spectroscopy. From Caliste-64 to Caliste-256, the number of spectroscopic channels was multiplied by 4 in the same volume. From Caliste-256 to Caliste-HD, the guard ring was reduced to 20 µm and the power consumption and electrical interface were drastically reduced thanks to the new ASIC generation. We created Caliste-SO to optimize the power consumption and the low threshold value on a limited number of channels with specific pixel pattern.

Parameters	Caliste-64	Caliste-256	Caliste-HD	Caliste-SO
Years of development	2005-2007	2008-2009	2010-2011	2011-2013
Pixel array	8 x 8	16 x 16	16 x 16	4 x 3
Pixel pitch	900 µm	580 µm	625 µm	2150/4550 µm
Guard ring width	900 µm	100 µm	20 µm	500 µm
Front-end electronics	IDeF-X V1.1 (16 channels)	IDeF-X V2 (32 channels)	IDeF-X HD (32 channels)	IDeF-X HD (32 channels)
Number of ASIC	4	8	8	1
Interface	7 x 7 PGA	7 x 7 PGA	4 x 4 PGA	2 x 10 SOP
Power consumption	200 mW	800 mW	200 mW	20 mW
Energy range	2 to 250 keV	1.5 to 250 keV	1.5 keV to 1 MeV	1.5 keV to 1 MeV
Energy resolution (FWHM at 60 keV)	900 eV	860 eV	670 eV	1000 eV
Dimensions[6]	10x10x18.6 mm^3	10x10x20.7 mm^3	10x10x16.5 mm^3	11x12x15.65 mm^3

6. The height of the module is given from the pixelized anode surface to the 3Dmodule bottom side, *i.e.* without the pin grids length neither the CdTe detector thickness which is chosen according to the user needs, typically from 0.5 up to 2 mm thick or more.

6. Going further with CdTe based detectors: MC2

In the hard X-ray domain, Caliste may be further refined to reach smaller pixel size in case of newly developed high angular resolution mirrors in the hard X-ray range. This goal may be reached within the next decade and would increase sensitivity in the hard X-ray domain. The challenge is to sample a point spread function of less than 10 arcsec mirrors with a 20 m focal length. In this situation, new efforts are necessary to get pixel pitch in the range from 200 μm up to 300 μm without sacrificing spectral performance. This also means that the number of channels per square centimeter would rise at least by a factor of ~4 from our current finest design and would require again a drastic reduction of the power consumption of each single channel. It would also be beneficial to integrate much larger surface crystals, up to 4 cm² or more in order to minimize dead zones between two consecutive elementary detection units. The complexity of the device becomes more and more challenging but Caliste constitutes a major step toward this goal.

Comparing Caliste-HD, our starting point, to other groups work as shown in Table 8, we clearly see that our key advantages are the spectral response in terms of energy range, energy resolution and low threshold which is a unique feature. Conversely, our design, due to initial requirements, offers a larger pitch at the moment. This is our main driver to start a new R&D.

	Hexitec [8.32, 8.33]	JAXA group [8.34]	Caltech [8.35]	Caliste HD [This work]	HXI/ASTRO-H [8.37]
Pixel/Strip pitch	250 μm pixel	270 μm pixel	498 μm pixel	625 μm pixel	250 μm strip
Number of position segments	80 x 80	12 x 12	24 x 44*	16 x 16	128 x 128
Number of channels	80 x 80	12 x 12	24 x 44*	16 x 16	128 x 2
CdTe thickness	1 mm	0.5 mm	0.5 mm*	1 mm	0.75 mm
Energy range	4-200 keV	4-300 keV	5 – 100 keV	2 – 1000 keV	5-80 keV
FWHM at $59,5 keV$	1 keV	900 eV	900 eV	666 eV	1.5 keV
Power cons. per channel**	-	330 μW	660 μW	800 μW	500 μW
ASIC power density***	-	1.9 mW/mm²	0.16 mW/mm²	2 mW/mm²	0.42mW/mm²
Module elements	CdTe, ASIC	CdTe, ASIC	CdTe, ASIC, ADC, processor	CdTe, 8xASIC	CdTe, 8xASIC

* 24 x 44 is the resolution of the HEFT prototype detector, the final CdTe modules placed in the NuSTAR space mission focal plane have resolution of 32 x 32 each with the pixel size of 0.6mm / NuStar

** Power cons. per channel is calculated for the whole modules. In case of Caltech - ADC and processor are included.

*** The power density is calculated per ASIC area. In case of Caltech, the ADC and processor are not included.

In this section, I introduce a new concept for a CdTe based miniature camera focused on these objectives. This work is still in progress and constitutes my middle term research project. I present the concept of the device we envision and preliminary results on "building blocks", essentially in microelectronics and detector prototyping that we obtained in my group in the last 5 years. I conclude on the forthcoming development aimed at producing a new device: Caliste-MC2.

1. Caliste-MC2 concept, find the limit

Since 2009, I have initiated with the support of CNES a new R&D program to create Caliste-MC2, (MC2 standing for Mini CdTe on Chip). The goal is to build a prototype of 3D hybrid equipped with a 300-µm pitch CdTe detector. The basic challenges that I raised are:

- Build a **2 x 2 cm² CdTe imaging spectrometer** compliant with space applications
- **4096 pixels** in total in a module
- Make this detection unit a **fully digital hard X-ray camera**. Consequently, the module must embed the sensor; the front-end analog electronics of the sensor, the analog-to-digital conversion stage (A/D or ADC), and necessary passive parts for power supply local filtering.
- Keep the property of Caliste technology of being a four-sides buttable device, which essentially justifies a **3D architecture**.
- Bring the front-end electronics noise sufficiently to achieve a Fano limited spectral response at 60 keV. For that purpose, we fixed the **upper noise limit to 20 electrons rms** (see Figure 51). The corresponding expected energy resolution at 60 keV will be 510 eV FWHM using a CdTe Schottky crystal.
- In addition to that, the attractive **low-threshold value of 2 keV** must be conserved or improved according to noise improvement.
- These performances must be obtained in a micro spectroscopy channel of less than 300 microns by side.
- **Automatically single photon-triggered architecture** is mandatory to enable time-tagging capability, low pile-up and low-dead time applications.
- From my experience, our ASIC developments are also interesting for Si based spectrometers for soft X-rays, ion or electron spectroscopy. They can be applied to Silicon Drift Detectors as well for soft X-ray specscopy and timing, where CCD and APS are limited in counting rate capabilities. We keep in mind in our development that Si sensors are possibly replacing native CdTe crystals.
- The power consumption must be kept as low as possible to keep the thermal properties of the new devices within the current power density of Caliste-HD, *i.e.*, **200 mW/cm²**. This requirement is directly linked to the maturity of our future design and its applicability to space projects where cooling power might be major system requirements.
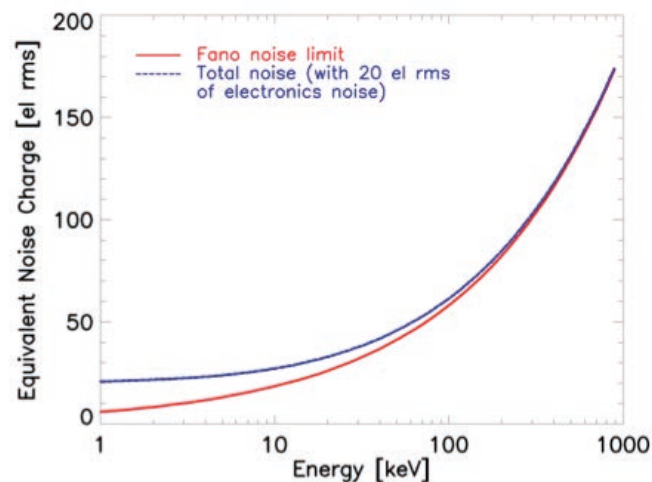

Figure 51. Calculated energy resolution expressed in the Equivalent Noise Charge (ENC) plotted as a function of photon energy. The Fano resolution limit converted in ENC is compared to system "contaminated" with the electronic noise of 20 e- rms. The value is low enough to become negligible above energies of few tens of keV.

My strategy was to start this new program following four different steps:

1. Firstly, we had to start an ambitious development of the front-end electronics. The goal is to evaluate the most appropriate strategy to build a low power, low noise and radiation hard tiny spectroscopy channel that will fit into the pixel surface. This first step requires to evaluate CMOS submicron technologies available on the market, build front-end prototypes, think of the front-end architecture as a system and realize a first 2D ASIC to be flip-chip bonded to a CdTe (or Si) prototype. This work in microelectronics design has been essentially performed in the

frame of the PhD thesis of Alicja Michalowska [8.19], directed by Dr. Olivier Gevin, our lead microelectronicist in the group.

2. The second phase of the program consists in optimizing the detector response and patterning to meet the Fano limited target. A cautious work is mandatory to go straight to a major step forward in terms of imaging spectroscopy. In addition to simulation task cross-checked by experimental data, we focused on the low energy response of the detector. Eventually, we built a series of prototypes to prepare a specific detector bonding technique and evaluate the response of our new ASICs when connected to CdTe or Si detectors. This work was performed during the PhD thesis of Sébastien Dubos [8.16], directed by myself.

3. The third step is to develop a dedicated A/D microcircuit having a suitable dynamic range, linearity, speed and radiation tolerance (SEL free, TID tolerant, low sensitivity to SEU). This chip must be integrated into the final module, constraining its geometry and architecture. Dr. Florent Bouyjou has performed this work during his postdoc at CEA. He was hired in the microelectronics group right after his successful design study.

4. The fourth and last step, which constitutes my middle term research plan, is to assemble the blocks into a 3D module to create Caliste-MC2. The concept is in place. We are ready to make it in association with 3D Plus Company, based on their new technology WDOD (Wirefree Die On Die) as soon as the activity is funded.

Based on these top level-requirements, Figure 52 illustrates what the final module could look like. From the top to the bottom, one sees a 4-cm^2 CdTe crystal (optionnally Si crystal). The front side is covered with a Pt plane electrode, the cathode. The thickness is between 750 microns and 2 mm (NB: I recall that a higher thickness is no problem in terms of crystal procurement but the polarization effect takes place into Schottky type diodes which is sensitive to the squared thickness – twice thicker is four times less stable). The backside is patterned with 300-μm pixels Al-Ti-Au Schottky contact, with a width-to-pitch ratio ideally set between 0.83 and 0.87. This range is derived from Sébastien Dubos calculations where he demonstrated that a higher value might harm the performance in terms of parasitics while lower values might harm the performances in terms of charge sharing and depletion at the pixel side.

A guard surrounds the whole pixel array, comprised of 4096 channels – a magic number for electronicists – we had previously demonstrated the importance to "protect" the inner pixels from unpredictable dark current excess from the periphery of the crystal. The width of the guard ring must be kept as low as possible to get rid of the dead zones between two modules that we would put next to the other. Note that the guard ring area is the unique surface we can use to route ASIC signals to the module sides. Consequently, the size of the guard ring will be dependent on and minimized according to 3D packaging technology constraints. The width is currently estimated to be as low as 200 μm.
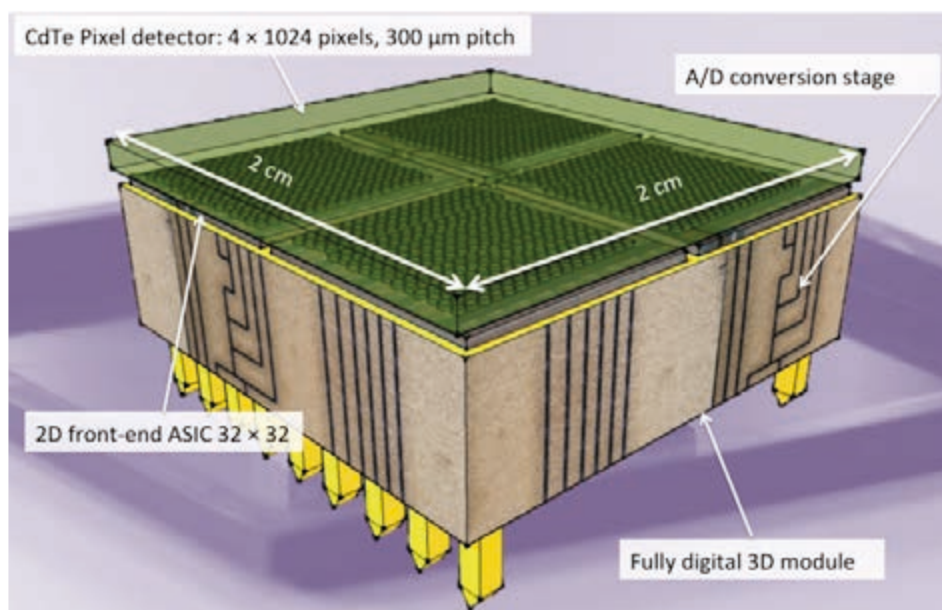

Figure 52. Artists view of Caliste-MC2 module (Credit: O. Gevin).

The CdTe patterned crystal is polymer flip chip bonded, polymer gold-stud bonded or indium gold-stud bonded onto a mosaic of four medium size front-end ASICs, 10 x 10 mm² each. One ASIC is reading out 1024 channels with a 32 x 32 array of micro spectroscopy channels. The idea of a mosaic comes with optimization of yield and cost of fabrication during the foundry.

Another option is to build a single chip with 4096 channels at the expense of the cost and yield of fabrication. Table 9 shows the yield of good dies for CMOS 180 nm and 350 nm by AMS for circuits with 10 x 10 or 20 x 20 mm². The yield value is the result of a worst-case simulation using AMS tool [5.8.29]. The latter is corrected by a factor determined according to our experience with IDeF-X HD production, taking into account a 100% visual inspection processing of the wafers and dies according to applicable standards [8.30]. The yield in the table does not take into account the very small number of circuits that fail due to issues during the mounting process. The cost of a single good chip is calculated on the base of CMP unit surface pricing list [8.31], for the procurement of 25 dies in a multi-customer ASIC run service. Note, that such prices are most often prohibitive for R&D context.

The mosaic of chips embedded into a 3D plastic module is entirely new and is one critical challenge of the project. This approach is, in my eyes, a smart way to extend the front-circuitry surface with a high yield of fabrication, the chip being tested before packaging. The creation of the ASIC mosaic on this front layer is based on WDOD technology and thru-polymer vias that are used to bring the chip signal to the backside using the perimeter of the chip. Because this technology is innovative, I cannot enter into more details in this document until the program is completed and the IP secured.

The core of the 3D module combines into a System-In-Package 3D technology, that is very close to the current Caliste-HD technology, a stack of micro PCBs hosting the A/D conversion stage, routing layers and a dozen of passive parts for local filtering of the power supplies. The electrical interface is also created into the module with a variety of options from BGA to PGA (most likely) or SOP. The most important is to consider this interface to be fully digital: slow control signals for both types of chips are accessible together with power lines. No analog signal from the front-end is distributed out of the module towards the Data AQcuisition system (DAQ).

Table 9. Impact of the chip size on the yield – trade-off. AMS technology [8.21], 200 mm diameter wafers, 180 nm CMOS and 350 nm CMOS.

Techno	Chip size (mm²)	gross Dice Per Wafer	net Dice Per Wafer	Yield	Corrected yield by screening	Cost/mm²	Corrected cost/die (25 dies)
CMOS 180 nm	10 x 10	257	233	91%	88%	1200€	5,5 k€
CMOS 180 nm	20 x 20	58	42	72%	67%	1200€	28,6 k€
CMOS 350 nm	10 x 10	256	232	91%	88%	650€	2,9 k€
CMOS 350 nm	20 x 20	58	42	72%	67%	650€	15,5 k€
CMOS 350 nm	3.5 x 5.9	1278	1240	97%	92%* *measured	650€	0,6 k€

2. Caterpylar, D2R1 and OBW-1

I present in this section the promising results obtained on the front-end ASICs that were recently obtained.

2.1 Caterpylar test chip
- **Design elements**

  During Alicja Michalowska PhD thesis, we decided to implement our first prototypes of the initial stages of the front-end electronics into an 180 nm CMOS technology by XFAB [5.8.20]. We repeated the design using 180 nm CMOS technology by AMS [8.21], the transistor propoerties fitting well to our needs and the design kit being more confortable for further developments. One motivation for using XFAB was the early availibility of the technology in 180 nm in the project, the cost for prototyping and the opportunity to evaluate the technology and design kit.

  We optimized a set of low noise and low power CSAs suited to 0.3-1pF input stray capacitance and ~1-5 pA dark current (see Table 10) to match a variety of crystal contact technologies and pattern. We computed the estimated input stray capacitance, solving the field distribution into the detector volume and its flip-chip interconnexion pads. We found the capacitance to be dominated by the surrounding pixels coupling at detector crystal level. Thus, the value is very sensitive to patterns definition, which requires an optimization separately to consider depletion, charge transport and charge sharing issues in addition to stray capacitance estimate. Despite the fact we found the stray capacitance to be in the order of 150 fF (a very low value) we took a sufficient margin to match any geometry in the final configuration of the detector pattern (width-to-pitch ratio or w/p) which may be decided later, after completion of a fine tuned and calibrated model by Sébastien Dubos. The 1 pF design value is considered to be very conservative.

Table 10. Review of dark current performance obtained in CdTe with Schottky blocking contact, with and without guard-rings. Results are shown for different conditions of the operating temperature and electric field. From the current densities in a pixel of known size, the estimated dark current in case of a small pixel 300×300 μm^2 is calculated for the corresponding operating conditions (after A. Michalowska PhD, directed by Olivier Gevin in my research group).

CdTe Description from refe-rence measurements:	Guard-ring	Temp. [°C]	Electric field [V/mm]	Dark current [pA]	Current estimation in a 300 μm pixel [pA]
In-CdTe-Pt, 2 x 2 mm², mono-pixel, cathode readout	No	-25	300	4	0.1
		25		1000	22.5
		20	200	400	9
In-CdTe-Pt, 2 x 2 mm², mono-pixel, anode readout	Yes	20	200	7	0.16
			1000	20	0.45
In-CdTe-Pt, 1 x 1 mm², mean of 8 x 8 matrix, anode readout	No	-35	200	3	0.27
		0		24	2.16
Al-CdTe-Pt, 1 x 1 mm², mean of 8 x 8 matrix, anode readout	Yes	-35	200	0.3	0.03
		0		4.7	0.42

Table 11. Summary of Caterpylar parameters.

Parameter	Unit	Value
IC technology		XFAB 0.18 µm, CMOS
Number of CSA channels		26 with different sets of W/L input transistors sizes types (NMOS or PMOS) and CSA architectures
Total external input capacitance	pF	0.3 … 1
Detector dark current	pA	<5
Detector current polarity		Positive and negative
Detector signal polarity		Negative – anode readout Positive – cathode readout
Maximum input dynamic range	fC	10 … 15
Maximum output dynamic range	V	0.5 … 1
Feedback capacitance	fF	25
Supply voltage	V	1.8
Max. CSA power consumption	µW	18
Noise simulation (ENC)	e- rms	14 to 40 depending on the CSA type

Our first test chip was named Caterpylar because it has a huge number of pads distributed in two parallel rows. This is the result of the implementation of 26 versions of different CSA. The explored parameters are centred on the type of input transistor, their area (WxL) and Width-over-Length (W/L) dimensions. Each CSA can be biased externally with diferent current values. The goal was find the most appropriate design for a forthcoming more complex ASIC and also to get a validation of our microelectronics models and optimization process as published by A. Michalowska [3.24]. The key parameters of the circuit are shown in Table 11.

In addition to the initial analog front-end stages, we installed a slow control logic circuitry to evaluate routing, dimensions and possibly evaluation of radiation tolerance of digital blocks.

• Caterpylar chip test performances
The chip has been tested to check design parameters and the noise performances. I summarize a considerable amount of work with the results obtained injecting calibrated test pulses at the input of the best CSAs (on-chip injecting capacitor), while the output was connected to an external CR-RC2 shaper with adjustable peaking time.
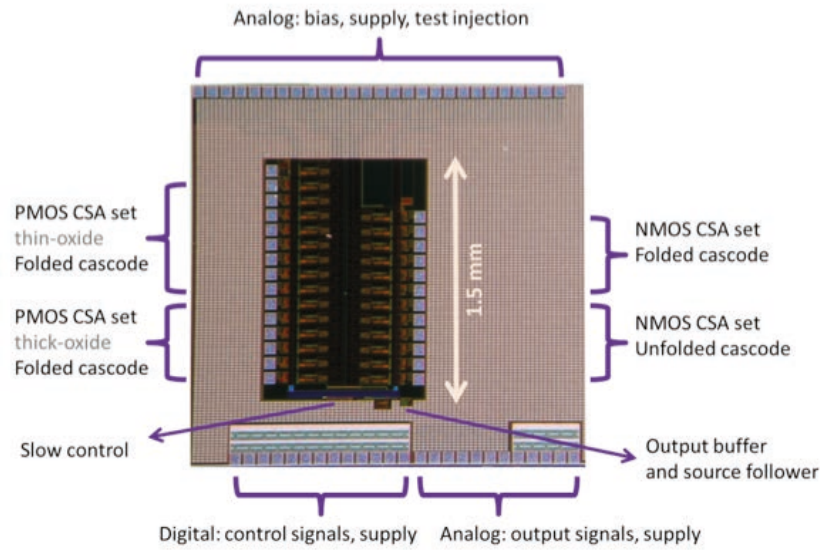
Figure 53. IDeF-X Caterpylar ASIC photograph with indication of PMOS CSA – on the left, NMOS CSA – on the right, as well as the digital Slow Control, analog output stage (including the output buffer and the source follower) and IO pads.

We firstly recorded ENC against peaking time with a standalone chip. We obtained a noise as low as 12 e- rms for peaking time of 10 μs, biasing the CSA with 10 μA (18 μW). As shown in Figure 54, the noise floor has not been reached for CSA T9 (W/L = 100 μm/0.3 μm) with this shaper and we expect the noise floor to be ~10 e- rms for longer shapers when no detector current flows into the chip and when no additional input capcitance is added.
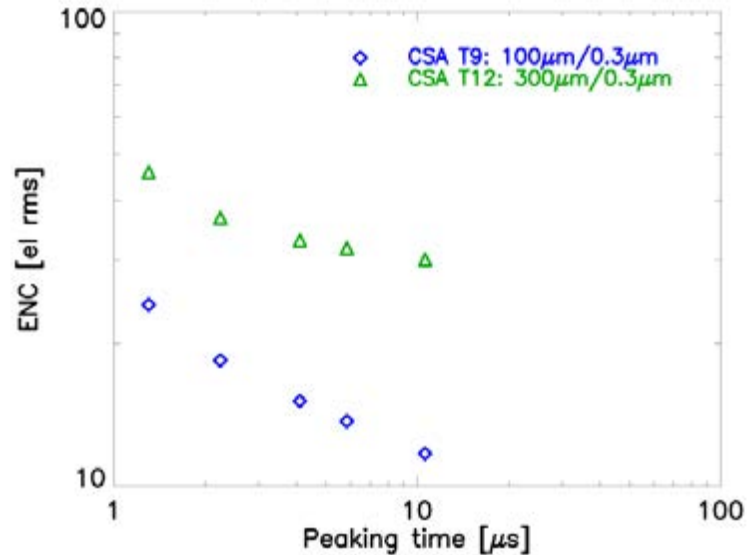
Figure 54. ENC vs peaking time of CSA T9 and T12 measured with the 2nd order semi-Gaussian shaper. Conditions: Ibias=10μA, there is no detector, no additional input capacitance and no input compensation current.

Naturally, it is not realistic to consider that the system will be free of current flow and input capacitance. The best CSA without input is not necessarily the best with a detector installed. As a matter of fact, the best CSA may show a higher sensitivity to additional stray capacitance than another having a higher noise without a detector. However, this kind of performance illustrates the achievable performance with such a technology and design. By studying extensilvely sensitivity of our set of CSA to the current and to the capacitance, we were able to choose the most promising couple of CSAs for the purpose of building a prototype and record a demonstration spectrum.

Thanks to the support of LBNL1 (courtesy of C. Tindall) in Berkeley, we have procured low current and low capacitance Silicon diodes and connected them at the input of these amplifiers. The diodes are very easy to connect to our testchip with a simple wire bonding that we perform in-house. This is not achievable with a CdTe prototype without bringing a lot more parasitic capacitance, severely degrading the noise figure simply because CdTe does not support direct wire-bonding.

We eventually installed a LBNL Silicon diode 800 x 670 μm^2, 330 μm thick, fully depleted under 65V into our vacuum tight and temperature-controlled bench and illuminated it with a Co-57 radioactive source. The corresponding stray capacitance was measured separately by C. Tindall and found to be 300 fF. The dark current was 500 fA when cooling down the device at -10°C. The current was estimated by measuring the CSA decay time, a direct measurement and compared to expectations from data acquired at LBNL at room temperature. Thanks to this low current level, the best resolution was expected for the largest available peaking time in our setup *i.e.* 11 μs.

I emphasize the fact that these values are typical of the expected properties of a single channel in Caliste-MC2 equiped with a CdTe Schottky diode.
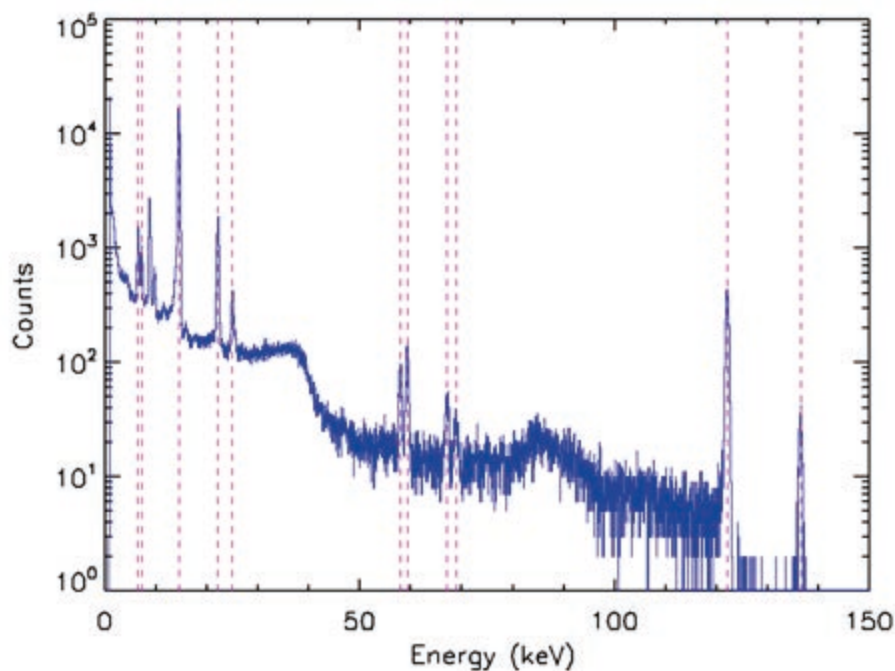

Figure 55. Co-57 spectrum recorded with a 800x670 μm^2, 330 μm thick, fully depleted at 65V bias and operated at -10°C. The diode is connected to a Caterpylar CSA powered with 14 μW. The CR-RC2 shaper is set at 11 μs, the longest peaking time available in our setup. The stray capacitance is close to 300 fF while the dark current is 500 fA.

We measured an energy resolution of:
- 336 eV FWHM at 6.4 keV (Fe Fluorescence line from Co-57 source)
- 375 eV FWHM at 14.41 keV Co-57 gamma ray line
- 502 eV FWHM at 59.32 keV (W collimator fluorescence line)
- 630 eV FWHM at 122.06 keV Co-57 gamma ray line

Silver fluorescence lines at 22.1 and 24.9 keV are also clearly visible as well as gold fluorescence lines at 66.99 and 68.8 keV. One can see the Compton edge at 39.46 keV of the 122.06 keV Co-57 main line and the backscattering bump around 82.6 keV.

Naturally, these very promising results are helped by the low pair-creation energy of silicon of 3.67 eV/pair. With similar current and capacitance in CdTe, having a pair creation energy of 4.42 eV/pair and a Fano factor of 0.15, we would have measured 414 eV, 448 eV, 604 eV and 771 eV FWHM at 6.4 keV, 14.4 keV, 59.32 keV and 122.06 keV respectively.
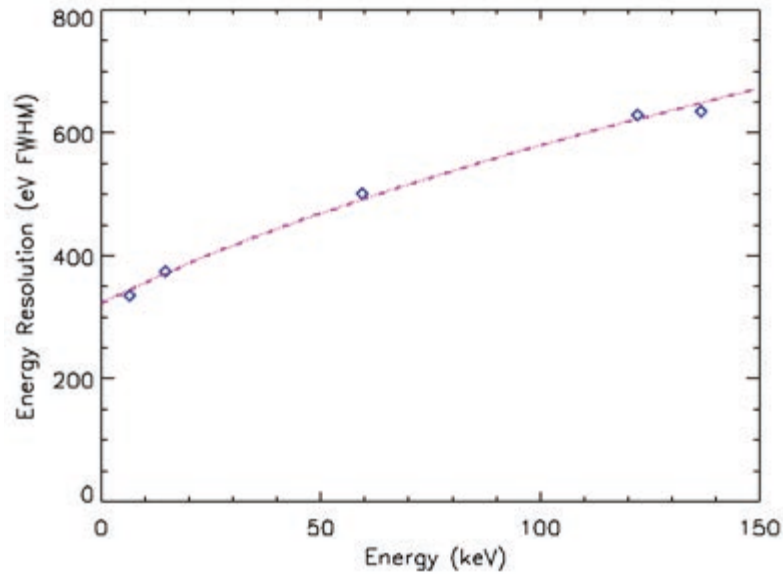
Figure 56. Energy resolution versus energy from spectrum of Figure 56. Fitting a square root law, one derives
the ENC to be 37 e- rms and the Fano factor to be 0.114, assuming a pair creation energy of 3.67 for silicon at -10°C.

Plotting the energy resolution against the energy, I derive the Equivalent Noise Charge as well as the Fano Factor assuming a pair creation energy of 3.67 for silicon at -10°C. I find the noise to be 37 e- rms and the Fano factor 0.114 (Eq. 19). This result is in good agreement with litterature [8.22].

To conclude this section on Caterpylar test chip, let us mention that the chip has been successfully exposed to a Total Ionizing Dose test up to 1 Mrad (see Figure 57). Up to 500 krad, approximately no change in the CSA performance has been observed. A slight degradation is visible from that point up to 1 Mrad where the chip is still operating well. A typical dose in a flight experiment using CdTe is in the range from 10 to 100 krad. This test was important to make sure that the choice of the technology remains valid with a view to use our chips in Space.
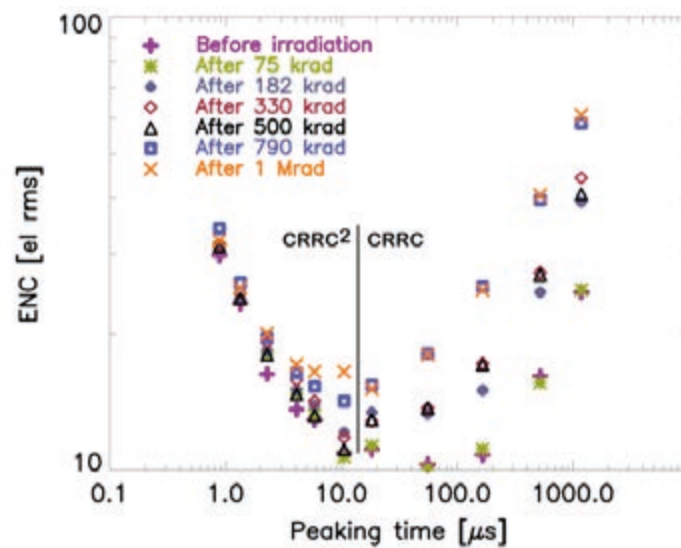

Figure 57. ENC as a function of peaking time. Evolution of the characteristic with increasing total ionizing dose
up to 1Mrad. Measurements conditions: CR-RC2 shaper up to 11 μs and CR-RC shaper up to 1 ms;
CSA bias current was set to 10μA, no input capacitance, minimized compensation current.

Based on these results, we initiated the development of our 2 dimensional ASIC in its first release: D^2R_1, standing for Dimension 2, Revision 1.

2.2. D^2R_1

The front-end CSA design being defined and successfully realized and tested, we decided to go in the design of a two-dimensional prototype to readout 300 microns pitch semiconductor detectors. During Alicja Michalowska thesis who extensively studied the various filter theory, two options stoud out: CR-RC^N "classical" shaper or MCDS (standing for Multi Correlated Double Sampling).

The semi-Gaussian shaper is often referred to as a CR-RC^N filter, since it is typically composed of a high pass filter followed by N^{th} order RC low pass filter. This type of analog filter is used in IDeF-X chip family (see §4.5.3). The shape of the output voltage pulse is illustrated in Figure 58 – Right. Three different values of the filter order N are illustrated.

The idea of a MCDS filter is to sample the CSA output directly and digitally filter the signal by using simple linear combination of samples as shown in Figure 58 – Left. The MCDS method was first introduced in CCD imaging in a simpler form of the Correlated Double Sampling (CDS). The technique is used in amplifiers and comparators for offset reduction. In the CDS processing a single measurement is accomplished with two samples: a baseline sample and a signal sample. The difference of the two samples gives the amplitude of the measured signal. The low frequency noise is highly reduced and the DC offset is totally removed in the final measurement. Noise has a decreasing correlation with increasing interval between the two samples, therefore a shorter interval between the two samples results in a higher accuracy of the measured amplitude. The MCDS is an extension of the CDS principle and relies on the acquisition of a multitude of samples before and after the signal, enabling averaging. The DC level is removed, the 1/f noise is filtered depending on the sampling rate while the high frequency noise is filtered by averaging the samples.
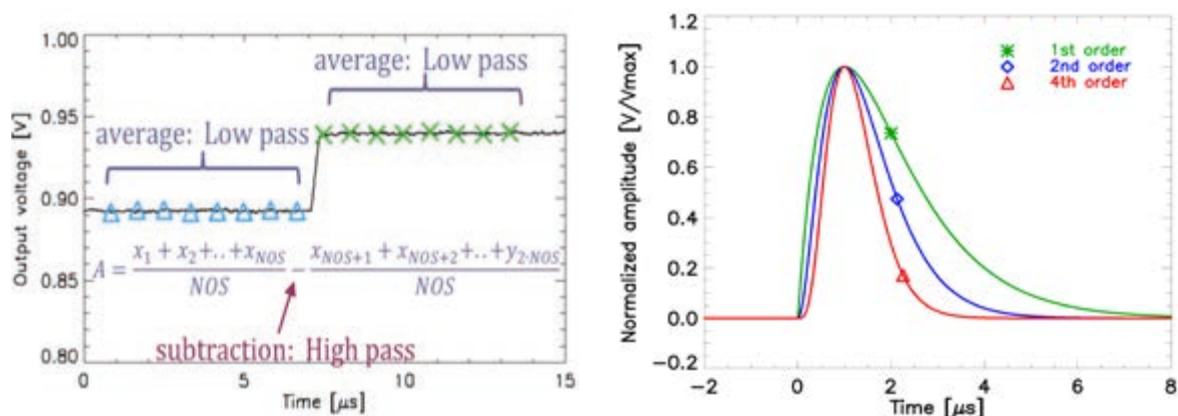

Figure 58. Basic principle of MCDS digital filter (Left) and Semi-Guassian or CR-RC^N analog filter.

Table 12. summarizes the analysis, which is fully justified in Alicja's thesis. I emphasize that despite the fact that the two types of analogue or digital filters are both promising and challenging, we finally chose to go to the implementation of the MCDS. One reason was related to novelty (and potentially a lot of fun) in our group. Another reason was linked to our motivation to read both polarities of detectors without any special configuration, because sampling the output of a preamp does not require anticipating the polarity of the signals.

The main drawback of the choice is that the circuit is complex to operate in its prototyped version.

Table 12. Trade-off assessment table for semi-gaussian analog filter vs MCDS digital filter types.

Functional issues in the detection chain	Semi-Gaussian	MCDS	Comments
Control logic	+	−	In MCDS it is a large and complex digital block; in semi-Gaussian it is a fairly simple logic
Peaking time control	−	+	Semi-Gaussian requires variable capacitors or resistors adjustment; in MCDS it is enough to modify sampling frequency
Total capacitance area	−	−	In semi-Gaussian: to achieve high peaking time; in MCDS to reduce the noise
Inversed dark current polarity – Dual polarity detector.	−	++	Semi-gaussian filter is usually associated with continuous reset [5.8.28, 3.3.30 and 3.4.17] Building a bi-directional continuous reset circuit that can handle both polarities of signal and/or inverse dark current is very difficult and/or a source of additional noise. However MCDS is a discrete time filter that is well suited to pulsed reset and is inherently adapted to both polarities of signal.
Noise simulations	+	−	The switching noise in MCDS takes too long to predict it with transient noise simulation – the estimation must be done with other means; in the analog semi-Gaussian the typical AC noise analysis is possible, it is rapid and accurate (with the indicated noise model)
Noise measurements on Caterpylar with the two filters	+	−	By experience
Reset noise	−	+	MCDS is well suited to active reset. Therefore, the reset noise is low.
Risk of digital noise	++	−	Semi-Gaussian is purely analog with the only digital signal from discriminator; MCDS based on switched capacitors requires extreme attention to prevent coupling with sensitive nets
Power consumption	−	+	Because of the higher number of functional blocks the semi-Gaussian option might require a higher power consumption, especially if realized as order CR-RC shaper
Necessity of additional circuitry	−	++	
Architecture maturity	+	−	MCDS design is new in our group for this type of photon detector application

- Architecture of the pixel
  The block-level diagram with the readout channel architecture is illustrated in Figure 60. It consists of an analog and a digital part. The analog blocks include the CSA with switched reset followed by a buffer. Its output is routed to the shaper and to the discriminators. The MCDS shaper is realized in two steps with a set of 17 parallel sampling cells connected through a unity gain buffer to the CDS amplifier input. The number of samples to be used is free and the sampling rate can be tuned with a baseline target of 1 MHz.

  The discriminator is composed of two dynamic comparators. Each one makes a simple CDS to periodically compare the CSA output signal with the reference level adjustable in each comparator with individual thresholds. The last analog block is a multiplexer.

The digital section also implemented within the individual channel includes the control logic and the slow control. The control logic continuously supervises the channel operation by commanding signals to discriminators, sampling capacitor array, CDS amplifier and multiplexer. Meanwhile the slow control block typically remains static during the

signal acquisition. Its purpose is to communicate with external link the programmable settings, specific to the pixel. For example, desired values of the discriminators threshold can be written and stored in this block.

The trigger system is based on a row-wise and column-wise register such as it is possible to read out the register in order to determine the hit position coordinates in the chip. Thus, when a photon hits a pixel, the X and Y coordinates are recorded in two hit registers and a global trigger is sent to the DAQ.

In case of double events in separated pixels, this technique generates an ambiguity in the hit positions. Therefore, four channels have to be read out. Two of them contain the real energy and two contain the baseline value. One option is to keep the four informations as the base line value is interesting to monitor the noise or it is then possible to find the real hit pixel pattern analyzing the energy values. The advantage of this system is that it requires only a single differential trigger line and register readout, saving a lot of interface and keeping the capability of an automatic triggering system. The trigger logic is shown in Figure 59.

The discriminators are tunable with a 5 bit DAC for values ranging from -10 to +11 keV (CdTe). Up to 3.5 keV, the threshold is adjusted by step of 350 eV. Beyond that, 1 keV step is used.

The total DC power is expected to be 117 µW per channel.

The ENC is anticipated to be 25 e- rms with 300 fF total stray capacitance at the input. 40 e-rms are expected with 1 pF. One difficulty of a MCDS design is that the noise simulation is very delicate. Consequently, it is far better to estimate the noise performance from measurements.

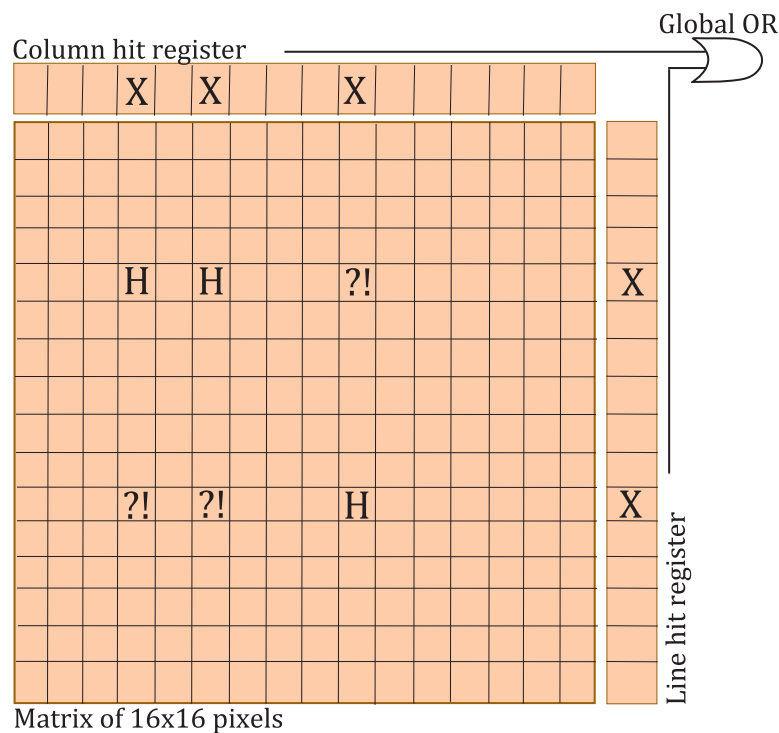The pixel structure is replicated 256 times in the chip.

Figure 59. Discrimination scheme in the D^2R_i ASIC. The event location is memorized in the corresponding column hit and line hit registers. Generation of a 1-bit **Global OR** signal to inform about occurrence of an event. "H" marks the hit pixels and "?!" the ambiguity generated by mutliple hits.
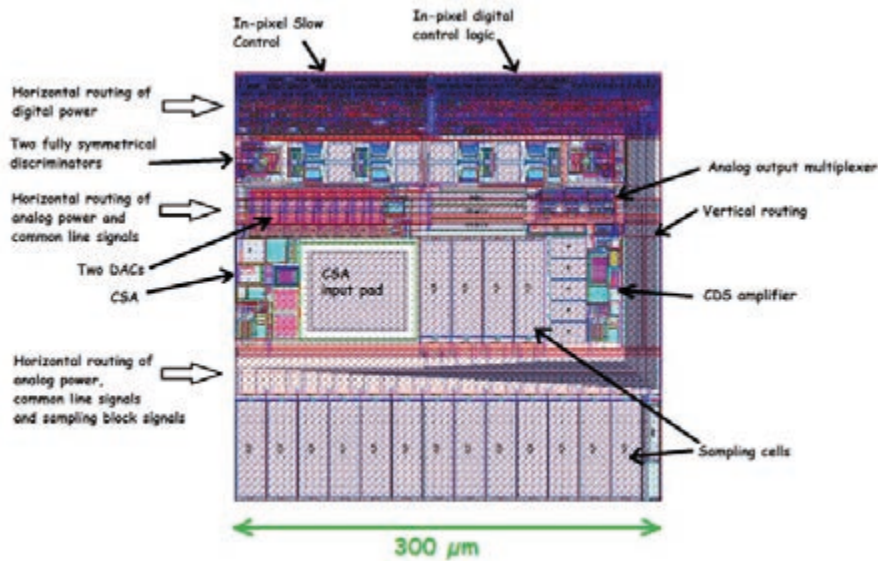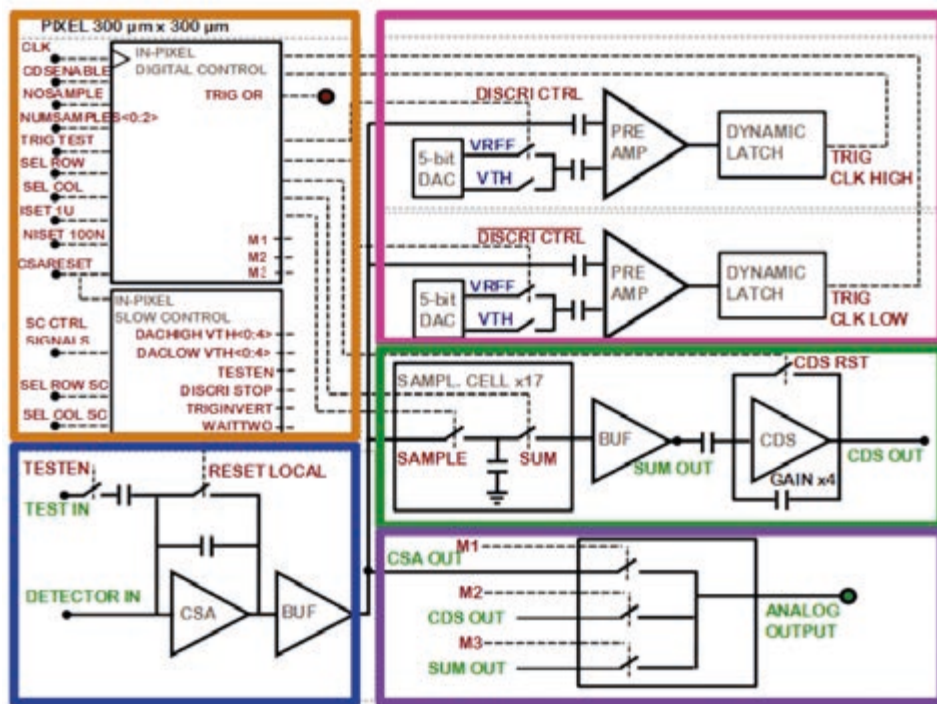
*Figure 60. Top - D²Rᵢ block diagram of one pixel. Blue is the CSA with active reset system,
pink is the double discriminator with programmable threshold, orange is the slow control register
and commande logic, green is the 17 sampling cells MCDS and gain stage and violet is the analog
output with different test modes (CSA, samples, MCDS). Bottom – View of the corresponding pixel layout.*

• Results

D²Rᵢ is shown in Figure 61. It has been bonded onto a test daughter board and installed into an electronics setup into the lab. The chip is controlled with a FPGA board installed next to it. The system is equiped with the required power suplies and A/D converters. The setup is also equiped with pulse generators and additional circuits to simulate various stray capacitances and dark currents. The data are recorded by a computer.
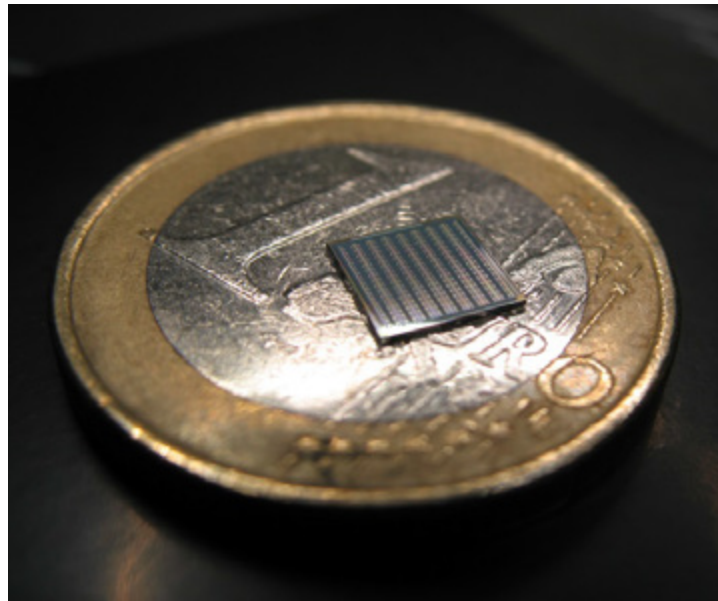
Figure 61. D2R1 ASIC die (5.4 mm×5.4 mm) and 1 EURO coin for scale.

Our chip is fully functional, including the MCDS and the triggering system. We were able to perform noise characterization rapidly and more extensive test and design verifications afterwards as shown in A. Michalowska and in S. Dubos PhD thesis. Next figures summarize the main results.
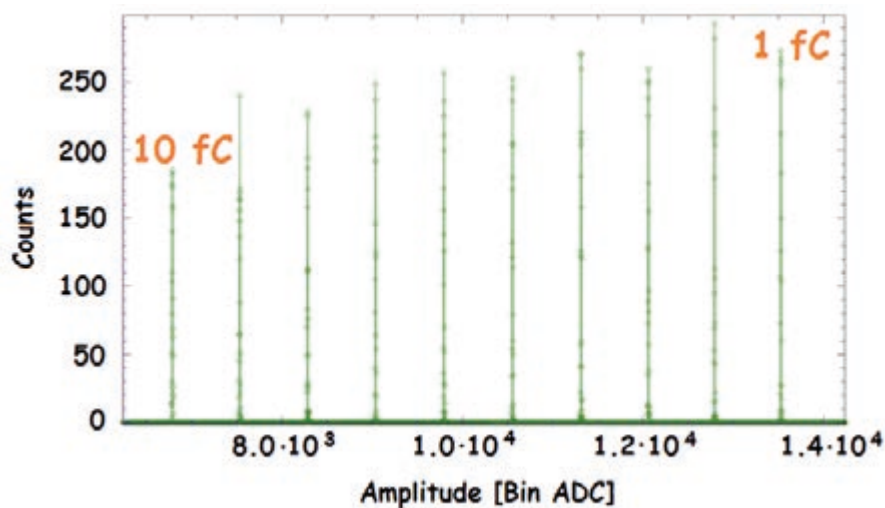

Figure 62. D2R1 response to the input signal from 1 to 10 fC after the ADC conversion. Input voltage step of the highest amplitude corresponds to the left hand side peak. The plot is obtained for a single pixel.

We have checked:
- The dynamic range to be 10 fC as expected, gain nominal
- The Integral Non Linearity to be <0.5%
- The ENC to be 29 e- rms in average over the whole array (See Figure 63)
- The low threshold to be about 1 keV (CdTe). As a matter of fact, even if the noise record is found to drop to zero after 800 eV, the closest discriminator setting is 1 keV.
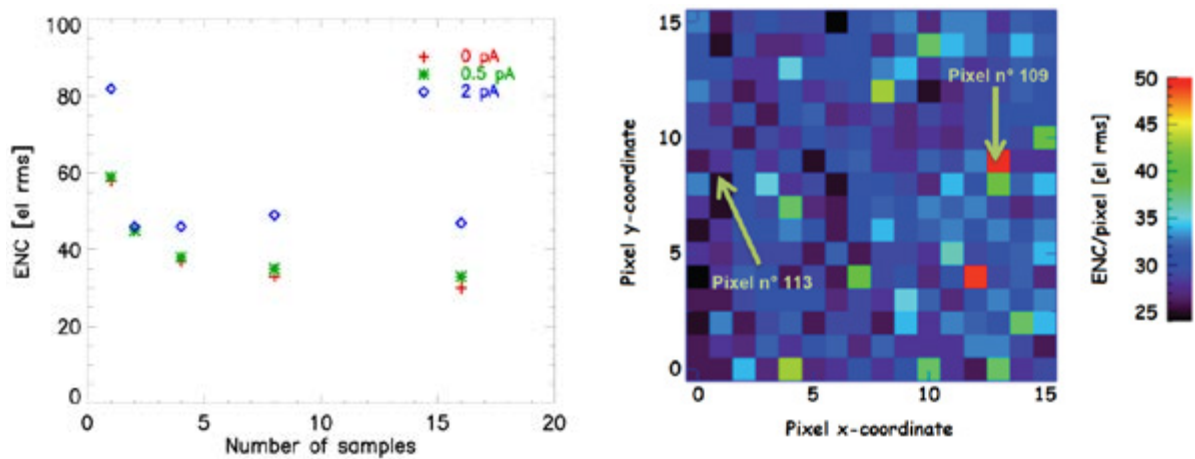
Figure 63. Top – D²R$_I$ ENC vs. MCDS number of samples (~equivalent to shaping time) measurement for different values of detector dark current. Bottom – Distribution of the ENC for each individual channel. The best pixel show 25 e- rms while the hottest have 50 e- rms. The average is 29 e- rms.

• Spectroscopy

According to successful ENC measurements that were performed on D²R$_I$, we were able to compute the expected performances once the chip is equipped with a CdTe Schottky pixel detector, assuming a conservative value of 37 e- rms as shown in Figure 64. We found that the energy resolution should be in the range of 600 eV FWHM at 60 keV.
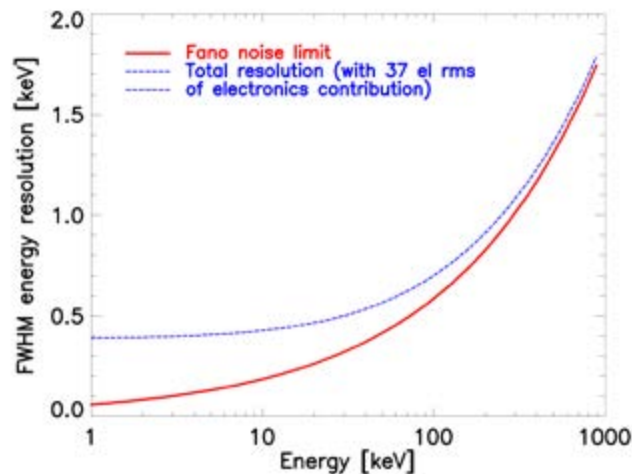

Figure 64. Calculation of the expected energy resolution with D²R$_I$ when equipped with a CdTe Schottky pixelated detector, assuming a conservative noise level of 37 e- rms.

We have built such a detector using Howa Sangyo (Japan) technology for indium gold stud bump bonding to flip chip a CdTe prototype on the chip as shown in Figure 66. Unfortunately, the operation was not a success and the flip chip process failed due to misconnections. Despite our efforts and the good cosmetic appearance of the prototype series, we were not able to get a spectrum from the detector assembly. A failure analysis has been conducted and the process has been revised with the help of JAXA/ISAS and MHI in Japan to get a new run of prototypes. At the time of writing these lines, the prototypes are not yet ready to be operated.
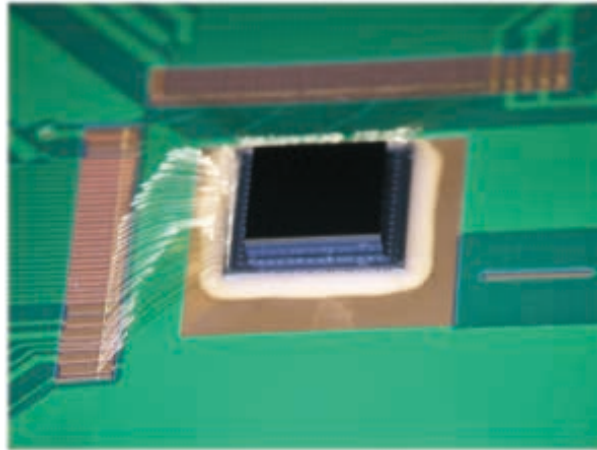
Figure 65. CdTe Schottky diode flip chiped on top of D²R₁ with a indium gold stud bump bonding technology by HowaSangyo (Japan).

In order to prove the capability of the chip to record a spectrum when connected to a pixelated semiconductor, we decided to simply wire bond a silicon diode, courtesy of C. Tindall, Lawrence Berkeley National Lab (USA). The process was successfully achieved in our lab but due to long wire bonds and 1mm² pixel array, the resulting stray capacitance exceeds the 300 fF that we aim at. The diode itself brings ~680 fF. However, we were able to record a spectrum of Co-57 as shown in Figure 66 and found an energy resolution of 850 eV FWHM at 6.4 keV and 1 keV FWHM at 14.41 keV, a sufficiently promising result to go ahead.
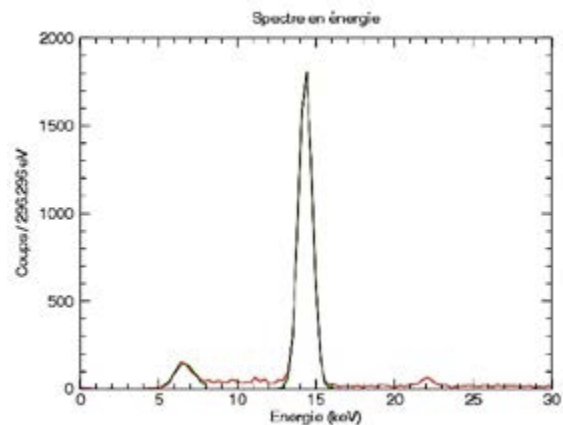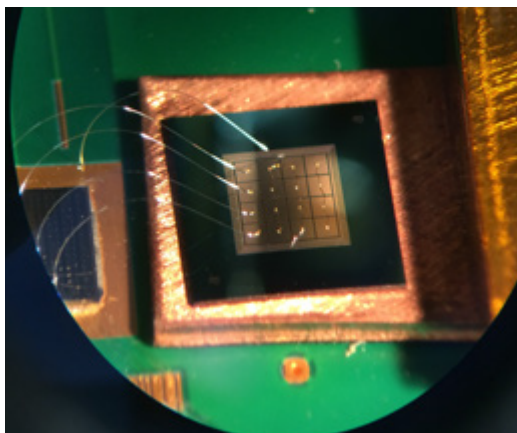

Figure 66. Left – Silicon 16-pixels detector wire bonded to D2R1 inputs. A pixel is 1 mm². Right – Spectrum acquired illuminating the sensor with a Co-57 radioactive source at room temperature, fully depleted under 65V. The energy resolution is found to be 850 eV FWHM at 6.4 keV Iron fluorescence line and 1 keV FWHM at 14.41 keV.

2.3. OWB-1 (On chip Wilkinson 13 Bit ADC, Revision 1)

Caliste-MC2 must be a fully digital interface detection module. Following the trend of advanced sensors is to proceed to data digitization as soon as possible in a system, saving power and delicate analog signal transmissions. To achieve that ambitious goal, I have proposed to intiate the development of a miniature full custom A/D conversion stage, able to convert the analogue outputs of D2R1 in parallel and in a very short time. We increased the challenge by trying to realize the conversion using a Wilkinson type ADC. This type of ADC is known to be relatively slow, as the code is generated waiting for a ramping up voltage to cross the value to encode. The reason for this choice relies on the high degree of linearity of this kind of component as well as its potential for parallel channels and low power.

We have decided to realize this circuitry using an AMS CMOS 0.35 μm standard technology, for which we have a excellent experience in radiation hardening.

- **OWB-1 Design**

  The chip we have designed (F. Bouyjou as lead designer) in the frame of Caliste-MC2 R&D program, supported by CNES, is based on the proven concept of a single slope Wilkinson ADC with a Delay Lock Loop (DLL) boost and a single ramp distributed to parallel ADC channels. The architecture inherits directly from E. Delagnes' work on the WILKY chip at CEA, in our microelectronics group at CEA/IRFU [8.23]. The OWB-1 ASIC brings significant innovations from the front-end versatile input buffer, the on-chip 100 MHz clock generator PLL, radiation hard design, temperature dependence compensation system, adjustable dynamic range from 10 to 13 bits, different readout modes and many other options to make this chips as flexible as possbile.

In single ramp architecture, the analog input voltage is converted into a time measured by using a clock counter. The operating principle is that a discriminator makes a comparison between the input voltage to convert V_{IN} and a ramp generator voltage V_{RAMP}. The counter starts simultaneously with the ramp. The value of the counter is stored when the discriminator triggers when the ramp voltage is equal to V_{IN}. The counter binary word corresponds to the digital value of V_{IN}. The resolution N of this ADC is formulated as follows:

$$N = \log_2(T_S \times F_{CLK}) \qquad \text{(Eq. 21)}$$

Where T_S is the sampling time and F_{CLK} the clock frequency. The advantages of this architecture are a lower power consumption and small surface design.

The main drawback of such a system is its slow speed and can be mitigated using a DLL boost. The idea is that the N most significant bits are obtained with a clock counter operating at a moderate frequency F_{CLK} while the M least significant bit are obtained by a time interpolator made of Delay Lock Loop (DLL) acting like vernier measurement of the ellapsed time from the trigger to the next clock.

The DLL is located right after the discriminator. A new multiple timing division F_{DLL} of the clock frequency F_{CLK} is expressed as $F_{DLL} = 1/(2^M \times F_{CLK})$. The number of DLL cells activated between the trigger of the discriminator (asynchronous) and the next rising edge clock FCLK improves the timing accuracy of the system. In our chip, the counter has 8 bits resolution with F_{CLK} = 100 MHz while the DLL run at a frequency of *FDLL = 3.2 GHz* bringing the final resolution to 13 bits.

It makes our ADC a "super fast" Wilkinson device with a conversion time of only 2.56 μs for 13 bits.

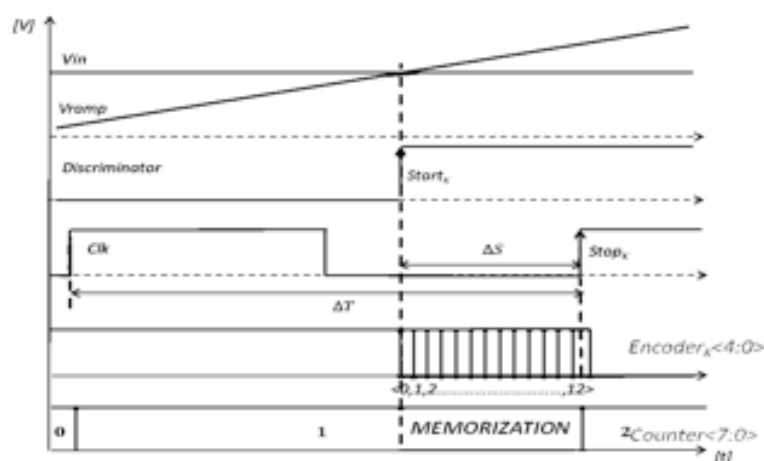A chronogram of the single ramp with a DLL boosts ADC architecture operation is presented in Figure 68.

Figure 67. Chronogram of the single ramp with a DLL boosts ADC architecture operation.

The ramp generator is common to all the 32 channels and each channel has its own counter, discriminator and DLL bank.

Using 16 differential inputs instead of 32 single channels, we bring the resolution up to 14 bits.

- Results

    The chip has been designed, realized and fully tested. The circuit is shown on Figure 68. Table 13 summarizes the experimental performances of our circuit.

All parameters were found nominal. We could measure a time conversion of 2.56 µs for 13 bits dynamic with a noise figure no larger than 0.29 LSB in the low end. Thanks to the Wilkinson architecture, the Integral Non Linearity is in the order of 0.01 %. The power was measured to ~1 mW/channel. I emphasize the fact that unused channels may be simply turned off to save power.

This work has been presented in IEEE/NSS conference in 2015 and will be submitted to IEEE Transaction In Nuclear Sciences.

Table 13. OWB-1 main facts.

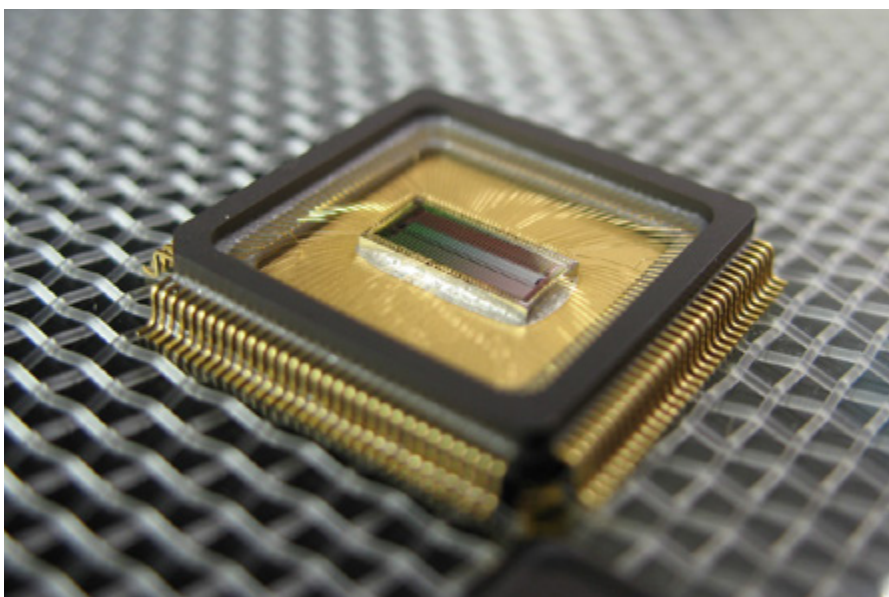| Performances	
Number of Channels	32
Resolution	13-bit
Conversion Time	2.56 µs
Input voltage	2 V
noise (rms)	From 0.29 up to 0.87 LSB over the full dynamic range Corresponds to a 71 to 212 µV rms noise level
DNL	-0.28/+0.31 LSB
INL	-1.3/+2.1 LSB
Power Consumption	Max: 57 mW Typical: 37 mW
Radiations	SEL threshold > 62.5 MeV.cm^2.mg^{-1}

Figure 68. OWB-1 chip encapsulated in a CQFP 128 ceramic carrier.

3. Conclusions

Preparing for the future, I initiated a new R&D program to create a new Caliste product having an excellent energy resolution down to 500 eV at 60 keV with a 300 micron pitch, pixelated CdTe Schottky detector. This new module will be fully digital and embed a new generation of fast A/D conversion stage based on a Wilkinson type architecture with DLL. This module will have a 4 cm^2 area and will be equipped with 4096 indepent pixels with automatic triggering capability. The threshold will be kept as low as 1 keV.

The realization of this mid term project relies on anticipated demonstration of building blocks like Caterpylar, D^2R_1 and OWB-1 ASICs. These ASIC protytpes have been successfully built and tested.

The promising results encourage us to pursue our efforts, starting to implement the module into an innovative 3D technology. For that purpose, I will lead the R&D program focusing on the upgrade of our front-end circuitry, on the delicate flip-chip technology and the hybridization of the parts into a single modular detection unit: Caliste-MC2.

7. General conclusions

I reported in this dissertation the main subject of the instrumental research I led during the last 12 years: The story of Caliste. This CdTe based device, is devoted to hard X-ray imaging spectrometry with the demanding challenge of offering the highest achievable energy resolution together with adequate spatial resolution to sample point sources at the focus of hard X-ray mirrors. Caliste has been designed with a very versatile technology. This modular detection unit is based on a 3D packaging System In Package technology promoted by 3D plus with the key idea of placing the electronics ASICs vertical, perpendicularly to the sensor plane. This technology enabled us to realize a high performance device in different versions, with pixel pitches ranging from 1 mm down to 580 µm. All our modules brought excellent and uniform energy response with an energy resolution better than 700 eV fwhm at 60 keV and a unique low-threshold value of 1.2 keV; a record.

These properties, in addition to the compliance of the system to space standards, supervised by CNES and approved by ESA in 2012, make the device, one of the best or the best device in the world in the family of CdTe based detections systems.

This success results from a united and large team that I built up across Irfu, bringing microelectronics engineers, seminconductor physicists, space engineers, technicians, and students to create a world class imaging spectrometer. We managed to demonstrate a high technological readiness level, combined with a high performance level. Thanks to this substantial effort, we finally earned our "ticket" for a space flight with STIX, a spectrometer on board Solar Orbiter to image the solar flares on board Solar Orbiter. At the time of writing these lines, we just succedded in the completion of the quadrant "Q2" of the FM#1, a major milestone for my team and for the project (Figure 69). We also fully completed the FM production of Caliste and we now proceed to the follow-up of the instrument until the end of the integration and the launch in 2018.
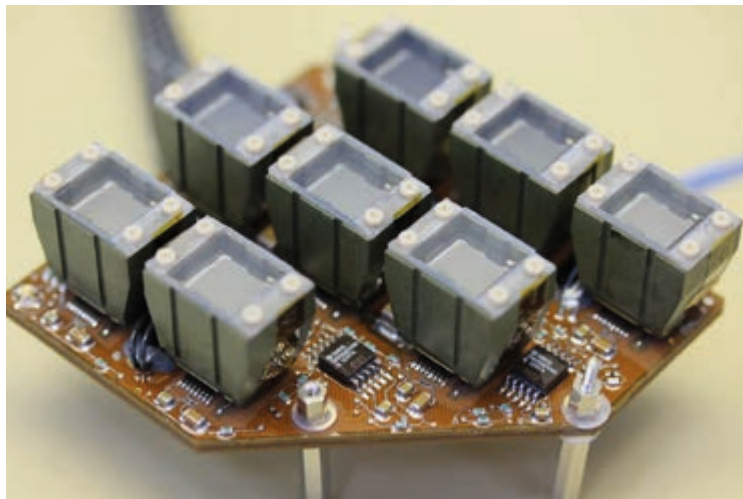

Figure 69. Quandrant Q2 of FM#1, Solar Orbiter/STIX. (Credit: F. Perrin, Syderal). The Caliste modules are mounted on our first flight model. A grey colour cover cap to prevent any damage at crystal level protects the modules.

The impact of our research is beyond this realization simply because the performances of our ASICs and hybrids are unique. I would like to illustrate some of the derivative projects that we were able to sustain in parallel with the core development program – projects that I did not mention in the dissertation:
- First of all, the attractive low-threshold value was a characteristic of our fully custom ASICs since the early versions of IDeF-X. We could demonstrate a value down to 4 keV or less since 2004. It had a major impact on the

ECLAIRs CdTe imager of the SVOM mission to study Gamma Ray Bursts, and led to a scientific requirement. For the first time, it was achievable to foresee GRB detection at cosmological distances with a unique X and gamma ray instrument. We completed the chip development and the delivery of flight models in 2007. The chip are now integrated in the instrument, scheduled to fly in 2021.

- In parallel, we were developing the HED (High Energy Detector) of the SIMBOL-X mission. In March 2009, CNES announced the termination of the project in phase B – a blow to my team. After this set-back, Pr. Tadayuki Takahashi invited me, as a CdTe expert, to evaluate the ASTRO-H CdTe based instruments (HXI and SGD), ans specifically the engineering degree of maturity of the instruments. After this meeting in late 2009, I raised few issues to be fixed and Pr. T. Takahashi asked me to join ASTRO-H and help in these matters. Philippe Laurent and I suggested to ESA to procure hardware contributions (BGO crystals for HXI and SGD vetos) and expertise activities (Radiation tolerance assessment on HXI and SGD ASICs, radiation tolerance assessment on CdTe Schottky detectors and long term stability of CdTe equipped with Schottky contacts). We built a team managed by Benoît Horeau as a project manager and we are still involved today in lab operations on HXI. Since that time, we are proud to be "ASTRO-H" team members (Andrea Goldwurm, Philppe Laurent, Daniel Maier and myself) in the HXI and SGD teams. At the time of writing down these lines, we are a week before ASTRO-H launch in Tanegashima… San, Ni, Ichi… I conclude from that opportunity that Caliste effort brought us into the light and led us to join one of the most advanced CdTe team in the world; a major impact of our work in my opinion.

- At the same period, dec. 2009, I had the chance and the honour to meet Pr. Robert Lin (UCB/SSL). He simply asked me if we could use our IDeF-X chips to read out Si diodes with IDeF-X in order to take advantage of our super low threshold for Energetic Neutral Atoms detection on board the CINEMA nanosat trio. We delivered circuits for that project and we installed a formal international collaboration that is still going on after Robert passed away in November 2012. Robert paved the way of electron and ion detection with Si diodes readout by IDeF-X. Today, CINEMA 4 is in preparation, EPD/STEP (Figure 70) on board Solar Orbiter uses the same technology with LBNL and the University of Kiel and many other opportunitites will come up for sure.

Beyond these realizations, I wish to emphasize the important effort of my team to promote our technologies in future space mission candidates following the ESA calls for L1, M3 and M4. We devoted a significant part of our development time to study the former IXO project in collaboration with JAXA/ISAS, the readout electronics of the large SDD array for LOFT or ASTROGAM, a large Compton based telescope where stacks of large silcon detectors covered by strips could be readout again by IDeF-X in a "Large capacitance" configuration. Each time, the high performance and high TRL of our devices and electronics were appreciated to support the proposals, even if, I must admit, they were not successful up to now.
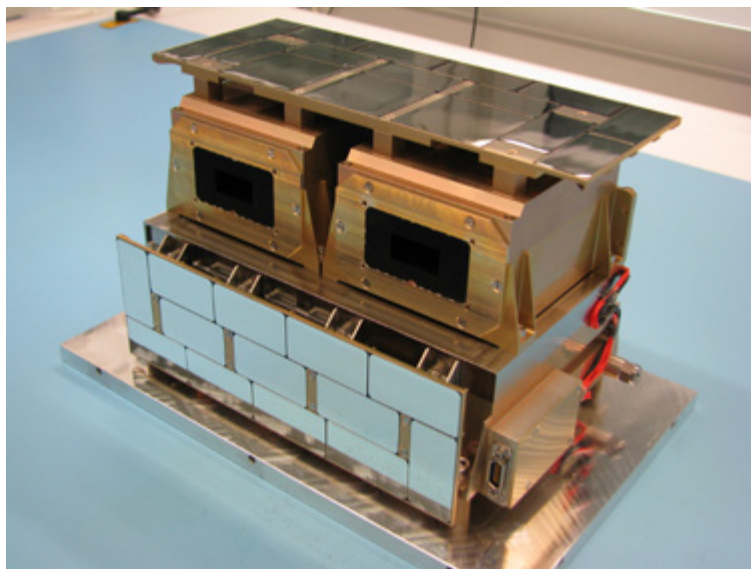

Figure 70. Picture of the EPD/STEP instrument Pre Qualification Model on Solar Orbiter. The two dark apertures are the location where electrons and ions enter into the instrument and hit the pixelated silicon sensor read out by IDeF-X BD, able to read diodes at the cathode.

Thanks to our results, my team has also been solicited to contribute to missions of opportunity, such as:

- SORENTO (Russian Academy of Sciences/Lebedev Physical Institute), an imaging spectrometer on board the Inter Helio Probe Solar mission. The program includes two satellites to observe the Sun with a stereoscopic capability. The program is planned for launch in 2025. SORENTO is very similar to STIX with a hardware extension using MACSI type of pixelated array, providing unique polarization capabilities in hard X-rays.

- Another promising opportunity could be a French participation to FOXSI, a SMEX[1] satellite by NASA to observe solar flares with a 5 arcseconds resolution grazing incidence mirror with 15 m focal length. In this project, high-count rate capabilities as well as excellent spatial resolution are required to sample the point-spread function. Naturally, a low threshold well below 3 keV and an excellent spectral response could be major characteristics of the focal planes. This proposal is in preparation. Our detectors could be in competition with other systems, however we have a key advantage: a high TRL.

- Microsatellite or emerging nanosatellite programs also constitute a field of interest. Here, low power capabilities and tiny dimensions of our modules are the main characterisitics to promote a Caliste solution. In these Low Earth Orbit programs, it is envisioned to observe solar flares and to combine observations with Solar Orbiter. From the Earth, the system constraints are much less demanding and allow a higher telemetry rate. Photon-photon downlink is achievable. The use of small pixels could also bring some bright flare polarization measurements.

Modern research in instrumentation also aims at bringing direct detection solutions for ground based applications in the industrial world, homeland security or medical science. For instance, we earned a grant in 2014 to use Caliste-HD in portable devices (called WIX) for nuclear inspection, in particular in the case of an accident in nuclear plants. The property of an imaging spectrometer is very useful for the identification and the localization of radioisotopes in an unknown landscape. This is the goal of the ORIGAMIX program for which we have developed a miniature probe with unprecedented performance. Figure 71 illustrates the results. We have installed a Caliste-HD unit into a tiny sealed chamber equipped with peltier coolers, electrical interface and readout electronics including an on-board computer. A coded mask aperture is easily positioned and aligned in front of the camera body and a gamma ray image can be recorded in a wide field of view (~ 90°x90°). Thanks to Caliste-HD performance, a radioactive source can be identified and located simultaneoulsy. In this example, a 70 MBq Am-241[2] is identified and located in less than a fraction of a second when the camera is place 1 meter away from the source. Our prototype weighs far less than 1 kg in total and can be operated wirelessly. WIX can be connected to a network of synchronized camera to increase the sensitivity and enable Compton imaging. It works in a range from 2 keV up to 1 MeV.
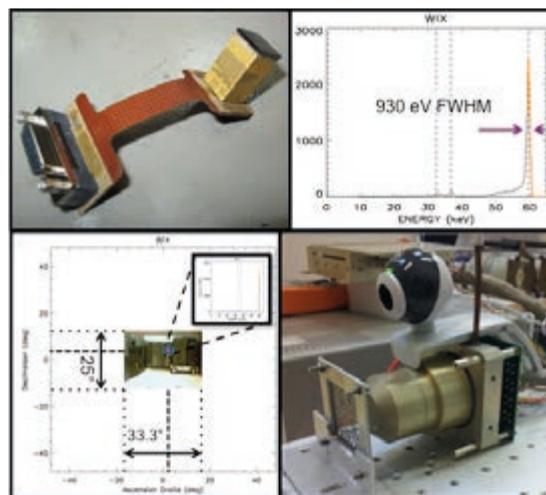

Figure 71. ORIGAMIX project: top-left – Caliste-HD mounted on a flex-rigid PCB; bottom-right – WIX: Caliste is emebeded into a tiny chamber equipped with peltier coolers; bottom-left: superimposition of the gamma ray field (90°x90°) and a video (25°x33°) of a scene where an Am-241 is positionef; top-right – the Am-241 is identified with its spectral signature recorded by Caliste-HD.

---

1. SMEX: Small Explorer mission by NASA

2. Equivalent to ~2500 smoke alarms (30 kBq).

It is highly probable that the WIX portable device can find many other applications, for instance in radiotherapy monitoring, active dosimetry, clinical tests on small animals, non destructive inspection, or drone-borne applications and more... Working with key players in a number of applications fields, such as DRT/LIST (Technological Research/ Nuclear instrumentation at CEA), DEN (Direction of Energy at CEA), DOSEO, and industrial actors like Canbera/ARE-VA and 3D plus will raise opportunities to quickly realize transfer of technology from fundamental research to society.

Regarding the forthcoming work, I demonstrated that I have already initiated the development of Caliste-MC2 for fine pitch and fine spectral response spectroscopy. This device will probably require another five years development to reach a high maturity level. This project has a high priority for me.

Beside this program that I extensively developed in my dissertation, I am also involved in R&D program towards soft X-ray polarization. I already demonstrated the power of Caliste in the hard X-ray and soft gamma ray domain. In the range of soft X-ray, gaseous detectors are proposed to measure the polarization by tracking the photoelectron trajectory [8.24, 8.25 and 8.26]. With Esther Ferrer-Ribas, I am co directing the PhD thesis of Paul Serrano, focused on the development of innovative gaseous detectors for soft X-ray polarimetry, based on photoelectron tracking. Instead of using GEM technology, we use Micromesh and Piggy Back technology developed at Saclay. The original idea of the concept is to readout a gaseous detector through a dielectric layer without direct electrical contact. This technique causes a deficit of the signal, which is compensated by inducing the signal on the supersensitive electronics of Caliste. Thanks to the pixelated surface of Caliste on one hand, and the use of a dispersive resistive layer in the gas on the other hand, we could image a magnified photoelectron track into a Piggy Back gaseous detector, a condition to extract the polarization parameters (Figure 72). The electronics being placed out of the gas vessel, we claim that our system is immune to sparks caused by cosmic rays in the instrument, a major improvement for this kind of apparatus. The first results are very promising and we just submitted a couple of papers on that new device named Caliste-MM [4.5 and 8.27].

Currently, at least two phase A studies are programmed to start for XIPE (ESA) and IXPE (NASA) devoted to polarization in soft X-rays and could constitute new opportunities to collabotate in future high-energy astronomy space missions.
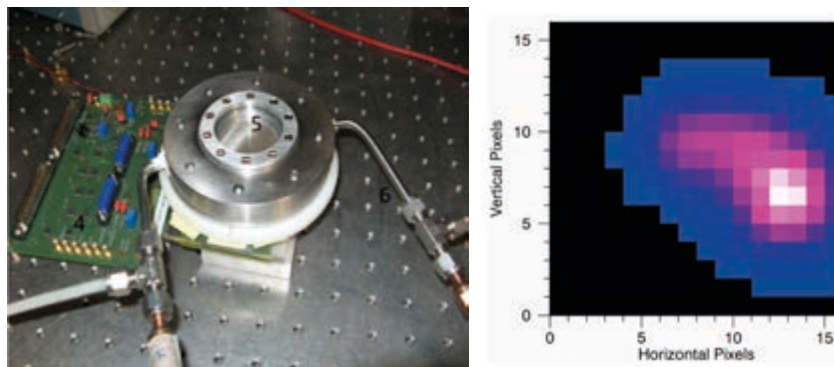

Figure 72. Left – Caliste-MM prototype, a gaseous detector for soft X-ray polarimetry with contact free readout electronics and PiggyBack detector. Right – Track of a photoelectron ejected after a 8 keV photon interaction in Helium at atmospheric pressure.

I would like to emphasize the essential role of the industry in my R&D work progress. From the beginning of Caliste project, I worked with 3D plus (Marie-Cécile Vassal and Fabrice Soufflet) in a very close relationship to install a long-term collaboration. Whatever the kind of contract we put in place at the start. 3D plus engineers played a major role in the success of Caliste, first constructing the devices of course, but also opening the doors of their technology, into the finest details, and factory in order to push the technology together. A long-term partnership based on innovation and trust is born and I believe Caliste is only the beginning.

Finally, and this is this certainly the sense of such a document, Caliste is the fruit of the motivation and competence of a team, including PhD students, research engineers and technicians that I had the chance to lead and with whom I share the success of our work everyday.

8. Supplementary bibiliographic references

1. E. Churazov, R. Sunyaev, J. Isern, J. Knödlseder, P. Jean, F. Lebrun, N. Chugai, S. Grebenev, E. Bravo, S. Sazonov, M. Renaud. SN2014J: Cobalt-56 γ-ray emission lines from the type Ia supernova 2014J, Nature, 512, 2014, p. 406

2. M. Renaud, J. Vink, A. Decourchelle, F. Lebrun, P. R. den Hartog, R. Terrier, C.Couvreur, J. Knödlseder, P. Martin, N. Prantzos, A. M. Bykov, H. Bloemen. The Signature of 44Ti in Cassiopeia A Revealed by IBIS/ISGRI on INTEGRAL, THE ASTROPHYSICAL JOURNAL LETTERS, Volume 647, Number 1, 2006.

3. Grefenstette, Harrison *et al.* Asymmetries in core-collapse supernovae from maps of radioactive 44Ti in Cassiopeia A, Nature, 506, 2014, p. 339.

4. Grebenev, *et al.*, Hard X-ray emission lines from the decay of 44Ti in the remnant of Supernova 1987A, S. A. Nature, 490, 2012, p. 373.

5. http://www.isdc.unige.ch/integral/science/catalogue

6. F. Lebrun, R. Terrier, A. Bazzano, G. Bélanger, A. Bird, L. Bouchet, A. Dean, M. Del Santo, A. Goldwurm, N. Lund, H. Morand, A. Parmar, J. Paul, J.-P. Roques, V. Schönfelder, A. W. Strong, P. Ubertini, R. Walter & C. Winkler. Compact sources s the origin of the soft gamma-ray emission of the Milky Way, , NATURE, 428, 2004, p. 293-296.

7. V. R. Rana *et al.* Development of Focal Plane Detectors for the Nuclear Spectroscopic Telescope Array (NuSTAR) Mission, Proc. SPIE Int.Soc.Opt.Eng., 7435, 2009, p. 2.

8. F.A., Cook, W. Rick, Forster, Karl, *et al.* The Nuclear Spectroscopic Telescope Array (NuSTAR) High-energy X-ray Mission, Harrison, 2013, ApJ, 770, Issue 2, p. 103.

9. M.D. Wilson, L. Dummott, D.D. Duarte, F.H. Green, S. Pani, A. Schneider, J.W. Scuffham, P. Sellera, P. Vealea. A 10 cm × 10 cm CdTe Spectroscopic Imaging Detector based on the HEXITEC ASIC, M.C., JOURNAL OF INSTRUMENTATION, vol. 10, October 2015.

10. R. Elsner, B. Ramsey, C. Wilson-Hodge, A. Tennant, S. Christe, A. Shih, K. Kilaru, D. Swartz, P. Seller, M. Wilson, D. Stuchlik, B. Weddendorf, SuperHERO: Design of a New Hard-X-ray Focusing Telescope, IEEE Aerospace Conference, 2015.

11. Funaki *et al.* Development of CdTe Detectors, http://www.acrorad.co.jp/_skin/pdf/Development_of_CdTe_detectors.pdf.

12. Shiraki *et al.* THM Growth and characterization of 100 mm Diameter CdTe Single Crystals, IEEE TNS, vol. 56, n° 4, 2009, p. 1717.

13. B.P.F. Dirks. Study and modelling of the new generation Cd(Zn)Te X- and gamma-ray detectors for space applications, Thèse de Doctorat, Université Paris 7, 2006.

14. Siefert *et al.* Polarization in Cadmium Telluride Nuclear Radiation Detectors, IEEE, TNS, vol. 23, n° 1, 1976, p. 159.

15. A. Meuris. Étude et optimisation du plan de détection de haute énergie en Cd(Zn)Te de la mission spatiale d'astronomie X et gamma Simbol-X, Thèse de Doctorat, Université Paris 7, 2009.

16. S. Dubos. Nouveau spectro-imageur CdTe à très haute resolution spatiale et spectrale pour l'astronomie X et gamma, Thèse de Doctorat, Université Paris 7, 2015.

17. Emerson Vernon, Kim Ackley, Gianluigi De Geronimo, Jack Fried, Zhong He, Cedric Herman, and Feng Zhang, ASIC for High Rate 3D Position Sensitive Detectors, IEEE TRANSACTIONS ON NUCLEAR SCIENCE, vol. 57, n° 3, June 2010.

18. Thomas A. Prince, Gordon. J. Horford, H. S. Hudson *et al.* "Gamma-Ray and Hard X-ray Imaging of Solar Flares", *Solar Physics* 118 (1998): 269-290.

19. A. Michalowska. Studies and development of a readout ASIC for pixelated CdTe detectors for space applications, Thèse de Doctorat, Université Paris Sud, 2013.

20. http://www.xfab.com/home/

21. http://ams.com/eng

22. M.N. Mazziotta. Electron–hole pair creation energy and Fano factor temperaturedependence in silicon, NIMA A, 584 (2008) 436-439.

23. E. Delagnes, D. Breton, F. Lugiez, R. Rahmanifard. A low power multi-channel single ramp ADC with up to 3.2 GHz virtual clock. Nuclear Science, IEEE Transactions on, 54(5), 2007, 1735-1742.

24. P. Soffitta *et al.*. XIPE: the X-ray Imaging Polarimetry Explorer, Experimental Astronomy, 2013.

25. S. Fiabiani *et al.*. The imaging properties of the gas pixel detector as a focal plane polarimeter, *Suppl. ApJ*, 2014.

26. R. Bellazzini *et al.* A sealed Gas Pixel Detector for X-ray astronomy, NIMA 579 (2007) p. 853.

27. P. Serrano, D. Attié, D. Desforges, E. Ferrer Ribas, F. Jeanneau, O. Limousin. Caliste-MM: A Spectro-Polarimeter based on the Micromegas concept for Soft X-ray Astrophysics, submitted to JINST, 2016.

28. G. De Geronimo, P. O'Connor. "A CMOS Fully Compensated Continuous Reset System", in Proc. IEEE NSS-MIC conf. Rec., 1999.

29. http://asic.ams.com/gelato/

30. MIL-STD-883H, Departement of Defense, Test Method Standard Microcircuits, 2010.

31. http://cmp.imag.fr/products/ic/?p=prices

32. Seller, *et al.*, Pixellated Cd(Zn)Te High Energy X-Ray Instrument, Journal of Instrumentation, Vol. 6, No. 12, 2011

33. Wilson, *et al.*, Multiple Module Pixellated CdTe Spectroscopic X-Ray Detector, IEEE Trans. On Nucl. Science, vol. 60, n° 2, April 2013, 1197-1200.

34. Sato, *et al.*, Development of Low Noise Front-End ASIC for Hybrid CdTe Pixel Detectors, IEEE Trans. On Nucl. Science, vol. 58, n° 3, June 2011, 1370-1375.

35. Chen, *et al.*, Characterization of the HEFT CdZnTe Pixel Detectors, Proc. SPIE5198, Hard X-Ray and Gamma-Ray Detector Physics V.9, January 2004.

36. Oonuki, *et al.*, Development of Uniform CdTe Pixel Detectors Based on Caltech ASIC, Proc. SPIE 2004.

37. Watanabe, *et al.*, High Energy Resolution Hard X-Ray and Gamma-Ray Imagers Using CdTe Diode Devices, IEEE Trans. On Nucl. Science, vol. 56, n° 3, June 2009.